Three Dimensional Atom-Diatom Reactive Scattering Calculations Using Symmetrized Hyperspherical Coordinates

Thesis by

Paul Gregory Hipes

In Partial Fulfillment of the Requirements

for the Degree of

Doctor of Philosophy

California Institute of Technology

Pasadena, California

1988

(Submitted November 6, 1987)

ACKNOWLEDGMENTS

Much of the work described in this thesis is the result of discussions with and support from the people around me. Most of these people have influenced me both as a scientist and as a person. It has been a pleasant surprise to discover that much science is done through interactions with my friends and colleagues.

The contributions of my thesis advisor, Aron Kuppermann, to this work and to my professional growth are many. Much of my research was originally suggested by him. I would like to thank him for his patience and broad perspective during times when progress was slow or mistakes were made. In addition, I wish to acknowledge his diligence in maintaining the resources necessary for the completion of my work.

My friends have provided an invaluable support network and many years of conversions both scientific and eclectic. Diane Zirin, Dan Zirin, Joseph Wong, Charlie Koerting, Jerry Winniczek, Jim Garvey, Mark Wu, Zhengwei Peng, Maria Arnazzi, Issac Zavier, Mary Rodgers, and Dave Moll have all made life at Caltech cheerful and interesting. Steve Cuccaro, Garth Parker, Kerry Walzl, Zeta Khundkar, and Chris Sipes have been good friends and more important than I can say.

Finally, I wish to acknowledge my family. My wife, Lesa Hipes, has always been interested in my research and has supported me through many years of long hours and emotional lows. Since this thesis is a product of my graduate years, it important to mention one of the greatest joys of this time: the births of David and Caroline. For her support during my years of study, I also wish to thank my mother.

ABSTRACT

The focus of this thesis is the use of symmetrized hyperspherical coordinate techniques in the accurate calculation of differential cross sections for the reactive collision of an atom with a diatomic molecule in three-dimensional space. A single set of symmetrized hyperspherical coordinates treats all regions of configuration space in an equivalent manner and thereby reduces the reactive scattering problem to an equivalent inelastic scattering problem which is conceptually and computationally easier to handle.

The work described here represents the first successful application of any accurate hyperspherical coordinate methodology to atom-diatom reactive scattering in three-dimensional space. This methodology has permitted the calculation of zero total angular momentum ($J = 0$) partial wave transition probabilities and associated phases over a significantly larger range of collision energies (up to 1.6 eV total energy) than previously possible for the system $H + H_2$. The numerical stability of the treatment is sufficiently high to permit the first lifetime matrix analysis of the resonance structure of $H + H_2$ based on scattering matrices from our accurate calculations. This analysis reveals a series of 6 resonance states in the $J = 0$ partial wave, some of which have not been seen before. The symmetrized hyperspherical coordinate methodology is presented in detail. A selection of surface functions and scattering results for $J = 0$ $H + H_2$ using the LSTH potential energy surface are presented and discussed. In addition, a small number of results from the Porter-Karplus potential energy surface are also given.

TABLE OF CONTENTS

Introduction

This thesis is composed of a series of papers in which different aspects of the computational methodology and results are presented. Some of these papers are already in the literature and some are not. Since they are papers, they can be read more or less independently. Motivational and background discussions are a component of the introduction in each chapter so this type of exposition is omitted from this introduction. Instead, an overview of each chapter is given below, in order to bring a measure of coherence to the thesis as a whole.

Chapter two contains a detailed exposition of the symmetrized hyperspherical coordinate approach to reactive atom-diatom scattering calculations using body-fixed coordinates and the necessary asymptotic analysis which transforms the numerical solutions into scattering matrices. The formal expansion in a basis set, the surface functions, and the resulting coupled set of ordinary differential equations are discussed. One novel feature of this chapter is that we have made full use of the permutation symmetry for the case where all three particles are identical. Such symmetry reduces the numerical effort required to solve the scattering problem. A second topic of interest in this chapter is the asymptotic analysis based on the hyperspherical logarithmic derivative matrix at a single value of the hyperradius.

Chapter three presents the details of the finite element method of calculating surface functions. The use of permutation symmetry to find boundary conditions for the surface functions on a subdomain of the complete domain of definition of these functions is novel and reduces the numerical effort needed to calculate the surface functions. Contour plots of some surface functions are used to explain the efficiency of the surface functions as a basis set for expanding the scattering wave function. The structure of the surface functions and their evolution with the hyperradius are discussed in detail.

Chapter four is a reprint of the publication presenting results from the first successful use of symmetrized hyperspherical coordinates to calculate results for three-dimensional reactive atom-diatom scattering. The calculations are for $J = 0$ $H + H_2$ on the Porter-Karplus potential energy surface II. Probability curves for several reactive transitions are shown along with results of previous independent calculations on the same system. The purpose of this communication is to validate the new symmetrized hyperspherical coordinate methodology.

Chapter five is a reprint of a publication which explores the resonance structure in $H + H_2$ and contains the results of extensive calculations on $J = 0$ $H + H_2$ using the Porter-Karplus potential energy surface II. The range of collision energies presented in this paper is considerably greater than any previous calculations.

Chapter six contains a large sample of scattering results for the $J = 0$ partial wave of $H + H_2$ on the LSTH potential energy surface. Included are transition probabilities, partial wave cross sections, and lifetime matrix analyses for all three irreducible representations of the P_3 permutation group. This chapter represents the most extensive set of three-dimensional atom-diatom reactive scattering results available. A unique feature of this chapter is the presentation of irreducible representation labeled results instead of the usual distinguishable particle representation results. One advantage to the former is that they are closely related to the Pauli antisymmetrized results.

The appendix is composed of two sections which describe work related to the topic of three-dimensional reactive scattering. In the first section, the Gauss-Jordan matrix inversion algorithm for the Caltech Hypercube is discussed. Matrix inversion is a necessary part of an algorithm for propagating the coupled ordinary differential equations which results from the expansion of the scattering wave function in a surface function basis set. The implementation of matrix inversion

on the hypercube is a first step in assembling the complete propagator. Detailed tests of the performance of the parallel matrix inverter are provided in this section. In section two of the appendix, a reprint of a collinear atom-diatom reactive scattering paper is presented. The reaction modeled is hydrogen atom transfer between two methyl radicals which are represented as mass points. The accurate numerical solutions to this problem were obtained using hyperspherical coordinates as applied to collinear reactive scattering. The purpose of this paper is to assess the accuracy of the vibrationally adiabatic model of light atom transfers in collinear reactive systems proposed by Babamov and Marcus. Their model is based on their recognition that hyperspherical coordinates are ideal for treating collinear light atom transfer. In this paper, the Babamov-Marcus model is shown to be very accurate.

The common theme of this thesis is easily seen to be the application of hyperspherical coordinates to reactive scattering problems. Their use is a decisive advance in the area of reactive scattering; however, accurate three-dimensional reactive scattering calculations remain very difficult to perform. The work found in these chapters is a first step towards the goal of accurate *ab initio* differential cross section calculations.

Three-dimensional Atom-Diatom Reactive Scattering Calculations Using Symmetrized Hyperspherical Coordinates I. Reactive Scattering Formalism †

Paul G. Hipes ¶ and Aron Kuppermann

Arthur Amos Noyes Laboratory of Chemical Physics,
Division of Chemistry and Chemical Engineering, ‡
California Institute of Technology,
Pasadena, California 91125

(Received)

Abstract

This paper describes an application of the symmetrized hyperspherical coordinate formalism to quantum mechanical atom-diatom reactive scattering. The implications of permutation symmetry, when it exists in a system, are investigated extensively because such symmetry implies significant savings in numerical applications. In addition, a simple, constant-hyperradius projection technique for obtaining the scattering matrix from the hyperspherical logarithmic derivative is presented.

1. Introduction

Accurate quantum mechanical solutions for reactive atom-diatom scattering have proved to be difficult and computationally expensive to obtain.[1] In fact, only three groups to date have published exact differential or integral cross sections, and all three calculations are based on the system $H + H_2$. In the last year, four groups have published preliminary results for several reactive atom-diatom systems, which is an exciting developement. Accurate numerical reactive cross sections would allow an interplay between theory and experiment which is vital to a healthy physical science. Perhaps more importantly, the existence of accurate benchmark calculations provides validation of approximate theories which in turn provides physical insights into the chemistry.

The first calculations of accurate quantum mechanical cross sections for $H + H_2$ are those of Schatz and Kuppermann[2a,c] and Elkowitz and Wyatt.[3] Both groups used the Porter Karplus potential energy surface PKII.[4] The collision energies are limited to those below the opening of $v = 1$. Integral cross sections for both LSTH[5-7] and PKII surfaces over the same energy range have been calculated using a third method by Walker, Stechel, and Light.[8] The methods used in these calculations have proven difficult to extend to higher energies.

One obstacle to the numerical treatment of the atom-diatom scattering problem has been the need for matching solutions which are based on the Jacobi coordinates in different arrangement channels.[2b] One technique to overcome the need for matching is the use of a set of coordinates which is appropriate for all arrangement channels. Hyperspherical coordinates are such a set of coordinates.

Hyperspherical coordinates have been extensively tested in collinear calculations on a large number of systems.[9,10] Matching of solutions is not a difficulty in collinear calculations; however, hyperspherical coordinates have made it possible to treat heavy-light-heavy mass combinations[11,12] and collision-induced dissociation[13,14] which are time consuming or very difficult by other methods. Furthermore, hyperspherical coordinate methodology in collinear calculations has

proven to be more efficient than the older propagation methods.[15] In addition, they have been used for a qualitative[16,17] and quantitative[18] understanding of dynamic resonances[19-21] in collinear scattering, and they are appropriate for the modeling of light atom transfer in these systems.[22] These kinds of coordinates have been used in other areas of atomic physics for over 50 years.

Hyperspherical coordinate methodologies have been applied to a variety of problems in atomic[23] and nuclear[24] physics. They are first discussed by Gronwall[25] and Bartlett[26] for the electronic structure of He and are used for electronic structure problems by Wannier[27] and Fock.[28] Macek[29] used hyperspherical coordinates to correctly model the doubly excited states inferred from the autoionization Rydberg series of He.[30] This success led to renewed interest in hyperspherical coordinates for electronic motion in two-electron systems.[23,31-35] The principal idea used in these systems is to consider the hyperradial motion (slow) as adiabatically decoupled from the hyperangular degrees of freedom (fast). Some of the quasibound excited states which result correspond to doubly excited states of the atomic system which may autoionize or autodetach or represent resonances in electron atom scattering. The adiabatic approach provides quantum numbers to associate with such states and the quantum numbers are in good accord with experimental information. The adiabatic states incorporate correlation of the hyperangular motion of the electrons, and such correlation is important for a understanding of doubly excited states of two-electron systems. In nuclear scattering theory,[24] hyperspherical coordinates are first discussed by Clapp[36] and later by Delves[37] as a technique for incorporating break-up collisions.

There are a number of different systems of hyperspherical coordinates in the literature and they have one important characteristic in common. All of the systems of hyperspherical coordinates use a coordinate which measures the size or extension of the system and is not specialized to one arrangement channel. It is called the hyperradius and is singled-out as the generalized collision (propagation) coordinate in scattering calculations and as the adiabatic coordinate in

bound and quasi-bound problems. The hyperspherical coordinates introduced by Gronwall[25] and Bartlett[26] and those used by Delves[37] are similar; the only difference is Delves' use of mass scaling. Another set of hyperspherical coordinates were introduced by Whitten and Smith.[38] One feature of the potential energy contours for three particle systems is that they do not reflect the symmetry of the potential energy function for identical particles. This happens because the three internal coordinates on which the potential depends do not undergo an orthogonal transformation when a different set of arrangement channel Jacobi coordinates is used. Kuppermann[39] introduced a symmetrized version of Delves' hyperspherical coordinates whose internal coordinate subset does undergo orthogonal transformations and suggested for the first time that they would be useful for the study of reactive scattering problems.[40] Other versions of symmetrized hyperspherical coordinates have subsequently been proposed by Johnson, [41,42] (based on the Smith-Whitten coordinates) by Mead,[43] and Pack.[44]

The application of hyperspherical coordinates to atom-diatom scattering in three-dimensional space has met with more difficulty than was the case for two electron systems. The main source of difficulty is the existence of three bound arrangement channels instead of two (as is the case in two electron systems). As a result, the numerical task for reactive atom-diatom scattering is significantly larger, even for the highly symmetric system $H + H_2$. It should be emphasized that the hyperspherical formalism is not more difficult in atom-diatom scattering than in other systems; rather, the numerical algorithms are simply more expensive to implement.

Two groups are employing hyperspherical coordinates for 3D atom-diatom reactive scattering and have very recently published scattering calculations on $J = 0$ $H + H_2$. We have calculated reaction probabilities over an energy range which extends beyond the opening of $v = 2$ and have found that the hyperspherical methodology is effective enough to allow us to calculate lifetime matrices over the entire energy range.[45] Parker, Pack, Archer, and Walker[46] have published reaction

probabilities over a slightly smaller energy range. Parker *et. al.* have also done the even parity component of $J = 1$ for $H+H_2$ for a smaller energy range and also some low energy $J = 0$ $H+D_2$ calculations. In addition to these scattering calculations, Linderberg and coworkers[47] are developing a hyperspherical coordinate approach.

Two groups have reported scattering probabilities in the last year for the lowest total angular momentum partial wave ($J = 0$) of $H+H_2$ and $D+H_2$ for an extensive range of collision energies using non-hyperspherical coordinate techniques. Webster and Light[48] have published reaction probabilities for the several isotopic analogues of $H + H_2$ using an extension of the methodology of Walker, Stechel, and Light and have shown that their approximate matching method can be extended beyond the earlier calculations. Haug, Schwenke, Shima, Truhlar, Zhang, and Kouri have used a L^2 method[49] to study the $J = 0$ partial wave scattering of $D+H_2$[50] and $O+H_2$.[51] Although Haug *et. al.* have not used a hyperspherical coordinate technique, they have nevertheless surmounted the matching problem and produced an innovative computational method for reactive scattering. The appearance of successfully implemented new methods for treating reactive scattering problems may indicate that differential cross sections for atom diatom reactions will soon be available for a wider class of reactions and over a substantially larger energy range than possible before.

The prospect for accurate calculations of differential and integral cross sections over a large energy range for $H + H_2$ and its isotopic analogues is especially exciting in view of the number of new experiments on this system.[52–57] Because only $J = 0, 1$ results have been calculated at the energies of these experiments, no direct comparisons have yet been possible between accurate quantum results and experiment.

Models for calculating reactive cross sections[58–65] are very important because they provide important physical insights in addition to requiring less numerical effort. This is not the place to review the variety of approximate quantum theories, but it would be a disservice to leave the impression that the field of

theoretical chemical dynamics is static due to the immaturity of accurate methodologies. An accurate (and expensive) approximate theory is the coupled states appoximation[58,59] (CS). This method ignores only the Coriolis-coupling in the body-fixed Hamiltonian.[2b] Bowman[60] and Walker and Hayes[61] have developed the collinear exact quantum bending corrected (CEQB) methodology which consists of incorporating an adiabatic bend approximation into the rotating linear theory of Wyatt[62] and of Connor and Child.[63] Several of the most important approximate theories are discussed in the excellent series of books edited by M. Baer.[65] The methods discussed there in detail include the quasiclassical trajectory method, the variational transition state technique, the reactive infinite order sudden approximation, and the T matrix based approximations.

Which of the approximate theories works best and in what circumstances? In order to answer this question, it is vital to have accurate benchmark treatments of several atom-diatom systems over an extended energy range. Since only for $H+H_2$ have such accurate solutions been obtained and those solutions are restricted to a limited range of collision energies, the validity of approximate theories is difficult to evaluate. Hopefully, these issues can be resolved for three particle reactive systems in the next few years.

This paper is arranged as follows. Section 2 presents the various Jacobi coordinates and the corresponding Schrödinger equation. Section 3 introduces the symmetry group of the Hamiltonian. Section 4 describes the symmetrized hyperspherical coordinates and associated surface functions. Section 5 has a discussion of the diabatic coupled channel expansion. Section 6 presents the Wigner rotation matrix expansion of the surface functions. Section 7 introduces the asymptotic scattering conditions. Section 8 describes the partial wave expansion of the scattering asymptotic boundary conditions. Section 9 introduces the constant ρ projection technique. Section 10 discusses the separable basis set used for intermediate values of the hyperradius. Section 11 presents the construction of

antisymmetrized cross sections from irreducible representation (of P_3) scattering amplitudes. In section 12, our main points are summarized.

2. Schrödinger's Equation

In this section, the Schrödinger equation in Jacobi coordinates and in the mass-scaled coordinates of Delves for a three particle system is examined. This discussion is entirely general with regard to the nature of the particles. All of this material can be found in other sources[2b] and is presented here for the convenience of the reader and to establish the notation used in this paper.

Given a system of three atoms A_λ, A_ν, and A_κ with masses m_λ, m_ν, and m_κ, respectively, the usual Jacobi coordinates are $(\mathbf{R}'_\lambda, \mathbf{r}'_\lambda)$ where $\mathbf{R}'_\lambda$ is the vector from the center of mass of the diatomic molecule $A_\nu A_\kappa$ to the atom A_λ and $\mathbf{r}'_\lambda$ is the vector from the atom A_ν to the atom A_κ. The Hamiltonian for the three particles in this Jacobi, center of mass coordinate system is

$$\hat{H} = \frac{-\hbar^2}{2\mu_{\lambda,\nu\kappa}} \nabla^2_{\mathbf{R}'_\lambda} - \frac{\hbar^2}{2\mu_{\nu\kappa}} \nabla^2_{\mathbf{r}'_\lambda} + V'^{\lambda}(R'_\lambda, r'_\lambda, \gamma_\lambda) \tag{1}$$

where

$$\mu_{\lambda,\nu\kappa} = \frac{m_\lambda(m_\nu + m_\kappa)}{m_\lambda + m_\nu + m_\kappa} \tag{2}$$

$$\mu_{\nu\kappa} = \frac{m_\nu m_\kappa}{m_\nu + m_\kappa} \tag{3}$$

are the reduced masses corresponding to the vectors $\mathbf{R}'_\lambda$ and $\mathbf{r}'_\lambda$. $V'^{\lambda}(R'_\lambda, r'_\lambda, \gamma_\lambda)$ is the potential energy function describing the interactions of the three particles and $\lambda\nu\kappa$ is a cyclic permutation of $\alpha\beta\gamma$. The coordinate γ_λ is the angle between the vectors $\mathbf{R}'_\lambda$ and $\mathbf{r}'_\lambda$ and the symbols R'_λ,r'_λ are the lengths of the vectors $\mathbf{R}'_\lambda$ and $\mathbf{r}'_\lambda$. In the case of three atoms, $V'^{\lambda}(R'_\lambda, r'_\lambda, \gamma_\lambda)$ is the single Born-Oppenheimer electronic potential energy surface governing the interaction of the three nuclei. The λ superscript on this function indicates that it is expressed in the λ Jacobi coordinates.

The Hamiltonian can be put in a simpler form by the introduction of mass-scaled coordinates,[2b,37] defined as

$$\mathbf{R}_\lambda = a_\lambda \mathbf{R}'_\lambda \tag{4}$$

$$\mathbf{r}_\lambda = a_\lambda^{-1} \mathbf{r}'_\lambda \tag{5}$$

$$a_\lambda = \left(\frac{\mu_{\lambda,\nu\kappa}}{\mu_{\nu\kappa}}\right)^{\frac{1}{4}} \tag{6}$$

The Schrödinger equation in mass-scaled, center of mass coordinates is

$$\left[\frac{-\hbar^2}{2\mu}\left(\nabla^2_{\mathbf{R}_\lambda} + \nabla^2_{\mathbf{r}_\lambda}\right) + V^\lambda(R_\lambda, r_\lambda, \gamma_\lambda) - E\right]\Psi(\mathbf{R}_\lambda, \mathbf{r}_\lambda) = 0 \tag{7}$$

where

$$\mu = \left(\frac{m_\lambda m_\nu m_\kappa}{m_\lambda + m_\nu + m_\kappa}\right)^{\frac{1}{2}} \tag{8}$$

is the single reduced mass for the system of particles and E is the total energy in the center of mass coordinate system. A change of coordinates, $\lambda \rightarrow \nu$, is a simple orthogonal transformation in the six dimensional configuration space spanned by $(\mathbf{R}_\lambda, \mathbf{r}_\lambda)$ when the mass scaled coordinates are used.[15] The mass-scaled Schrödinger equation has the same form as that for a single particle of mass μ in a six dimensional Euclidean space. Unless explicitly stated otherwise, all coordinates are mass scaled.

We now turn to the characterization of solutions to the Schrödinger equation when the particles are identical. These solutions will be chosen to belong to the irreducible representations of the symmetry group of the Hamiltonian. Although our main topic is the significance of the group of permutations of three identical particles in scattering, we will treat all of the symmetries of the Hamiltonian at once.

3. Symmetry Group of the Hamiltonian

In this paper, except for Section 11, we will consider only the spatial coordinate part of configuration space. The spin degrees of freedom associated with the particles will be treated in Section 11 where the Pauli principle is considered.

The complete symmetry group of the Hamiltonian is the set of all operators which commute with the Hamiltonian and is organized into operator subgroups which follow naturally from the character of the symmetry operations. The operators do not all commute among themselves and so a wave function cannot be chosen to be a simultaneous eigenfunction of all of the operators. Instead, the wave function can be chosen to transform according to an irreducible representation of each subgroup of operators. We will discuss each of these subgroups of operators beginning with the rotation group.

Rotational invariance of the Hamiltonian permits us to choose the spatial wave function to belong to an irreducible representation of the subgroup $SO(3)$ of the complete symmetry group of the Hamiltonian. Because we are considering only the spatial part of the wave functions, only the single-valued representations of $SO(3)$ need be considered. The labelling of these representations follows from the their behavior under $\hat{J}^2$, the operator for the square of the total spatial angular momentum. The spectrum for this operator consists of the values $J(J+1)\hbar^2$, where $J = 0, 1, 2, \ldots$; hence, the quantum number J is a convenient label for the irreducible representations. The J irreducible representation has dimensionality $2J+1$. A basis for the invariant subspace corresponding to an irreducible representation is fixed by choosing each function to be an eigenfunction of the operator $\hat{J}_Z$, the operator for the space-fixed Z component of the total angular momentum, with eigenvalues $M\hbar$ where $M = 0, \pm 1, \pm 2, \ldots, \pm J$. That the wave function can be chosen to transform as an irreducible representation of $SO(3)$ and that it is a simultaneous eigenfunction of $\hat{J}^2$ and $\hat{J}_Z$ are equivalent statements. The language of irreducible representations of groups of operators is chosen because it is natural for the case of discrete symmetry operations.

The discrete symmetry subgroups of the symmetry group of the Hamiltonian are the inversion group, the time-reversal group, and the group of permutations of the identical particles among themselves. The inversion group is denoted $\mathfrak{S}$ and consists of the two operators $\hat{I}$ and $\hat{E}$, where $\hat{E}$ denotes the identity and

$\hat{I}$ inverts the spatial coordinates of all the particles through the center of mass. $\Im$ has two irreducible representations labelled by $\Pi = \pm$. The second discrete subgroup is composed of the identity operator and the time reversal operator which reverses the direction of time, The time reversal subgroup permits us to chose the time-independent wave function to be a real function which leads to a symmetric scattering matrix. The final group of discrete symmetry operations is the set of all possible permutations of three identical particles and is denoted as P_3[66] (more recently S_3[67a]). It has irreducible representations labelled by $\Gamma \in (A_1, A_2, E)$. It will be recognized that these are the labels commonly used for the irreducible represenations of the point group C_{3v} which is isomorphic with the group P_3. We employ these irreducible representation labels because they have familiar meanings. The E representation is doubly degenerate while A_1 and A_2 are nondegenerate. In the asymptotic regions of configuration space, the spatial solutions which transform as A_1 (A_2) are composed of even (odd) rotational states of the diatomic molecules. Those that transform as E contain both even and odd rotational diatomic states. These facts will be discussed in much more detail in later sections.

The existence of symmetry in a physical system leads to the ability to construct solutions to the Schrödinger equation which transform under the symmetry operations as irreducible representations of the operator groups. The irreducibility means that a solution is uniquely specified by its representation labels. Solutions which do not transform as irreducible representations are found by taking linear combinations of the irreducible solutions. Let us assemble together the labels which identify the irreducible representations to which the spatial wave function belongs and affix them as superscripts to the solution: $\Psi^{J,M,\Pi,\Gamma,i}$. $J = 0, 1, 2, \ldots$ is the total angular momentum quantum number and $M = 0, \pm 1, \pm 2, \ldots, \pm J$ is the quantum number associated with the projection of the total angular momentum onto a space-fixed axis. $\Pi = \pm$ is the parity label. $\Gamma \in (A_1, A_2, E)$ is the irreducible representation of the permutation group P_3. The superscript i denotes

the row within this irreducible represenation. To proceed with the construction of solutions with these irreducible representation labels, we next discuss the choice of internal coordinates (*i.e.*, those three parameters on which the interaction energy depends).

4. Symmetrized Hyperspherical Coordinates and Surface Functions

It has been proposed[39,40] and validated[45] for $J = 0$ that symmetrized hyperspherical coordinates which are derived from the $R_\lambda, r_\lambda, \gamma_\lambda$ coordinates are well suited for 3D reactive atom-diatom scattering. They have the attribute of treating all arrangement channels equivalently and are defined as[39]

$$\rho = \left(R_\lambda^2 + r_\lambda^2\right)^{\frac{1}{2}}; \qquad 0 < \rho \leq \infty \tag{9}$$

$$\omega_\lambda = 2\arctan\left(\frac{r_\lambda}{R_\lambda}\right); \qquad 0 \leq \omega_\lambda \leq \pi \tag{10}$$

and the corresponding Hamiltonian is

$$\hat{H} = -\frac{\hbar^2}{2\mu}\left(\frac{\partial^2}{\partial\rho^2} + \frac{5}{\rho}\frac{\partial}{\partial\rho}\right) + \frac{\hat{\Lambda}^2}{2\mu\rho^2} + \overline{V}(\rho, \omega_\lambda, \gamma_\lambda) \tag{11}$$

where

$$\hat{\Lambda}^2 = -4\hbar^2\left(\frac{\partial^2}{\partial\omega_\lambda^2} + 2\cot\omega_\lambda\frac{\partial}{\partial\omega_\lambda}\right) + \frac{\hat{j}_\lambda^2}{\sin^2\frac{\omega_\lambda}{2}} + \frac{\hat{l}_\lambda^2}{\cos^2\frac{\omega_\lambda}{2}} \tag{12}$$

and $\hat{j}_\lambda$ is the angular momentum operator corresponding to $\mathbf{r}_\lambda$ and $\hat{l}_\lambda$ is that corresponding to $\mathbf{R}_\lambda$. The parameter ρ is independent of $\lambda \in (\alpha, \beta, \gamma)$ and *is invariant under all of the symmetry operations of the Hamiltonian.* This characteristic of the hyperradius is an indication of its special nature. We leave unspecified the system of axes needed to resolve the vectors $\vec{R}_\lambda$ and $\vec{r}_\lambda$ for the moment.

Any set of coordinates can be used to express the wave function; however, the coordinate choice becomes important when the wave function is expanded in a basis set where the basis functions depend on a subset of the coordinates. In order for such an expansion to converge in a small number of terms, the Schrödinger

equation must be nearly separable in the coordinates chosen. This property exists in the hyperspherical coordinates: ρ is nearly separable from the remaining five coordinates. Hyperspherical coordinate methods have been extensively tested and validated in collinear quantum reactive scattering calculations where coupled channel expansions converge rapidly.[9,10] As the expansion basis set, we define surface functions[40] for 3D scattering by $\Phi_n^{J,M,\Pi,\Gamma,i}(\zeta_\lambda;\rho)$ by

$$\left[\frac{\hat{\Lambda}^2}{2\mu\rho^2} + \overline{V}(\rho,\omega_\lambda,\gamma_\lambda) - \epsilon_n(\rho)\right]\Phi_n^{J,M,\Pi,\Gamma,i}(\zeta_\lambda;\rho) = 0 \tag{13}$$

and

$$\int \Phi_{n'}^{*J',M',\Pi',\Gamma',i}(\zeta_\lambda;\rho)\Phi_n^{J,M,\Pi,\Gamma,j}(\zeta_\lambda;\rho)d\tau_1 = \delta_{J,M}^{J',M'}\delta_{\Pi}^{\Pi'}\delta_{\Gamma,j}^{\Gamma',i}\delta_n^{n'} \tag{14}$$

with $d\tau_1 = \sin^2\omega_\lambda d\omega_\lambda d^2\hat{R}_\lambda d^2\hat{r}_\lambda$ as the correct volume element. We have used the symbol ζ_λ for the five hyperangles $(\omega_\lambda, \hat{r}_\lambda, \hat{R}_\lambda)$, where $\hat{R}_\lambda$ and $\hat{r}_\lambda$ stand for the pairs of angles necessary to specify the direction of the vectors $\mathbf{r}_\lambda$ and $\mathbf{R}_\lambda$, respectively in a coordinate system which we leave completely general, at present. In Section 6, we will define the body-fixed set of coordinates which we used in our calculations.

The surface functions are labeled with J, M, Π, Γ, i because they are defined to transform as irreducible representations of the groups $SO(3)$, $\Im$, and P_3. This is possible since the operator $\hat{\Lambda}^2$ is invariant under all of the symmetry operations of the Hamiltonian. The subscript n on $\Phi_n^{J,M,\Pi,\Gamma,i}$ and ϵ_n provides a labelling for the infinite discrete surface function spectrum. The surface function eigenvalues are discrete because of the bounded nature of their domain: they depend on a set of five angles.

The recent papers of Pack and Parker[46] and of Wolniewicz and Hinze[42] analyze the differences in some of the common hyperspherical systems of coordinates and both papers raise a criticism of the present hyperspherical coordinates: the points $\omega_\lambda = 0, \pi$ are singular points in the canonical angular momentum operator (12). The $\omega_\lambda = \pi$ point appears especially troubling because it cuts though one of the saddle points in a collinearly dominated reaction. However, we will see in

Section 6 that the volume element vanishes at these singular points as $\sin^2\omega_\lambda$, so the second order zero in the volume element removes the second order pole in the equation (12). In other words, the singular points have measure zero. For this reason, they do not represent a pathology in the symmetrized hyperspherical coordinates, and no difficulty is expected by their use, contrary to the statements in the literature. To elaborate on this point, we note that the singular points in the variable ω_λ can be removed from equation (13) by an appropriate change of dependent variables as

$$\overline{\Phi}_n^{J,M,\Pi,\Gamma,i}(\zeta_\lambda;\rho) = \sin\omega_\lambda \Phi_n^{J,M,\Pi,\Gamma,i}(\zeta_\lambda;\rho) \tag{15}$$

The new dependent variables vanish at the points $\omega_\lambda = 0, \pi$. In paper II, the variational principle for the surface functions is discussed and the variational integrals will be shown to exist in spite of the singular points, due to the presence of the appropriate volume element. The same conclusion holds for the interaction and overlap matrices.

5. Locally Diabatic Surface Function Expansion

The surface functions, in addition to being discrete, span the three arrangement channels and provide an effective basis set in which to expand the scattering wave function. We expand the scattering wave function as

$$\Psi^{J,M,\Pi,\Gamma,i}(\rho,\omega_\lambda,\hat{r}_\lambda,\hat{R}_\lambda) = \rho^{-\frac{5}{2}} \sum_n G_n^{J,\Pi,\Gamma}(\rho;\overline{\rho})\Phi_n^{J,M,\Pi,\Gamma,i}(\zeta_\lambda;\overline{\rho}) \tag{16}$$

where the surface functions are calculated at $\overline{\rho}$. This is an efficient expansion when ρ is near $\overline{\rho}$. In this sense we say that the surface function basis set is a local basis set. As a result of the isotropicity of space and the indistinguishability of the particles, it can be shown that the coefficients in the expansion are independent of the labels M and i, so these labels do not appear in the differential equation for the coefficients. Since the parameter $\overline{\rho}$ is considered to be fixed in any given expansion, the surface function basis set is diabatic in ρ.

The expansion in surface functions yields the following set of coupled ordinary differential equations in the variable ρ:

$$\frac{d^2}{d\rho^2}G_n^{J,\Pi,\Gamma}(\rho;\overline{\rho}) + \sum_{n'} U_{n,n'}^{J,\Pi,\Gamma}(\rho;\overline{\rho})G_{n'}^{J,\Pi,\Gamma}(\rho;\overline{\rho}) = 0 \tag{17}$$

where

$$U_{n,n'}^{J,\Pi,\Gamma}(\rho;\overline{\rho}) = \delta_{n,n'}\left\{\frac{2\mu}{\hbar^2}\left[E - \left(\frac{\overline{\rho}}{\rho}\right)^2 \epsilon_n(\overline{\rho})\right] - \frac{15}{4\rho^2}\right\} + \Delta V_{n,n'}^{J,\Pi,\Gamma}(\rho;\overline{\rho}) \tag{18}$$

with

$$\Delta V_{n,n'}^{J,\Pi,\Gamma}(\rho,\overline{\rho}) = \frac{2\mu}{\hbar^2}\int \Phi_n^{*J,M,\Pi,\Gamma,i}\left[\left(\frac{\overline{\rho}}{\rho}\right)^2 \overline{V}(\overline{\rho},\omega_\lambda,\gamma_\lambda) - \overline{V}(\rho,\omega_\lambda,\gamma_\lambda)\right]\Phi_{n'}^{J,M,\Pi,\Gamma,i} d\tau_1 \tag{19}$$

In the next section we will see that the integral over five angles can be reduced analytically to an integral over the two angles ω_λ and γ_λ on which the potential energy depends.

With a given set of surface functions at $\overline{\rho}$, the interaction matrix $\mathbf{U}^{J,\Pi,\Gamma}(\rho;\overline{\rho})$ is calculated as a function of ρ and the system of ordinary differential equations (17) is integrated by any of a number of standard algorithms.[68] We have used Johnson's logarithmic derivative integrator[69] in our numerical work. One important point to be emphasized is the independence of the surface functions (13) and numerical integrals (19) of the collision energy E. The surface functions and their integrals are calculated only once and the ordinary differential equations (17) are propagated for each collision energy using the same surface function set. Such propagation is a well developed tool and the collision energy independence of the surface functions allows a large number of collision energies to be calculated.

Surface functions at a single $\overline{\rho}$ are not efficient for expanding the wave function for all values of ρ. The strategy is to calculate a set of surface functions at each of a family of values of the hyperradius $\overline{\rho}_i$, $\quad i = 0, 1, 2, \ldots$. For each value of $\overline{\rho}_i$, the system of ordinary differential equations is integrated as an initial value problem. The range of ρ over which a single surface function set is used is called a sector.

With the exception of the very first sector beginning at ρ_0, the initial conditions follow from continuity of the wave function and its ρ derivative between sectors. This information is carried in overlap matrices which are calculated for surface function sets at adjoining values of the hyperradius: $\overline{\rho}_i$ and $\overline{\rho}_{i+1}$. The overlap matrices are

$$O^{J,\Pi,\Gamma}_{n,n'}(\overline{\rho}_{i+1},\overline{\rho}_i) = \int \Phi^{*J,M,\Pi,\Gamma,i}_{n}(\zeta_\lambda;\overline{\rho}_{i+1})\Phi^{J,M,\Pi,\Gamma,i}_{n'}(\zeta_\lambda;\overline{\rho}_i)d\tau_1 \qquad (20)$$

These overlap matrices provide a means of calculating the $G^{J,\Pi,\Gamma}_{n}(\rho;\overline{\rho}_{i+1})$ from the $G^{J,\Pi,\Gamma}_{n'}(\rho;\overline{\rho}_i)$. The transformation from the $G^{J,\Pi,\Gamma}_{n'}(\rho;\overline{\rho}_i)$ to the $G^{J,\Pi,\Gamma}_{n}(\rho;\overline{\rho}_{i+1})$ is accomplished by

$$G^{J,\Pi,\Gamma}_{n}(\rho;\overline{\rho}_{i+1}) = \sum_{n'} O^{J,\Pi,\Gamma}_{n,n'}(\overline{\rho}_{i+1},\overline{\rho}_i)G^{J,\Gamma,\Pi}_{n'}(\rho;\overline{\rho}_i) \qquad (21)$$

The ρ derivative of $G^{J,\Gamma,\Pi}_{n'}(\rho;\overline{\rho}_i)$ is transformed by the same equation (21) because the surface functions are used as a diabatic basis set.

The overlap matrices (20) are unitary if the surface function sets at the two values of $\overline{\rho}_i$ are complete. Completeness of the surface function sets requires that the expansion in (16) include an infinite number of terms. In applications, this is not the case, and the overlap matrices are only approximately unitary. The lack of unitarity leads to loss of particle flux when changing surface function sets. Fortunately, it is possible to determine the total loss of flux in the final results of the scattering calculation. The loss of flux is determined by the lack of unitarity of the scattering matrix. In addition, it is possible to reduce the particle flux loss in basis set changes by including more terms in the expansion (16) or by decreasing the distance $\Delta\overline{\rho}_i = \overline{\rho}_{i+1} - \overline{\rho}_i$ between successive diabatic basis sets. Therefore, the flux losses are easily determined and can be made as small as desired.

The initial conditions for the very first sector are the only missing pieces of information in the formal algorithm (given the surface functions). The second order ordinary differential equations (17) require a choice of the values of the functions $G^{J,\Pi,\Gamma}_{n}(\rho,\overline{\rho})$ and their ρ derivative at the initial value $\overline{\rho}_0$ of ρ. The first

datum is simple; for sufficiently small ρ, the three particles are very close spatially and the potential energy is large and positive. Under this condition, the initial scattering wave functions can be set to zero. This leaves the ρ derivative to be specified.

It would be ideal if a judicious choice of the first derivative in ρ could be made so that a specific asymptotic behavior in ρ is obtained. However, it is not known how to accomplish this. Instead, the well known S matrix method[70] is used. In this method, a set of linearly independent solutions to the initial value problem are calculated by choosing arbitrary, but distinct, values for the ρ derivatives of $G_{n'}^{J,\Gamma,\Pi}(\rho;\overline{\rho}_i)$. Linear combinations of these integrated solutions then approximate the scattering boundary conditions. In Section 9, a method will be described for linearly combining the integrated solutions in order to construct a desired set of asymptotic boundary conditions.

The superscripts J,Π,Γ on $G_n^{J,\Pi,\Gamma}(\rho;\overline{\rho})$ denote the irreducible representation of the associated surface functions and not the transformation properties of the $G_n^{J,\Pi,\Gamma}(\rho;\overline{\rho})$ themselves. As remarked earlier, the hyperradius is invariant under all of the symmetry operations of the Hamiltonian. Any function of the hyperradius alone is likewise invariant under all of the symmetry operations, so the $G_n^{J,\Pi,\Gamma}(\rho;\overline{\rho})$ are invariant under all symmetry operations. The conclusion is that the transformation properties of the surface functions determine the transformation properties of the entire solutions.

6. Surface Functions in the Wigner Rotation Matrix Representation

The surface functions are defined to belong to the irreducible representations of $SO(3)$. To fulfill this requirement, it is useful to remember that the potential energy depends on only three "internal" variables $\rho,\omega_\lambda,\gamma_\lambda$. Three remaining "external" variables describe the overall orientation of the instantaneous triangle defined by the three particles. A set of Cartesian axes fixed with respect to the instantaneous triangle and independent of $\rho,\omega_\lambda,\gamma_\lambda$ is called the body-fixed

frame.[71-73] The external variables are the three Euler angles needed to relate the body-fixed axes to the center of mass non-rotating axes.[74]

There are, of course, an infinity of possible body-fixed axes. Our choice[2b] is to make the positive direction of the body-fixed z axis be in the same direction as $\mathbf{R}_\lambda$. Then the first two Euler angles are $\varphi_\lambda, \vartheta_\lambda$, the spherical polar angles of the vector $\mathbf{R}_\lambda$ with respect to a non-rotating, center of mass system of axes. This specifies the body-fixed axes to within a rotation about the body-fixed z axis which is given by the third and last Euler angle ψ_λ. We choose ψ_λ to make the final body-fixed y axis fall along $\mathbf{R}_\lambda \times \mathbf{r}_\lambda$ (in direction and orientation). With this choice, the body-fixed y axis is normal to the plane of the three particles. A λ subscript on the Euler angles reminds us that the body-fixed z axis is in the direction of $\mathbf{R}_\lambda$. It is easily seen that $y_\alpha = y_\beta = y_\gamma$; the same body-fixed y axis results from each of the Jacobi coordinate systems. An implication is that the transformation from one set of body-fixed coordinates, say λ, to another, say ν, consists of a single rotation about the common body-fixed y axis.

The complete set of symmetrized hyperspherical body-fixed coordinates are $(\rho, \omega_\lambda, \gamma_\lambda, \vartheta_\lambda, \varphi_\lambda, \psi_\lambda)$. The final set of body-fixed axes are denoted by $x_\lambda, y_\lambda, z_\lambda$ and the center of mass, nonrotating axes by X, Y, Z. We will use the term space-fixed axes for center of mass axes that are not rotating with respect to the laboratory. The volume element in these body-fixed symmetrized hyperspherical coordinates is

$$d\tau = \frac{1}{8}\rho^5 d\rho d\tau_1 \tag{22}$$

$$d\tau_1 = \sin^2\omega_\lambda \sin\gamma_\lambda \sin\vartheta_\lambda d\omega_\lambda d\gamma_\lambda d\vartheta_\lambda d\varphi_\lambda d\psi_\lambda \tag{23}$$

Equation (23) is the explicit form of the volume element with the body-fixed angles that was defined after equation (14) with four of the angles unspecified.

The behavior of the system under rigid rotations is represented by the dependence of its wave function on the Euler angles. If the surface functions belong to

an irreducible representation of $SO(3)$, then their dependence on the Euler angles must be identical with that of the Wigner rotation matrices.[74]

The irreducible representations of the group $SO(3)$ are commonly called the Wigner rotation functions and are denoted by $D^J_{M,\Omega}(\varphi_\lambda, \vartheta_\lambda, \psi_\lambda)$[74] where $\varphi_\lambda, \vartheta_\lambda, \psi_\lambda$ are the Euler angles corresponding to our choice of body-fixed axes. J is the quantum number corresponding to the operator $\hat{J}^2$, M is that corresponding to $\hat{J}_Z$, and Ω is that corresponding to $\hat{J}_{z_\lambda}$. In other words, these functions satisfy

$$\hat{J}^2 D^J_{M,\Omega}(\varphi_\lambda, \vartheta_\lambda, \psi_\lambda) = J(J+1)\hbar^2 D^J_{M,\Omega}(\varphi_\lambda, \vartheta_\lambda, \psi_\lambda) \tag{24}$$

$$\hat{J}_Z D^J_{M,\Omega}(\varphi_\lambda, \vartheta_\lambda, \psi_\lambda) = M\hbar D^J_{M,\Omega}(\varphi_\lambda, \vartheta_\lambda, \psi_\lambda) \tag{25}$$

$$\hat{J}_{z_\lambda} D^J_{M,\Omega}(\varphi_\lambda, \vartheta_\lambda, \psi_\lambda) = \Omega\hbar D^J_{M,\Omega}(\varphi_\lambda, \vartheta_\lambda, \psi_\lambda) \tag{26}$$

as well as the orthogonality relationship

$$\int D^{*J'}_{M',\Omega'}(\varphi_\lambda, \vartheta_\lambda, \psi_\lambda) D^J_{M,\Omega}(\varphi_\lambda, \vartheta_\lambda, \psi_\lambda) \sin^2\vartheta_\lambda d\varphi_\lambda d\vartheta_\lambda d\psi_\lambda = \frac{8\pi^2}{2J+1}\delta^{J',M',\Omega'}_{J,M,\Omega} \tag{27}$$

For the present application, the labels J and M are conserved quantum numbers. Ω is the projection quantum number of the total spatial angular momentum onto the body-fixed z_λ axis and is not conserved quantum number because $\hat{J}_{z_\lambda}$ does not commute with the canonical angular momentum operator (12). Therefore, using the Wigner rotation functions to express the dependence of the surface functions on the Euler angles requires that we take a linear combination of the $D^J_{M,\Omega}(\varphi_\lambda, \vartheta_\lambda, \psi_\lambda)$ with different values of Ω. The coefficients of the expansion depend on the variables $\omega_\lambda, \gamma_\lambda$ and parametrically on ρ. This permits us to write

$$\Phi^{J,M,\Pi,\Gamma,i}_n(\omega_\lambda, \gamma_\lambda, \psi_\lambda, \vartheta_\lambda, \varphi_\lambda; \rho) = \sum_{\Omega=-J}^{J} D^J_{M,\Omega}(\varphi_\lambda, \vartheta_\lambda, \psi_\lambda) \phi^{\lambda,J,\Pi,\Gamma,i}_{\Omega,n}(\omega_\lambda, \gamma_\lambda; \rho) \tag{28}$$

The set of $2J+1$ coupled partial differential equations which the two-angle surface functions, $\phi^{\lambda,J,\Pi,\Gamma,i}_{\Omega,n}(\omega_\lambda, \gamma_\lambda; \rho)$, must satisify follows from insertion of the expansion (28) into the partial differential equation for the surface functions (13)

and the orthogonality of the Wigner rotation matrices. The λ superscript on the $\phi^{\lambda,J,\Pi,\Gamma,i}_{\Omega,n}(\omega_\lambda,\gamma_\lambda;\rho)$ is a reminder that the λ body-fixed axes are used. We discuss the construction of the surface functions via a finite element discretization in paper II. Here we simply wish to introduce the body-fixed coordinates and the usual expansion in Wigner rotation matrices. The existence of body-fixed surface functions is assumed.

The orthonormality of the five angle surface functions and the orthogonality of the $D^J_{M,\Omega}$ lead to the following orthogonality relation for the two angle surface functions.

$$\sum_{\Omega=-J}^{J}\int \phi^{*\lambda,J,\Pi,\Gamma,i}_{\Omega,n}(\omega_\lambda,\gamma_\lambda;\rho)\phi^{\lambda,J,\Pi',\Gamma',j}_{\Omega,n'}(\omega_\lambda,\gamma_\lambda;\rho)d\tau_2 = \left(\frac{2J+1}{8\pi^2}\right)\delta^n_{n'}\delta^\Pi_{\Pi'}\delta^\Gamma_{\Gamma'}\delta^i_j \tag{29}$$

with $d\tau_2 = \sin^2\omega_\lambda d\omega_\lambda \sin\gamma_\lambda d\gamma_\lambda$. The $\phi^{\lambda,J,\Pi,\Gamma,j}_{\Omega,n}(\omega_\lambda,\gamma_\lambda;\rho)$ are orthogonal in n,n' only if the sum over Ω is included along with integration over the continuous variables.

Since the potential energy function does not depend on the Euler angles, the integration over $(\vartheta_\lambda,\varphi_\lambda,\psi_\lambda)$ which appears in (19) can be performed analytically, giving

$$\Delta V^{J,\Pi,\Gamma}_{n,n'}(\rho,\overline{\rho}) =$$
$$C_J\sum_{\Omega=-J}^{J}\int \phi^{*\lambda,J,\Pi,\Gamma,i}_{\Omega,n}\left[\left(\frac{\overline{\rho}}{\rho}\right)^2\overline{V}(\overline{\rho},\omega_\lambda,\gamma_\lambda)-\overline{V}(\rho,\omega_\lambda,\gamma_\lambda)\right]\phi^{\lambda,J,\Pi,\Gamma,i}_{\Omega,n'}d\tau_2 \tag{30}$$

where $C_J = \frac{2\mu}{\hbar^2}\left(\frac{8\pi}{2J+1}\right)$ and the arguments of the $\phi^{\lambda,J,\Pi,\Gamma,i}_{\Omega,n}(\omega_\lambda,\gamma_\lambda;\overline{\rho})$ have been omitted for brevity. Similarly, the overlap matrix integrals in (20) can be rewritten as

$$O^{J,\Pi,\Gamma}_{n,n'}(\overline{\rho}_{i+1},\overline{\rho}_i) =$$
$$\left(\frac{8\pi}{2J+1}\right)\sum_{\Omega=-J}^{J}\int \phi^{*\lambda,J,\Pi,\Gamma,i}_{\Omega,n}(\omega_\lambda,\gamma_\lambda;\overline{\rho}_{i+1})\phi^{\lambda,J,\Pi,\Gamma,i}_{\Omega,n'}(\omega_\lambda,\gamma_\lambda;\overline{\rho}_i)d\tau_2 \tag{31}$$

Notice that there is no explicit Ω label on the interaction and overlap matrices because of the summation over Ω. This agrees with the original construction of the propagation equations (17) through (19) where no Ω exists.

All $2J+1$ components of the two-angle surface functions are associated with a single surface function energy. In other words, the two-angle surface functions with different values of Ω are not to be considered as different surface functions. Instead, they are the components of a single surface function for each energy ϵ_n.

7. Asymptotic Forms

In this section, the asymptotic boundary conditions are considered. The numerical solutions to the Schrödinger equation are labelled by J, Π, and Γ whereas the asymptotic boundary conditions which represent a scattering experiment have no such labels. In this section, we expand the asymptotic boundary conditions as linear combinations of terms which carry the labels J, Π, Γ. This analysis motivates the definition and construction of the P_3 irreducible representation scattering and reactance matrices. The P_3 irreducible representation helicity scattering wave function is most easily derived by first constructing the P_3 irreducible representation space-fixed scattering wave function and transforming it to the helicity form. Such a procedure avoids the difficulty of operating on the wave function with permutation operators when the coordinates themselves depend on the particle labels. The space-fixed coordinates are independent of the particle labels.

A. Distinguishable Particle Representation

The goal of a scattering calculation is to find accurate solutions to Schrödinger's equation which correspond to a scattering experiment. An asymptotic form which describes a scattering experiment has an incident plane wave multiplying the initial state wave function of the diatomic molecule and outgoing spherical waves multiplying each energetically accessible diatom state. One possible form for the asymptotic scattering spatial wave function arises if the identical particles are

assumed to be distinguishable. This assumption is artificial in a quantum mechanical world since the free diatom spectra are identical; however, this asymptotic form corresponds to a classical mechanical world where particle trajectories make even identical particles distinguishable and has been used in other quantum calculations. The coordinates and diatom rotational angular momentum projection quantum numbers are refered to the space-fixed system of axes. For energies significantly below the dissociation energy into three separated atoms, these distinguishable atom boundary conditions are

$$\begin{aligned}
\Psi^{\alpha,t'} \quad &\overset{\alpha}{\sim} \quad e^{i\mathbf{k}_{t'}\cdot\mathbf{R}_\alpha}\phi_{t'}(\mathbf{r}_\alpha) + \sum_t f_{\alpha t}^{\alpha t'}(\vartheta_\alpha,\varphi_\alpha)\frac{e^{ik_t R_\alpha}}{R_\alpha}\phi_t(\mathbf{r}_\alpha) \\
&\overset{\beta}{\sim} \quad \sum_t f_{\beta t}^{\alpha t'}(\vartheta_\beta,\varphi_\beta)\frac{e^{ik_t R_\beta}}{R_\beta}\phi_t(\mathbf{r}_\beta) \qquad (32) \\
&\overset{\gamma}{\sim} \quad \sum_t f_{\gamma t}^{\alpha t'}(\vartheta_\gamma,\varphi_\gamma)\frac{e^{ik_t R_\gamma}}{R_\gamma}\phi_t(\mathbf{r}_\gamma)
\end{aligned}$$

where the first line holds when $R_\alpha \sim \infty$ and r_α is small, the second line holds when $R_\beta \sim \infty$ and r_β is small, and the third line holds when $R_\gamma \sim \infty$ and r_γ is small. The functions $\phi_t(\mathbf{r}_\lambda)$ are the isolated diatom bound state wave functions with energy e_t and satisfy

$$[\frac{-\hbar^2}{2\mu}\nabla_{r_\lambda}^2 + v(r_\lambda) - e_t]\phi_t(\mathbf{r}_\lambda) = 0 \qquad (33)$$

$$\int_0^{r_\lambda^{max}} |\phi_t(\mathbf{r}_\lambda)|^2 d^3\mathbf{r}_\lambda = 1 \qquad (34)$$

The function $v(r_\lambda)$ is the interaction potential of the isolated diatom. The single quantum number t denotes the three diatomic molecule quantum numbers vjm. The quantum number v labels the vibrational levels for a given j where $j(j+1)\hbar^2$ is the square of the diatom rotational angular momentum. The projection of the diatom rotational angular momentum onto the space-fixed Z axis is $m\hbar$. There is no arrangement channel subscript on these quantum numbers since the diatoms are identical by assumption. The incident wave vector is defined by

$$\mathbf{k}_{t'} = \sqrt{\frac{2\mu(E-e_{t'})}{\hbar^2}}\hat{Z} \qquad (35)$$

where $\hat{Z}$ is a unit vector along the positive space-fixed Z axis. The direction of initial wave vector is the same for all arrangement channels. The magnitude of the open ($E > e_t$) scattering wave number vectors is given by

$$k_t = \sqrt{\frac{2\mu(E - e_t)}{\hbar^2}} \tag{36}$$

and for closed states ($E < e_t$) by

$$k_t = \imath\sqrt{\frac{2\mu|E - e_t|}{\hbar^2}} = \imath\kappa_t \tag{37}$$

so that the closed state terms in (32) consist of decaying exponentials only.

The superscipts α, t' on $\Psi^{\alpha,t'}$ and on the scattering amplitudes $f^{\alpha,t'}_{\lambda,t}$ ($\lambda = \alpha, \beta, \gamma$) in equation (32) denote the arrangement channel and diatom state for the incident particles. The subscripts λ, t denote the final arrangement channel and diatom state. (In reference 2b, superscripts on scattering amplitudes denoted final states and the subscripts denoted initial states, which pratice is the opposite of that used here.) Since the quantum numbers t' refer to the initial state of the diatomic molecule in the α arrangement channel, they must refer to an open state. The summations over the quantum numbers t in equation (32) extend over all open and closed states of the diatomic molecule in each arrangement channel.

This form of the asymptotic wave function (32) is known as the distinguishable atom representation because the incident plane wave appears in the α arrangement channel only. Other distinguishable atom asymptotic forms are found by placing the incident plane wave in other diatom states t' or in other arrangement channels. A compact notation for this general asymptotic form is

$$\Psi^{\lambda',t'} \sim \sum_{\lambda}\sum_{t}\left\{e^{\imath\mathbf{k}_t\cdot\mathbf{R}_\lambda}\delta^{\lambda' t'}_{\lambda t} + f^{\lambda' t'}_{\lambda t}(\vartheta_\lambda, \varphi_\lambda)\frac{e^{\imath k_t R_\lambda}}{R_\lambda}\right\}\phi_t(\mathbf{r}_\lambda) \tag{38}$$

The sum over λ is permissible because the $\phi_t(\mathbf{r}_\lambda)$ are nonvanishing in the λ arrangement channel only, so the contribution to the spatial asymptotic form from the other arrangement channels ν and κ vanishes in the λ channel.

If the three particles are identical, then there are only two independent scattering amplitudes (*e.g.*, $f_{\alpha,t}^{\alpha,t'}$ and $f_{\beta,t}^{\alpha,t'}$) for each value of t and t'. The Hamiltonian commutes with all of the permutation operators, so applying a permutation operator to the asymptotic form (32) produces another solution to the Schrödinger equation. Uniqueness of the solutions permits us to relate all the remaining scattering amplitudes to the $f_{\alpha,t}^{\alpha,t'}$ and $f_{\beta,t}^{\alpha,t'}$. For example, applying the 3-cycle permutation operator to a asymptotic form (32),

$$\begin{aligned}
\hat{O}\left[\begin{pmatrix} \alpha & \beta & \gamma \\ \gamma & \alpha & \beta \end{pmatrix}\right]\Psi^{\alpha,t'} &\overset{\gamma}{\sim} e^{i\mathbf{k}_{t'}\cdot\mathbf{R}_\gamma}\phi_{t'}(\mathbf{r}_\gamma) + \sum_t f_{\alpha t}^{\alpha t'}(\vartheta_\gamma,\varphi_\gamma)\frac{e^{ik_tR_\gamma}}{R_\gamma}\phi_t(\mathbf{r}_\gamma) \\
&\overset{\alpha}{\sim} \sum_t f_{\beta t}^{\alpha t'}(\vartheta_\alpha,\varphi_\alpha)\frac{e^{ik_tR_\alpha}}{R_\alpha}\phi_t(\mathbf{r}_\alpha) \qquad (39) \\
&\overset{\beta}{\sim} \sum_t f_{\gamma t}^{\alpha t'}(\vartheta_\beta,\varphi_\beta)\frac{e^{ik_tR_\beta}}{R_\beta}\phi_t(\mathbf{r}_\beta)
\end{aligned}$$

where $\mathbf{k}_{t'}$, the incident wave vector for the γ arrangement channel, points in the direction of the same space-fixed Z as did the incident wave vector for the α arrangement channel. Comparing this solution with equation (38), with $\lambda' = \gamma$, we conclude

$$f_{\gamma,t}^{\gamma,t'} = f_{\alpha,t}^{\alpha,t'} \qquad (40)$$

$$f_{\alpha,t}^{\gamma,t'} = f_{\beta,t}^{\alpha,t'} \qquad (41)$$

$$f_{\beta,t}^{\gamma,t'} = f_{\gamma,t}^{\alpha,t'} \qquad (42)$$

If we apply instead a two-cycle operator to the asymptotic form (32), we find

$$\begin{aligned}
\hat{O}\left[\begin{pmatrix} \alpha & \beta & \gamma \\ \beta & \alpha & \gamma \end{pmatrix}\right]\Psi^{\alpha,t'} &\overset{\beta}{\sim} e^{i\mathbf{k}_{t'}\cdot\mathbf{R}_\beta}\phi_{t'}(-\mathbf{r}_\beta) + \sum_t f_{\alpha t}^{\alpha t'}(\vartheta_\beta,\varphi_\beta)\frac{e^{ik_tR_\beta}}{R_\beta}\phi_t(-\mathbf{r}_\beta) \\
&\overset{\alpha}{\sim} \sum_t f_{\beta t}^{\alpha t'}(\vartheta_\alpha,\varphi_\alpha)\frac{e^{ik_tR_\alpha}}{R_\alpha}\phi_t(-\mathbf{r}_\alpha) \qquad (43) \\
&\overset{\gamma}{\sim} \sum_t f_{\gamma t}^{\alpha t'}(\vartheta_\gamma,\varphi_\gamma)\frac{e^{ik_tR_\gamma}}{R_\gamma}\phi_t(-\mathbf{r}_\gamma)
\end{aligned}$$

Comparing equation (43) with equation (38) with $\lambda' = \beta$, we conclude

$$f^{\beta,t'}_{\beta,t} = (-1)^{\Delta j} f^{\alpha,t'}_{\alpha,t} \tag{44}$$

$$f^{\beta,t'}_{\alpha,t} = (-1)^{\Delta j} f^{\alpha,t'}_{\beta,t} \tag{45}$$

$$f^{\beta,t'}_{\gamma,t} = (-1)^{\Delta j} f^{\alpha,t'}_{\gamma,t} \tag{46}$$

where we have the symbols $t = (v, j, m)$, $t' = (v', j', m')$, and $\Delta j = (j - j')$ and have used the property of the diatomic wave function $\phi_{v,j,m}(-\mathbf{r}_\lambda) = (-1)^j \phi_{v,j,m}(\mathbf{r}_\lambda)$.

Using this technique, it is possible to relate all of the distinguishable particle scattering amplitudes to the independent ones. These relationships are listed in reference 2b.

B. Irreducible Representations of P_3

The distinguishable atom representation asymptotic form, $\Psi^{\lambda',t'}$, does not transform according to any irreducible representation of P_3. To find spatial asymptotic forms that do transform as irreducible representations of P_3, the distinguishable atom asymptotic form (38) is multiplied by the appropriate group theoretic projection operator. This projection operator is given by[67b]

$$\hat{P}^{\Gamma}_{i,i'} = \frac{l_\Gamma}{h} \sum_{\hat{R}} M^{\Gamma^*}_{i,i'}(\hat{R}) \hat{R} \tag{47}$$

where Γ is the irreducible representation, i, i' are the row and column of the representation, l_Γ is the dimensionality of the representation, h is the order (*i.e.*,number of operators) of the group and $M^{\Gamma}_{i,i'}(\hat{R})$ is the i, i' element of the matrix representing the operator $\hat{R}$ for the Γ irreducible representation. The sum in equation (47) is over all of the operators in the group.

We want a scattering wave function corresponding to equation (38) which transforms as an irreducible representation of P_3. Such an irreducible asymptotic wave function is denoted by $\Psi^{\Gamma,i,v'j'm'}$ and is derived by applying the projection operator (47) to the asymptotic form (38) followed by normalization of the resulting wave function. The superscript $\Gamma \in (A_1, A_2, E)$ indicates the irreducible

representation and the superscript i indicates the row of this representation. The irreducible asymptotic form is

$$\Psi^{\Gamma,i,v'j'm'} \sim$$
$$\sum_{\lambda}\sum_{v,j,m}\left\{e^{i\mathbf{k}_{vj}\cdot\mathbf{R}_\lambda}\delta_{vjm}^{v'j'm'} + f_{vjm}^{\Gamma,v'j'm'}(\vartheta_\lambda,\varphi_\lambda)\frac{e^{ik_{vj}R_\lambda}}{R_\lambda}\right\}c_{\lambda,j}^{\Gamma,i}\phi_{vjm}(\mathbf{r}_\lambda) \qquad (48)$$

where for j even, the $c_{\lambda,j}^{\Gamma,i}$ are

$$\begin{array}{lll} c_{\alpha,j}^{A_1} = +\sqrt{\frac{1}{3}}; & c_{\beta,j}^{A_1} = +\sqrt{\frac{1}{3}}; & c_{\gamma,j}^{A_1} = +\sqrt{\frac{1}{3}} \\ c_{\alpha,j}^{A_2} = 0; & c_{\beta,j}^{A_2} = 0; & c_{\gamma,j}^{A_2} = 0 \\ c_{\alpha,j}^{E,1} = +\sqrt{\frac{2}{3}}; & c_{\beta,j}^{E,1} = -\sqrt{\frac{1}{6}}; & c_{\gamma,j}^{E,1} = -\sqrt{\frac{1}{6}} \\ c_{\alpha,j}^{E,2} = 0; & c_{\beta,j}^{E,2} = +\sqrt{\frac{1}{2}}; & c_{\gamma,j}^{E,2} = -\sqrt{\frac{1}{2}} \end{array} \qquad (49)$$

and, for j odd are

$$\begin{array}{lll} c_{\alpha,j}^{A_1} = 0; & c_{\beta,j}^{A_1} = 0; & c_{\gamma,j}^{A_1} = 0 \\ c_{\alpha,j}^{A_2} = +\sqrt{\frac{1}{3}}; & c_{\beta,j}^{A_2} = +\sqrt{\frac{1}{3}}; & c_{\gamma,j}^{A_2} = +\sqrt{\frac{1}{3}} \\ c_{\alpha,j}^{E,1} = 0; & c_{\beta,j}^{E,1} = +\sqrt{\frac{1}{2}}; & c_{\gamma,j}^{E,1} = -\sqrt{\frac{1}{2}} \\ c_{\alpha,j}^{E,2} = -\sqrt{\frac{2}{3}}; & c_{\beta,j}^{E,2} = +\sqrt{\frac{1}{6}}; & c_{\gamma,j}^{E,2} = +\sqrt{\frac{1}{6}} \end{array} \qquad (50)$$

These scattering wave functions (48) are constructed to transform according to the following representation of the group P_3:

$$\begin{array}{l} \begin{pmatrix} \alpha & \beta & \gamma \\ \alpha & \beta & \gamma \end{pmatrix} \leftrightarrow \begin{pmatrix} 1 & 0 \\ 0 & 1 \end{pmatrix} \\ \begin{pmatrix} \alpha & \beta & \gamma \\ \alpha & \gamma & \beta \end{pmatrix} \leftrightarrow \begin{pmatrix} 1 & 0 \\ 0 & -1 \end{pmatrix} \\ \begin{pmatrix} \alpha & \beta & \gamma \\ \gamma & \beta & \alpha \end{pmatrix} \leftrightarrow \frac{1}{2}\begin{pmatrix} -1 & -\sqrt{3} \\ -\sqrt{3} & +1 \end{pmatrix} \\ \begin{pmatrix} \alpha & \beta & \gamma \\ \beta & \alpha & \gamma \end{pmatrix} \leftrightarrow \frac{1}{2}\begin{pmatrix} -1 & +\sqrt{3} \\ +\sqrt{3} & +1 \end{pmatrix} \\ \begin{pmatrix} \alpha & \beta & \gamma \\ \gamma & \alpha & \beta \end{pmatrix} \leftrightarrow \frac{1}{2}\begin{pmatrix} -1 & +\sqrt{3} \\ -\sqrt{3} & -1 \end{pmatrix} \\ \begin{pmatrix} \alpha & \beta & \gamma \\ \beta & \gamma & \alpha \end{pmatrix} \leftrightarrow \frac{1}{2}\begin{pmatrix} -1 & -\sqrt{3} \\ +\sqrt{3} & -1 \end{pmatrix} \end{array} \qquad (51)$$

The irreducible representation matrices for A_1 and A_2 are one dimensional: in A_1, every operator is represented by unity; and, in A_2, the two-cycle operators are represented by -1 while the three-cycle operators are represented by $+1$.

The irreducible representation asymptotic form (48) has some interesting characteristics. The plane wave appears in all arrangement channels and the scattering amplitude has the same functional form in all arrangement channels. The A_1 (A_2) spatial asymptotic form is composed of only even (odd) diatomic rotational states. Neither of these nondegenerate asympotic forms contains transitions which change the diatom parity. The E asymptotic form contains transitions between all possible states of the diatomic molecule including those that change the diatom parity.

The group theoretic projection also leads to expressions for the irreducible representation scattering amplitudes in terms of the independent space-fixed distinguishable atom scattering amplitudes:

$$f_{vjm}^{A_1,v'j'm'}(\vartheta_\lambda,\varphi_\lambda) = f_{\alpha,vjm}^{\alpha,v'j'm'}(\vartheta_\lambda,\varphi_\lambda) + 2f_{\beta,vjm}^{\alpha,v'j'm'}(\vartheta_\lambda,\varphi_\lambda); \quad j',j \in \text{even} \tag{52}$$

$$f_{vjm}^{A_2,v'j'm'}(\vartheta_\lambda,\varphi_\lambda) = f_{\alpha,vjm}^{\alpha,v'j'm'}(\vartheta_\lambda,\varphi_\lambda) + 2f_{\beta,vjm}^{\alpha,v'j'm'}(\vartheta_\lambda,\varphi_\lambda); \quad j',j \in \text{odd} \tag{53}$$

$$f_{vjm}^{E,v'j'm'}(\vartheta_\lambda,\varphi_\lambda) = f_{\alpha,vjm}^{\alpha,v'j'm'}(\vartheta_\lambda,\varphi_\lambda) - f_{\beta,vjm}^{\alpha,v'j'm'}(\vartheta_\lambda,\varphi_\lambda); \quad j',j \in \text{even} \tag{54}$$

$$f_{vjm}^{E,v'j'm'}(\vartheta_\lambda,\varphi_\lambda) = f_{\alpha,vjm}^{\alpha,v'j'm'}(\vartheta_\lambda,\varphi_\lambda) - f_{\beta,vjm}^{\alpha,v'j'm'}(\vartheta_\lambda,\varphi_\lambda); \quad j',j \in \text{odd} \tag{55}$$

$$f_{vjm}^{E,v'j'm'}(\vartheta_\lambda,\varphi_\lambda) = +\sqrt{3}f_{\beta,vjm}^{\alpha,v'j'm'}(\vartheta_\lambda,\varphi_\lambda); \qquad j' \in \text{even}, \quad j \in \text{odd} \tag{56}$$

$$f_{vjm}^{E,v'j'm'}(\vartheta_\lambda,\varphi_\lambda) = -\sqrt{3}f_{\beta,vjm}^{\alpha,v'j'm'}(\vartheta_\lambda,\varphi_\lambda); \qquad j' \in \text{odd}, \quad j \in \text{even} \tag{57}$$

Expressions for the distinguishable particle scattering amplitudes, $f_{\lambda,vjm}^{\lambda',v'j'm'}$, in terms of the irreducible representation scattering amplitudes, $f_{vjm}^{\Gamma,v'j'm'}$, are found by taking the linear combinations of the $\Psi^{A_1,v'j'm'}$, $\Psi^{A_2,v'j'm'}$, and $\Psi^{E,i,v'j'm'}$ that leave the incident plane wave in the λ' arrangement channel only. The expressions for the $f_{\lambda,vjm}^{\lambda',v'j'm'}$ are

$$f_{\alpha,vjm}^{\alpha,v'j'm'}(\vartheta_\lambda,\varphi_\lambda) = \frac{1}{3}f_{vjm}^{A_1,v'j'm'}(\vartheta_\lambda,\varphi_\lambda) + \frac{2}{3}f_{vjm}^{E,v'j'm'}(\vartheta_\lambda,\varphi_\lambda); \quad j',j \in \text{even} \tag{58}$$

$$f_{\alpha,vjm}^{\alpha,v'j'm'}(\vartheta_\lambda,\varphi_\lambda) = \frac{1}{3}f_{vjm}^{A_2,v'j'm'}(\vartheta_\lambda,\varphi_\lambda) + \frac{2}{3}f_{vjm}^{E,v'j'm'}(\vartheta_\lambda,\varphi_\lambda); \quad j',j \in \text{odd} \tag{59}$$

$$f^{\alpha,v'j'm'}_{\beta,vjm}(\vartheta_\lambda,\varphi_\lambda) = \frac{1}{3}f^{A_1,v'j'm'}_{vjm}(\vartheta_\lambda,\varphi_\lambda) - \frac{1}{3}f^{E,v'j'm'}_{vjm}(\vartheta_\lambda,\varphi_\lambda); \quad j',j \in \text{even} \tag{60}$$

$$f^{\alpha,v'j'm'}_{\beta,vjm}(\vartheta_\lambda,\varphi_\lambda) = \frac{1}{3}f^{A_2,v'j'm'}_{vjm}(\vartheta_\lambda,\varphi_\lambda) - \frac{1}{3}f^{E,v'j'm'}_{vjm}(\vartheta_\lambda,\varphi_\lambda); \quad j',j \in \text{odd} \tag{61}$$

$$f^{\alpha,v'j'm'}_{\beta,vjm}(\vartheta_\lambda,\varphi_\lambda) = +\frac{1}{\sqrt{3}}f^{E,v'j'm'}_{vjm}(\vartheta_\lambda,\varphi_\lambda); \qquad j' \in \text{even}, \quad j \in \text{odd} \tag{62}$$

$$f^{\alpha,v'j'm'}_{\beta,vjm}(\vartheta_\lambda,\varphi_\lambda) = -\frac{1}{\sqrt{3}}f^{E,v'j'm'}_{vjm}(\vartheta_\lambda,\varphi_\lambda); \qquad j' \in \text{odd}, \quad j \in \text{even} \tag{63}$$

$$f^{\alpha,v'j'm'}_{\alpha,vjm}(\vartheta_\lambda,\varphi_\lambda) = 0; \qquad j' \in \text{even}, \quad j \in \text{odd} \tag{64}$$

$$f^{\alpha,v'j'm'}_{\alpha,vjm}(\vartheta_\lambda,\varphi_\lambda) = 0; \qquad j' \in \text{odd}, \quad j \in \text{even} \tag{65}$$

Expressions (58) through (65) can obviously also be obtained by inverting equations (52) through (57).

Although the asymptotic scattering wave function in (48) transforms as an irreducible representation of the group P_3, it is not an eigenfunction of $\hat{J}^2$ or $\hat{O}_{\hat{I}}$. In contrast, it is desirable that the numerical solutions to be constructed have definite total angular momentum and parity. We will next express the asymptotic forms as a partial wave expansion in body-fixed coordinates. In this way, the connection between the numerical partial wave solutions and the irreducible scattering amplitudes can be obtained.

8. Partial Wave Expansion of the Asymptotic Forms

A. Helicity Asymptotic Form

The Γ irreducible representation, space-fixed, asymptotic form discussed in Section 7.B will now be transformed into the corresponding helicity asymptotic form.[75,2b] In this way, we can identify the helicity scattering wave function and scattering amplitude which belong to the Γ irreducible representation of the permutation group P_3. The helicity asymptotic form is convenient when body-fixed coordinates are used to express the scattering wave function and permit a simple expansion of the latter into a total angular momentum partial wave series. In the

helicity asymptotic form, the axis of quantization of the final diatom rotational states is the final wave vector direction (*i.e.*, the body-fixed z_λ axis), and that of the initial rotational state is the direction of the initial wave vector. For simplicity, the space-fixed Z axis is in the direction of the initial wave vector (35).

We have introduced two different sets of projection quantum numbers for the diatom rotational state. The helicity projection quantum numbers are denoted by k for final states and k' for initial states. In Section 7, the axis of quantization of the diatom rotational states is the single space-fixed Z axis and the symbols m and m' are used for the space-fixed final and initial diatom angular momentum projection quantum numbers. The special choice of space-fixed Z axis given by equation (35) reveals that the projection quantum numbers m' and k' both refer to the component of the diatom rotational angular momentum along the space-fixed Z axis. The quantum numbers k and m are the projection quantum numbers for the body-fixed z_λ and space-fixed Z axes, respectively.

The isolated space-fixed diatom wave functions (33) and (34) have the separable form

$$\phi_{vjm}(\mathbf{r}_\lambda) = h_{v,j}(r_\lambda) Y_{j,m}(\vartheta_{r_\lambda}, \varphi_{r_\lambda}) \tag{66}$$

where $(\vartheta_{r_\lambda}, \varphi_{r_\lambda})$ are the spherical polar angles of the vector $\mathbf{r}_\lambda$ with respect to space-fixed system of axes X, Y, Z, and the $Y_{j,m}$ are the usual spherical harmonics, with m being the quantum number associated with the projection of the diatom rotational angular momentum along the space-fixed Z axis.

The transformation of the final diatom projection quantum number to the corresponding helicity quantum number is accomplished by using the definition of the Wigner rotation matrices:[74]

$$Y_{j,m}(\vartheta_{r_\lambda}, \varphi_{r_\lambda}) = \sum_{k=-j}^{j} D^j_{m,k}(\varphi_\lambda, \vartheta_\lambda, 0) Y_{j,k}(\gamma_\lambda, \psi_\lambda) \tag{67}$$

Combining equations (48), (66), and (67), we find

$$\Psi^{\Gamma,i,v',j',m'} \sim \sum_{\lambda} \sum_{v,j,m} \left\{ e^{i\mathbf{k}_{v,j}\cdot\mathbf{R}_\lambda} \delta^{v',j',m'}_{v,j,m} + f^{\Gamma,v',j',m'}_{v,j,m}(\vartheta_\lambda,\varphi_\lambda) \frac{e^{ik_{v,j}R_\lambda}}{R_\lambda} \right\}$$

$$\left\{ c^{\Gamma,i}_{\lambda,j} h_{v,j}(r_\lambda) \sum_{k=-j}^{j} D^{j}_{m,k}(\varphi_\lambda,\vartheta_\lambda,0) Y_{j,k}(\gamma_\lambda,\psi_\lambda) \right\} \quad (68)$$

The asymptotic form (68) can be rewritten as

$$\Psi^{\Gamma,i,v',j',m'} \sim \sum_{\lambda} \sum_{v,j,k} \left[c^{\Gamma,i}_{\lambda,j} h_{v,j}(r_\lambda) Y_{j,k}(\gamma_\lambda,\psi_\lambda) \right]$$

$$\left\{ e^{i\mathbf{k}_{v,j}\cdot\mathbf{R}_\lambda} \delta^{v',j'}_{v,j} D^{j}_{m',k}(\varphi_\lambda,\vartheta_\lambda,0) + \tilde{f}^{\Gamma,v',j',m'}_{v,j,k}(\vartheta_\lambda,\varphi_\lambda) \frac{e^{ik_{v,j}R_\lambda}}{R_\lambda} \right\} \quad (69)$$

where we have introduced a scattering amplitude which belongs to the P_3 irreducible representation Γ and is given by

$$\tilde{f}^{\Gamma,v',j',m'}_{v,j,k}(\vartheta_\lambda,\varphi_\lambda) = \sum_{m=-j}^{j} f^{\Gamma,v',j',m'}_{v,j,m}(\vartheta_\lambda,\varphi_\lambda) D^{j}_{m,k}(\varphi_\lambda,\vartheta_\lambda,0) \quad (70)$$

The correspondence of equation (69) in this paper with the distinguishable particle helicity scattering wave function appearing in equation (5.24) of reference 2b permits us to identify the irreducible representation (of P_3) helicity amplitude as the left hand side of equation (70) in this paper, where we identify the indices $k' = m'$. With this change in indices, the Γ irreducible representation helicity scattering wave function is

$$\Psi^{\Gamma,i,v',j',k'} \sim \sum_{\lambda} \sum_{v,j,k} \left[c^{\Gamma,i}_{\lambda,j} h_{v,j}(r_\lambda) Y_{j,k}(\gamma_\lambda,\psi_\lambda) \right]$$

$$\left\{ e^{i\mathbf{k}_{v,j}\cdot\mathbf{R}_\lambda} \delta^{v',j'}_{v,j} D^{j}_{k',k}(\varphi_\lambda,\vartheta_\lambda,0) + \tilde{f}^{\Gamma,v',j',k'}_{v,j,k}(\vartheta_\lambda,\varphi_\lambda) \frac{e^{ik_{v,j}R_\lambda}}{R_\lambda} \right\} \quad (71)$$

In the symbol $\tilde{f}^{\Gamma,v',j',k'}_{v,j,k}$, the superscript k' is the component of the diatom's initial rotational angular momentum along the space-fixed Z axis and k is the component

of the final diatom's rotational angular momentum along the corresponding body-fixed axis z_λ, so we see that this scattering amplitude agrees with the discussion preceeding equation (5.24) in reference 2b.

B. Partial Wave Expansion of the Helicity Asymptotic Form

The next step is to transform equation (71) into the total angular momentum representation. The Hamiltonian commutes with the operators of $SO(3)$, so any solutions to the Schrödinger equation can be written as a linear combination of solutions which separately transform as irreducible representations of $SO(3)$. If the decomposition is done using body-fixed coordinates, then the partial wave series is given in terms of the Wigner rotation matrices. The plane wave term and the helicity scattering amplitude are expanded in a series of total angular momentum partial waves as[73]

$$e^{i\mathbf{k}_{v,j}\cdot\mathbf{R}_\lambda} D^j_{k',k}(\varphi_\lambda,\vartheta_\lambda,0) \sim$$
$$\left(\frac{1}{2k_{v,j}R_\lambda}\right) \sum_{J=max(|k'|,|k|)}^{\infty} \Big\{ D^J_{k',k}(\varphi_\lambda,\vartheta_\lambda,0)(2J+1)(i)^{J+j+1} \tag{72}$$
$$\left(-\delta_k^{k'} e^{i[k_{v,j}R_\lambda-(J+j)\frac{\pi}{2}]} + \delta_k^{-k'} e^{-i[k_{v,j}R_\lambda-(J+j)\frac{\pi}{2}]}\right)\Big\}$$

The corresponding expansion of the helicity scattering amplitude is

$$\tilde{f}^{\Gamma,v',j',k'}_{v,j,k}(\vartheta_\lambda,\varphi_\lambda) = \sum_{J=max(|k'|,|k|)}^{\infty} \left(a^{\Gamma,J}\right)^{v',j',k'}_{v,j,k} D^J_{k',k}(\varphi_\lambda,\vartheta_\lambda,0) \tag{73}$$

where the $\left(a^{\Gamma,J}\right)^{v',j',k'}_{v,j,k}$ are constant coefficients which are determined by solving the Schrödinger equation for the scattering wave function. They are related to the elements of the scattering matrix as will be discussed below.

The particular choice of subscripts for the Wigner rotation matrices in the the expansion of the helicity scattering amplitude requires some explanation. The second subscript, k, on the Wigner function in equation (73) must agree with the projection quantum number of the diatom's rotational angular momentum in

equation (71) in order for that expansion to solve Schrödinger's equation term by term. Recall that the projection of the total (3-particle) spatial angular momentum onto the space-fixed Z axis is a constant of the motion. This total angular momentum Z component is also equal to the projection of the rotational angular momentum of the initial diatomic molecule onto that axis, because the incident wave vector is parallel to that axis, by definition, and contributes nothing to that component of the total angular momentum. Since the total angular momentum projection quantum number is determined by the first subscript on the Wigner rotation matrix, it must be k', the initial diatom projection quantum number.

Substituting the expansion of the plane wave (72) and that of the scattering amplitude (73) into equation (71) we find, after some straightforward rearrangements:

$$\Psi^{\Gamma,i,v'j'k'} \sim \sum_{J=0}^{\infty}\left(\frac{(2J+1)\sqrt{\hbar}(\imath)^{J+j'+1}}{2\sqrt{\mu k_{v',j'}}}\right)$$
$$\sum_{\lambda}\sum_{v,j,k}\left\{c_{\lambda,j}^{\Gamma,i}D_{k',k}^{J}(\varphi_\lambda,\vartheta_\lambda,0)h_{v,j}(r_\lambda)Y_{j,k}(\gamma_\lambda,\psi_\lambda)\left(b_S^{J,\Gamma}\right)_{v,j,k}^{v',j',k'}(R_\lambda)\right\} \qquad (74)$$

where

$$\left(b_S^{J,\Gamma}\right)_{v,j,k}^{v',j',k'} = \frac{|V_{v,j}|^{-\frac{1}{2}}}{R_\lambda}\left\{\delta_{v,j,k}^{v',j',-k'}\begin{pmatrix} e^{-\imath[k_{v,j}R_\lambda-(J+j)\frac{\pi}{2}]} \\ 0 \end{pmatrix}\right.$$
$$\left. -\left(S^{J,\Gamma}\right)_{v,j,k}^{v',j',k'}\begin{pmatrix} e^{\imath[k_{v,j}R_\lambda-(J+j)\frac{\pi}{2}]} \\ e^{-\kappa_{v,j}R_\lambda} \end{pmatrix}\right\} \qquad (75)$$

with

$$\left(S^{J,\Gamma}\right)_{v,j,k}^{v',j',k'} = \delta_{v,j,k}^{v',j',k'} - \frac{2(\imath)^{j-j'-1}\sqrt{k_{v',j'}k_{v,j}}}{(2J+1)}\left(a^{J,\Gamma}\right)_{v,j,k}^{v',j',k'} \qquad (76)$$

The left hand side of equation (76) represents the elements of the body-fixed scattering matrix for partial wave J and irreducible representation Γ. This equation shows their relationship to the expansion coefficients $\left(a^{J,\Gamma}\right)_{v,j,k}^{v',j',k'}$. Note from equation (76) that in the absence of any interaction, the scattering amplitude vanishes, so its expansion coefficients $\left(a^{J,\Gamma}\right)_{v,j,k}^{v',j',k'}$ vanish and the scattering matrix becomes the identity matrix as desired.

The upper (lower) line in equation (75) represents the open (closed) channel terms. The closed channels in the first term on the right of equation (75) vanish because the incident plane wave multiplies only open channels since it represents the initial state part of the scattering wave function. In other words, the initial state cannot be a closed state in a wave function which represents a scattering experiment.

Given the body-fixed scattering matrices for each J and Γ, the coefficients $\left(a^{J,\Gamma}\right)_{v,j,k}^{v',j',k'}$ are determined by inverting equation (76) and the irreducible representation helicity scattering amplitudes can be expressed in terms of the irreducible representation body-fixed scattering matrix elements as

$$\tilde{f}_{v,j,k}^{\Gamma,v',j',k'} = \left(\frac{V_{v',j'}}{V_{v,j}}\right)^{\frac{1}{2}} \frac{(i)^{j'-j+1}}{2k_{v',j'}} \sum_{J=0} (2J+1) D^{J}_{k',k}(\varphi_\lambda, \vartheta_\lambda, 0) \left(T^{J,\Gamma}\right)_{v,j,k}^{v',j',k'} \qquad (77)$$

where

$$\left(T^{J,\Gamma}\right)_{v,j,k}^{v',j',k'} = \left[\delta_{v,j,k}^{v',j',k'} - \left(S^{J,\Gamma}\right)_{v,j,k}^{v',j',k'}\right] \qquad (78)$$

Equation (77) is the irreducible representation helicity amplitude partial wave expansion which corresponds to the distinguishable particle one given by Schatz and Kuppermann[2b] and is identical to their equation (5.31) except for the presence of Γ in equation (77) of the present paper which associates the helicity amplitude with the scattering wave function which transforms as the Γ irreducible representation of the group P_3.

We have previously restricted the initial state to be an open diatomic molecule state while final states can be open or closed. Equations (74) and (75) derive from an analysis of a physically meaningful scattering asymptotic form. As such, they will not include any exponentially diverging terms. For this reason, there is a zero in the closed channel part of the first term of equation (75). It should be pointed out that the general definition of the scattering matrix includes exponentially diverging terms; however, these are not needed for the construction of differential cross sections and do not arise naturally from asymptotic boundary conditions like

equation (48). To distinguish the open-open parts of the scattering matrix, we will use the notation ${}^{o}\mathbf{S}^{J,\Gamma}$. The transformation to matrix notation is accomplished by regarding superscripts as a single column index and subscripts as a single row index.

C. Parity Decomposition of the Helicity Asymptotic Form

There is one remaining symmetry decomposition of the asymptotic form. The parity label has not appeared in the foregoing analysis but is a label for the numerical solutions, so it is desirable to have the asymptotic form expanded in the corresponding parity components. The parity labeled components have a simple phase change when the sign of the final state k index changes sign.

Multiplying by the parity projection operators, which are special cases of equation (47), we can find the parity components of the asymptotic form and express the asymptotic form as an expansion in the parity components. Writing $\hat{P}^{(+)}$ and $\hat{P}^{(-)}$ for the projection operators for the positive and negative three-particle parity:

$$\hat{P}^{(\Pi)} = \frac{1}{2}(1 + \Pi\hat{O}_{\hat{I}}), \tag{79}$$

we can define asymptotic forms which carry the parity label Π

$$\Psi^{\Pi,\Gamma,i,v',j',m'} = \hat{P}^{(\Pi)}\Psi^{\Gamma,i,v',j',m'}. \tag{80}$$

To recover the original function from the parity labelled functions we simply sum over the parity label

$$\Psi^{\Gamma,i,v',j',k'} = \sum_{\Pi} \Psi^{\Pi,\Gamma,i,v',j',k'} \tag{81}$$

The parity labelled Γ representation asymptotic form is

$$\Psi^{\Pi,\Gamma,i,v'j'k'} \sim \sum_{J=0}^{\infty}\left(\frac{(2J+1)\sqrt{\hbar}(\imath)^{J+j'+1}}{2\sqrt{\mu k_{v',j'}}}\right)$$
$$\sum_{\lambda}\sum_{v,j,k}\left\{c^{\Gamma,i}_{\lambda,j}D^{J}_{k',k}(\varphi_\lambda,\vartheta_\lambda,0)h_{v,j}(r_\lambda)Y_{j,k}(\gamma_\lambda,\psi_\lambda)\left(b_S^{J,\Pi,\Gamma}\right)^{v',j',k'}_{v,j,k}(R_\lambda)\right\} \tag{82}$$

where

$$\left(b_S^{J,\Pi,\Gamma}\right)_{v,j,k}^{v',j',k'}(R_\lambda) = \frac{1}{2}\left[\left(b_S^{J,\Gamma}\right)_{v,j,k}^{v',j',k'}(R_\lambda) + \Pi(-1)^J\left(b_S^{J,\Gamma}\right)_{v,j,-k}^{v',j',k'}(R_\lambda)\right] \tag{83}$$

Observe that with the addition of parity labels, the $\left(b_S^{J,\Pi,\Gamma}\right)_{v,j,k}^{v',j',k'}(R_\lambda)$ with $k<0$ are not linearly independent of those with $k>0$:

$$\left(b_S^{J,\Pi,\Gamma}\right)_{v,j,-k}^{v',j',k'}(R_\lambda) = \Pi(-1)^J\left(b_S^{J,\Pi,\Gamma}\right)_{v,j,k}^{v',j',k'}(R_\lambda) \tag{84}$$

The explicit form for $\left(b_S^{J,\Pi,\Gamma}\right)_{v,j,k}^{v',j',k'}(R_\lambda)$ is

$$\left(b_S^{J,\Pi,\Gamma}\right)_{v,j,k}^{v',j',k'} = \frac{|V_{v,j}|^{-\frac{1}{2}}}{R_\lambda}\left\{\left(E^{J,\Pi}\right)_{v,j,k}^{v',j',k'}\begin{pmatrix} e^{-i[k_{v,j}R_\lambda-(J+j)\frac{\pi}{2}]} \\ 0 \end{pmatrix} - \left(S^{J,\Pi,\Gamma}\right)_{v,j,k}^{v',j',k'}\begin{pmatrix} e^{i[k_{v,j}R_\lambda-(J+j)\frac{\pi}{2}]} \\ e^{-\kappa_{v,j}R_\lambda} \end{pmatrix}\right\} \tag{85}$$

where we have defined

$$\left(E^{J,\Pi}\right)_{v,j,k}^{v',j',k'} = \frac{1}{2}\left[\delta_k^{-k'} + \Pi(-1)^J\delta_k^{k'}\right]\delta_{v,j}^{v',j'} \tag{86}$$

$$\left(S^{J,\Pi,\Gamma}\right)_{v,j,k}^{v',j',k'} = \frac{1}{2}\left[\left(S^{J,\Gamma}\right)_{v,j,k}^{v',j',k'} + \Pi(-1)^J\left(S^{J,\Gamma}\right)_{v,j,-k}^{v',j',k'}\right] \tag{87}$$

Both $\left(E^{J,\Pi}\right)_{v,j,k}^{v',j',k'}$ and $\left(S^{J,\Pi,\Gamma}\right)_{v,j,k}^{v',j',k'}$ have the symmetry properties

$$\left(S^{J,\Pi,\Gamma}\right)_{v,j,-k}^{v',j',k'} = \Pi(-1)^J\left(S^{J,\Pi,\Gamma}\right)_{v,j,k}^{v',j',k'} \tag{88}$$

$$\left(E^{J,\Pi}\right)_{v,j,-k}^{v',j',k'} = \Pi(-1)^J\left(E^{J,\Pi}\right)_{v,j,k}^{v',j',k'} \tag{89}$$

so if the parity labelled scattering matrix elements with $k \geq 0$ are calculated, then the elements with $k<0$ are known by equation (88) and the non-parity labelled elements are found from the inverse of relationship (87):

$$\left(S^{J,\Gamma}\right)_{v,j,k}^{v',j',k'} = \sum_{\Pi}\left(S^{J,\Pi,\Gamma}\right)_{v,j,k}^{v',j',k'} \tag{90}$$

In addition, from the fact that the scattering matrix is a symmetric matrix in the usual linear algebra sense, we can derive relationships similar to equations (88) and (89) for the superscripts in place of the subscripts.

$$\left(S^{J,\Pi,\Gamma}\right)^{v',j',-k'}_{v,j,k} = \Pi(-1)^J \left(S^{J,\Pi,\Gamma}\right)^{v',j',k'}_{v,j,k} \tag{91}$$

$$\left(E^{J,\Pi}\right)^{v',j',-k'}_{v,j,k} = \Pi(-1)^J \left(E^{J,\Pi}\right)^{v',j',k'}_{v,j,k} \tag{92}$$

The utility of equations (88) and (91) is that only part of the parity labelled scattering matrix must be calculated. If the elements of the scattering matrix with $k \geq 0$ and $k' \geq 0$ are known, then the remaining parts are expressible in terms of these elements by equations (88) and (91).

D. Reactance (R) Matrix Asymptotic Form

The preceding scattering asymptotic boundary conditions involve plane waves and spherical waves because these are familiar boundary conditions for a scattering wave function; however, it is most convenient for numerical purposes to calculate solutions to the Schrödinger equation which are real functions of R_λ corresponding to equations (82) and (85). These are the well known reactance matrix solutions[70,76] with the addition of the appropriate Π and Γ labels:

$$\left(b_R^{J,\Pi,\Gamma}\right)^{v',j',k'}_{v,j,k}(R_\lambda) = \frac{|V_{v,j}|^{-\frac{1}{2}}}{R_\lambda}\left\{\left(E^{J,\Pi,\Gamma}\right)^{v',j',k'}_{v,j,k}\begin{pmatrix}\sin\left[k_{v,j}R_\lambda - (J+j)\frac{\pi}{2}\right] \\ 0\end{pmatrix} + \left(R^{J,\Pi,\Gamma}\right)^{v',j',k'}_{v,j,k}\begin{pmatrix}\cos\left[k_{v,j}R_\lambda - (J+j)\frac{\pi}{2}\right] \\ e^{-\kappa_{v,j}R_\lambda}\end{pmatrix}\right\} \tag{93}$$

$\mathbf{R}^{J,\Pi,\Gamma}$ is called the reactance matrix. The relationship between the open-channel parts of the scattering and reactance matrices is also well known.[70,76] For a fixed collision energy, the number of open initial states and final states is equal. By choosing an ordered set of the three initial state quantum numbers v', j', k' as

a column index and likewise a similarly chosen ordered set for the final state quantum numbers v, j, k as a row index, it is simple to show that

$$ {}^{o}\mathbf{S}^{\mathbf{J},\Pi,\Gamma} = (\mathbf{1} + \imath\ {}^{o}\mathbf{R}^{\mathbf{J},\Pi,\Gamma})(\mathbf{1} - \imath\ {}^{o}\mathbf{R}^{\mathbf{J},\Pi,\Gamma})^{-1} \tag{94} $$

where the left hand superscript o indicates that we are referring to the open parts of the corresponding matrices. Once ${}^{o}\mathbf{R}^{\mathbf{J},\Pi,\Gamma}$ is obtained, we calculate ${}^{o}\mathbf{S}^{\mathbf{J},\Pi,\Gamma}$ from (94), ${}^{o}\mathbf{S}^{\mathbf{J},\Gamma}$ from the open channel part of (90), the corresponding ${}^{o}\mathbf{T}^{\mathbf{J},\Gamma}$ from (78) and the helicity amplitude from (77). These will then be used to calculate cross sections, as shown in Section 7.E and 11.

E. P_3 Irreducible Representation Helicity Differential Cross Sections

In this chapter, the expression for P_3 irreducible representation differential cross section is given. For transitions from odd initial rotational states of the diatomic molecule, these are not yet physically observerable differential cross sections, but are related to them in a simple manner as shown in Section 11. For transitions from even initial rotational states of the diatomic molecule, these are the physically observable differential cross sections. This is all discussed at some length in Section 10 and is mentioned here for clarity. The differential cross section is defined as the outgoing flux into a unit solid angle for some final state of the diatomic molecule divided by the total incident flux. Before writing down this expression in terms of the helicity scattering amplitude, it is necessary to undo the effects of mass-scaling on the latter.

The use of mass scaled coordinates affects the normalization of the diatomic molecule wave functions, the wave vectors, and the spherical wave terms of the asymptotic form. First, consider the diatomic molecule normalization.

$$ \int_0^{r_\lambda^{max}} |\phi_t(\mathbf{r}_\lambda)|^2 d^3\mathbf{r}_\lambda = 1 = (a_\lambda)^{-3} \int_0^{r_\lambda'^{max}} |\phi_t(\mathbf{r}'_\lambda)|^2 d^3\mathbf{r}'_\lambda \tag{95} $$

If the diatomic molecule wave functions in unscaled Jacobi coordinates $\phi'_t(\mathbf{r}'_\lambda)$ are defined to have the normalization

$$\int_0^{r'^{max}_\lambda} |\phi'_t(\mathbf{r}'_\lambda)|^2 d^3\mathbf{r}'_\lambda = 1 \tag{96}$$

then the following relationship exists between the mass-scaled and unscaled diatomic wave functions:

$$\phi'_t(\mathbf{r}'_\lambda) = (a_\lambda)^{\frac{3}{2}} \phi_t(\mathbf{r}'_\lambda) \tag{97}$$

Also, the wave vector corresponding to unscaled coordinates is

$$\mathbf{k}'_{v,j} = a_\lambda^{-1} \mathbf{k}_{v,j} \tag{98}$$

which implies that

$$\mathbf{k}'_{v,j} \cdot \mathbf{R}'_\lambda = \mathbf{k}_{v,j} \cdot \mathbf{R}_\lambda \tag{99}$$

$$k'_{v,j} R'_\lambda = k_{v,j} R_\lambda \tag{100}$$

To transform equation (71) to unscaled coordinates, multiply (71) by $a_\lambda^{\frac{3}{2}}$. Because the particles are identical, the mass scaling factors are the same for each arrangement channel, and the diatomic molecule wave functions become those appropriate for the unscaled coordinates. R_λ in the denominator of the spherical wave terms can be replaced by R'_λ, if the unscaled helicity scattering amplitude is defined by

$$\tilde{f}'^{\Gamma,v',j',k'}_{v,j,k}(\vartheta_\lambda, \varphi_\lambda) = (a_\lambda)^{-1} \tilde{f}^{\Gamma,v',j',k'}_{v,j,k}(\vartheta_\lambda, \varphi_\lambda) \tag{101}$$

The last equation is essentially equation (5.27) in Schatz and Kuppermann[2b] when the particles are identical. From the unscaled helicity scattering amplitude, the irreducible representation differential cross section can be defined:

$$\sigma^{\Gamma,v',j',k'}_{v,j,k}(\vartheta_\lambda, \varphi_\lambda) = \left(\frac{V'_{v,j}}{V'_{v',j'}}\right) |\tilde{f}'^{\Gamma,v',j',k'}_{v,j,k}(\vartheta_\lambda, \varphi_\lambda)|^2 \tag{102}$$

where $V'_{v,j} = \frac{\hbar k'_{v,j}}{\mu_{\lambda,\nu\kappa}}$ is the unscaled relative speed. This is the usual helicity scattering differential cross section with the addition of a label for the irreducible

representation Γ of the group P_3 indicating the transformation properties of the corresponding scattering wave function. In section 11, the construction of the properly antisymmetrized differential cross sections from the irreducible representation ones will be presented.

9. Asymptotic Projection of Numerical Solutions

A. General Jacobi Asymptotic Wave Function

The goal is to construct numerical solutions to the Schrödinger equation for each partial wave, parity, and P_3 irreducible representation that have a similar asymptotic form as equations (82) and (93) in order to obtain from them ${}^{o}\mathbf{R}^{\mathbf{J},\Pi,\Gamma}$. Unfortunately, it is not known how to pick directly the initial conditions such that the asymptotic form of the integrated solutions is a scattering matrix (85) or reactance matrix (93) form. One method for constructing scattering (reactance) matrix solutions is to integrate the system of ODEs in the variable ρ as an initial value problem without trying to achieve any special asymptotic form. The scattering (reactance) matrix asymptotic form is then obtained by linearly combining a complete set of linearly independent solutions to the initial value problem. One technique for doing this is reviewed in this section.[70]

Arbitrary intitial conditions, denoted by p', lead to wave functions which are composed of both open and closed channels, as ρ becomes large, so the asymptotic behavior of the integrated solutions will include diverging waves. The general body-fixed solution labelled with J, M, Π, Γ, i, p' has the asymptotic form

$$\Psi^{J,M,\Pi,\Gamma,i,p'} \sim \sum_{\lambda} \sum_{v,j,\Omega} c^{\Gamma,i}_{\lambda,j} D^{J}_{M,\Omega}(\varphi_\lambda, \vartheta_\lambda, 0) h_{v,j}(r_\lambda) Y_{j,\Omega}(\gamma_\lambda, \psi_\lambda) B^{J,\Pi,\Gamma,p}_{v,j,\Omega}(R_\lambda) \tag{103}$$

where we define

$$B^{J,\Pi,\Gamma,p'}_{v,j,\Omega}(R_\lambda) = R_\lambda^{-1}|V_{v,j}|^{-\frac{1}{2}}\left\{C^{J,\Pi,\Gamma,p'}_{v,j,\Omega}\begin{pmatrix}\sin[k_{v,j}R_\lambda - (J+j)\frac{\pi}{2}]\\ e^{\kappa_{v,j}R_\lambda}\end{pmatrix}\right.$$
$$\left. + D^{J,\Pi,\Gamma,p'}_{v,j,\Omega}\begin{pmatrix}\cos[k_{v,j}R_\lambda - (J+j)\frac{\pi}{2}]\\ e^{-\kappa_{v,j}R_\lambda}\end{pmatrix}\right\} \quad (104)$$

where the summation over Ω includes only nonnegative values because of the enforcement of parity. The p' superscript on the coefficients $C^{J,\Pi,\Gamma,p'}_{v,j,\Omega}$ and $D^{J,\Pi,\Gamma,p'}_{v,j,\Omega}$ is an integer index which distinguishes the solutions obtained from different initial conditions to the initial value problem. The upper (lower) terms in the equation (104) are for open (closed) states. The superscript i which appears on the left hand side of (103) denotes the particular row within the irreducible representation Γ to which a solution belongs. This index does not appear in the term $B^{J,\Pi,\Gamma,p'}_{v,j,\Omega}(R_\lambda)$ because that would imply that the $G^{J,\Pi,\Gamma}_n(\rho;\overline{\rho}_i)$ depend on this index which, we argued in section 5, is not the case. In principle, the sum over v,j,Ω in equation (103) must include all asymptotic states both open and closed. In practice, the sum includes all open states and some closed states. The number of states included is an adjustable parameter in the numerical treatment and its finite value represents an approximation. It is usually found that the error from the finite number of asymptotic states included can be made as small as desired by increasing their number. If the number of initial conditions is equal to the number of asymptotic states in the expansion, then the $C^{J,\Pi,\Gamma,p'}_{v,j,\Omega}$ and $D^{J,\Pi,\Gamma,p'}_{v,j,\Omega}$ form square matrices with row indices v,j,Ω and column index p'. If $C^{J,\Pi,\Gamma,p}_{v,j,\Omega}$ is nonsingular, then we can form

$$\tilde{\mathbf{R}}^{J,\Pi,\Gamma} = \mathbf{D}^{J,\Pi,\Gamma}(\mathbf{C}^{J,\Pi,\Gamma})^{-1} \quad (105)$$

where we have moved to matrix notation. We have implicitly assumed an arbitrary, but fixed, mapping from the triplet of indices v,j,Ω to a single integer index used to label the row the matrices. This is not quite the reactance matrix defined in equation (93) but is closely related to it as we will see momentarily.

The inverse matrix $(\mathbf{C}^{J,\Pi,\Gamma})^{-1}$ can be used to transform equation (103) into a form very similar to the terms in the partial wave expansion (82)

$$\tilde{\Psi}^{J,M,\Pi,\Gamma,i,v',j',\Omega'} = \sum_{p'} \left[(\mathbf{C}^{J,\Pi,\Gamma})^{-1} \right]_{p'}^{v',j',\Omega'} \Psi^{J,M,\Pi,\Gamma,i,p'} \tag{106}$$

We now have

$$\tilde{\Psi}^{J,M,\Pi,\Gamma,i,v',j',\Omega'} \sim \sum_{\lambda} \sum_{v,j,\Omega} c_{\lambda,j}^{\Gamma,i} D_{M,\Omega}^{J}(\varphi_\lambda, \vartheta_\lambda, 0) h_{v,j}(r_\lambda) Y_{j,\Omega}(\gamma_\lambda, \psi_\lambda) \frac{1}{R_\lambda |V_{v,j}|^{\frac{1}{2}}}$$
$$\left\{ \delta_{v,j,\Omega}^{v',j',\Omega'} \begin{pmatrix} \sin[k_{v,j} R_\lambda - (J+j)\frac{\pi}{2}] \\ e^{\kappa_{v,j} R_\lambda} \end{pmatrix} + (\tilde{R}^{J,\Pi,\Gamma})_{v,j,\Omega}^{v',j',\Omega'} \begin{pmatrix} \cos[k_{v,j} R_\lambda - (J+j)\frac{\pi}{2}] \\ e^{-\kappa_{v,j} R_\lambda} \end{pmatrix} \right\} \tag{107}$$

Using the numerical solutions represented in equation (107), we can expand the Γ irreducible representation helicity scattering wave function (82).

$$\Psi^{\Pi,\Gamma,i,v'j'k'} \sum_{J,M,v'',j'',\Omega''} \left(A^{J,M,\Pi} \right)_{v'',j'',\Omega''}^{v',j',k'} \tilde{\Psi}^{J,M,\Pi,\Gamma,i,v'',j'',\Omega''} \tag{108}$$

Comparing equation (108) with equations (82) and (93), the expansion coefficients needed for equation (108) to become (82) are

$$\left(A^{J,M,\Pi} \right)_{v'',j'',\Omega''}^{v',j',k'} = \delta_M^{k'} \delta_{v''}^{v'} \delta_{j''}^{j'} \delta_{-\Omega''}^{k'} \left(\frac{(2J+1)\sqrt{\hbar}(i)^{J+j''+1}}{2\sqrt{\mu k_{v'',j''}}} \right) \frac{\Pi(-1)^J}{2} \tag{109}$$

and we can now relate the calculated reactance matrix in equation (105) with that defined in equation (93)

$$(R^{J,\Pi,\Gamma})_{v,j,k}^{v',j',k'} = (\tilde{R}^{J,\Pi,\Gamma})_{v,j,k}^{v',j',-k'} \tag{110}$$

We have related the linearly independent numerical solutions to Schrödinger's equation to the body-fixed reactance matrix solutions. The uniqueness of the reactance matrix[70] permits us to use equation (110) without worrying about which reactance matrix is found. The matrix $\tilde{\mathbf{R}}^{J,\Pi,\Gamma}$ is labelled with nonnegative values of k and k' only. Equation (110) permits this matrix to be related to a part of the

body-fixed reactance matrix $\mathbf{R}^{J,\Pi,\Gamma}$. This part of the body-fixed reactance matrix can be used to construct the rest of the reactance matrix using equations (88) and (91) with the reactance matrix substituted for the scattering matrix. In the next section, the direct construction of the open part of the reactance matrix from the integrated solutions will be discussed.

B. Coriolis-Coupled General Asymptotic Wave Function

The asymptotic solutions written down so far are valid for R_λ large enough to allow the neglect of both the atom-diatom interaction and Coriolis coupling resulting from the use of a body-fixed Hamiltonian. The Coriolis coupling varies as R_λ^{-2} and is rather long range. In constrast, the interaction between an atom and a diatomic molecule vanishes as R_λ^{-6} if neither has a permanent electric charge. The Coriolis coupling has not appeared explicitly in this paper because it manifests itself entirely in the partial differential equations defining the two-angle surface function which is discussed in paper II.

It is possible to write down the analytic form of solutions to the Schrödinger equation valid at values of R_λ which are sufficiently small for the Coriolis coupling to be nonnegligible, and at the same time sufficiently large for the interaction between the atom and the diatomic molecule to be negligible. The object in writing down the functional form which holds for the corresponding smaller values of the hyperradius is to minimize the range over which the ordinary differential equations (17) must be integrated numerically.

The body-fixed functions of R_λ which hold when the interaction between the atom and the diatomic molecule is negligible, but the Coriolis coupling need not be, are given by Schatz and Kuppermann.[2b] (We have used a slightly different notation than that used in reference 2b.)

$$B^{J,\Pi,\Gamma,p'}_{v,j,\Omega}(R_\lambda) = k_{v,j}|V_{v,j}|^{-\frac{1}{2}} \sum_{\Omega'} \left\{ C^{J,\Pi,\Gamma,p'}_{v,j,\Omega'} S^{J,\Pi}_{v,j,\Omega,\Omega'}(R_\lambda) + D^{J,\Pi,\Gamma,p'}_{v,j,\Omega'} C^{J,\Pi}_{v,j,\Omega,\Omega'}(R_\lambda) \right\} \tag{111}$$

where

$$S^{J,\Pi}_{v,j,\Omega,\Omega'}(R_\lambda) = (-1)^{\Omega+\Omega'} \sum_\ell \Bigg\{ \left(\frac{1+\Pi(-1)^{j-\ell}}{2} \right) C(J,j,\ell;\Omega,-\Omega,0)$$

$$C(J,j,\ell;\Omega',-\Omega',0) \left(\cos[(J+j-\ell)\frac{\pi}{2}] j_\ell(k_{v,j}R_\lambda) + \sin[(J+j-\ell)\frac{\pi}{2}] y_\ell(k_{v,j}R_\lambda) \right) \Bigg\} \tag{112}$$

and

$$C^{J,\Pi}_{v,j,\Omega,\Omega'}(R_\lambda) = (-1)^{\Omega+\Omega'} \sum_\ell \Bigg\{ \left(\frac{1+\Pi(-1)^{j-\ell}}{2} \right) C(J,j,\ell;\Omega,-\Omega,0)$$

$$C(J,j,\ell;\Omega',-\Omega',0) \left(\sin[(J+j-\ell)\frac{\pi}{2}] j_\ell(k_{v,j}R_\lambda) - \cos[(J+j-\ell)\frac{\pi}{2}] y_\ell(k_{v,j}R_\lambda) \right) \Bigg\} \tag{113}$$

for open states and

$$S^{J,\Pi}_{v,j,\Omega,\Omega'}(R_\lambda) = 2(-1)^{\Omega+\Omega'} \sum_\ell C(J,j,\ell;\Omega,-\Omega,0) C(J,j,\ell;\Omega',-\Omega',0)$$

$$\left(\frac{1+\Pi(-1)^{j-\ell}}{2} \right) i_\ell(\kappa_{v,j}R_\lambda) \tag{114}$$

$$C^{J,\Pi}_{v,j,\Omega,\Omega'}(R_\lambda) = \frac{2}{\pi}(-1)^{\Omega+\Omega'} \sum_\ell C(J,j,\ell;\Omega,-\Omega,0) C(J,j,\ell;\Omega',-\Omega',0)$$

$$\left(\frac{1+\Pi(-1)^{j-\ell}}{2} \right) k_\ell(\kappa_{v,j}R_\lambda) \tag{115}$$

for closed states. The symbols $j_\ell(k_{v,j}R_\lambda)$ and $y_\ell(k_{v,j}R_\lambda)$ stand for the spherical Bessel and Neumann functions, respectively. In addition, $i_\ell(\kappa_{v,j}R_\lambda)$ and $k_\ell(\kappa_{v,j}R_\lambda)$ are the modified spherical Bessel functions of the first and third kind, respectively.[77] $C(j_1,j_2,j_3;m_1,m_2,m_3)$ are the Clebsch-Gordan coefficients using the notation of Rose.[78] As $R_\lambda \sim \infty$, equations (111)-(115) become equations (103)-(104).

The asymptotic projection of the numerical solutions of the initial value problem in hyperspherical coordinates onto the Coriolis-coupled asymptotic Jacobi solutions is found by equating the numerical solutions (16) with the general asymptotic form (103) and (110) through (115):

$$\rho^{-\frac{5}{2}} \sum_{n} G_n^{J,\Pi,\Gamma,p'}(\rho;\overline{\rho}) \Phi_n^{J,M,\Pi,\Gamma,i}(\omega_\lambda,\gamma_\lambda,\psi_\lambda,\vartheta_\lambda,\varphi_\lambda;\overline{\rho}) =$$

$$\sum_{\lambda} \sum_{v,j,\Omega} c_{\lambda,j}^{\Gamma,i} D_{M,\Omega}^{J}(\varphi_\lambda,\vartheta_\lambda,0) h_{v,j}(r_\lambda) Y_{j,\Omega}(\gamma_\lambda,\psi_\lambda) B_{v,j,\Omega}^{J,\Pi,\Gamma,p'}(R_\lambda) \qquad (116)$$

Both sides of (116) are evaluated at the same point in configuration space and ρ must be large enough that the corresponding asymptotic form given in equation (110) is valid. $\overline{\rho}$ indicates the hyperradial position of the associated surface function set. Multiplying through by $\left(\Phi_n^{J,M,\Pi,\Gamma,i}(\omega_\lambda,\gamma_\lambda,\psi_\lambda,\vartheta_\lambda,\varphi_\lambda;\overline{\rho})\right)^*$, integrating over the variables $(\omega_\lambda,\gamma_\lambda,\psi_\lambda,\vartheta_\lambda,\varphi_\lambda)$, and recalling that the surface functions are expanded in Wigner rotation matrices, we find

$$\mathbf{g}^{J,\Pi,\Gamma}(\rho;\overline{\rho}) = \alpha^{J,\Pi,\Gamma}(\rho,\overline{\rho})\mathbf{C}^{J,\Pi,\Gamma} + \beta^{J,\Pi,\Gamma}(\rho,\overline{\rho})\mathbf{D}^{J,\Pi,\Gamma} \qquad (117)$$

where

$$(\alpha^{J,\Pi,\Gamma})_n^{v,j,\Omega'}(\rho,\overline{\rho}) = \rho^{\frac{5}{2}} |V_{v,j}|^{-\frac{1}{2}} \sum_{\lambda} \sum_{\Omega} \int \sin^2\omega_\lambda \sin\gamma_\lambda d\omega_\lambda d\gamma_\lambda$$

$$\phi_{\Omega,n}^{*\lambda,J,\Pi,\Gamma,i}(\omega_\lambda,\gamma_\lambda,\overline{\rho}) c_{\lambda,j}^{\Gamma,i} h_{v,j}(r_\lambda) P_j^{\Omega}(\cos\gamma_\lambda) \mathcal{S}_{v,j,\Omega,\Omega'}^{J,\Pi}(R_\lambda) \qquad (118)$$

$$(\beta^{J,\Pi,\Gamma})_n^{v,j,\Omega'}(\rho,\overline{\rho}) = \rho^{\frac{5}{2}} |V_{v,j}|^{-\frac{1}{2}} \sum_{\lambda} \sum_{\Omega} \int \sin^2\omega_\lambda \sin\gamma_\lambda d\omega_\lambda d\gamma_\lambda$$

$$\phi_{\Omega,n}^{*\lambda,J,\Pi,\Gamma,i}(\omega_\lambda,\gamma_\lambda,\overline{\rho}) c_{\lambda,j}^{\Gamma,i} h_{v,j}(r_\lambda) P_j^{\Omega}(\cos\gamma_\lambda) \mathcal{C}_{v,j,\Omega,\Omega'}^{J,\Pi}(R_\lambda) \qquad (119)$$

The subscript n corresponds to an arbitrary labelling of the two-angle surface functions and is the row index on the $\mathbf{g}^{J,\Pi,\Gamma}$, $\alpha^{J,\Pi,\Gamma}$, and $\beta^{J,\Pi,\Gamma}$ matrices. The superscripts v,j,Ω' on the latter two matrices are interpreted as a set of column indices and correspond to the row indices on the integration constants $\mathbf{C}^{J,\Pi,\Gamma}$ and $\mathbf{D}^{J,\Pi,\Gamma}$. The columns of $\mathbf{g}^{J,\Pi,\Gamma}$, $\mathbf{C}^{J,\Pi,\Gamma}$ and $\mathbf{D}^{J,\Pi,\Gamma}$ are labelled by p', the initial condition index.

In practice, the logarithmic derivative matrix[69] contains all of the information necessary to construct the reactance matrix as we will show in this paragraph. Let a dot denote differentiation with respect to ρ. The logarithmic derivative matrix associated with the propagation equation (17) is defined as

$$\mathbf{Y}^{J,\Pi,\Gamma}(\rho,\overline{\rho}) = \dot{\mathbf{g}}^{J,\Pi,\Gamma}(\rho,\overline{\rho})\Big(\mathbf{g}^{J,\Pi,\Gamma}(\rho,\overline{\rho})\Big)^{-1} \tag{120}$$

Omitting the arguments ρ and $\overline{\rho}$, we find

$$\tilde{\mathbf{R}}^{J,\Pi,\Gamma} = \left[\mathbf{Y}^{J,\Pi,\Gamma}\beta^{J,\Pi,\Gamma} - \dot{\beta}^{J,\Pi,\Gamma}\right]^{-1}\left[\dot{\alpha}^{J,\Pi,\Gamma} - \mathbf{Y}^{J,\Pi,\Gamma}\alpha^{J,\Pi,\Gamma}\right] \tag{121}$$

Equation (121) shows explicitly that the hyperspherical logarithmic derivative matrix, the two-angle surface functions, and the isolated diatomic molecule wave function are all that is necessary to construct the R matrix.

In summary, a logarithmic matrix with a set of arbitrary, but linearly independent initial conditions, whose number is equal to the number of asymptotic diatomic molecule states included in the projection, is propagated from small ρ, where the wave function vanishes, to a range of ρ where the atom-diatomic molecule interaction vanishes. Matrices, whose elements represent the projection of the two-angle surface functions onto the Coriolis-coupled asymptotic Jacobi wave functions, provide the means for converting the logarithmic derivative matrix into a reactance matrix. From the open-channel part of the reactance matrix, the open-channel part of the scattering matrix, the P_3 irreducible representation helicity scattering amplitude, and corresponding differential cross sections are calculable. Different collision energies produce different logarithmic derivative matrices from the propagation equations (17).

10. Separable Basis Set

In this section, we define a basis set which is more efficient than the finite element surface functions for moderate to large values of ρ. This new basis set is composed of products of associated Legendre functions of γ_λ and hyperspherical

vibrational functions of ω_λ. We describe how the transformation into this basis set is accomplished, the associated set of coupled ordinary differential equations, and the projection integrals for asymptotic analysis.

The separable basis set is much less expensive to calculate than the surface functions because the separable basis set is constructed of one dimensional numerical functions and analytic functions while the finite element surface functions exist on a two dimensional domain. For sufficiently large values of ρ, the scattering wave function is vanishingly small in the regions of configuration space between the arrangement channels and the separable basis set is efficient for expanding it. For these values of ρ, the surface functions are localized in the arrangement channels, since they have negligible amplitude between arrangement channels, and are well approximated by the separable functions described below. The sole reason for using a separable basis set is because the finite element calculation of surface functions is expensive and unnecessary in the weak interaction region of configuration space. In fact, the separable basis set provides an effective variational basis set for calculating surface functions at all values of ρ.

The separable basis set is defined by

$$F_{\hat{t}}^{J,M,\Pi,\Gamma,i}(\zeta_\lambda;\overline{\rho}) = \sum_\lambda c_{\lambda,j}^{\Gamma,i} D_{M,\Omega}^J(\varphi_\lambda,\vartheta_\lambda,\psi_\lambda) P_j^\Omega(\cos\gamma_\lambda) f_{\hat{t}}^J(\omega_\lambda;\overline{\rho}) \tag{122}$$

where $\hat{t} = (s,j,\Omega)$ and

$$\left(\hat{h}_{\rm ref}^{J,\Omega,j} - \overline{e}_{\hat{t}}(\overline{\rho})\right) f_{\hat{t}}^J(\omega_\lambda;\overline{\rho}) = 0 \tag{123}$$

with the definition

$$\begin{aligned}\hat{h}_{\rm ref}^{J,\Omega,j} = {} & \frac{-2\hbar^2}{\mu\overline{\rho}^2}\left(\frac{\partial^2}{\partial\omega_\lambda^2} + 2\cot\omega_\lambda\frac{\partial}{\partial\omega_\lambda}\right) + \frac{2j(j+1)\hbar^2}{\mu\overline{\rho}^2\sin^2\omega_\lambda} \\ & + \frac{[J(J+1)-2\Omega^2]\hbar^2}{2\mu\overline{\rho}^2\cos^2\frac{\omega_\lambda}{2}} + \overline{V}(\overline{\rho},\omega_\lambda,\gamma_\lambda=0)\end{aligned} \tag{124}$$

defines a set of one dimensional numerical functions. Since they are one dimensional, they are inexpensive to calculate. To complete their definition, the following boundary conditions are enforced:

$$f_{\hat{t}}^{J}(\omega_\lambda = 0; \overline{\rho}) = f_{\hat{t}}^{J}(\omega_\lambda = \omega_\lambda^{max}; \overline{\rho}) = 0. \tag{125}$$

ω_λ^{max} is large enough that the potential energy is very large, but not so large that the other arrangement channels are approached.

Next, we expand the scattering wave function in the separable basis set in a manner analagous to that of equation (16):

$$\Psi^{J,M,\Pi,\Gamma,i,p'}(\rho, \zeta_\lambda) = \rho^{-\frac{5}{2}} \sum_{\hat{t}} g_{\hat{t}}^{J,\Pi,\Gamma,p'}(\rho; \overline{\rho}) F_{\hat{t}}^{J,M,\Pi,\Gamma,i}(\zeta_\lambda; \overline{\rho}) \tag{126}$$

The differential equation for the $g_{\hat{t}}^{J,\Pi,\Gamma,p'}(\rho; \overline{\rho})$ is

$$\frac{d^2}{d\rho^2} g_{\hat{t}}^{J,\Pi,\Gamma,p'}(\rho; \overline{\rho}) + \sum_{\hat{t}'} u_{\hat{t},\hat{t}'}^{J,\Pi,\Gamma}(\rho; \overline{\rho}) g_{\hat{t}'}^{J,\Pi,\Gamma,p'}(\rho; \overline{\rho}) = 0 \tag{127}$$

where

$$u_{\hat{t},\hat{t}'}^{J,\Pi,\Gamma}(\rho; \overline{\rho}) = \int F_{\hat{t}}^{J,M,\Pi,\Gamma,i}(\zeta_\lambda; \overline{\rho}) \left[\frac{-\hat{\Lambda}^2}{\hbar^2 \rho^2} - \frac{2\mu}{\hbar^2} \overline{V}(\rho, \omega_\lambda, \gamma_\lambda) \right] F_{\hat{t}'}^{J,M,\Pi,\Gamma,i}(\zeta_\lambda; \overline{\rho}) d\tau_1 - \delta_{\hat{t}'}^{\hat{t}} \left(\frac{15}{4\rho^2} + \frac{2\mu E}{\hbar^2} \right) \tag{128}$$

The initial conditions for the propagation of the coupled set of ordinary differential equations (127) follows from the requirement that the wave function and its ρ derivative be continuous and this requirement is satisfied by the use of overlap matrices. Overlap matrices must be calculated between the final set of surface functions and the first set of separable functions in order to transform the hyperspherical logarithmic derivative from the surface function set to the separable set. This integrals are

$$\overline{o}_{\hat{t},n'}^{J,\Pi,\Gamma}(\overline{\rho}_{i+1}, \overline{\rho}_i) = \int F_{\hat{t}}^{*J,M,\Pi,\Gamma,i}(\zeta_\lambda; \overline{\rho}_{i+1}) \Phi_{n'}^{J,M,\Pi,\Gamma,i}(\zeta_\lambda; \overline{\rho}_i) d\tau_1 \tag{129}$$

and the ρ dependent coefficients in the separable basis set expansion (126) become

$$g_{\hat{t}}^{J,\Pi,\Gamma,p'}(\rho;\overline{\rho}_{i+1}) = \sum_{n'} \overline{o}_{\hat{t},n'}^{J,\Pi,\Gamma}(\overline{\rho}_{i+1},\overline{\rho}_i) G_{n'}^{J,\Gamma,\Pi,p'}(\rho;\overline{\rho}_i) \tag{130}$$

Many sets of separable basis functions at different values of $\overline{\rho}$ are needed in a scattering calculation just as is the case for the surface function basis set. The separable basis set is effective for expanding the scattering wave function only for values of ρ near $\overline{\rho}$. The overlap matrices for transforming the $g_{\hat{t}'}^{J,\Pi,\Gamma,p'}(\rho;\overline{\rho}_i)$ into $g_{\hat{t}'}^{J,\Pi,\Gamma,p'}(\rho;\overline{\rho}_{i+1})$ is

$$g_{\hat{t}}^{J,\Pi,\Gamma,p'}(\rho;\overline{\rho}_{i+1}) = \sum_{\hat{t}'} o_{\hat{t},\hat{t}'}^{J,\Pi,\Gamma}(\overline{\rho}_{i+1},\overline{\rho}_i) g_{\hat{t}'}^{J,\Gamma,\Pi,p'}(\rho;\overline{\rho}_i) \tag{131}$$

where

$$o_{\hat{t},\hat{t}'}^{J,\Pi,\Gamma}(\overline{\rho}_{i+1},\overline{\rho}_i) = \int F_{\hat{t}}^{*J,M,\Pi,\Gamma,i}(\zeta_\lambda;\overline{\rho}_{i+1}) F_{\hat{t}'}^{J,M,\Pi,\Gamma,i}(\zeta_\lambda;\overline{\rho}_i) d\tau_1 \tag{132}$$

Since the wave function in the asymptotic region is expanded in the separable basis set, we need to write down the projection integrals corresponding to equations (118) and (119). To make clear the distinction between the projection of the separable basis functions onto the asymptotic states and the corresponding projection of the surface functions, we will place bars over the symbols used for the projection integrals of the separable functions.

$$\begin{aligned}(\overline{\alpha}^{J,\Pi,\Gamma})_{s,j,\Omega}^{v,j,\Omega'}(\rho,\overline{\rho}) &= \rho^{\frac{5}{2}} |V_{v,j}|^{-\frac{1}{2}} \sum_{\Omega} \int \sin^2 \omega_\lambda d\omega_\lambda \\ & f_{s,j,\Omega}^{*J,\Pi,\Gamma,i}(\omega_\lambda;\overline{\rho}) h_{v,j}(r_\lambda) \mathcal{S}_{v,j,\Omega,\Omega'}^{J,\Pi}(R_\lambda)\end{aligned} \tag{133}$$

$$\begin{aligned}(\overline{\beta}^{J,\Pi,\Gamma})_{s,j,\Omega}^{v,j,\Omega'}(\rho,\overline{\rho}) &= \rho^{\frac{5}{2}} |V_{v,j}|^{-\frac{1}{2}} \sum_{\Omega} \int \sin^2 \omega_\lambda d\omega_\lambda \\ & f_{s,j,\Omega}^{*J}(\omega_\lambda;\overline{\rho}) h_{v,j}(r_\lambda) \mathcal{C}_{v,j,\Omega,\Omega'}^{J,\Pi}(R_\lambda)\end{aligned} \tag{134}$$

In equation (121), which gives the formation of the $\tilde{\mathbf{R}}^{J,\Pi,\Gamma}$ matrix from the hyperspherical logarithmic derivative and the projection integrals, the unbarred α and β are replaced by their barred counterpoints given by equations (133) and (134).

11. Nuclear Spin and the Pauli Principle

At this point it is convenient to recognize the possibility that the particles have intrinsic spin and that the complete wave function has spin components. The Hamiltonian considered here does not include spin dependent terms; therefore, the complete wave function can be written as a direct product of a spatial wave function, which satisfies the Schrödinger equation, and a spin wave function for the three particles. In earlier sections we have discussed the explicit construction of the spatial part of the scattering wave function. From the direct product of the spatial and spin functions, differential cross sections for appropriately antisymmetrized scattering wave functions can be extracted. The existence of nuclear spin does not affect the previous sections and becomes important here in connection with the Pauli principle.

Rotational invariance implies conservation of the spin total angular momenta squared and one of its space-fixed components. The spin functions that we will use are chosen to be eigenfunctions of $\hat{S}^2$, the square of the total spin angular momentum operator and $\hat{S}_Z$, its space-fixed Z component.

The permutation operators also affect the spin functions. Since the operators of P_3 all commute with those of $SO(3)$, the spin functions just chosen form irreducible representations of P_3. For example, if the three nuclei are spin $\frac{1}{2}$, then the possible spin states are quartet $S = \frac{3}{2}$ and doublet $S = \frac{1}{2}$. There are four quartet spin states distinguished by different space-fixed Z spin component quantum numbers: $S_Z = \pm\frac{1}{2}, \pm\frac{3}{2}$, each of which transforms independently as A_1. There are two doublet spin functions for each value of $S_Z = \pm\frac{1}{2}$ that transform as partners in an E irreducible representation. The explicit spin functions are not important for extracting the spin-averaged antisymmetrized cross sections.

The term antisymmetrized is a brief way of saying that the total scattering wave function (spatial times spin) transforms as the A_2 irreducible representation of P_3. Since the spatial and spin wave functions separately form irreducible representations of P_3, then the product of these yields a direct product representation

of P_3 which is reducible. The irreducible decompositions of the direct products are (spin $\otimes$ spatial)

$$A_1 \otimes A_1 = A_1 \tag{135}$$

$$A_1 \otimes A_2 = A_2 \tag{136}$$

$$A_1 \otimes E = E \tag{137}$$

$$E \otimes A_1 = E \tag{138}$$

$$E \otimes A_2 = E \tag{139}$$

$$E \otimes E = A_1 \oplus A_2 \oplus E \tag{140}$$

It is seen that in the case of fermions the only irreducible representation spatial solutions that contribute to nature are A_2 and E. When the Pauli principle is satisfied, we associate the quartet nuclear spin state with the A_2 spatial scattering amplitude and the doublet nuclear spin state with the E spatial scattering amplitude for spin $\frac{1}{2}$ nuclei like hydrogen. It is easily seen that bosons require spatial solutions that transform as A_1 and E.

If the initial rotational state of the diatomic j is even (para hydrogen), then the corresponding spatial wave function must belong to the E irreducible representation because A_2 solutions contain no even rotational states. By implication, the total nuclear spin state is doublet for experiments with even j initial diatom rotational states. Since the nuclear spin state is known and is a constant of the motion, no spin state average need be taken and the antisymmetrized cross section is entirely composed of E spatial scattering amplitudes

$$\sigma^{para,v',j',k'}_{para,v,j,k}(\vartheta,\varphi) = \left(\frac{V'_{v,j}}{V'_{v',j'}}\right)|f^{E,v',j',k'}_{v,j,k}(\vartheta,\varphi)|^2 = \sigma^{E,v',j',k'}_{v,j,k}(\vartheta,\varphi) \tag{141}$$

$$\sigma^{para,v',j',k'}_{ortho,v,j,k}(\vartheta,\varphi) = \left(\frac{V'_{v,j}}{V'_{v',j'}}\right)|f^{E,v',j',k'}_{v,j,k}(\vartheta,\varphi)|^2 = \sigma^{E,v',j',k'}_{v,j,k}(\vartheta,\varphi) \tag{142}$$

The *para* and *ortho* indices indicate para and ortho hydrogen, respectively. If the initial rotational state of the diatomic molecule j is odd (ortho hydrogen), then the spatial solution can be either E or A_2. If the initial diatomic molecule

preparation and final state measurement are insensitive to the nuclear spin states, then the three particles have a $\frac{2}{6}$ chance to be in the doublet spin configurations and a $\frac{4}{6}$ chance to be in the quartet spin configurations. This follows because there are 4 A_1 spin states and 2 E spin states accessible for a total of 6 possible spin states. The antisymmetrized cross sections are the weighted average of the E and A_2 scattering amplitudes, where the weights are those implied by the number of accessible spin states.

$$\sigma_{para,v,j,k}^{ortho,v',j',k'}(\vartheta,\varphi) = \frac{1}{3}\left(\frac{V'_{v,j}}{V'_{v',j'}}\right)|f_{v,j,k}^{E,v',j',k'}(\vartheta,\varphi)|^2 = \frac{1}{3}\sigma_{v,j,k}^{E,v',j',k'}(\vartheta,\varphi) \qquad (143)$$

$$\begin{aligned}\sigma_{ortho,v,j,k}^{ortho,v',j',k'}(\vartheta,\varphi) &= \frac{1}{3}\left(\frac{V'_{v,j}}{V'_{v',j'}}\right)\left[|f_{v,j,k}^{E,v',j',k'}(\vartheta,\varphi)|^2 + 2|f_{v,j,k}^{A_2,v',j',k'}(\vartheta,\varphi)|^2\right] \\ &= \frac{1}{3}\sigma_{v,j,k}^{E,v',j',k'}(\vartheta,\varphi) + \frac{2}{3}\sigma_{v,j,k}^{A_2,v',j',k'}(\vartheta,\varphi) \qquad (144)\end{aligned}$$

The ortho to para differential cross section includes only the E irreducible representation scattering amplitude because there is no corresponding A_2 scattering amplitude. Summing up, all differential cross sections are composed solely of E differential cross sections except the ortho to ortho ones which are a simple linear combination of the E and A_2 differential cross sections. Even in the ortho to ortho transitions, there is no interference between the E and A_2 contributions. This contrasts with the interference terms obtained when Pauli antisymmetrized cross sections are expressed in terms of reactive and nonreactive cross sections. As a consistency check, if the irreducible representation scattering amplitudes are written in terms of the distinguishable scattering amplitudes, then the antisymmetrized differential cross sections agree with those given in Schatz and Kuppermann[2b] and by Doll, George, and Miller.[79]

Finally, we note that for experiments which state select the nuclear spin states, it is possible to study independently the quartet nuclear spin system and the doublet spin system. The measured cross sections would then be interpreted as arising from the A_2 and E spatial scattering amplitude, respectively. Of course, such nuclear spin selection is probably not feasible, but it violates no principles to

consider such a gedanken experiment for the purposes of interpretation of our P_3 labeled results.

12. Summary

We have presented in detail a methodology for performing accurate quantum mechanical reactive scattering calculations based on symmetrized body-fixed hyperspherical coordinates. In this approach, the emphasis is on the surface functions, their effectiveness as an expansion basis set simultaneously in all arrangement channels, and their evolution with $\overline{\rho}$ from the strong interaction region to the asymptotic region. By making use of the highly developed methods for integrating coupled sets of ordinary differential equation, the propagation phase of the calculation is efficient and well understood. A new constant hyperradius projection technique allows the conversion of integrated solutions into partial wave reactance matrices from which all other quantities of experimental interest are calculable.

The most important attribute of scattering calculations based on hyperspherical coordinate techniques and the associated expansion in local surface functions is that nowhere in the paper did we need to consider matching between arrangement channels or the bifurcation problem. In effect, this method reduces multi-arrangement channel reactive scattering to the same form as a nonreactive inelastic scattering problem. The only catch is that the surface function basis set is currently expensive to calculate; however, they provide rapidly converging coupled channel expansions and their cost simply reflects the reluctance of nature to part easily with her secrets.

References

† Work supported in part by the U.S. Air Force Office of Scientific Research, Contract No. AFOSR-82-0341. Support from the U.S. Department of Energy, Grant No. DE-AS03-83ER 13118 is also acknowledged. We thank the San Diego Supercomputer Center on whose Cray X-MP/48 the calculations were performed.

¶ Work performed in partial fulfillment of the requirements for the Ph.D. degree in Chemistry at the California Institute of Technology.

‡Contribution number

1. D. G. Truhlar and R. E. Wyatt, *Ann. Rev. Phys. Chem.* **27**, 1 (1976); G. C. Schatz, in: **Theory of Chemical Reaction Dynamics**, ed. by D. C. Clary, Proceedings of NATO Workshop, Orsay, France, 1986, p.1; B. C. Garrett and D. G. Truhlar, *Ann. Rev. Phys. Chem.* **35**, 159 (1984); J. M. Bowman, *Adv. Chem. Phys.* **61**, 115 (1985).
2. (a) G. C. Schatz and A. Kuppermann, *J. Chem. Phys.* **62**, 2502 (1975); (b) **65**, 4642 (1976); (c) 4668 (1976).
3. A. B. Elkowitz and R. E. Wyatt, *J. Chem. Phys.* **62**, 2504 (1975); **63**, 702 (1975).
4. R. N. Porter and M. Karplus, *J. Chem. Phys.* **40**, 1105 (1964).
5. B. Liu, *J. Chem. Phys.* **58**, 1925 (1973); P. Siegbahn and B. Liu, *J. Chem. Phys.* **68**, 2457 (1978).
6. D. G. Truhlar and C. J. Horowitz, *J. Chem. Phys.* **68**, 2468 (1978); **E71**, 1514 (1979).
7. R. B. Johnson, *J. Chem. Phys.* **74**, 754 (1981).
8. R. B. Walker, E. B. Stechel, and J. C. Light, *J. Chem. Phys.* **69**, 2922 (1978).
9. A. Kuppermann, J. A. Kaye, and J. P. Dwyer, *Chem. Phys. Lett.* bf 74, 257 (1980).

10. G. Haug, J. Manz, and J. Römelt, *J. Chem. Phys.* **73**, 5040 (1980); J. Römelt, *Chem. Phys. Lett.* **74**, 263 (1980); for a review see: J. Manz, *Comments At. Mol. Phys.* **17**, 91 (1985).
11. J. A. Kaye and A. Kuppermann, *Chem. Phys. Lett.* **77**, 573 (1981).
12. J. Manz and J. Römelt, *Chem. Phys. Lett.* **81**, 179 (1981).
13. J. Manz and J. Römelt, *Chem. Phys. Lett.* **77**, 172 (1981).
14. J. A. Kaye and A. Kuppermann, *Chem. Phys. Lett.* **78**, 546 (1981).
15. A. Kuppermann, in: **Theoretical Chemistry - Theory of Scattering: Papers in Honor of Henry Eyring,**Vol 6, Part A, ed. D. Henderson (Academic Press, Orlando, 1981) pp. 79,122
16. A. Kuppermann and J. P. Dwyer, in: **Electronic and Atomic Collisions, Abstracts of Contributed Papers,** *11th International Conference on the Physics of Electronic and Atomic Collisions, Kyoto, Japan* (The Society for Atomic Collision Research, Tokyo, 1979) pp. 888,889.
17. A. Kuppermann, in: **Potential Energy Surface and Dynamics Calculations,** ed. by D. G. Truhlar (Plenum Press, New York, 1981) pp. 405, 414.
18. J. Römelt and E. Pollak, *Chem. Phys.* **79**, 197 (1983); in: **Resonances,** *Am. Chem. Soc. Symp. Ser.* **263** (Am. Chem. Soc., Washington, 1984) pp. 353,374; and references therein.
19. R. D. Levine and S. Wu, *Chem. Phys. Lett.* **11**, 557 (1971).
20. B. C. Garrett and D. G. Truhlar, *J. Phys. Chem.* **86**, 1136 (1982); **87**, 4554 (1983); B. C. Garrett, D. W. Schwenke, R. T. Skodje, D. Thirumalai, T. C. Thompson, and D. G. Truhlar, in: **Resonances,** *Am. Chem. Soc. Symp. Ser.* **263**, 375.
21. E. Pollak, *J. Phys. Chem.* **90**, 3619 (1986); *Chem. Phys. Lett.* **137**, 171 (1987).
22. V. K. Babamov and R. A. Marcus, *J. Chem. Phys.* **74**, 1790 (1981).
23. C. D. Lin, Adv. Atom. Mol. Phys. **22**, 77 (1986).

24. S. Y. Larsen, in: **Few-Body Methods: Principles and Applications**, eds. T. K. Lim, C. G. Bao, D. P. Hou, and S. Huber (World Scientific Pub., Singapore, 1986).
25. T. H. Gronwall, *Ann. Math.* **33**, 279 (1932); *Phys. Rev.* **51**, 655 (1937).
26. J. H. Bartlett, *Phys. Rev.* **51**, 661 (1937).
27. G. H. Wannier, *Phys. Rev.* **90**, 817 (1953).
28. V. Fock, *Det Kong. Norske Vidensk. Selsk. Forhandl.* **31**, 138,145 (1958).
29. J. Macek, *J. Phys. B* **1**, 831 (1968).
30. R. P. Madden and K. Codling, *Phys. Rev. Lett.* **10**, 516 (1963).
31. H. Klar and M. Klar, *Z. Phys. A* **307**, 75 (1982).
32. U. Fano, *Phys. Rev. A* **24**, 2402 (1981).
33. C. H. Greene and C. W. Clark, *Phys. Rev. A* **30**, 2161 (1984).
34. A. F. Starace, in: **Fundamental Processes in Energetic Atomic Collisions**, eds. H. O. Luta, J. S. Briggs, and H. Kleinpoppen (Plenum Press, New York, 1983) p. 69.
35. D. M. Hood and A. Kuppermann, in: **Theory of Chemical Reaction Dynamics**, ed. D. C. Clary (D. Reidel, Boston, 1986) pp. 193,214.
36. R. E. Clapp, *Phys. Rev.* **76**, 873 (1949).
37. L. M. Delves, *Nucl. Phys.* **9**, 391 (1958/59); **20**, 275 (1960).
38. F. T. Smith, *J. Math. Phys.* **3**, 735 (1962); *J. Chem. Phys.* **38**, 1304 (1963); R. C. Whitten and F. T. Smith, *J. Math. Phys.* **9**, 1103 (1968).
39. A. Kuppermann, *Chem. Phys. Lett.* **32**, 374 (1975).
40. R. T. Ling and A. Kuppermann, in: **Electronic and Atomic Collisions, Abstracts of Papers of the 9th International Conference on the Physics of Electronic and Atomic Collisions**, Seattle, Washington, 24-30 July, 1975, Vol 1., eds. J. S. Risley and R. Geballe (Univ. Washington Press, Seatle, 1975) pp. 353,354.
41. B. R. Johnson, *J. Chem. Phys.* **73**, 5051 (1980).
42. L. Wolniewicz and J. Hinze, *J. Chem. Phys.* **85**, 2012 (1986).

43. C. A. Mead, *J. Chem. Phys.* **72**, 3839 (1980); *Chem. Phys.* **49**, 23 (1980).

44. R. T. Pack, *Chem. Phys. Lett.* **108**, 333 (1984).

45. A. Kuppermann and P. G. Hipes, *J. Chem. Phys.* **84**, 5962 (1986); P. G. Hipes and A. Kuppermann, *Chem. Phys. Lett.* **133**, 1 (1987).

46. G. A. Parker, R. T. Pack, B. J. Archer, and R. B. Walker, *Chem. Phys. Lett.* **137**, 564 (1987); R. T. Pack and G. A. Parker, submitted to *J. Chem. Phys.*.

47. M. Mishra, J. Linderberg, and Y. Öhrn, *Chem. Phys. Lett.* **111**, 439 (1984); J. Linderberg, *Intern. J. Quantum Chem.* **19**, 467 (1986).

48. F. Webster and J. C. Light, *J. Chem. Phys.* **85**, 4744 (1986).

49. D. W. Schwenke, D. G. Truhlar, and D. J. Kouri, *J. Chem. Phys.* **86**, 2772 (1987).

50. K. Haug, D. W. Schwenke, Y. Shima, D. G. Truhlar, J. Zhang, and D. J. Kouri, *J. Phys. Chem.* **90**, 6757 (1986).

51. K. Haug, D. W. Schwenke, and D. G. Truhlar, *J. Chem. Phys.* **87**, 1892 (1987).

52. D. P. Gerrity and J. J. Vallentini, *J. Chem. Phys.* **81**, 1298 (1984); **82**, 1323 (1985); bf 83, 2207 (1985).

53. E. E. Marinero, C. T. Rettner, and R. N. Zare, *J. Chem. Phys.* **80**, 4142 (1984).

54. U. Gerlach-Meyer, K. Kleinermanns, E. Linnebach, and J. Wolfrum, *J. Chem. Phys.* **86**, 3047 (1987).

55. K. Tsukiyama, B. Katz, and R. Bersohn, *J. Chem. Phys.* **84**, 1446 (1986).

56. R. Götting, H. R. Mayne, and J. P. Toennies, *J. Chem. Phys.* **85**, 6396 (1986); R. Götting, J. P. Toennies, and M. Vodegel, *Intern. J. Chem. Kinet.* **18**, 949 (1987); R. Götting, V. Herrero, J. P. Toennies, and M. Vodegel, *Chem. Phys. Lett.* **137**, 524 (1987).

57. S. A. Buntin, C. F. Giese, and W. R. Gentry, *J. Chem. Phys.* **87**, 1443 (1987).

58. A. Kuppermann, G. C. Schatz, and J. P. Dwyer, *Chem. Phys. Lett.* **45**, 71 (1977).

59. G. C. Schatz, *Chem. Phys. Lett.* **94**, 183 (1983); G. C. Schatz, *Chem. Phys. Lett.* **108**, 532 (1984); G. C. Schatz, *J. Chem. Phys.* **83**, 3441 (1985); M. C. Colton and G. C. Schatz, *Intern. J. Chem. Kinet.* **18**, 961 (1986).

60. J. M. Bowman, *Adv. Chem. Phys.* **61**,115 (1985).

61. R. B. Walker and E. F. Hayes, *J. Phys. Chem.* **87**, 1255 (1983).

62. R. E. Wyatt, *J. Chem. Phys.* **51**, 3489 (1969).

63. J. N. L. Connor and M. S. Child, *Mol. Phys.* **18**, 653 (1970).

64. D. C. Clary, *J. Chem. Phys.* **83**, 1685 (1985).

65. **Theory of Chemical Reaction Dynamics**, ed. M. Baer (CRC Press, Boca Raton, Florida, 1985).

66. E. Wigner, **Group Theory**, (Academic Press, New York, 1959).

67. (a) M. Hammermesh, **Group Theory**, (Addison-Wesley, Reading, Mass., 1962), (a) p. 182; (b) p. 113.

68. L. D. Thomas, M. H. Alexander, B. R. Johnson, W. A. Lester, Jr., J. C. Light, K. D. McLenithan, G. A. Parker, M. J. Redmon, T. G. Schmalz, D. Secrest, and R. B. Walker, *J. Comp. Phys.* **41**, 407 (1981) and references therein.

69. B. R. Johnson, *J. Comp. Phys.* **13**, 445 (1973); *J. Chem. Phys.* **67**, 4086 (1977); NRCC Workshop, Lawrence Berkeley Laboratory, Report No. LBL-9501, 1979.

70. A. M. Lane and R. G. Thomas, *Rev. Mod. Phys.* **30**, 257 (1958).

71. J. O. Hirschfelder and E. P. Wigner, *Proc. Natl. Acad. Sci.* **21**, 113 (1935).

72. C. F. Curtiss, J. O. Hirschfelder, and F. T. Adler, *J. Chem. Phys.* **18**, 1638 (1950).

73. R. T. Pack, *J. Chem. Phys.* **60**, 633 (1974).

74. A. S. Davydov, **Quantum Mechanics, 2nd ed.** (Pergamon Press, Oxford, 1976) pp. 167,178.

75. M. Jacob and G. C. Wick, *Ann. Phys.* **7**, 404 (1959).

76. N. F. Mott and H. S. W. Massey, **The Theory of Atomic Collisions, 3rd ed.**, (Oxford Univ. Press, Oxford, 1987) pp. 390,391.

77. **Handbook of Mathematical Functions**, eds. M. Abramowitz and I. A. Stegun (National Bureau of Standards, Washington, D. C., 1970) p. 443.

78. M. E. Rose, **Elementary Theory of Angular Momentum** (Wiley, New York, 1957) pp. 32,47.

79. J. D. Doll, T. F. George, and W. H. Miller, *J. Chem. Phys.* **58**, 1343 (1973).

Three-Dimensional Atom-Diatom Reactive Scattering Calculations using Symmetrized Hyperspherical Coordinates II. Surface Functions †

Paul G. Hipes ‡ and Aron Kuppermann

Arthur Amos Noyes Laboratory of Chemical Physics,
Division of Chemistry and Chemical Engineering, §
California Institute of Technology,
Pasadena, California 91125

(Received)

Abstract

In this paper, the mathematical definition and properties of surface functions are considered for the general case of a three particle system. Because the surface function differential equation includes the potential energy surface, the surface functions are parametrized by the hyperradius. Their evolution with hyperradius makes these surface functions efficient as the expansion basis set for the scattering wave function expressed in hyperspherical coordinates. The calculation of surface functions using the finite element method is outlined. Results for the H_3 system are presented and discussed. The use of boundary conditions to control the symmetry characteristics of the numerical solutions is discussed in detail.

1. Introduction

It is our purpose to discuss the definition, properties, and numerical construction of surface functions, *i.e.*, a hyperangular basis set which appears naturally in the application to atom-diatom reactive scattering of symmetrized hyperspherical coordinate techniques.[1-5] These coordinates[1] consist of a hyperradius and a set of five hyperangles. The basis set[2] depends explicitly on the five hyperangles and parametrically on the hyperradius, and so the functions are defined on the surface of a hypersphere and span all three arrangement channels, thereby eliminating the necessity of matching[6] solutions from different arrangement channels. Recently, surface functions have been shown in numerical applications to constitute a good basis set for expanding accurate solutions to the atom-diatom reactive scattering problem.[3,4] The use of hyperspherical coordinate techniques in atom-diatom reactive scattering is recent;[1,7,8] however, they have a long history in other areas of physics.

Hyperspherical coordinates are first discussed by Gronwall[9] and Bartlett[10] in connection with the electronic structure of the He atom. Their application to two-electron dynamics of He and H^- has been extensively developed by Wannier,[11] Fock,[12] Macek,[13] Klar,[14] Lin,[15] Fano,[16] Greene,[17] Starace,[18] and Hood.[19] Clapp[20] and Delves[21] have pioneered their use in nuclear physics,[22] and the mathematical properties of the eigenfunctions of the generalized angular momentum operator or canonical angular momentum operator are developed by Smith,[23] Zickendraht,[24] Efros,[25] Arribas,[26] Simonov,[27] Smorodinskii,[28] Knirk,[29] and Smirnov.[30] Hyperspherical coordinates have also found extensive use in the calculation of reactive atom-diatom collinear scattering probabilities.[31,32]

In both the electronic structure problems[13-17] and the collinear scattering problems,[33,34] these coordinates, coupled with the adiabatic approximation,[13] are important in modeling of metastable states (resonances, autodetaching states, and autoionizing states). In the adiabatic approximation, the hyperradial motion (slow) is decoupled from the remaining angular degrees of freedom (fast),

resulting in an effective one dimensional hyperradial problem. The usefulness of the adiabatic approximation indicates that the surface function basis set is effective for expanding the accurate solutions to the atom-diatom scattering problems.

Three groups are employing hyperspherical coordinates and an associated surface functions basis set for accurate reactive 3D atom-diatom scattering calculations. Pack, Parker, Archer, and Walker[4] using Pack's APH coordinates,[35] have published reaction probabilities for $J = 0, 1$ $H + H_2$ up to 1.5 eV and for $J = 0$ $H + D_2$ over a lower collision energy range. Mishra, Linderberg, and coworkers,[5] using the Mead's hyperspherical coordinates,[36] have published surface functions and the associated adiabatic curves for $J = 0$ $H + H_2$. We have presented reactive and nonreactive probabilities and the associated time delay and lifetime analysis for $J = 0$ $H + H_2$ for energies up to 1.6 eV[3] using Kuppermann's symmetrized hyperspherical coordinates.[1] Wolneiwicz and Hinze[37] have considered the relative merits of the symmetrized hyperspherical coordinates of Johnson[38] and of Kuppermann.[1]

This paper, along with the preceding paper in the series provides complete documentation of one approach using one system of body-fixed symmetrized hyperspherical coordinates to atom-diatom reactive scattering. In section 2, the surface functions are defined. In section 3, body-fixed coordinates are introduced. In section 4, the surface functions in the Wigner rotation matrix representation are given. In section 5, a variational principle for the surface functions in the Wigner rotation matrix representation is presented. In section 6, the finite element method is discussed. In section 7, the boundary conditions for collinear configurations is given. In section 8, the permutation group appropriate for a system of 3 identical particles in introduced. In section 9, the boundary conditions imposed on the surface functions are derived from the transformation laws governing the behavior of the surface functions. In section 10, contour plots of numerical surface functions are presented for $J = 0$ $H + H_2$. Section 11 is a summary.

2. Definition of Surface Functions

Given the mass-scaled Jacobi coordinates[1] $\mathbf{R}_\lambda$ and $\mathbf{r}_\lambda$, where $\mathbf{R}_\lambda$ is the mass-scaled vector from the center of mass of the diatomic molecule $A_\nu A_\kappa$ to the atom A_λ and $\mathbf{r}_\lambda$ is the mass-scaled vector from atom A_ν to atom A_κ, symmetrized hyperspherical coordinates[1] are defined by the hyperradius given by

$$\rho = \left(R_\lambda^2 + r_\lambda^2\right)^{\frac{1}{2}}; \qquad 0 < \rho \leq \infty \tag{1}$$

which is a measure of the overall size of the three particle system and five angles: the two internal angles, γ_λ and ω_λ given by

$$\gamma_\lambda = \arccos\left(\frac{\mathbf{R}_\lambda \cdot \mathbf{r}_\lambda}{R_\lambda r_\lambda}\right); \qquad 0 \leq \gamma_\lambda \leq \pi \tag{2}$$

$$\omega_\lambda = 2\arctan\left(\frac{r_\lambda}{R_\lambda}\right); \qquad 0 \leq \omega_\lambda \leq \pi \tag{3}$$

and to fix the overall orientation of the system, the three Euler angles $(\varphi_\lambda, \vartheta_\lambda, \psi_\lambda)$ which will be defined in section 3.

The corresponding three particle Hamiltonian is

$$\hat{H} = -\frac{\hbar^2}{2\mu}\left(\frac{\partial^2}{\partial\rho^2} + \frac{5}{\rho}\frac{\partial}{\partial\rho}\right) + \hat{h}(\varphi_\lambda, \vartheta_\lambda, \psi_\lambda, \omega_\lambda, \gamma_\lambda, \rho) \tag{4}$$

where

$$\hat{h}(\varphi_\lambda, \vartheta_\lambda, \psi_\lambda, \omega_\lambda, \gamma_\lambda, \rho) = \frac{\hat{\Lambda}^2}{2\mu\rho^2} + \overline{V}^\lambda(\rho, \omega_\lambda, \gamma_\lambda) \tag{5}$$

and

$$\hat{\Lambda}^2 = -4\hbar^2\left(\frac{\partial^2}{\partial\omega_\lambda^2} + 2\cot\omega_\lambda\frac{\partial}{\partial\omega_\lambda}\right) + \frac{\hat{j}_\lambda^2}{\sin^2\frac{\omega_\lambda}{2}} + \frac{\hat{l}_\lambda^2}{\cos^2\frac{\omega_\lambda}{2}} \tag{6}$$

$\hat{j}_\lambda$ is the angular momentum operator corresponding to $\mathbf{r}_\lambda$ and $\hat{l}_\lambda$ is that corresponding to $\mathbf{R}_\lambda$. μ is the reduced mass appropriate for the mass-scaled coordinates.

$\hat{\Lambda}^2$ is referred to as the grand angular momentum operator.[23] It commutes with three operators in general: $\hat{J}^2$, the square of the total angular momentum; $\hat{J}_Z$, the space-fixed component of the total angular momentum; and $\hat{O}_I$, the three-particle inversion operator. These facts are justified by the following argument.

The three-particle Hamiltonian commutes with the operators $\hat{J}^2$, $\hat{J}_Z$, and $\hat{O}_I$. The hyperradius is invariant under each of the three operators, so the first term in the Hamiltonian (4) is also invariant. The potential energy function commutes with $\hat{J}^2$, $\hat{J}_Z$, and $\hat{O}_I$. Since the first and third terms in the Hamiltonian (4) commute with each of the operators, the grand canonical angular momentum operator must also commute with each.

The form of the Hamiltonian in hyperspherical coordinates motivates the definition of surface functions,[2] $\Phi_n^{J,M,\Pi}(\varphi_\lambda, \vartheta_\lambda, \psi_\lambda, \omega_\lambda, \gamma_\lambda; \rho)$ by

$$\left[\hat{h}(\varphi_\lambda, \vartheta_\lambda, \psi_\lambda, \omega_\lambda, \gamma_\lambda; \rho) - \epsilon_n^{J\Pi}(\rho)\right] \Phi_n^{J,M,\Pi}(\varphi_\lambda, \vartheta_\lambda, \psi_\lambda, \omega_\lambda, \gamma_\lambda; \rho) = 0 \quad (7)$$

$$\hat{J}^2 \Phi_n^{J,M,\Pi}(\varphi_\lambda, \vartheta_\lambda, \psi_\lambda, \omega_\lambda, \gamma_\lambda; \rho) = J(J+1)\hbar^2 \Phi_n^{J,M,\Pi}(\varphi_\lambda, \vartheta_\lambda, \psi_\lambda, \omega_\lambda, \gamma_\lambda; \rho) \quad (8)$$

$$\hat{J}_Z \Phi_n^{J,M,\Pi}(\varphi_\lambda, \vartheta_\lambda, \psi_\lambda, \omega_\lambda, \gamma_\lambda; \rho) = M\hbar \Phi_n^{J,M,\Pi}(\varphi_\lambda, \vartheta_\lambda, \psi_\lambda, \omega_\lambda, \gamma_\lambda; \rho) \quad (9)$$

$$\hat{O}_I \Phi_n^{J,M,\Pi}(\varphi_\lambda, \vartheta_\lambda, \psi_\lambda, \omega_\lambda, \gamma_\lambda; \rho) = \Pi \Phi_n^{J,M,\Pi}(\varphi_\lambda, \vartheta_\lambda, \psi_\lambda, \omega_\lambda, \gamma_\lambda; \rho) \quad (10)$$

The surface functions are single-valued and bounded. They are labeled with J, M, Π and n because they are chosen to be eigenfunctions of the operators $\hat{J}^2$, $\hat{J}_Z$, $\hat{O}_I$, and $\hat{h}$ with eigenvalues $\hbar^2 J(J+1)$, $\hbar M$, Π, and $\epsilon_n(\rho)$, respectively. The subscript n on $\Phi_n^{J,M,\Pi}$ and ϵ_n provides a labelling for the discrete surface function spectrum. The surface function eigenvalues are discrete because of the bounded nature of their domain: they depend on a set of five angles. In addition, the surface functions and their energies depend on ρ parametrically, and constitute an effective basis set for expanding the solutions to the Schrödinger equation corresponding to the Hamiltonian in equation (4) around ρ. Because the full atom-diatom potential appears in (7), the surface functions have a built in structure which is appropriate for the system. Finally, they span all three arrangement channels and avoid the need of matching. The use of surface functions in reactive scattering calculations is the topic of the first paper in this series.

It is convenient to normalize the surface functions over the 5D hyperangular space according to

$$\int \Phi_{n'}^{*J',M',\Pi'} \Phi_n^{J,M,\Pi} d\tau_1 = \delta_J^{J'} \delta_M^{M'} \delta_\Pi^{\Pi'} \delta_n^{n'} \quad (11)$$

with $d\tau_1 = \sin\vartheta_\lambda \sin^2\omega_\lambda \sin\gamma_\lambda d\varphi_\lambda d\vartheta_\lambda d\psi_\lambda d\omega_\lambda d\gamma_\lambda$ as the necessary volume element.

3. Body-Fixed Coordinates

In paper I, a set of body-fixed axes[6,39] is defined. Because of its importance in the present paper, we repeat its definition. The body-fixed z axis is chosen to point in the direction $\mathbf{R}_\lambda$. This is accomplished by setting the first two Euler angles[40] to be the spherical polar angles of the vector $\mathbf{R}_\lambda$: $(\vartheta_\lambda, \varphi_\lambda)$. The final Euler angle ψ_λ, is a rotation about the body-fixed z axis and is defined to bring the final body-fixed y axis into the direction of $\mathbf{R}_\lambda \times \mathbf{r}_\lambda$. In other words, the final body-fixed y axis is perpendicular to the plane defined by the three particles. The body-fixed axes are denoted by $\hat{x}_\lambda, \hat{y}_\lambda, \hat{z}_\lambda$ and rotate as the particles move in space. The λ subscript is a reminder that the body-fixed axes are based on the $\mathbf{R}_\lambda, \mathbf{r}_\lambda$ coordinates. The non-rotating center of mass axes are denoted by $\hat{X}, \hat{Y}, \hat{Z}$.

The rotational properties of the surface functions are determined by their dependence on the three Euler angles, and they will automatically be eigenfunctions of $\hat{J}^2$ and J_Z, when they are expanded[39] in the Wigner rotation matrices[40] according to

$$\Phi^{J,M,\Pi}(\varphi_\lambda, \vartheta_\lambda, \psi_\lambda, \omega_\lambda, \gamma_\lambda; \rho) = \sum_{\Omega=-J}^{J} D^J_{M,\Omega}(\varphi_\lambda, \vartheta_\lambda, \psi_\lambda) \phi^{\lambda,J,\Pi}_{\Omega,n}(\omega_\lambda, \gamma_\lambda; \rho) \qquad (12)$$

The sum over Ω in (12) is necessary because it is not a conserved quantum number: Ω is the component of the total angular momentum along the body-fixed z_λ axis.[40] The rotational properties of a surface function of the form (12) is the same as those of Wigner rotation matrices[40] which are irreducible representations of the rotation group. The surface function's dependence on the Euler angles has been factored away and multiple solution components, identified by the index Ω which takes on $2J+1$ values, have been introduced.

The coefficients in (12), $\phi^{\lambda,J,\Pi}_{\Omega,n}(\omega_\lambda,\gamma_\lambda;\rho)$, are referred to in the rest of this paper as two-angle surface functions or more precisely as surface functions in the Wigner rotation matrix representation.

In order to derive the differential equation governing the two-angle surface functions, it is necessary to express the grand canonical angular momentum operator (6) in the body-fixed coordinates. The operator $\hat{j}^2_\lambda$ in body-fixed coordinates is given in reference 6 as

$$\hat{j}^2_\lambda = -\hbar^2\left(\frac{\partial^2}{\partial\gamma_\lambda^2} + \cot\gamma_\lambda\frac{\partial}{\partial\gamma_\lambda} + \frac{1}{\sin^2\gamma_\lambda}\frac{\partial^2}{\partial\psi_\lambda^2}\right) \tag{13}$$

An expression for $\hat{l}^2_\lambda$ in a form useful for the present purposes is

$$\begin{aligned}\hat{l}^2_\lambda = \hat{J}^2 + \hat{j}^2_\lambda + 2\hbar^2\frac{\partial^2}{\partial\psi_\lambda^2} - \sqrt{2}\hbar\left[\frac{\partial}{\partial\gamma_\lambda} + \cot\gamma_\lambda\left(1 - \imath\frac{\partial}{\partial\psi_\lambda}\right)\right]\hat{J}^+_\lambda \\ - \sqrt{2}\hbar\left[\frac{\partial}{\partial\gamma_\lambda} + \cot\gamma_\lambda\left(1 + \imath\frac{\partial}{\partial\psi_\lambda}\right)\right]\hat{J}^-_\lambda\end{aligned} \tag{14}$$

where

$$\hat{J}^\pm_\lambda = \frac{\mp}{\sqrt{2}}\left(\hat{J}_{x_\lambda} \pm \imath\hat{J}_{y_\lambda}\right) \tag{15}$$

The operators $\hat{J}^2$ and $\hat{J}^\pm_\lambda$ have the properties[40]

$$\hat{J}^2 D^J_{M,\Omega}(\varphi_\lambda,\vartheta_\lambda,\psi_\lambda) = J(J+1)\hbar^2 D^J_{M,\Omega}(\varphi_\lambda,\vartheta_\lambda,\psi_\lambda) \tag{16}$$

$$\hat{J}^\pm_\lambda D^J_{M,\Omega}(\varphi_\lambda,\vartheta_\lambda,\psi_\lambda) = C^\pm_{J,\Omega} D^J_{M,\Omega\mp1}(\varphi_\lambda,\vartheta_\lambda,\psi_\lambda) \tag{17}$$

$$C^\pm_{J,\Omega} = \frac{\mp\hbar}{\sqrt{2}}\Big[(J\pm\Omega)(J\mp\Omega+1)\Big]^{\frac{1}{2}} \tag{18}$$

The explicit forms for $\hat{J}_x$, $\hat{J}_y$, and $\hat{J}_z$ are given by Landau and Lifshitz,[41,42] but they will not be needed.

4. Surface Function Hamiltonian in Rotation Matrix Representation

The partial differential equation for the surface functions in the Wigner rotation matrix representation is

$$\sum_{\Omega'=-J}^{J}\Big[\hat{h}^{\lambda,J}_{\Omega,\Omega'} - \delta_{\Omega,\Omega'}\epsilon^{J,\Pi}_n(\rho)\Big]\phi^{\lambda,J,\Pi}_{\Omega',n}(\omega_\lambda,\gamma_\lambda,\rho) = 0 \tag{19}$$

where

$$\hat{h}^{\lambda,J}_{\Omega,\Omega} = \frac{-2\hbar^2}{\rho^2\mu}\left\{\left(\frac{\partial^2}{\partial\omega_\lambda^2} + 2\cot\omega_\lambda\frac{\partial}{\partial\omega_\lambda}\right) + \frac{1}{\sin^2\omega_\lambda}\left(\frac{\partial^2}{\partial\gamma_\lambda^2} + \cot\gamma_\lambda\frac{\partial}{\partial\gamma_\lambda} - \frac{\Omega^2}{\sin^2\gamma_\lambda}\right) - \frac{J(J+1)-2\Omega^2}{4\cos^2(\frac{\omega_\lambda}{2})}\right\} + \overline{V}^{\lambda}(\rho,\omega_\lambda,\gamma_\lambda) \tag{20}$$

and

$$\hat{h}^{\lambda,J}_{\Omega,\Omega\pm1} = \frac{\hbar\sqrt{2}C^{\mp}_{J,\Omega}}{2\mu\rho^2\cos^2(\frac{\omega_\lambda}{2})}\left[\frac{\partial}{\partial\gamma_\lambda} \pm (\Omega\pm1)\cot\gamma_\lambda\right] \tag{21}$$

All terms in (19) with $|\Omega'| > |\Omega|+1$ vanish. Equations (19)-(21) are derived by using the expressions for $\hat{j}^2_\lambda$ and $\hat{l}^2_\lambda$ in body-fixed coordinates (13)-(15) in the surface function differential equation (7), the relations (16)-(18), and the orthogonality of the Wigner rotation matrices.[40]

Equation (19) represents a set of $2J+1$ coupled partial differential equations in the independent variables $\omega_\lambda, \gamma_\lambda$ and a continuous parameter ρ. In the Wigner rotation matrix representation, the grand canonical angular momentum operator (6) is non-diagonal in Ω, Ω', but the potential energy function is diagonal.

Some authors have raised concern[4,37] about the second order poles in the kinetic energy term of equation (20) at $\omega_\lambda = 0, \pi$. The important observation is that $\omega_\lambda = 0, \pi$ are second order zeros of the volume element and so have measure zero. Alternatively, a simple change of dependent variables given by

$$\overline{\phi}^{\lambda,J,\Pi}_{\Omega,n}(\omega_\lambda,\gamma_\lambda;\rho) = \phi^{\lambda,J,\Pi}_{\Omega,n}(\omega_\lambda,\gamma_\lambda;\rho)\sin\omega_\lambda \tag{22}$$

removes the singularity from the resulting differential equation for the new dependent variables.

The surface functions are eigenfunctions of the inversion operator $\hat{O}_I$. $\hat{I}$ which inverts the coordinates of all of the particles through the center of mass, acts only on the Euler angles. Since the Wigner rotation matrices are not eigenfunctions of $\hat{O}_I$, the $\phi^{\lambda,J,\Pi}_{\Omega,n}(\omega_\lambda,\gamma_\lambda;\rho)$ must satisfy the relationship

$$\phi^{\lambda,J,\Pi}_{-\Omega,n}(\omega_\lambda,\gamma_\lambda;\rho) = \Pi(-1)^{J+\Omega}\phi^{\lambda,J,\Pi}_{\Omega,n}(\omega_\lambda,\gamma_\lambda;\rho) \tag{23}$$

To derive this result, it is necessary to first establish how the $D^J_{M,\Omega}(\varphi_\lambda, \vartheta_\lambda, \psi_\lambda)$ transform under inversion of all coordinates through the center of mass. It is an easy matter to show the effect of the inversion operator $\hat{I}$ on the body-fixed coordinates is[6]

$$\hat{I} \quad (R_\lambda, \vartheta_\lambda, \varphi_\lambda, r_\lambda, \gamma_\lambda, \psi_\lambda) = (R_\lambda, \pi - \vartheta_\lambda, \pi + \varphi_\lambda, r_\lambda, \gamma_\lambda, \pi - \psi_\lambda) \tag{24}$$

Using the well known properties of the Wigner rotation matrices, it is straightforward to show that

$$D^J_{M,\Omega}(\pi + \varphi_\lambda, \pi - \vartheta_\lambda, \pi - \psi_\lambda) = (-1)^{J+\Omega} D^J_{M,-\Omega}(\varphi_\lambda, \vartheta_\lambda, \psi_\lambda) \tag{25}$$

We conclude that

$$\hat{O}_I D^J_{M,\Omega}(\varphi_\lambda, \vartheta_\lambda, \psi_\lambda) = (-1)^{J+\Omega} D^J_{M,-\Omega}(\varphi_\lambda, \vartheta_\lambda, \psi_\lambda) \tag{26}$$

From equations (10) and (26) we have

$$\sum_{\Omega=-J}^{J} (-1)^{J+\Omega} D^J_{M,-\Omega}(\varphi_\lambda, \vartheta_\lambda, \psi_\lambda) \phi^{\lambda,J,\Pi}_{\Omega,n}(\omega_\lambda, \gamma_\lambda; \rho) =$$

$$\Pi \sum_{\Omega'=-J}^{J} D^J_{M,\Omega'}(\varphi_\lambda, \vartheta_\lambda, \psi_\lambda) \phi^{\lambda,J,\Pi}_{\Omega',n}(\omega_\lambda, \gamma_\lambda; \rho) \tag{27}$$

Replacing the summation index Ω in the first sum in equation (27) by $-\Omega$ and employing the orthogonality of the Wigner rotation matrices, we obtain (23).

The inclusion of a definite parity in the surface functions has several consequences. Indeed, equation (23) shows that, for a given parity, Π, only those $\phi^{\lambda,J,\Pi}_{\Omega,n}(\omega_\lambda, \gamma_\lambda; \rho)$ with nonnegative values of Ω are linearly independent. That equation also shows that $\phi^{\lambda,J,\Pi}_{\Omega=0,n}(\omega_\lambda, \gamma_\lambda; \rho)$ is identically zero when $\Pi(-1)^J = -1$. In particular, for $J = \Omega = 0$, odd parity wave functions do not exist. In addition, inclusion of parity labels decouples the set of $2J + 1$ coupled partial differential equations (19) into a set of $J + 1$ coupled equations for $\Omega \geq 0$ and a set of J coupled equations for $\Omega > 0$. This is verified by replacing the unknowns with

$\Omega < 0$ in the system of $2J+1$ equations (19) by the related functions with $\Omega > 0$ using (23). The result is duplicate equations for all $\Omega \neq 0$. Therefore, the differential equations, after enforcing parity, are the same as before except that terms with $\Omega < 0$ are omitted. The expressions for the interaction and overlap matrices given in paper I can be simplifed by the inclusion of parity: the sums over $\Omega = -J, -J+1, \ldots, J-1, J$ can be replaced by sums over $\Omega = 0, 1, 2, \ldots, J$ by using equation (23). When this is done, it is important to include all terms with $\Omega \neq 0$ twice and the $\Omega = 0$ term once. In the following all sums over Ω will extend from $-J$ to $+J$ so that the factor of two is retained.

5. Minimum Principle for Surface Functions

In this section, a minimum principle for the surface functions in the Wigner rotation matrix representation is presented for a general system of three particles.

From the usual minimum principle for the $\Phi_n^{J,M,\Pi}$,

$$\delta \int \Phi_n^{*J,M,\Pi} \left(\hat{h} - \epsilon_n^{J\Pi} \right) \Phi_n^{J,M,\Pi} d\tau_1 = 0 \tag{28}$$

Using the orthogonality of the Wigner rotation matrices, the minimum principle for the $\phi_{\Omega,n}^{\lambda,J,\Pi}(\omega_\lambda, \gamma_\lambda; \rho)$ is found to be

$$\delta \sum_{\Omega=-J}^{J} \sum_{\Omega'=-J}^{J} \int_D \phi_{\Omega,n}^{*\lambda,J,\Pi}(\omega_\lambda, \gamma_\lambda; \rho) \left[\hat{h}_{\Omega,\Omega'}^{\lambda,J} - \epsilon_n^{J,\Pi}(\rho) \delta_{\Omega,\Omega'} \right] \phi_{\Omega',n}^{\lambda,J,\Pi}(\omega_\lambda, \gamma_\lambda; \rho) d\tau_2 = 0 \tag{29}$$

where D is the domain of integration:

$$D = \{(\omega_\lambda, \gamma_\lambda) | \, 0 \leq \omega_\lambda \leq \pi; 0 \leq \gamma_\lambda \leq \pi\} \tag{30}$$

and the surface element is

$$d\tau_2 = \sin^2 \omega_\lambda \sin \gamma_\lambda d\omega_\lambda d\gamma_\lambda \tag{31}$$

Integration by parts results in the following variational principle for the two-angle surface functions

$$\delta\Big\{\int_D \Big(K_0^{\lambda,J}\Big[\phi_{\Omega,n}^{\lambda,J,\Pi}\Big] + K_+^{\lambda,J}\Big[\phi_{\Omega,n}^{\lambda,J,\Pi}\Big] + K_-^{\lambda,J}\Big[\phi_{\Omega,n}^{\lambda,J,\Pi}\Big]\Big)\, d\tau_2 + \int_{B_1} \mathcal{F} dl\Big\} = 0 \tag{32}$$

where

$$K_0^{\lambda,J} = \sum_{\Omega=-J}^{J}\Big\{\Big|\frac{\partial}{\partial\omega_\lambda}\phi_{\Omega,n}^{\lambda,J,\Pi}(\omega_\lambda,\gamma_\lambda;\rho)\Big|^2 + \Big|\frac{1}{\sin\omega_\lambda}\frac{\partial}{\partial\gamma_\lambda}\phi_{\Omega,n}^{\lambda,J,\Pi}(\omega_\lambda,\gamma_\lambda;\rho)\Big|^2 + \Big|\phi_{\Omega,n}^{\lambda,J,\Pi}(\omega_\lambda,\gamma_\lambda;\rho)\Big|^2\Big[V_{\text{eff}}^{J,\Omega}(\omega_\lambda,\gamma_\lambda,\rho) - \Big(\frac{\mu\rho^2}{2\hbar^2}\Big)\epsilon_n^{J,\Pi}(\rho)\Big]\Big\} \tag{33}$$

with

$$V_{\text{eff}}^{J,\Omega}(\omega_\lambda,\gamma_\lambda,\rho) = \frac{\mu\rho^2}{2\hbar^2}\overline{V}^{\lambda}(\rho,\omega_\lambda,\gamma_\lambda) + \frac{\Omega^2}{\sin^2\omega_\lambda\sin^2\gamma_\lambda} + \frac{J(J+1)-2\Omega^2}{4\cos^2(\frac{\omega_\lambda}{2})} \tag{34}$$

and

$$K_\pm^{\lambda,J} = \sum_{\Omega=-J}^{J}\phi_{\Omega,n}^{*\,\lambda,J,\Pi}(\omega_\lambda,\gamma_\lambda;\rho)\Big[\Big(\frac{\mu\rho^2}{2\hbar^2}\Big)\hat{h}_{\Omega,\Omega\pm1}^{\lambda,J}\Big]\phi_{\Omega\pm1,n}^{\lambda,J,\Pi}(\omega_\lambda,\gamma_\lambda;\rho) \tag{35}$$

The integrand of the boundary integral $\int_{B_1}\mathcal{F}dl$ in (32) is defined by

$$\mathcal{F} = \sum_{\Omega=-J}^{J}\phi_{\Omega,n}^{\lambda,J,\Pi}(\omega_\lambda,\gamma_\lambda;\rho)\frac{\partial}{\partial n}\phi_{\Omega,n}^{\lambda,J,\Pi}(\omega_\lambda,\gamma_\lambda;\rho) \tag{36}$$

with $\frac{\partial}{\partial n}$ representing the outward normal derivative at the boundary of the domain ($= \pm\frac{\partial}{\partial\gamma_\lambda}$). The boundary of the domain is the curve $B_1 = \{(\omega_\lambda,\gamma_\lambda)|\gamma_\lambda = 0,\pi;\ 0 \le \omega_\lambda \le \pi\}$ which refers to collinear configurations of the three particles. The line element along B_1 is denoted dl and its explicit form is unnecessary because the integrand (36) of the boundary integral in equation (32) vanishes in all cases: either the surface function or its normal derivative vanishes on the collinear boundary B_1 as will been discussed in section 6.

The orthogonality relationship satisfied by the two-angle surface functions is obtained from equations (11) and (12)

$$\sum_{\Omega=-J}^{J} \int_D \phi^{*\lambda,J,\Pi}_{\Omega,n}(\omega_\lambda,\gamma_\lambda;\rho)\phi^{\lambda,J,\Pi'}_{\Omega,n'}(\omega_\lambda,\gamma_\lambda;\rho)d\tau_2 = \delta^{\Pi}_{\Pi'}\delta^{n}_{n'}. \tag{37}$$

The sum over the index Ω is necessary. The $\delta^{\Pi}_{\Pi'}$ follows from (23).

The geometry of the domain D and its boundary B_1 can be visualized by interpreting the coordinates $(\rho,\omega_\lambda,\gamma_\lambda)$ as the spherical polar coordinates of an abstract three dimensional space:[1] ρ is the radius: ω_λ is the polar angle; and γ_λ is the azimuthal angle. The domain D and the boundary B_1 is shown in figure 6. The boundary B_1 is the outer circle representing the intersection of the hemisphere with the $Z_\lambda - X_\lambda$ plane. Since $0 \leq \gamma_\lambda \leq \pi$, this space is only half of the usual spherical polar space. With this interpretation, it has been shown that a change of Jacobi coordinates, say $\lambda \rightarrow \nu$, is a rotation about the Y_λ axis. The domain D is the surface of a hemisphere and the boundary B_1 is the circle formed by the intersection of the hemisphere with the $X_\lambda - Z_\lambda$ plane. The quotes are used to emphasize that the axes refer to the abstract space.

6. Boundary Conditions Implied by Single-valuedness

In this section, it is shown that the integrand of the boundary integral vanishes ($\mathcal{F} = 0$) for collinear configurations because either the two-angle surface function or its γ_λ derivative vanishes for these configurations. These boundary conditions for collinear configurations hold for any system of particles, because they follow from the grand canonical angular momentum operator. The two cases, $\Omega = 0$ and $\Omega \neq 0$ are treated separately.

The boundary condition for $\phi^{\lambda,J,\Pi}_{\Omega,n}(\omega_\lambda,\gamma_\lambda;\rho)$ with $\Omega \neq 0$ on the curve B_1 is

$$\phi^{\lambda,J,\Pi}_{\Omega\neq 0,n}(\omega_\lambda,\gamma_\lambda;\rho)|_{\gamma_\lambda=0,\pi} = 0 \tag{38}$$

and is deduced from equation (12) and the requirement of single-valuedness of the surface functions. For $\Omega \neq 0$, the Wigner rotation matrix depends on the Euler

angle ψ_λ as $e^{i\Omega\psi_\lambda}$; therefore, the surface functions have the same dependence on ψ_λ. When $\gamma_\lambda = 0, \pi$ (three atoms are collinear), then all values of the angle ψ_λ refer to the same configuration of the atoms. If the surface functions are non-constant in ψ_λ, then they are multivalued for collinear configurations unless the $\phi^{\lambda,J,\Pi}_{\Omega,n}(\omega_\lambda, \gamma_\lambda; \rho)$ vanish at $\gamma_\lambda = 0, \pi$ when $\Omega \neq 0$. As a complementary observation, notice that the effective potential $V^{J,\Omega}_{\rm eff}$ (34) has a second order pole at the collinear configurations and the volume element (31) has a simple zero. If the $\phi^{\lambda,J,\Pi}_{\Omega,n}(\omega_\lambda, \gamma_\lambda; \rho)$ with $\Omega \neq 0$ did not vanish at the collinear configurations, then the integral (34) would be singular.

For the case $\Omega = 0$, the two-angle surface function is not required to vanish on B_1 to be single-valued; however, the normal derivative must vanish at $\gamma_\lambda = 0, \pi$:

$$\frac{\partial}{\partial \gamma_\lambda} \phi^{\lambda,J,\Pi}_{\Omega=0,n}(\omega_\lambda, \gamma_\lambda; \rho)|_{\gamma_\lambda = 0,\pi} = 0 \tag{39}$$

This boundary condition is derived from an analysis of the poles in the operator given by equation (20) on B_1. These poles are the same as those in the Legendre differential equation. In fact, the part of the surface function operator which has poles at B_1 is fundamentally $\hat{j}^2_\lambda$ (13) and this operator has the same singularities in γ_λ as the Legendre differential equation. As a result, the boundary conditions on the surface functions in the Wigner rotation matrix representation are the same as those for the associated Legendre functions $P^\Omega_J(\cos\gamma_\lambda)$ at $\gamma_\lambda = 0, \pi$. This conclusion is supported by the observation that the γ_λ dependence of the two-angle surface functions must become that of the associated Legendre functions as ρ becomes large and the boundary conditions at the collinear configurations do not depend on ρ.

7. Finite Element Procedure

In the finite element scheme,[43] the unknown function is approximated by an expansion in a finite basis set (Rayleigh-Ritz). This is in contrast to the more

familiar finite difference approach in which the differential operators are approximated with finite differences. In the Rayleigh-Ritz scheme, the expansion coefficients are variational parameters. The finite element approach differs from the usual Rayleigh-Ritz procedure by using basis functions (shape functions in the engineering jargon) that are nonzero only over a small subregion of the domain (the elements). These basis functions are typically low order polynomials. The only restriction on the basis functions is that continuity of the solutions between neighboring elements is insured. The finite element method approximates the differential eigenvalue problem for the surface functions by an algebraic eigenvalue problem for the variational parameters.

The question of whether it is better to use global basis functions (nonzero over most of the domain) which have detailed structure similar to that of the true solutions, or to use simple local basis functions as in the finite element method is answered by the relative costs of these alternatives. If a small number of global basis functions span the subspace containing the true solution, then they will be cost effective. On the other hand, if a large global basis set is necessary, then the finite element method may be superior because a global basis set yields a dense algebraic eigenvalue problem while the finite element basis set yields a sparse one. The sparse algebraic eigenvalue problem can be treated efficiently with a variety of methods (*e.g.*, Bathe's subspace iteration[44] or Lanczos' method[45]).

The first step in transforming the variational equation into an algebraic eigenvalue problem is to express the variational integral as a sum of integrals over small subregions of the domain. The domain D is partitioned into subregions D_e which do not overlap ($D_e \cap D_{e'} = 0$) and which cover the entire domain ($D = \cup_e D_e$). The D_e are called the elements. The variational integral (32) I becomes

$$I = \sum_e \left\{ \int_{D_e} \left(K_0^{\lambda,J}\left[\phi_{\Omega,n}^{\lambda,J,\Pi}\right] + K_+^{\lambda,J}\left[\phi_{\Omega,n}^{\lambda,J,\Pi}\right] + K_-^{\lambda,J}\left[\phi_{\Omega,n}^{\lambda,J,\Pi}\right] \right) d\tau_2 + \int_{B_e} \mathcal{F} dl \right\} \tag{40}$$

where B_e is that part of the boundary of D which is also a boundary of element e. The $\sum_e$ denotes a sum over the elements D_e. Most elements do not have an edge at the boundary of D.

Within each element e, the $\phi_{\Omega,n}^{\lambda,J,\Pi}$ are approximated by

$$\phi_{\Omega,n}^{\lambda,J,\Pi,}(\omega_\lambda,\gamma_\lambda)|_e \approx \Big\langle N(\omega_\lambda,\gamma_\lambda)\Big\rangle \Big\{ f_{\Omega,n}^{\lambda,J,\Pi}|_e \Big\} \tag{41}$$

where $\langle N(\omega_\lambda,\gamma_\lambda)\rangle$ is a row matrix and $\{f_{\Omega,n}^{\lambda,J,\Pi}|_e\}$ is a column matrix. Matrix notation is used to avoid the introduction of another index for the finite element expansion; the reader will no doubt be thankful. In order to avoid any confusion, the finite element expansion will be given once with the sum over basis functions explicitly shown.

$$\Big\langle N(\omega_\lambda,\gamma_\lambda)\Big\rangle \Big\{ f_{\Omega,n}^{\lambda,J,\Pi}|_e \Big\} = \sum_\ell N_\ell(\omega_\lambda,\gamma_\lambda) f_{\Omega,n,\ell}^{\lambda,J,\Pi}|_e \tag{42}$$

where ℓ enumerates the terms in the expansion (42). (In our applications, $\ell = 1,2,3,4$ because we use bilinear shape functions in each element.) The notation $f|_e$ implies that these quantities are restricted to element e.

The two-angle surface functions are chosen to be real-valued functions and the expansion (41) employs real-valued functions and real coefficients. (Time reversal invariance of the Schrödinger equation insures that the solutions can be chosen to be real-valued as long as no other properties of the solutions are inconsistent with their real-valuedness.) The $\{f_{\Omega,n}^{\lambda,J,\Pi}|_e\}$ are real constants with respect to the variables $(\omega_\lambda,\gamma_\lambda)$ and are the variational parameters which, once determined, specify the solution in element e through expansion (41). The $\langle N(\omega_\lambda,\gamma_\lambda)\rangle$ are called shape or basis functions and are predetermined real-valued functions (*e.g.*, polynomials). They are the same for all elements and do not carry an element label e.

The variational integral (40) is now approximated as a sum of integrals of known functions with unknown coefficients. The kernels (33) and (35) of equation (40) restricted to element e become:

$$K_0^{\lambda,J}|_e = \sum_{\Omega=-J}^{J} \left\{ \left[\left\langle \frac{\partial}{\partial \omega_\lambda} N(\omega_\lambda, \gamma_\lambda) \right\rangle \left\{ f_{\Omega,n}^{\lambda,J,\Pi}|_e \right\} \right]^2 + \left[\frac{1}{\sin \omega_\lambda} \left\langle \frac{\partial}{\partial \gamma_\lambda} N(\omega_\lambda, \gamma_\lambda) \right\rangle \left\{ f_{\Omega,n}^{\lambda,J,\Pi}|_e \right\} \right]^2 + \left[\left\langle N(\omega_\lambda, \gamma_\lambda) \right\rangle \left\{ f_{\Omega,n}^{\lambda,J,\Pi}|_e \right\} \right]^2 \left[V_{\text{eff}}^{J,\Omega}(\omega_\lambda, \gamma_\lambda, \rho) - \left(\frac{\mu \rho^2}{2\hbar^2} \right) \epsilon_n^{J,\Pi}(\rho) \right] \right\} \tag{43}$$

and

$$K_\pm^{\lambda,J}|_e = \sum_{\Omega=-J}^{J} \left\langle N(\omega_\lambda, \gamma_\lambda) \right\rangle \left\{ f_{\Omega,n}^{\lambda,J,\Pi}|_e \right\} \left[\left(\frac{\mu \rho^2}{2\hbar^2} \right) \hat{h}_{\Omega,\Omega\pm1}^{\lambda,J} \right] \left\langle N(\omega_\lambda, \gamma_\lambda) \right\rangle \left\{ f_{\Omega\pm1,n}^{\lambda,J,\Pi}|_e \right\} \tag{44}$$

where we used equation (41).

With these shape functions (41), the integrations can be done quite accurately by numerical quadrature over the domain of each element D_e. Since the shape functions are typically low order polynomials, the necessary number of quadrature points per element is small. (In our applications, we use four Gauss-Legendre quadrature points per element.) Most of the time needed for the quadrature is consumed by the calculation of the potential energy functions $\overline{V}^{\lambda}(\rho, \omega_\lambda, \gamma_\lambda)$ at the quadrature points.

The variation $\delta I = 0$ becomes

$$\frac{\partial I}{\partial f_{\Omega,n,\ell}^{\lambda,J,\Pi}|_e} = 0 \tag{45}$$

When the unknowns from each element are assembled into a single column vector, omitting all redundant occurrences of an unknown, then the result of the this overall procedure is a generalized algebraic eigenvalue problem

$$\mathbf{H}^{J,\Pi} \mathbf{f}_n^{J,\Pi} = \epsilon_n^{J,\Pi} \mathbf{M}^{J,\Pi} \mathbf{f}_n^{J,\Pi} \tag{46}$$

for the variational parameters $f^{\lambda,J,\Pi}_{\Omega,n,\ell}|_e$ and the approximate surface function eigenvalues, $\epsilon^{J,\Pi}_n(\rho)$. The $\mathbf{H}^{J,\Pi}$ and $\mathbf{M}^{J,\Pi}$ are banded, symmetric, positive definite matrices of large dimension. The elements of the solution vector are labelled with Ω as well as an index which denumerates the variational parameters from each element. This latter index is *not* ℓ because ℓ specifies a variational parameter only when the corresponding element is also given. The matrix $\mathbf{M}^{J,\Pi}$ appears in (46) because of the nonorthogonality of the shape functions and is a collection of overlap integrals between these functions. The systematic construction of the $\mathbf{H}^{J,\Pi}$ and $\mathbf{M}^{J,\Pi}$ matrices from equations (40), (43), and (44) is discussed in any finite element textbook, for example, see Dhatt and Touzot.[43]

The solution of equation (46) is demanding on computer resources. Bathe's subspace iteration[44] has been used in the present calculations and is summarized as follows. Begin with a set of initial vectors which are guessed or are the result of a previous iteration. This set of vectors defines a subspace. The $\mathbf{H}^{J,\Pi}$ and $\mathbf{M}^{J,\Pi}$ matrices are projected onto this subspace. Minimization of $\mathbf{H}^{J,\Pi}$ in the subspace leads to a dense algebraic eigenvalue problem for the best eigenvectors/values within the subspace. Inverse iteration updates the iteration vectors and the corresponding subspace. The procedure is repeated until the desired degree of convergence is obtained.

All that remains is to specify the decomposition of the domain into elements and the choice of shape functions. In the present application, the domain is decomposed into quadrilateral elements. The precise decomposition characteristices are given at the end of section 8. Within each quadrilateral element, bilinear (Lagrange) shape functions are used and are given below.

$$N^e_1 = \frac{1}{4}(1+\xi)(1+\eta)$$

$$N^e_2 = \frac{1}{4}(1-\xi)(1+\eta)$$

$$N^e_3 = \frac{1}{4}(1-\xi)(1-\eta)$$

$$N^e_4 = \frac{1}{4}(1+\xi)(1-\eta)$$

or in matrix notation

$$\langle N^e \rangle = \frac{1}{4} \begin{pmatrix} (1+\xi)(1+\eta) \\ (1-\xi)(1+\eta) \\ (1-\xi)(1-\eta) \\ (1+\xi)(1-\eta) \end{pmatrix} \tag{47}$$

where the shape functions are defined for a reference (or parent) element. The parent element is defined as a square with sides of length 2 and center at $(0,0)$ in the (ξ,η) coordinate system. The four nodes of the parent element are at $(1,1)$, $(-1,1)$, $(-1,-1)$, and $(1,-1)$ and are numbered 1,2,3,and 4, respectively. The i_{th} shape function in (47) has the property that it is unity at node i and vanishes at the other three nodes. This property of the Lagrange shape functions permits the interpretation of the variational parameters as the unknown function at the nodes of the mesh.

A parent element point (ξ,η) is mapped onto a point $(\omega_\lambda,\gamma_\lambda)$ of an actual element by a simple mapping from (ξ,η) to $(\omega_\lambda,\gamma_\lambda)$ which is based on the Lagrange shape functions:

$$\omega_\lambda|_e = \sum_\ell N_\ell(\xi,\eta)\omega_\lambda^\ell|_e \tag{48}$$

$$\gamma_\lambda|_e = \sum_\ell N_\ell(\xi,\eta)\gamma_\lambda^\ell|_e \tag{49}$$

where $(\omega_\lambda^\ell|_e, \gamma_\lambda^\ell|_e)$ are the λ- symmetrized hyperspherical coordinates of node ℓ of element e. Notice that the corners of the parent are mapped onto the corners of each actual element. Likewise edges of the parent element are mapped onto corresponding edges of the actual element. Mapping a parent element onto the actual elements is standard in finite element analysis and is discussed here so that the actual shape functions can be given. In addition, the quadrature points are given in the coordinate system of the parent element. The use of a parent element shows that the shape functions are not precisely linear functions of the coordinates of the actual element due to the nonlinearity of the mapping.

In applications, integrals of the surface functions are required. To evaluate integrals with the finite element approximations to the continuous solutions, some

numerical quadrature scheme is required. In the present applications, all quadratures involving surface functions are calculated with the same method as that used to evaluate the integrals in equation (40) (*i.e.*, Gauss-Legendre quadrature within each element). This technique has the advantage of being consistent with the finite element approximations to the surface functions.

8. Configuration Space Mappings Induced by the Operators of P_3

When all three particles are identical, the grand canonical angular momentum operator and the potential energy function commute with all of the operators which permute the particles. The group of all permutations of three identical objects (*i.e.*, the symmetric group) is denoted by P_3.[46] It will be shown that the P_3 symmetry allows the domain D over which numerical surface functions are constructed to be reduced in area by a factor of 6. The effect of the permutation operators on the functions themselves will be deferred to section 9.

In this section, we will examine the effect of the permutation operators on the six-dimensional space spanned by $(\mathbf{R}_\lambda, \mathbf{r}_\lambda)$ and on the three-dimensional symmetrized hyperspherical coordinate space of the three spherical polar variables $\rho, \omega_\lambda, \gamma_\lambda$. We will not use the $\lambda\nu\kappa$ labelling scheme in this section in order to avoid confusion.

An example of a permutation operator is $\begin{pmatrix} \alpha & \beta & \gamma \\ \beta & \gamma & \alpha \end{pmatrix}$. The first row gives the original ordering and the second gives the resultant ordering. One interpretation is that the particles are labelled with α, β, or γ. The permutation operator prescribes that particle α replaces particle γ, that particle β replaces particle α, and that particle γ replaces particle β.

A matrix representation of the irreducible representations of P_3 is provided below. The surface functions plotted in section 10 transform according to this matrix representation. The matrix representation chosen for the E irreducible representation is

$$\begin{pmatrix} \alpha & \beta & \gamma \\ \alpha & \beta & \gamma \end{pmatrix} \leftrightarrow \quad \begin{pmatrix} 1 & 0 \\ 0 & 1 \end{pmatrix} \tag{50}$$

$$\begin{pmatrix} \alpha & \beta & \gamma \\ \alpha & \gamma & \beta \end{pmatrix} \leftrightarrow \begin{pmatrix} 1 & 0 \\ 0 & -1 \end{pmatrix} \tag{51}$$

$$\begin{pmatrix} \alpha & \beta & \gamma \\ \gamma & \beta & \alpha \end{pmatrix} \leftrightarrow \frac{1}{2}\begin{pmatrix} -1 & -\sqrt{3} \\ -\sqrt{3} & +1 \end{pmatrix} \tag{52}$$

$$\begin{pmatrix} \alpha & \beta & \gamma \\ \beta & \alpha & \gamma \end{pmatrix} \leftrightarrow \frac{1}{2}\begin{pmatrix} -1 & +\sqrt{3} \\ +\sqrt{3} & +1 \end{pmatrix} \tag{53}$$

$$\begin{pmatrix} \alpha & \beta & \gamma \\ \gamma & \alpha & \beta \end{pmatrix} \leftrightarrow \frac{1}{2}\begin{pmatrix} -1 & +\sqrt{3} \\ -\sqrt{3} & -1 \end{pmatrix} \tag{54}$$

$$\begin{pmatrix} \alpha & \beta & \gamma \\ \beta & \gamma & \alpha \end{pmatrix} \leftrightarrow \frac{1}{2}\begin{pmatrix} -1 & -\sqrt{3} \\ +\sqrt{3} & -1 \end{pmatrix} \tag{55}$$

The irreducible representation matrices for A_1 and A_2 are one dimensional: in A_1 every operator is represented by unity; and in A_2, the two-particle permutation operators are represented by -1 while the remaining operators are represented by 1.

The permutation operators map the six-dimensional configuration space onto itself. A point in this configuration space can be specified in any of the three Jacobi coordinate systems: $(\mathbf{R}_\alpha, \mathbf{r}_\alpha)$, $(\mathbf{R}_\beta, \mathbf{r}_\beta)$, or $(\mathbf{R}_\gamma, \mathbf{r}_\gamma)$. Let $(\mathbf{R}_\lambda, \mathbf{r}_\lambda)$ be the coordinates of a point Q, and let $\overline{Q}$, with coordinates $(\overline{\mathbf{R}}_\lambda, \overline{\mathbf{r}}_\lambda)$, be the image point of Q under the transformation induced by a permutation operator. It is straightforward to show that

$$(\overline{\mathbf{R}}_\alpha, \overline{\mathbf{r}}_\alpha) = \begin{pmatrix} \alpha & \beta & \gamma \\ \alpha & \gamma & \beta \end{pmatrix} Q = (\mathbf{R}_\alpha, -\mathbf{r}_\alpha) \tag{56}$$

$$(\overline{\mathbf{R}}_\gamma, \overline{\mathbf{r}}_\gamma) = \begin{pmatrix} \alpha & \beta & \gamma \\ \gamma & \beta & \alpha \end{pmatrix} Q = (\mathbf{R}_\alpha, -\mathbf{r}_\alpha) \tag{57}$$

$$(\overline{\mathbf{R}}_\beta, \overline{\mathbf{r}}_\beta) = \begin{pmatrix} \alpha & \beta & \gamma \\ \beta & \alpha & \gamma \end{pmatrix} Q = (\mathbf{R}_\alpha, -\mathbf{r}_\alpha) \tag{58}$$

$$(\overline{\mathbf{R}}_\gamma, \overline{\mathbf{r}}_\gamma) = \begin{pmatrix} \alpha & \beta & \gamma \\ \gamma & \alpha & \beta \end{pmatrix} Q = (\mathbf{R}_\alpha, \mathbf{r}_\alpha) \tag{59}$$

$$(\overline{\mathbf{R}}_\beta, \overline{\mathbf{r}}_\beta) = \begin{pmatrix} \alpha & \beta & \gamma \\ \beta & \gamma & \alpha \end{pmatrix} Q = (\mathbf{R}_\alpha, \mathbf{r}_\alpha) \tag{60}$$

The configuration space mappings induced by the permutation operators have been expressed in terms of the initial configuration space point specified by its α

Jacobi coordinates. We can also give the image point in terms of the initial point's β Jacobi coordinates

$$(\overline{\mathbf{R}}_\gamma, \overline{\mathbf{r}}_\gamma) = \begin{pmatrix} \alpha & \beta & \gamma \\ \alpha & \gamma & \beta \end{pmatrix} Q = (\mathbf{R}_\beta, -\mathbf{r}_\beta) \tag{61}$$

$$(\overline{\mathbf{R}}_\beta, \overline{\mathbf{r}}_\beta) = \begin{pmatrix} \alpha & \beta & \gamma \\ \gamma & \beta & \alpha \end{pmatrix} Q = (\mathbf{R}_\beta, -\mathbf{r}_\beta) \tag{62}$$

$$(\overline{\mathbf{R}}_\alpha, \overline{\mathbf{r}}_\alpha) = \begin{pmatrix} \alpha & \beta & \gamma \\ \beta & \alpha & \gamma \end{pmatrix} Q = (\mathbf{R}_\beta, -\mathbf{r}_\beta) \tag{63}$$

$$(\overline{\mathbf{R}}_\alpha, \overline{\mathbf{r}}_\alpha) = \begin{pmatrix} \alpha & \beta & \gamma \\ \gamma & \alpha & \beta \end{pmatrix} Q = (\mathbf{R}_\beta, \mathbf{r}_\beta) \tag{64}$$

$$(\overline{\mathbf{R}}_\gamma, \overline{\mathbf{r}}_\gamma) = \begin{pmatrix} \alpha & \beta & \gamma \\ \beta & \gamma & \alpha \end{pmatrix} Q = (\mathbf{R}_\beta, \mathbf{r}_\beta) \tag{65}$$

or in terms of the initial point Q in γ coordinates

$$(\overline{\mathbf{R}}_\beta, \overline{\mathbf{r}}_\beta) = \begin{pmatrix} \alpha & \beta & \gamma \\ \alpha & \gamma & \beta \end{pmatrix} Q = (\mathbf{R}_\gamma, -\mathbf{r}_\gamma) \tag{66}$$

$$(\overline{\mathbf{R}}_\alpha, \overline{\mathbf{r}}_\alpha) = \begin{pmatrix} \alpha & \beta & \gamma \\ \gamma & \beta & \alpha \end{pmatrix} Q = (\mathbf{R}_\gamma, -\mathbf{r}_\gamma) \tag{67}$$

$$(\overline{\mathbf{R}}_\gamma, \overline{\mathbf{r}}_\gamma) = \begin{pmatrix} \alpha & \beta & \gamma \\ \beta & \alpha & \gamma \end{pmatrix} Q = (\mathbf{R}_\gamma, -\mathbf{r}_\gamma) \tag{68}$$

$$(\overline{\mathbf{R}}_\beta, \overline{\mathbf{r}}_\beta) = \begin{pmatrix} \alpha & \beta & \gamma \\ \gamma & \alpha & \beta \end{pmatrix} Q = (\mathbf{R}_\gamma, \mathbf{r}_\gamma) \tag{69}$$

$$(\overline{\mathbf{R}}_\alpha, \overline{\mathbf{r}}_\alpha) = \begin{pmatrix} \alpha & \beta & \gamma \\ \beta & \gamma & \alpha \end{pmatrix} Q = (\mathbf{R}_\gamma, \mathbf{r}_\gamma) \tag{70}$$

(Notice that the configuration space mapping induced by the two particle exchange operators is most simply expressed in the Jacobi coordinates which are based on the particle which is not affected by the operator. In such coordinates, the mapping is simply a sign change in the vector $\mathbf{r}_\lambda$.) Given a point, Q, in 6-dimensional configuration space with the numerical values of its coordinates in any of the three coordinate systems, its image point, $\overline{Q}$, under the action of any of the permutation operators is located by a reinterpretation of the numerical coordinates.

What about the mapping of the internal coordinates by the permutation operators? To address this, a few facts are necessary. Recall that $\lambda \rightarrow \nu$ coordinate

transformations induce an orthogonal transformation in the space spanned by $(\mathbf{R}_\lambda, \mathbf{r}_\lambda)$ because of the use of mass-scaled coordinates.[21] Secondly, a $\lambda \rightarrow \nu$ coordinate transformation does not mix the two subspaces spanned by $(\varphi_\lambda, \vartheta_\lambda, \psi_\lambda)$ and by $(\rho, \omega_\lambda, \gamma_\lambda)$. In other words, the space spanned by $(\rho, \omega_\lambda, \gamma_\lambda)$ is the same space as that spanned by $(\rho, \omega_\nu, \gamma_\nu)$ and by $(\rho, \omega_\kappa, \gamma_\kappa)$ Therefore, the internal subspace can be considered separately from the Euler angles. It is a remarkable fact[1] that the $\lambda \rightarrow \nu$ coordinate transformation induces an *orthogonal* transformation of the $(\rho, \omega_\lambda, \gamma_\lambda)$ subspace. The $(R_\lambda, r_\lambda, \gamma_\lambda)$ coordinates do not possess this property nor do the Delves' hyperspherical coordinates.

The action of the permutation operators is equivalent to a reinterpretation of the coordinate labels (*cf.*, equations (56) through (70)), so they do not mix the two subspaces spanned by $(\varphi_\lambda, \vartheta_\lambda, \psi_\lambda)$ and by $(\rho, \omega_\lambda, \gamma_\lambda)$. The orthogonal nature of the internal subspace spanned by $(\rho, \omega_\lambda, \gamma_\lambda)$ and the isomorphism between P_3 and C_{3v} lead to the potential energy contours for identical particles that belong to the C_{3v} point group: two particle exchange operators induce reflections in the half-planes $\gamma_\alpha = \frac{\pi}{2}$, $\gamma_\beta = \frac{\pi}{2}$, and $\gamma_\gamma = \frac{\pi}{2}$; and cyclic permutation operators induce rotations about the Y_λ axis in the internal space by $\frac{2\pi}{3}$. The three reflection half-planes are indicated in figure 6.

It is now possible to show how the domain D of the surface integrals can be reduced by a factor of $\frac{1}{6}$ when all three particles are identical. This reduction introduces two additional boundary (line) integrals at the boundaries between the subdomain and its complement. These new boundary integrals provide the means of controlling the symmetry properties of the solutions and are discussed in section 9.

The subdomain d of D in the internal space spanned by the spherical polar variables $\rho, \omega_\lambda, \gamma_\lambda$ is found by considering the minimal domain which can be mapped into all the remaining parts of D by the permutation operations of P_3 (or the symmetry operations of C_{3v}). A solution known in this minimal domain and which transforms as an irreducible representation of P_3 can be mapped into all

remaining regions of D. By use of the reflection planes or equivalently the two-particle permutation operators, the minimal subdomain can be easily identified.

Two permutation operators are sufficient to identify the minimal subdomain. The permutation operator $\begin{pmatrix} \alpha & \beta & \gamma \\ \alpha & \gamma & \beta \end{pmatrix}$ induces a reflection in the $\gamma_\alpha = \frac{\pi}{2}$ half-plane. The points in the range $0 \leq \gamma_\alpha \leq \frac{\pi}{2}$ are reflected by this permutation operator into the the rest of D. The operator $\begin{pmatrix} \alpha & \beta & \gamma \\ \beta & \alpha & \gamma \end{pmatrix}$ induces a reflection in the $\gamma_\gamma = \frac{\pi}{2}$ half-plane. Again, the region $0 \leq \gamma_\gamma \leq \frac{\pi}{2}$ is mapped into the remainder of the domain D by this permutation operator. We see that it is sufficient to find the irreducible representation solutions in the subdomain

$$d = \{0 \leq \gamma_\alpha \leq \frac{\pi}{2}\} \cap \{0 \leq \gamma_\gamma \leq \frac{\pi}{2}\} \tag{71}$$

bounded by two half-planes: $\gamma_\alpha = \frac{\pi}{2}$ and $\gamma_\gamma = \frac{\pi}{2}$. They are half-planes in the 3D spherical polar space but if ρ is fixed, then they become curves where the half-planes intersect the spherical surface. Examining the effects of the third two-cycle permutation operator shows that no further reduction in the subdomain is possible. Likewise, the three-cycle permutation operators (rotations) add nothing new to the discussion.

It has been stated that two reflection half-planes are sufficient to fix the subdomain. It is interesting to note that the existence of two reflection planes implies the rest of the symmetry elements of the group C_{3v}. This is easily seen by drawing two of the reflection half-planes and considering products of reflections in these two half-planes. All other operations from C_{3v} are found to be products of two or three reflections in the two original half-planes.

Figure 6 shows the reduced domain in the abstract 3D symmetrized hyperspherical coordinate space. The fundamental observation is that solutions which are known in the domain, d and which transform according to the irreducible representations of P_3 can be mapped into all the remaining regions by applying the permutation operators to the function. The use of a subregion, $d \subset D$, introduces

two new boundaries, B_2 and B_3, in addition to the collinear boundary B_1. These boundaries are:

$$B_1 = \left\{(\omega_\alpha, \gamma_\alpha) | \gamma_\alpha = 0, 0 \leq \omega_\alpha \leq \frac{\pi}{3}\right\} \tag{72}$$

$$B_2 = \left\{(\omega_\alpha, \gamma_\alpha) | \gamma_\alpha = \frac{\pi}{2}, 0 \leq \omega_\alpha \leq \frac{\pi}{2}\right\} \tag{73}$$

$$B_3 = \left\{(\omega_\alpha, \gamma_\alpha) | \gamma_\gamma = \frac{\pi}{2}, \frac{\pi}{2} \leq \omega_\gamma \leq \pi\right\} \tag{74}$$

The actual domain for the finite element construction is d and it is now possible to describe the domain decomposition into elements. In the present calculations, the domain, d, is first divided into constant γ_α cuts. The ω_α range of a constant γ_α cut varies with the value of γ_α. If $\gamma_\alpha = 0$, then the range is $0 \leq \omega_\alpha \leq \frac{\pi}{3}$, and if $\gamma_\alpha = \frac{\pi}{2}$ then the range is $0 \leq \omega_\alpha \leq \frac{\pi}{2}$. Each constant γ_α cut is further divided into an equal number of intervals. Connecting the i th point along each constant γ_α cut yields a partition of the domain into quadrilateral elements. As a result, these connecting lines are *not* lines of constant ω_λ.

9. Boundary Conditions Implied by the P_3 Symmetry Group

When the particles are identical, it is possible to include additional labels on the surface functions reflecting their transformation properties under the action of the permutation operators. The advantage in doing so is a reduction in the numerical effort. It has been shown in the last section that the domain in which the surface functions are constructed can be reduced by a factor of 6 because of permutation symmetry. This domain reduction from D to d is possible only if the surface functions transform as irreducible representation of the group of permutations P_3.

Two new labels are added to the surface functions, Γ and i. Γ denotes the irreducible representation of P_3 to which the surface function belongs. The index i denotes the row within a degenerate representation. For a nondegenerate irreducible representation, the index i is superfluous. The permutation group P_3 is

isomorphic with the point group C_{3v} and, in fact, the potential energy contours has this point group symmetry when the particles are identical. The labels for the irreducible representations of C_{3v} are convenient for distinguishing the irreducible representation of P_3. Therefore, Γ can take on the values A_1, A_2, or E. The first two are nondegenerate and the last is doubly degenerate.

The surface functions for a system of three identical particles are written as

$$\Phi_n^{J,M,\Pi,\Gamma,i}(\omega_\alpha,\gamma_\alpha,\varphi_\alpha,\vartheta_\alpha,\psi_\alpha;\rho)$$

and in the Wigner rotation matrix representation the corresponding two-angle surface functions as

$$\phi_{\Omega,n}^{\alpha,J,\Pi,\Gamma,i}(\omega_\alpha,\gamma_\alpha;\rho).$$

The irreducible representation labels for the group P_3 have been affixed as superscripts to the surface functions.

Given the reduced domain for the variational integrals (32) and the accompanying new boundaries (73) and (74), it is necessary to specify the boundary conditions which the $\phi_{\Omega,n}^{\alpha,J,\Pi,\Gamma,i}(\omega_\alpha,\gamma_\alpha;\rho)$ satisfy. These constraints follow from stipulation that the $\Phi_n^{J,M,\Pi,\Gamma,i}(\omega_\alpha,\gamma_\alpha,\psi_\alpha,\vartheta_\alpha,\varphi_\alpha;\rho)$ transform as irreducible representations of P_3 and the properties of the Wigner rotation matrices. Of the six permutation operators, we shall only require two of the two-particle exchange operators: one corresponding to each of the two reflection half-planes $\gamma_\alpha = \frac{\pi}{2}$ and $\gamma_\gamma = \frac{\pi}{2}$. The simplest boundary condition to deduce is that at B_2.

The use of transformation properties to fix boundary conditions is well known. If a function is even at a surface, then the normal derivative of the functions at the surface vanishes. If a function is odd at a surface, then the function must vanish there. The implications of more general transformation properties of functions is not available in the literature to the knowledge of the authors. If a function is a member of a set of functions which transform as an irreducible representation of the symmetry group, then the operators of the group induce a transformation of the function which mixes it with the other members of the set. It is possible

to extract from the transformation properties, a set of constraints on the set of functions. The constraints are sufficient to fix the irreducible representations to which the functions belong. A numerical procedure with these constraints builtin leads directly to solutions which have the desired transformation properties. In this paper, the emphasis is on three-particle systems in a total angular momentum representation; however, the ideas have broad generality and are applicable to any system of identical particles.

A two-cycle permutation operator induces a well-defined transformation of the surface functions, and from this, the behavior of the two-angle surface functions at the corresponding reflection plane is found. In general, a change of coordinates $\mathbf{x}' = R\mathbf{x}$ induces a transformation $\hat{O}_R$ of a general scalar function $f(\mathbf{x})$ that is given by the law[40]

$$\hat{O}_R f(\mathbf{x}') = f(\mathbf{x}) \quad \text{where } \mathbf{x}' = R\mathbf{x} \tag{75}$$

so for the present case we have

$$\hat{O}\left[\begin{pmatrix} \alpha & \beta & \gamma \\ \alpha & \gamma & \beta \end{pmatrix}\right] \Phi_n^{J,M,\Pi,\Gamma,i}(\omega_\alpha, \pi - \gamma_\alpha, \vartheta_\alpha, \varphi_\alpha, \pi + \psi_\alpha; \rho) = \Phi_n^{J,M,\Pi,\Gamma,i}(\omega_\alpha, \gamma_\alpha, \vartheta_\alpha, \varphi_\alpha, \psi_\alpha; \rho) \tag{76}$$

where $\hat{O}\left[\begin{pmatrix} \alpha & \beta & \gamma \\ \alpha & \gamma & \beta \end{pmatrix}\right]$ denotes the function transformation operator associated with $\begin{pmatrix} \alpha & \beta & \gamma \\ \alpha & \gamma & \beta \end{pmatrix}$. In words, the transformed function at the image point is equal to the original function at the original point. The permutation operators do not affect the space-fixed coordinate axes, so the surface functions do indeed transform as scalar functions under P_3.

The surface functions are defined to transform as irreducible representations of P_3 which is expressed as

$$\hat{O}\left[\begin{pmatrix} \alpha & \beta & \gamma \\ \alpha & \gamma & \beta \end{pmatrix}\right] \Phi_n^{J,M,\Pi,\Gamma,i}(\omega_\alpha, \pi - \gamma_\alpha, \vartheta_\alpha, \varphi_\alpha, \pi + \psi_\alpha; \rho) = \sum_j \Phi_n^{J,M,\Pi,\Gamma,j}(\omega_\alpha, \pi - \gamma_\alpha, \vartheta_\alpha, \varphi_\alpha, \pi + \psi_\alpha; \rho) M_{j,i}^{\Gamma}\left[\begin{pmatrix} \alpha & \beta & \gamma \\ \alpha & \gamma & \beta \end{pmatrix}\right] \tag{77}$$

where $M^{\Gamma}_{j,i}\left[\begin{pmatrix}\alpha & \beta & \gamma\\ \alpha & \gamma & \beta\end{pmatrix}\right]$ is element j,i of the Γ irreducible representation matrix for the operator $\begin{pmatrix}\alpha & \beta & \gamma\\ \alpha & \gamma & \beta\end{pmatrix}$. Notice that both sides of the last equation are evaluated at the same configuration space point. Equating the right hand sides of equations (76) and (77), we have

$$\Phi_n^{J,M,\Pi,\Gamma,i}(\omega_\alpha,\gamma_\alpha,\vartheta_\alpha,\varphi_\alpha,\psi_\alpha;\rho) = \sum_j \Phi_n^{J,M,\Pi,\Gamma,j}(\omega_\alpha,\pi-\gamma_\alpha,\vartheta_\alpha,\varphi_\alpha,\pi+\psi_\alpha;\rho) M^{\Gamma}_{j,i}\left[\begin{pmatrix}\alpha & \beta & \gamma\\ \alpha & \gamma & \beta\end{pmatrix}\right] \tag{78}$$

Now, moving to the Wigner rotation matrix expansion of the surface functions, we have

$$\sum_{\Omega=-J}^{J} D^J_{M,\Omega}(\varphi_\alpha,\vartheta_\alpha,\psi_\alpha)\phi^{\alpha,J,\Pi,\Gamma,i}_{\Omega,n}(\omega_\alpha,\gamma_\alpha;\rho) = \sum_j \sum_{\Omega'=-J}^{J} D^J_{M,\Omega'}(\varphi_\alpha,\vartheta_\alpha,\pi+\psi_\alpha)\phi^{\alpha,J,\Pi,\Gamma,j}_{\Omega',n}(\omega_\alpha,\pi-\gamma_\alpha;\rho) M^{\Gamma}_{j,i}\left[\begin{pmatrix}\alpha & \beta & \gamma\\ \alpha & \gamma & \beta\end{pmatrix}\right] \tag{79}$$

The Wigner rotation matrix[40] satisfies

$$D^J_{M,\Omega}(\varphi_\alpha,\vartheta_\alpha,\pi+\psi_\alpha) = e^{i\Omega\pi} D^J_{M,\Omega}(\varphi_\alpha,\vartheta_\alpha,\psi_\alpha) \tag{80}$$

The orthogonality of the $D^J_{M,\Omega}$ functions, equations (83) and (82) allow the conclusion that

$$\phi^{\alpha,J,\Pi,\Gamma,i}_{\Omega,n}(\omega_\alpha,\gamma_\alpha;\rho) = (-1)^{\Omega}\sum_j \phi^{\alpha,J,\Pi,\Gamma,j}_{\Omega,n}(\omega_\alpha,\pi-\gamma_\alpha;\rho) M^{\Gamma}_{j,i}\left[\begin{pmatrix}\alpha & \beta & \gamma\\ \alpha & \gamma & \beta\end{pmatrix}\right] \tag{81}$$

is the relationship between the two-angle surface functions at image points under reflection in the $\gamma_\alpha = \frac{\pi}{2}$ half-plane. A glance at the particular representation matrix (51) shows that it is diagonal for this permutation operator for all Γ. We conclude that the boundary conditions at B_2 are

$$\phi^{\alpha,J,\Pi,\Gamma,i}_{\Omega,n}(\omega_\alpha,\gamma_\alpha=\frac{\pi}{2};\rho) = 0 \tag{82}$$

if Ω is odd and $\Gamma \in \{A_1, E(i=1)\}$ or if Ω is even and $\Gamma \in \{A_2, E(i=2)\}$. Otherwise,

$$\frac{\partial}{\partial \gamma_\alpha} \phi_{\Omega,n}^{\alpha,J,\Pi,\Gamma,i}(\omega_\alpha, \gamma_\alpha = \frac{\pi}{2}; \rho) = 0 \tag{83}$$

if Ω is even and $\Gamma \in \{A_1, E(i=1)\}$ or if Ω is odd and $\Gamma \in \{A_2, E(i=2)\}$. Notice that there is no coupling of two-angle surface functions with different values of the indices Ω or i in the boundary conditions on B_2.

The boundary conditions on B_3 are most simply expressed in the γ coordinates and the corresponding surface functions. Substituting the γ coordinates for the α coordinates and $\begin{pmatrix} \alpha & \beta & \gamma \\ \beta & \alpha & \gamma \end{pmatrix}$ for $\begin{pmatrix} \alpha & \beta & \gamma \\ \alpha & \gamma & \beta \end{pmatrix}$ in the preceding discussion, it is easily verified that

$$\phi_{\Omega,n}^{\gamma,J,\Pi,\Gamma,i}(\omega_\gamma, \gamma_\gamma; \rho) = (-1)^\Omega \sum_j \phi_{\Omega,n}^{\gamma,J,\Pi,\Gamma,j}(\omega_\gamma, \pi - \gamma_\gamma; \rho) M_{j,i}^\Gamma \left[\begin{pmatrix} \alpha & \beta & \gamma \\ \beta & \alpha & \gamma \end{pmatrix} \right] \tag{84}$$

provides the boundary condition for $\phi_{\Omega,n}^{\gamma,J,\Pi,\Gamma,i}(\omega_\gamma, \gamma_\gamma; \rho)$ on the $\gamma_\gamma = \frac{\pi}{2}$ half-plane. We now need to relate this boundary condition for two-angle surface functions expressed in γ coordinates to one for the two-angle surface functions defined in α coordinates.

The relationship between the two-angle surface functions defined with different sets of arrangement channel coordinates follows from the properties of the Wigner rotation matrices.[40] We begin by relating the Wigner rotation matrices appropriate for different sets of body-fixed axes $(\hat{x}_\alpha, \hat{y}_\alpha, \hat{z}_\alpha)$, $(\hat{x}_\beta, \hat{y}_\beta, \hat{z}_\beta)$, and $(\hat{x}_\gamma, \hat{y}_\gamma, \hat{z}_\gamma)$. Recall that $\hat{z}_\lambda$ points in the direction of $\mathbf{R}_\lambda$. All three systems of body-fixed axes have a common $\hat{y}_\alpha = \hat{y}_\beta = \hat{y}_\gamma$ axis which is in the direction of $\mathbf{R}_\lambda \times \mathbf{r}_\lambda$ (*i.e.*, perpendicular to the plane of the three particles). Therefore, the three systems of body-fixed axes are related by a rotation about this common body-fixed $\hat{y}$ axis. The rotation angles are[6]

$$\cos \Delta_{\lambda \to \nu}(\omega_\kappa, \gamma_\kappa) = \frac{\mathbf{R}_\lambda \cdot \mathbf{R}_\nu}{R_\lambda R_\nu} \qquad 0 \le \Delta_\kappa \le 2\pi \tag{85}$$

They depend on the angular coordinates of the internal space (*i.e.*, $\omega_\kappa, \gamma_\kappa$), and are always assumed to take the $\hat{z}_\lambda$ axis into the $\hat{z}_\nu$ axis and be in the positive

sense about the $\mathbf{R}_\lambda \times \mathbf{r}_\lambda$ direction. From the definition, it follows that $\Delta_{\nu\to\lambda} = 2\pi - \Delta_{\lambda\to\nu}$. The group property of the Wigner rotation matrices takes the form [46]

$$D^J_{M,\Omega}(\varphi_\nu, \vartheta_\nu, \psi_\nu) = \sum_{\Omega'} D^J_{M,\Omega'}(\varphi_\lambda, \vartheta_\lambda, \psi_\lambda) d^J_{\Omega',\Omega}\Big(\Delta_{\lambda\to\nu}(\omega_\kappa, \gamma_\kappa)\Big) \tag{86}$$

Using this relationship between the Wigner rotation matrices appropriate for different body-fixed axes and the uniqueness of the surface functions, the two angle surface functions are easily seen to be related by

$$\phi^{\gamma,J,\Pi,\Gamma,i}_{\Omega,n}(\omega_\gamma, \gamma_\gamma; \rho) = \sum_{\Omega'} d^J_{\Omega,\Omega'}\Big(\Delta_{\gamma\to\alpha}(\omega_\beta, \gamma_\beta)\Big) \phi^{\alpha,J,\Pi,\Gamma,i}_{\Omega',n}(\omega_\alpha, \gamma_\alpha; \rho) \tag{87}$$

where all three sets of coordinates $(\omega_\gamma, \gamma_\gamma)$ and $(\omega_\beta, \gamma_\beta)$, and $(\omega_\alpha, \gamma_\alpha)$ refer to the same point, q, in the internal configuration space spanned by $(\rho, \omega_\lambda, \gamma_\lambda)$. Since the angle $\Delta_{\gamma\to\alpha}$ is a function of the variables ω_β and γ_β, the linear combination of the $\phi^{\alpha,J,\Pi,\Gamma,i}_{\Omega,n}(\omega_\alpha, \gamma_\alpha; \rho)$ necessary to form the $\phi^{\gamma,J,\Pi,\Gamma,i}_{\Omega,n}(\omega_\gamma, \gamma_\gamma; \rho)$ varies from point to point in the internal configuration space.

The boundary condition for $\phi^{\alpha,J,\Pi,\Gamma,i}_{\Omega,n}(\omega_\alpha, \gamma_\alpha; \rho)$ at $\gamma_\gamma = \frac{\pi}{2}$ is found by inserting the expression for the $\phi^{\gamma,J,\Pi,\Gamma,i}_{\Omega,n}(\omega_\gamma, \gamma_\gamma; \rho)$ in terms of the $\phi^{\alpha,J,\Pi,\Gamma,i}_{\Omega,n}(\omega_\alpha, \gamma_\alpha; \rho)$ into the boundary conditions on the $\phi^{\gamma,J,\Pi,\Gamma,i}_{\Omega,n}(\omega_\gamma, \gamma_\gamma; \rho)$.

$$\sum_{\Omega'} d^J_{\Omega,\Omega'}\Big(\Delta_{\gamma\to\alpha}(\omega_\beta, \gamma_\beta)\Big) \phi^{\alpha,J,\Pi,\Gamma,i}_{\Omega',n}(\omega_\alpha, \gamma_\alpha; \rho) =$$

$$(-1)^\Omega \sum_j \sum_{\Omega''} d^J_{\Omega,\Omega''}\Big(\Delta_{\gamma\to\alpha}(\overline{\omega}_\beta, \overline{\gamma}_\beta)\Big) \phi^{\alpha,J,\Pi,\Gamma,j}_{\Omega'',n}(\overline{\omega}_\alpha, \overline{\gamma}_\alpha; \rho) M^\Gamma_{j,i}\left[\begin{pmatrix} \alpha & \beta & \gamma \\ \beta & \alpha & \gamma \end{pmatrix}\right] \tag{88}$$

We emphasize that the coordinates $(\omega_\alpha, \gamma_\alpha)$, $(\omega_\beta, \gamma_\beta)$, and $(\omega_\gamma, \gamma_\gamma)$ all refer to the same internal configuration space point q. The point $\overline{q}$ is the reflection of the point q in the $\gamma_\gamma = \frac{\pi}{2}$ plane. The bars on $(\overline{\omega}_\alpha, \overline{\gamma}_\alpha)$, and $(\overline{\omega}_\beta, \overline{\gamma}_\beta)$ denote the configuration space point $\overline{q}$ whose γ coordinates are given by $(\omega_\gamma, \pi - \gamma_\gamma)$. That is

$$\overline{q} = \begin{pmatrix} \alpha & \beta & \gamma \\ \beta & \alpha & \gamma \end{pmatrix} q \tag{89}$$

For $\Gamma = A_1(A_2)$, the matrix

$$\mathbf{M}^{\Gamma}\left[\begin{pmatrix} \alpha & \beta & \gamma \\ \beta & \alpha & \gamma \end{pmatrix}\right] \tag{90}$$

is a single number: $1(-1)$. For $\Gamma = E$, it is a real, symmetric, orthogonal matrix of dimension 2; hence its eigenvalues are ± 1 and there exists a matrix $\mathbf{A}^E$ such that

$$\mathbf{M}^{E}\left[\begin{pmatrix} \alpha & \beta & \gamma \\ \beta & \alpha & \gamma \end{pmatrix}\right] = \mathbf{A}^{E}\mathrm{diag}(1,-1)\left(\mathbf{A}^{E}\right)^{-1} \tag{91}$$

In fact its is easily verified that

$$\mathbf{A}^{E} = \mathbf{M}^{E}\left[\begin{pmatrix} \alpha & \beta & \gamma \\ \gamma & \beta & \alpha \end{pmatrix}\right] \tag{92}$$

Defining

$$\mathbf{A}^{A_1} = \mathbf{A}^{A_2} = 1 \tag{93}$$

we conclude that on B_3, the linear combination

$$\sum_{j}\sum_{\Omega'} d^{J}_{\Omega,\Omega'}\left(\Delta_{\gamma\to\alpha}(\omega_\beta,\gamma_\beta)\right)\phi^{\alpha;J,\Pi,\Gamma,j}_{\Omega',n}(\omega_\alpha,\gamma_\alpha;\rho)A^{\Gamma}_{j,i} \tag{94}$$

is even or odd on B_3. More explicitly, expression (94) is even when Ω is even and $\Gamma \in \{A_1, E(i=1)\}$ or when Ω is odd and $\Gamma \in \{A_2, E(i=2)\}$ and it is odd when Ω is even and $\Gamma \in \{A_2, E(i=2)\}$ or when Ω is odd and $\Gamma \in \{A_1, E(i=1)\}$. If the linear combination is even, then the normal derivative $\frac{\partial}{\partial\gamma_\gamma}$ of (94) vanishes; if odd then the linear combination itself vanishes. The boundary conditions provide $2J+1$ constraints on the unknown two-angle surface functions and their normal derivative at the boundary B_3.

This completes the specification of the boundary conditions required to construct surface functions which transform as irreducible representations of P_3 on the subdomain d of configuration space D. The collinear boundary conditions (on B_1) are a consequence of the single-valuedness of the surface function and its derivatives (and are related to the singularities in the grand canonical angular momentum operator); they are valid for any three particle system. If the three

particles are identical, then the domain on which the solutions are constructed can be reduced in area by a factor of 6 in comparison with the complete domain. This introduces two new boundary integrals requiring boundary conditions which are derived from the assumed transformation properties of the functions.

The boundary conditions on B_1 and B_2 do not couple the different Ω components of the unknown functions. In constrast, the boundary conditions on B_3 do couple the Ω components in a nontrivial manner. This Ω coupling in the boundary conditions is a consequence of our choice of body-fixed axes. If the body-fixed z axis is chosen to point in the $\mathbf{R}_\lambda \times \mathbf{r}_\lambda$ direction, then the boundary conditions do not couple the different Ω components. There is a disadvantage to this new set of body-fixed coordinates: the surface functions cannot be chosen to be real and be a representation of P_3. We emphasize that the Ω coupling on B_3 is *not* related to the Ω coupling in the equations of motion. The former can be eliminated by a judicious choice of body-fixed axes while the latter cannot.

10. Results and Discussion

A. General Discussion

The numerical procedure outlined above has been implemented successfully for a system of three hydrogen atoms in the zero total angular momentum state ($J = 0$) using the LSTH potential energy surface.[48,49]

Related calculations of surface functions for $J = 0$ $H+H_2$ have been published by Mishra, Linderberg, and coworkers[5], by Parker, Pack, and coworkers[4], and by Wolniewicz and Hinze.[37] The main difference between our methodology and others is that we made full use of the permutation symmetry of three identical particles to minimize the domain of integration for the finite element scheme and thereby minimized the numerical effort. In addition, a different system of hyperspherical coordinates is employed. For $J > 0$, our formulation includes the full Coriolis coupling in the surface function differential equation. Parker, Pack, and coworkers

omit these Coriolis terms which are then entirely included in the propagation stage of the scattering calculations. It will be interesting to see which of these approaches is computationally more efficient. At the $J = 0$ level, the two choices are identical because Coriolis coupling is absent.

The surface functions are parametrized by their P_3 irreducible representation, hyperradius, and energy, and in this section, the characteristics of the two-angle surface functions are discussed with the aid of contour plots. (The word energy will be used in this paper as synonomous with eigenvalue of the surface function (7).) These plots show graphically how the two-angle surface functions belonging to different irreducible representations differ. By examining surface function contour plots at relatively large values of the hyperradius ($\rho = 6.0$ bohr), where the atom and diatomic molecule are only weakly interacting and the surface functions are localized within each arrangement channel region, the nodal structure of the asymptotic diatomic molecule states is observed. The partial loss of interpretable nodal structure at the saddle point ($\rho = 3.270145$ bohr) and the extensive overlap of the surface functions between different arrangement channels is shown. At even smaller hyperradii ($\rho = 2.0$ bohr), the surface functions are very different in structure from the isolated diatomic molecule states. Because the surface function differential equation contains the full potential energy function, the solutions evolve as a function of ρ from ones with complex nodal structure describing the strongly interacting particles to ones which have a nodal structure of isolated diatomic molecules. Lastly, the two-angle E representation surface functions with increasing degrees of excitation are plotted to display the interesting growth of nodal structure. At $\rho = 6.0$ bohr, the nodal structure shows clearly the increase in rotational and vibrational excitation. At the smaller hyperradii, the nodal structure reveals a mixing of vibrational and rotational excitation character.

All results shown in this section correspond to the $J = 0$ total angular momentum states on the LSTH potential energy surface for H_3. We shall refer to the two-angle surface functions as surface functions in this section for simplicity. For

$J = 0$, the five angle surface functions are independent of the Euler angles. For $J > 0$, this is not the case. Although the surface functions were calculated only in the subdomain d, we have used their irreducible representation transformation properties to extend them into the entire domain D, so that the symmetry of the functions is manifested.

The numerical parameters used to calculate the two-angle surface functions shown in the plots that follow correspond to those used in our most refined scattering calculations. The two-angle surface functions are calculated on a domain which is covered with quadrilateral elements. Each element supports bilinear shape functions. The elements are defined by a grid consisting of $70\omega_\lambda$ and $70\gamma_\lambda$ points The finite element approximation gives rise to roughly 5000 equations (46) with a half-band width of 70 in the A_1 and A_2 irreducible representations. This becomes 10,000 equations with a half-band width of 70 in the case of the E irreducible representation. The variational integral (40) is computed using four Gauss-Legendre quadrature points per element. The surface function eigenvalues are found with Bathe's subspace iteration method.[44] The subspace iteration is terminated when the relative change in the highest eigenvalue is less than 1 ppm in successive iterations. Since the two-angle surface functions are real, all of the arithmetic necessary involves real numbers. The calculations were performed on the Cray X-MP/48 at the San Diego Supercomputer Center using 64 bit precision.

The amount of computational effort expended to calculate a set of surface functions at a value of ρ depends on the closeness of the beginning iteration vectors to the final solution vectors. As remarked in section 7, Bathe's subspace iteration method is used to find the lowest n eigenvalues and corresponding eigenvectors. Because Bathe's method is iterative, it is necessary to begin with some set of iteration vectors. If these vectors span the same subspace spanned by the surface functions, then the iteration converges in one step. Otherwise, the subspace must be updated using the inverse power method. The first set of surface functions typically requires 50 or more iterations because the initial iteration vectors are

chosen to excite every degree of freedom in the system and are not close in character to the surface functions. This choice of initial iteration vectors is made to insure that the set is not orthogonal to any solution. At subsequent values of ρ, the situation is different: the surface functions from the previous value of ρ provide an excellent set of beginning iteration vectors. Depending on the proximity of the successive ρ values, the method converges in 5 to 10 iterations. This saving is very important since 40 to 100 *sets* of surface functions were required in the scattering calculations for $H + H_2$. The average time required to calculate a single surface function with the parameters given is 6.6 seconds for the A_1 and A_2 representations and 16.6 seconds for both rows of the E representation on the Cray X/MP 48 computer.

B. Definition of Mapping and LSTH Potential Contours

In the remainder of this paper, plots of the mesh, LSTH potential energy contours, and two-angle surface function contours at fixed ρ are presented. The internal symmetrized hyperspherical coordinate space is defined as follows.[1] The angles $(\omega_\lambda, \gamma_\lambda)$ are interpreted as the spherical polar angles in the abstract internal 3D space in which a point P has the Cartesion coordinates $(X_\lambda, Y_\lambda, Z_\lambda)$ defined by

$$X_\lambda = \rho \sin\omega_\lambda \cos\gamma_\lambda \tag{95}$$

$$Y_\lambda = \rho \sin\omega_\lambda \sin\gamma_\lambda \tag{96}$$

$$Z_\lambda = \rho \cos\omega_\lambda \tag{97}$$

Since $0 \leq \omega_\lambda \leq \pi$ and $0 \leq \gamma_\lambda \leq \pi$, these internal angles parametrize the surface of a hemisphere. One important point is that only the half-space of positive Y_λ coordinates provides a one-to-one correspondence between points in configuration space and points in the 3D internal space. In order to visualize the variation of the potential energy or surface functions with the internal angles $(\omega_\lambda, \gamma_\lambda)$, a mapping of the hemispherical surface onto a plane is defined. Consider the plane polar

radius ϱ and plane polar angle ϖ as parametrizing the plane of the figures. These plane polar coordinates are defined from the internal angles $(\omega_\lambda, \gamma_\lambda)$ by

$$\varrho = \omega_\lambda \qquad 0 \leq \varrho \leq \frac{\pi}{2} \tag{98}$$

$$\varpi = \gamma_\lambda \qquad 0 \leq \varpi \leq 2\pi \tag{99}$$

In words, given a point on a plot, the radial distance from the origin of the figure to the point is equal to the ω_λ coordinate for that point. The plane polar angle is equal to the γ_λ coordinate of that point. The central point in such a plot is the Z_λ axis. The curve $\omega_\lambda = \frac{\pi}{2}$ is a circle in this mapping centered on the Z_λ axis. We will call this the north pole view because it is a certain projection of the spherical surface onto a plane tangent to the sphere at the Z_λ axis or north pole. In figure 1, the contours of the LSTH potential energy surface at $\rho = 6.$ bohr are shown using the north pole view. (All energies are measured with respect to the bottom of the isolated diatomic molecule interaction potential.) For regions near the center of figure 1, the potential energy contours are nearly circular, indicating their independence of the angle γ_λ. By implication, the rotation of the diatomic molecule is hardly perturbed by the presence of the atom for hyperradii larger than 6 bohr. In this figure, as one moves along a line radiating from the center of the figure, the potential energy begins quite large, decreases to a minimum, and then increases. This variation of the potential energy with ω_λ represents the quasivibrational potential in the diatomic molecule. Speaking roughly, the north pole view is a mapping which looks down one arrangement channel region of configuration space.

The south pole view is defined similarly to the north pole view. Whereas the north pole view is a projection onto a plane tangent to the sphere at the north pole, the south pole view is the projection onto a plane tangent to the sphere at the negative Z_λ axis or south pole. The south pole mapping is defined by replacing ω_λ by $\pi - \omega_\lambda$ in equations (98) and (99). Figure 2 shows the LSTH potential energy contours again at $\rho = 6$ bohr in the south pole view. Instead of a single

arrangement channel region which is seen in figure 1, the other two arrangement channels are easily seen in figure 2.

We now wish to define a similar mapping of the angles $(\omega_\lambda, \gamma_\lambda)$ which parametrize the surface of a sphere onto a plane tangent to the sphere at the Y_λ axis. This axis is the C_3 axis of the potential energy surface and a view from this axis shows all regions of the internal configuration space simultaneously and also shows the symmetry of the functions plotted. It is this equatorial view that we shall adopted in all of the remaining figures. The north and south pole views defined in the last paragraphs are intuitively defined from the internal angles $(\omega_\lambda, \gamma_\lambda)$ and show the arrangement channel regions clearly.

Let us define a pair of spherical polar angles $(\overline{\omega}_\lambda, \overline{\gamma}_\lambda)$ which parametrized the surface of the sphere and use the positive Y_λ axis as their polar axis. The new spherical polar coordinates $(\overline{\omega}_\lambda, \overline{\gamma}_\lambda)$ are defined from the internal angles $(\omega_\lambda, \gamma_\lambda)$ by

$$\cos \overline{\omega}_\lambda = \sin \omega_\lambda \tag{100}$$

$$\tan \overline{\gamma}_\lambda = \tan \omega_\lambda \cos \gamma_\lambda \tag{101}$$

Replacing the unbarred coordinates $(\omega_\lambda, \gamma_\lambda)$ in equations (98) and (99), with the barred coordinates $(\overline{\omega}_\lambda, \overline{\gamma}_\lambda)$ the plane polar coordinates of the figure are defined. Figure 3 shows the LSTH potential energy contour at $\rho = 6$ bohr in this mapping. The C_{3v} symmetry of the contours is evident. Also evident are the three arrangement channel regions.

Figures 4 and 5 show contours of the LSTH potential energy surface at $\rho = 2$ bohr and $\rho = 3.270145$ bohr (contains the saddle point). The potential energy contours are quite different at different hyperradii. At 6.0 bohr (figure 3), the three arrangement channel regions are clearly discernible. In each arrangement channel region, the low potential energy contours are nearly independent of γ_λ. At 2.0 bohr (figure 4), the distinction between arrangement channels is lost and the minimum in the potential energy is around the Y_λ axis. At 3.270145 bohr (figure

5), the arrangement channels regions are again not discernible and the minima in the potential occur at the three saddle points which are located at the intersection of the symmetry planes $\gamma_\lambda = \frac{\pi}{2}, (\lambda = \alpha, \beta, \gamma)$ and the collinear circle $(\gamma_\lambda = 0, \pi)$.

C. Finite Element Mesh

In figure 6, a course version of the finite element mesh is displayed having 20 ω_α and 20 γ_α points. The courser mesh is shown for clarity. The solutions in parts of the domain D where the mesh is absent are fixed by the irreducible representation transformation properties of the solutions calculated in the domain d where the mesh is shown. The computational effort depends on the cube of the number of mesh points so use of only this subdomain yields considerable savings. If only two of the three particles are identical, then the minimal domain is $\{(\omega_\lambda, \gamma_\lambda) | \, 0 \leq \omega_\lambda \leq \pi, 0 \leq \gamma_\lambda \leq \frac{\pi}{2}\}$. If none of the particles are identical, then the entire hemisphere is the minimal domain. Finally, we note that the strong classically forbidden region where ω_λ is nearly zero is excluded from the finite element domain because the surface functions are negligible there and it is undesirable to waste elements. This exclusion is implemented by setting the two-angle surface functions to zero at a small value of ω_λ. The particular value of ω_λ is ρ-dependent.

D. Surface Function Eigenvalue Curves

The surface function eigenvalues are parametrized by the generalized collision coordinate ρ. Curves for the A_1, A_2, and E representation surface function eigenvalues versus ρ are shown in figures 7 through 9, respectively. (The zero of energy is the bottom of the isolated diatom's internuclear potential energy.) The curves have the same general structure for all three representations. Beginning at small values of ρ, they rapidly decrease as ρ increases. At large values of ρ, they each approach some constant value. This general behavior has a simple physical interpretation: at small ρ, the interaction of the three atoms is strongly repulsive and

the kinetic energy is large (varying as ρ^{-2}) leading to high eigenvalues. At large ρ, one of the atoms interacts with the diatomic molecule only weakly or not at all. The constant values which the surface function eigenvalues tend to asymptotically at large ρ are the discrete energies of the isolated diatomic molecule indicated at the right hand side of the figures. The A_1 surface functions asymptotically ($\rho \rightarrow \infty$) become only the even rotational states of the diatomic molecules. The A_2 surface functions become only the odd diatom rotational states. The E surface function spectrum includes both even and odd diatomic molecule rotational states. These statements follow from the irreducible representation nature of the surface functions. The eigenvalue curves in figures 7 through 9 may or may not have local minima and maxima near the saddle point depending on the symmetry of the surface function and the nature of the interaction potential. Finally, note that the density of states is almost independent of ρ (*i.e.*, almost the same as that for the asymptotic diatom molecules). Of course, the E representation has twice the number of states in a given energy range as the A_1 or A_2 surface functions. This semiconstant density of surface function states implies that the number of surface functions required for a converged scattering calculation will not be greatly different from the number of open asymptotic states (within about a factor of 2) and is in contrast to the situation in the older collinear methods especially for heavy-light-heavy atom-diatom reactions.[50-52]

In figure 7, the surface function eigenvalues as a function of ρ are shown for lowest 34 states of the A_1 representation between 1.8 and 5.9 bohr. Notice the shallow minima in some of these curves (*e.g.*, curve number 5) for values of ρ near the saddle point. Such minima in the corresponding curves in collinear reactive triatomic scattering[31-34] and electron-hydrogen atom scattering[13,19] have been related to resonance structure. Resonance structure also has been demonstrated in full scattering calculations for 3D $J = 0$ $H + H_2$ and in particular for the A_1 irreducible representation.[3]

The connection between minima in the surface function eigenvalue curves and resonances rests on the adiabatic approximation. If the hyperradial motion (slow) is approximately adiabatically decoupled from the fast hyperangular motion, then it is meaningful to consider the hyperradial motion on a single eigenvalue curve. The presence of a local minimum in such a curve can lead to resonances in the corresponding decoupled hyperradial scattering. This model has been used with great success in collinear reactive scattering[31,33,34] and in electron-hydrogen atom scattering[13] to model resonances and may be similarly useful in the modeling of resonances in 3D reactive scattering. The presence of nonadiabatic coupling in the correct equations of motion leads to the manifestation of resonance structure in transitions other than the one transition represented by the adiabatic approximation. In another paper, we will present the results of applications of this model to 3D $J = 0$ $H + H_2$.

In figure 8, the lowest 33 A_2 eigenvalue curves are displayed. These curves are entirely replusive with no discernible minima. The A_2 surface functions are required by symmetry for $J = 0$ to have nodal lines on B_3 (see equation (74) and figure 6) which contains one of the three collinear saddle points. In paper III, it will be shown that the A_2 scattering probabilities do not reveal any structure attributable to resonances. It is very likely that the lack of minima in the surface function eigenvalue curves and the lack of resonances in A_2, $J = 0$ is due to the presence of the nodal line between the arrangement channels.

Figure 9 shows the lowest 65 E representation surface function eigenvalues. The density of states is higher for the E curves because all asymptotic states are present. The E representation curves again show local minima and the corresponding reaction probabilities show resonance structure as discussed in paper III. The boundary conditions on the E representation surface functions do not require that they have nodes on B_3 and the contour plots of E surface functions do indeed show that they do not have nodes there.

E. Low Energy Surface Functions at Three Hyperradii

Figures 10 through 12 show contour plots of the two-angle surface functions at 6, 2, and 3.270145 bohr, respectively. All of the figures have the same format, but correspond to different values of ρ. Each figure contains the lowest A_1 (panel (a)) and A_2 (panel (d)) surface functions four E surface functions (panels (b), (c), (e), and (f)). For each E surface function eigenvalue, there are two orthogonal, degenerate functions which transform according to different rows of the E irreducible representation. Panels (b) and (c) display the degenerate pair with the lowest energy where (b) is row one and (c) is row two. Panels (e) and (f) display the degenerate E pair with the next lowest energy where (e) is row one and (f) is row two. The E surface function pair with the lowest eigenvalue becomes degenerate with the lowest A_1 surface function and the first excited E surface function pair becomes degenerate with the lowest A_2 surface function as ρ becomes large (see figure 10). This is the reason for plotting the two lowest E representation surface functions. The surface function contours in figures 10 through 12 correspond to the potential energy contours in figures 3 through 5, respectively.

The first observation upon examining figures 10-12 is that part of the nodal structure is due to the transformation properties imposed by the irreducible representation property of the surface functions and hence is independent of ρ. Such nodal structure takes the form of straight lines in these plots corresponding to $\gamma_\lambda = \frac{\pi}{2}$ $(\lambda = \alpha, \beta, \gamma)$. (They are curves on the surface of a hemisphere in the internal symmetrized hyperspherical coordinate space and become straight lines on the equatorial projection.) Permutation symmetry imposes no nodes on the A_1 irreducible representation $J = 0$ surface function because it is even under reflections through B_2 and B_3. In contrast, the $J = 0$ A_2 surface function must have nodes at B_2, B_3, and $\gamma_\beta = \frac{\pi}{2}$. This last node is not explicitly imposed but follows from the other two. The surface functions transforming as the two rows of E have different behavior. The surface function belonging to row 1 is even at B_2 whereas that belonging to row 2 vanishes at B_2. On B_3, the surface functions belonging to

the two rows of E are neither even nor odd and are not required to vanish there. The boundary conditions which follow from the transformation properties of the irreducible representation surface functions are independent of ρ. If they demand the vanishing of the surface function on a curve, then it must vanish there for all ρ. If the boundary conditions demand a function be even at a curve, it will not vanish there.

In order to interpret the nodal structure of the two-angle surface functions at 2.0, 3.27, and 6.0 bohr, it is important to understand the nodal structure of the surface functions at large values of the hyperradius where the arrangement channels have completely separated, the interaction between the atom and diatomic molecule has essentially vanished and the centrifugal potential is also negligible. Each surface function is then a linear combination of a separable function in each arrangement channel of the form:

$$\phi^{\lambda,J,\Pi,\Gamma,i}_{\Omega,v,j} \sim \sum_{\lambda'} c^{\Gamma,i}_{\lambda',v,j} \sum_{\Omega'} a^{\Gamma,i}_{\Omega,\Omega'} \sum_{\Omega''} d^{J}_{\Omega',\Omega''}(\Delta_{\lambda\to\lambda'}) \xi_{v,j}(\omega_{\lambda'};\rho) \wp^{\Omega''}_{j}(\cos\gamma_{\lambda}) \quad (102)$$

where

$$\wp^{\Omega''}_{j}(\cos\gamma_{\lambda}) = \left(\frac{(j-|\Omega'|)!(2j+1)}{2(j+|\Omega'|)!}\right)^{\frac{1}{2}} P^{\Omega''}_{j}(\cos\gamma_{\lambda}) \quad (103)$$

and $\xi_{v,j}(\omega_{\lambda};\rho)$ satisfies

$$\left\{\frac{-2\hbar^2}{\rho^2\mu}\left(\frac{\partial^2}{\partial\omega_{\lambda}^2}+2\cot\omega_{\lambda}\frac{\partial}{\partial\omega_{\lambda}}-\frac{j(j+1)}{\sin^2\omega_{\lambda}}\right)+v(\rho\sin\frac{\omega_{\lambda}}{2})-e_{v,j}\right\}\xi_{v,j}(\omega_{\lambda};\rho)=0 \quad (104)$$

and are normalized

$$\int_0^{r_{\lambda}^{max}} |\xi_{v,j}(\omega_{\lambda};\rho)|^2 \sin^2\omega_{\lambda} d\omega_{\lambda} = 1 \quad (105)$$

where $v(\rho\sin\frac{\omega_{\lambda}}{2}) = \overline{V}(\rho\to\infty,\omega_{\lambda},\gamma_{\lambda})$ is the potential energy function for the isolated diatomic molecule. $P^{\Omega}_{j}(\cos\gamma_{\lambda})$ is the associated Legendre function. The coefficients $c^{\Gamma,i}_{\lambda',v,j}$ are given by equations (49) and (50) in paper I. The coefficients $a^{J,\Gamma,i}_{\Omega,\Omega'}$ are constants which can be determined by first order perturbation theory and are necessary in equation (102) because the separable functions are degenerate

in Ω'' and the remnant of interaction between three particles mixes the degenerate states. Each of the separable functions $\xi_{v,j}(\omega_\lambda;\rho)\wp_j^\Omega(\cos\gamma_\lambda)$ approaches a state of the isolated diatomic molecule only as $\rho(\frac{\omega_\lambda}{2}) \rightarrow r_\lambda$. For this reason, we do *not* call these separable functions in each arrangement channel, states of the isolated diatomic molecule. Within an arrangement channel, the surface function is the product of an associated Legendre function in γ_λ and a one dimensional oscillator-like function in ω_λ. The nodes of such separable functions are along constant γ_λ and constant ω_λ curves within an arrangement channel.

In equation (102) there are three summations. The summation over λ' is because the irreducible representation surface functions have amplitude in more than one arrangement channel region. The summation over Ω'' is required because the two-angle surface function on the right of equation (102) is associated with the Wigner rotation matrix expressed in λ coordinates and the separable functions are associated with the λ' coordinates. The summation over Ω' is required to the degeneracy breaking residual interactions which exist at all finite values of ρ.

At 6.0 bohr (figure 10), the contours of the $J = 0$ surface functions are similar to asymptotic diatom states in each arrangement channel region. There is a very wide classically forbidden region separating the arrangement channels regions and the surface functions are negligible between these channels. Examination of the potential energy contours at $\rho = 6$ bohr in figure 3 shows that the minima in the contours are localized with wide classically forbidden regions in between them. It is the regions containing the minima that we refer to as the arrangement channel regions. Physically, the low energy regions correspond to the bound diatomic molecule configurations and a free atom. The wide classically forbidden regions of configuration space correspond to the configurations with the three atoms widely separated. Low surface function probability density in this classically forbidden region reflects the small likelihood that the atom and diatomic molecule will react at large separations. To do so would require tunnelling over large distances.

At $\rho = 6$ bohr, the structure of the surface functions is simple to understand. The A_1 function shown in panel (a) of figure 10 is well represented by a $j = 0, v = 0$ diatom state in each arrangement channel. The amplitude contours are approximately along constant ω_λ curves in each arrangement channel region. The A_2 function in panel (d) is well represented by a $j = 1, v = 0$ diatom state in each arrangement channel. In panel (d), the quantum of rotational excitation is revealed by the node in each arrangement channel region on $\gamma_\lambda = \frac{\pi}{2}$ $(\lambda = \alpha, \beta, \gamma)$ lines. One degenerate pair of E surface functions is shown in panels (b) and (c) where (b) belongs to row one of E and (c) belongs to row two of E. Another degenerate pair of E surface functions is shown in panels (e) and (f). The lowest E surface function pair is degenerate with the lowest A_1 surface function and the first excited E surface function pair is degenerate with the lowest A_2 surface function. Notice that the E functions in panels (b) and (c) look like a constant multiple of the A_1 function in the corresponding arrangement channel regions. The same remark holds for the relation between the first excited E functions in panels (e) and (f) and the A_2 function in panel (d).

In figure 10, we see that the amplitude of one of the degenerate pair of E surface functions vanishes in the α arrangement channel region and this is true for all E irreducible representation pairs at large ρ. Of the degenerate pair in panels (b) and (c), it is the function belonging to the second row of E in panel (c) that vanishes in the α arrangement channel region. Similarly, the surface function belonging to row one of E in panel (e) vanishes in the α arrangement channel region. This is a simple consequence of the particular matrix representation of E that is used. Any surface function which transforms as the first (second) row of E is even (odd) at B_2. In the $\lambda = \alpha, \beta, \gamma$ arrangement channel, the diatom states are either even or odd about $\gamma_\lambda = \frac{\pi}{2}$. In the α arrangement channel, the surface functions must become one of the diatom rotational states and this state will transform as one or the other of the rows of E. The other row must have a vanishing amplitude in that arrangement channel.

The vanishing of the E surface function belonging to one row of each E degenerate pair in the α arrangement channel occurs only for ρ large enough that the arrangement channels are completely separated and the surface functions become multiples of Legendre polynomials $P_j(\cos\gamma_\lambda)$ (for $J = 0$) and oscillator functions in ω_λ (see equation (102). At smaller ρ, the arrangement channels regions are not isolated by wide classically forbidden regions and the γ_λ behavior of the surface functions is no longer that of the simple Legendre polynomials. For these regions, surface functions corresponding to boths rows of the E representation are nonvanishing in all three arrangement channel regions.

The asymptotic spectrum of states that a set of surface functions tends to as ρ becomes large is determined by the irreducible representation of the surface function in P_3. In general, the presence of three symmetry planes at $\gamma_\lambda = \frac{\pi}{2}$ $(\lambda = \alpha, \beta, \gamma)$ at which the A_1 (A_2) surface functions are even (odd) implies that the A_1 (A_2) surface functions become only even (odd) rotational states of the diatomic molecule as ρ becomes large. The E irreducible representation surface functions have less restrictive boundary conditions on B_3, and for this reason, both even and odd diatom rotational states are included in the asymptotic behavior of this representation.

The surface function contours for $\rho = 2$ bohr are shown in figure 11 and the potential energy contours for the same hyperradius are shown in figure 4. At $\rho =$ 2 bohr, the surface function contours are centered around the Y_λ axis for all three representations. The region of the internal configuration space around the Y_λ axis represents configurations of the three particles which are close to an equilateral triangle in physical space and is also the low energy region of the potential energy surface as shown in figure 4. The A_1 function in panel (a) contains no nodal lines. The degenerate E pair of functions in panels (b) and (c) each have one node. Any A_2 surface function, such as that shown in panel (d) must vanish along all three $\gamma_\lambda = \frac{\pi}{2}, (\lambda = \alpha, \beta, \gamma)$ lines because of transformation properties of this representation. The degenerate E pair of excited functions in panels (e) and (f)

each have two nodal lines. The vertical node in panels (c) and (f) are due to symmetry with respect to the B_2 line. It is not obvious from nodal structure of the pair of functions in panels (b) and (c) that they are degenerate nor, similarly is that obvious for the degenerate pair in panels (e) and (f).

We next examine the same selection of $J = 0$ surface functions at the value of the hyperradius ($\rho = 3.270145 \sim 3.27$ bohr) which intersects the saddle point for H_3 in the LSTH potential energy surface. In figure 12, the surface function contours are plotted for a hyperradius of 3.27 bohr. Figure 5 shows the corresponding potential energy contours. At 3.27 bohr, the maxima in the surface function contours have moved toward the collinear configurations following the potential energy minima. In the 3D internal space the saddle point becomes the minimum potential energy when restricted to a spherical shell as the surface functions are. The A_1 surface function in panel (a) is nodeless and the maxima are at the saddle points where the symmetry lines ($\gamma_\lambda = \frac{\pi}{2}, \lambda = \alpha, \beta, \gamma$) intersect the collinear configuration circle. The A_2 contours shown in panel (d) have nodal lines at the symmetry lines because of their symmetry characteristics; however, they are localized near these symmetry lines and are extrema on the collinear configuration circle. In a similar way, the E surface functions have moved toward the saddle point regions, and in fact, look like their A_1 and A_2 counterparts. In fact, not only do the E functions look like their A_1 and A_2 counterparts, there have the same eigenvalues to 3 significant digits.

From figure 12, it is interesting to note that the E surface function belonging to one row of each of the degenerate pair has a very small amplitude at the saddle point which lies on the B_2 line. This phenomenon is quite different from the large ρ vanishing of one row of E in the α arrangement channel. At 3.27 bohr, the potential energy contours are far from their asymptotic form and the surface functions have vanishing amplitude in the regions of configuration space corresponding to the asymptotic arrangement channels. The key to understanding this behavior of the surface functions is to notice that the surface functions are

localized at the saddle points. Examination of the potential energy contours in figure 5 shows why the localization occurs. As already remarked, the minima in the potential are centered at the saddle points. Separating the saddle point regions are small barriers of height less that 1 eV but greater than the surface function eigenvalues shown in figure 12. As is the case for large hyperradii where the surface function amplitude is localized in the arrangement channel regions and vanishing between arrangement channels, so at 3.27 bohr we see localized regions of the internal configuration space where the surface function amplitude is located. We see from the A_1 surface function in panel (a) what the E surface function with which it is degenerate would tend to resemble. When the character of the E representation surface function in the localized density regions is in conflict with the symmetry requirements on the function, then the amplitude of the surface function in the region around the line B_2 will vanish.

The movement of the high probability density regions of the surface functions from equilateral triangle configurations at 2 bohr, to symmetric collinear configurations at 3.27 bohr, and to nearly separable functions localized in each arrangement channel at 6 bohr is simple to follow in figures 10 through 12 for each representation. In the case of the lowest A_1 and A_2 surface functions (panels (a) and (d)), the nodal lines or lack of them are due entirely to the symmetry and are independent of ρ. Hence the movement of the high density regions is almost obvious. In the case the E irreducible representation, some of the nodal lines are not due to symmetry and evolve with the hyperradius. This evolution of the two-angle surface functions with ρ is a result of the use of the potential energy function in the surface function hamiltonian (5) (as compared, for example, with the hyperspherical harmonics[14] obtained without including the potential). This inclusion is the principal reason why these local surface functions form an efficient basis set for expanding the scattering wave functions.

The ρ evolution of the nodal lines and high density regions in the lowest E two-angle surface functions is seen by comparing figures 10 through 12. The single

nodal line in panel (c) of figures 10 through 12 is due to symmetry, so that it is invariant with ρ. Movement of the high density regions of this surface function from around the Y_λ axis in figure 10 to the saddle points in figure 11 and to the asymptotic arrangement channel regions in figure 12 coincides with the movement of the minimum of the potential. The single nodal line in panel (b) of these figures is not due to symmetry and changes with ρ. The node has the same appearance at 2 bohr (figure 12) and 3.27 bohr (figure 11) although the function contours move in response to the potential energy. Between 3.27 and 6 bohr (figure 10), this node moves and changes shape. As a final example, consider panel (f) in figures 10 through 12. One node is a symmetry-generated node (the vertical one along $\gamma_\alpha = \frac{\pi}{2}$) and the other is not. The second node changes shape as a function of ρ while the first does not.

F. Penetration Into Classically Forbidden Regions

One theme in discussing the surface functions has been the penetration of the surface functions into classically forbidden regions of configuration space and the resulting overlap of distinct localized high probability density regions or lack of overlap. In figures 13 through 15, we superimpose the probability density of the lowest $J = 0$ A_1 surface function with the potential energy contours corresponding to the energy of the surface function. In figure 13, the value of ρ is 2 bohr and the surface function energy is 3.199 eV. Figure 14 displays the associated function at 3.270145 bohr with energy 0.5686 eV. In figure 15, the lowest A_1 surface function at 6 bohr with energy 0.2666 eV is shown. At all three hyperradii, the surface functions penetration far into the classically forbidden region. From figure 14 we see that the probability density is less than 0.01 in the classically *allowed* regions which connect the saddle point regions and has significantly larger probability density in classically forbidden regions especially along the collinear configuration circle. From this same figure we also observe that there is significant probability density away from the collinear configuration circle even into noncollinear geometries

which are classically forbidden. Since the scattering wave function is expanded in surface functions, these observations carry over to the scattering wave functions. Our earlier observation that at 3.270145 bohr the lowest energy surface functions are composed of isolated regions of probability density centered around the saddle points is even more interesting because the localized regions of density are not even separated by a potential energy barrier. In figure 15, the localized high probability density regions localized in the arrangement channel regions are clearly seen to be separated by a wide classically forbidden regions of configuration space.

G. Excited Surface Functions at Three Hyperradii

As the next topic, we display some more highly excited $J = 0$ E representation surface functions at the same three values of ρ in figures 16 through 19. In each of these figures, both rows of the representation are shown at the three hyperradii. Different figures correspond to different levels of excitation in the surface functions. Figures 16 through 19 display the third, fourth, ninth, and tenth surface functions, respectively. It should be emphasized that these are not adiabatic functions of ρ. In other words, the functions at the three ρ values are not necessarily connected in a correlation diagram. Instead, the functions are energy-ordered at each ρ and, therefore, the energy eigenvalue curves are not allowed to cross. Nevertheless, an examination of figures 16 through 19, shows how the number of nodal lines increases with surface function energy and how the nodal structure at a given level of excitation is quite different at the three hyperradii.

The increasing rotational and vibrational structure in an isolated diatomic molecule is evident at $\rho = 6$ bohr in panels (c) and (f) of figures 16 through 19. Panels (c) and (f) of figure 16 show that in each of the three arrangement channel regions, the surface function is proportional to the $v = 0, j = 2$ diatomic molecule wave function expressed in hyperspherical coordinates. Similarly, panels (c) and (f) of figures 17, 18, and 19 reveal $\rho = 6$ bohr surface functions which are proportional to the diatom wave functions for $v = 0, j = 3$, $v = 1, j = 0$, and $v = 1, j = 1$,

respectively in each arrangement channel. Specifically, in panels (c) and (f) of figure 17, within each arrangement channel region, three nodal lines corresponding to constant $\gamma_\lambda(\lambda = \alpha, \beta, \gamma)$ lines are seen and these three nodal lines are interpreted as rotational excitation in each arrangement channel. The absence of probability density in the α arrangement channel in panel (c) is a consequence of the same symmetry properties that were discussed in connection with figures 10 through 12. In panels (c) and (f) of figure 18, the single nodal line in the parts of the figure which show high probability density is a constant $\omega_\lambda(\lambda = \alpha, \beta, \gamma)$ line and corresponds in each arrangement channel region to diatomic molecule wave functions with one quantum of vibrational excitation. The complicated nodal structure in the central part of panels (c) and (f) of figure 18 where there are no other contours is the result of the very small amplitude of the two-angle surface functions there. This structure has no significance and may even be due to small numerical inaccuracies. Finally, in panel (c) and (f) of figure 19, in each arrangement channel region, both constant γ_λ and ω_λ nodal lines are seen and these nodal lines correspond to diatomic molecule wave functions which have one quantum of rotational and one quantum of vibrational excitation.

For some of the E surface functions in figures 16 through 19, the nodal structure at 3.270145 or 2.0 bohr is reminiscent of vibrational or rotational excitation. At 3.27 bohr in panels (b) and (e) of figures 16 through 18, the nodal patterns are consistent with rotational excitation. To elaborate, nodal lines can be said to be consistent with rotational excitation when they are approximately constant γ_λ lines in the coordinate system appropriate to the λ arrangement channel. Likewise, nodal lines which are approximately constant ω_λ lines are consistent with vibrational excitation. Of course, such reasoning is heuristic and qualitative and is presented in order to provide some sense of the structure of the two-angle surface functions. The rotational excitation is most dramatic in panels (b) and (e) of figure 18. Panels (b) and (e) of figure 19 show nodal structure which is not easily interpreted as corresponding to rotational or vibrational excitation. Before

leaving the 3.270145 bohr surface functions, it is interesting to note that the more highly excited surface functions shown in figures 16 through 19 are not localized as the lower energy ones shown in figure 12. The excited surface functions at 3.270145 bohr are still centered at the saddle points, but are not composed of isolated high probability density regions. Said roughly, the surface functions centered at different saddle points overlap.

At 2.0 bohr, the nodal structure shown in panels (a) and (d) of figures 16 through 19 is very different from that at 3.27 or 6.0 bohr. It does not resemble either rotational or vibrational excitation. The potential energy function at 2 bohr (figure 4) is very different from its asymptotic form (figures 1 through 3), and the structure of the canonical angular momentum operator becomes increasingly important with respect to the potential energy because of the $\frac{1}{\rho^2}$ which multiplies that operator in equations (5) and (7) as already mentioned in section 10.E. One feature of interest in the 2.0 bohr surface functions is the presence of closed nodal curves in all of the functions in panels (a) and (d) of figures 16 through 19. Such closed nodal curves are absent in the corresponding 3.270145 and 6.0 bohr surface functions. It would be very interesting to examine the hyperspherical harmonics at 2 bohr to see if they resemble the surface functions or not. If the surface functions do resemble hyperspherical harmonics at 2 bohr, then the nodal structure will not be anything like rotational or vibrational structure.

11. Summary

In this paper, we have discussed the general definition and characteristics of surface functions for systems consisting of three particles. A finite element method for constructing surface functions for a general system of three particles is also presented. The potential energy function is used in the surface function hamiltonian so they evolve with the hyperradius. This evolution makes the surface functions a very effective basis set for expanding the scattering wave functions as is discussed in paper I and validated for $J = 0$ $H + H_2$ in paper III. In the present paper, we

have shown examples of surface functions for $J = 0$ $H + H_2$. The character of the resulting surface functions is analyzed in some detail. P_3 permutation symmetry of three identical particles is used to obtain the numerical solutions. This minimizes the domain over which the surface function differential equation must be solved and introduces novel boundary conditions on the boundaries of the domain. As a result, the numerical effort required is significantly decreased. Some of the formalism developed is also valid for other methods of calculating surface functions than the finite element one.

References

† Work supported in part by the U.S. Air Force Office of Scientific Research, Contract No. AFOSR-82-0341. Support from the U.S. Department of Energy, Grant No. DE-AS03-83ER 13118 is also acknowledged. We thank the San Diego Supercomputer Center on whose Cray X-MP/48 the calculations were performed.

‡ Work performed in partial fulfillment of the requirements for the Ph.D. degree in Chemistry at the California Institute of Technology.

§ Contribution number

1. A. Kuppermann, *Chem. Phys. Lett.* **32**, 374 (1975).
2. R. T. Ling and A. Kuppermann, in: **Electronic and Atomic Collisions, Abstracts of Papers of the 9th International Conference on the Physics of Electronic and Atomic Collisions**, Seattle, Washington, 24-30 July 1975, Vol. 1, eds. J. S. Risley and R. Geballe (Univ. Washington Press, Seattle, 1975) pp.353, 354.
3. A. Kuppermann and P. G. Hipes, *J. Chem. Phys.* **84**, 5962 (1986); P. G. Hipes and A. Kuppermann, *Chem. Phys. Lett.* **133**, 1 (1987).
4. G. A. Parker, R. T. Pack, B. J. Archer, and R. B. Walker, *Chem. Phys. Lett.* **137**, 564 (1987); R. T. Pack and G. A. Parker, submitted to *J. Chem. Phys.*.
5. M. Mishra, J. Linderberg, and Y. Öhrn, *Chem. Phys. Lett.* **111**, 439 (1984); J. Linderberg, *Intern. J. Quantum Chem.* **19**, 467 (1986).
6. G. C. Schatz and A. Kuppermann, *J. Chem. Phys.* **65**, 4642 (1976); 4668 (1976).
7. G. Hauke, J. Manz, and J. Römelt, *J. Chem. Phys.* **73**, 5040 (1980); J. Römelt, *Chem. Phys. Lett.* **74**, 263 (1980).
8. A. Kuppermann, J. A. Kaye, and J. P. Dwyer, *Chem. Phys. Lett.* **74**, 257 (1980).
9. T. H. Gronwall, *Ann. Math.* **33**, 279 (1932); *Phys. Rev.* **51**, 655 (1937).
10. J. H. Bartlett, *Phys. Rev.* **51**, 661 (1937).

11. G. H. Wannier, *Phys. Rev.* **90**, 817 (1953).

12. V. Fock, *Det Kong. Norske Vidensk. Selsk. Forhandl.* **31**, 138,145 (1958).

13. J. Macek, *J. Phys. B* **1**, 831 (1968).

14. H. Klar, in: **Electronic and Atomic Collisions**, eds. J. Eichler, I. V. Hertel, and N. Stolterfoht (Elsevier, 1984) p. 767.

15. C. D. Lin, *Adv. Atom. Mol. Phys.* **22**, 77 (1986) and references therein.

16. U. Fano, *Rep. Prog. Phys.* **46**, 97 (1983).

17. C. H. Greene and C. W. Clark, *Phys. Rev. A* **30**, 2161 (1984).

18. A. F. Starace, in: **Fundamental Processes in Energetic Atomic Collisions**, eds. H. O. Luta, J. S. Biggs, and H. Kleinpoppen (Plenum Press, New York, 1983) p. 69.

19. D. M. Hood and A. Kuppermann, in **Theory of Chemical Reaction Dynamics** (D. Reidel, Boston, 1986) pp. 193,214; and references therein.

20. R. E. Clapp, *Phys. Rev.* **76**, 873 (1949).

21. L. M. Delves, *Nucl. Phys.* **9**, 3091 (1959); **20**, 275 (1960).

22. S. Y. Larsen, in: **Few-Body Methods: Principles and Applications**, eds. T. K. Lim, C. G. Bao, D. P. Hou, and S. Huber (World Scientific Pub., Singapore, 1986); and references therein.

23. F. T. Smith, *J. Math. Phys.* **3**, 735 (1962); R. C. Whitten and F. T. Smith, *J. Math. Phys.* **9**, 1103 (1968).

24. W. Zickendraht, *Ann. Phys.* **35**, 18 (1965).

25. V. D. Éfros, *Soviet J. Nucl. Phys.* **13**, 758 (1971).

26. E. Arribas, J. Navarro, and M. Fabre de la Ripelle, *J. Math. Phys.* **24**, 1992 (1983).

27. Yu. A. Simonov, *Soviet J. Nucl. Phys.* **3**, 461 (1966); A. M. Badalyan and Yu. A. Simonov, *Soviet J. Nucl. Phys.* **3**, 755 (1966).

28. J. Nyiri and Ya. A. Smorodinskii, *Soviet J. Nucl. Phys.* **9**, 515 (1969); **12**, 109 (1971); **29**, 429 (1979).

29. D. L. Knirk, *J. Chem. Phys.* **60**, 66 (1974); 760 (1974); *Phys. Rev. Lett.* **32**, 651 (1974).

30. Yu. F. Smirnov and K. V. Shitikova, *Soviet J. Particles Nucl.* **8**, 344 (1977).

31. J. Römelt, *Chem. Phys.* **79**, 197 (1983); in: **The Theory of Chemical Reaction Dynamics**, ed. D. C. Clary (D. Reidel Publishing, Dordrecht,1986) pp.77,104; and references therein.

32. J. Manz, *Comments At. Mol. Phys.* **17**, 91 (1985).

33. A. Kuppermann and J. P. Dwyer, in: **Electronic and Atomic Collisions, Abstracts of Contributed Papers,** *11th International Conference on the Physics of Electronic and Atomic Collisions, Kyoto, Japan* (The Society for Atomic Collision Research, Tokyo, 1979) pp. 888,889; A. Kuppermann, in: **Potential Energy Surface and Dynamics Calculations**, ed. D. G. Truhlar (Plenum Press, New York, 1981) pp. 405,414.

34. J. Römelt, *Chem. Phys.* **79**, 197 (1983); J. Römelt and E. Pollak, in: **Resonances in Electron Molecule Scattering, van der Waals Complexes and Reactive Chemical Reactions**, ed. D. G. Truhlar (Plenum Press, 1984) p. 353.

35. R. T. Pack, *Chem. Phys. Lett.* **108**, 333 (1984).

36. C. A. Mead, *J. Chem. Phys.* **72**, 3839 (1980).

37. L. Wolniewicz and J. Hinze, *J. Chem. Phys.* **85**, 2012 (1986).

38. B. R. Johnson, *J. Chem. Phys.* **73**, 5051 (1980); **79**, 1906 (1983); 1916 (1983).

39. D. Jepson and J. O. Hirschfelder, *Proc. Nat. Acad. Sci.* **45**, 249 (1959); C. F. Curtiss, J. O. Hirschfelder, and F. T. Alder, *J. Chem. Phys.* **18**, 1638 (1950).

40. A. S. Davydov, **Quantum Mechanics 2nd ed.** (Pergamon Press, Oxford, 1976) pp. 167,178. All references to Euler angles and Wigner rotation matrices are based on the conventions in Davydov.

41. L. D. Landau and E. M. Lifshitz, **Quantum Mechanics, 3rd ed.** (Pergamon Press, Oxford, 1977) p. 416.

42. The expressions for $\hat{J}^2$ given in Schatz and Kuppermann[6] and in Davydov[40] contain typographical errors.

43. G. Dhatt and G. Touzot, **The Finite Element Method Displayed** (Wiley, New York, 1984).

44. K. Bathe, **Finite Element Procedures in Engineering Analysis** (Prentice-Hall, Englewood Cliffs, 1982) pp. 672,695.

45. G. H. Golub and C. F. Van Loan, **Matrix Computations** (Johns Hopkins Univ. Press, Baltimore, Maryland, 1985) pp. 322,341.

46. E. Wigner, **Group Theory**, (Academic Press, New York, 1959).

47. The group property of the Wigner rotation matrices as expressed in the notation of Davydov[40] is the transpose of the more familiar group property. As a consequence, equation 43.18 on page 171 of reference 40 is wrong.

48. B. Liu, *J. Chem. Phys.* **58**, 1925 (1973); P. Siegbahn and B. Liu, *J. Chem. Phys.* **68**, 2457 (1978).

49. D. G. Truhlar and C. J. Horowitz, *J. Chem. Phys.* **68**, 2468 (1978); **71**, 1514 (1979).

50. M. Baer, *J. Chem. Phys.* **62**, 305 (1975).

51. A. Kuppermann, in: **Theoretical Chemistry-Theory of Scattering: Papers in Honor of Henry Eyring**, ed. D. Henderson (Academic Press, New York, 1981) pp. 79,122.

52. J. A. Kaye and A. Kuppermann, *Chem. Phys. Lett.* **78**, 546 (1981).

Figure Captions

Figure 1. North pole view of the potential energy contours from the LSTH potential energy surface at $\rho = 6.$ bohr. The mapping is defined by equations (99) and (100) in section 10.B. The interval between successive contours is 0.5 eV and some contours are labeled. The energy units are eV.

Figure 2. South pole view of the LSTH potential energy surface contours at $\rho = 6$ bohr. See the caption to figure 1 for details.

Figure 3. Equatorial view of the LSTH potential energy surface contours at $\rho = 6$ bohr. See the caption to figure 1 for details.

Figure 4. Equatorial view of the LSTH potential energy surface contours at $\rho = 2$ bohr. See the caption of figure 1 for details.

Figure 5. Potential energy contours from the LSTH potential energy surface at $\rho = 3.270145$ bohr. See caption for figure 2 for other details.

Figure 6. The constant hyperradius hemispherical surface on which the two-angle surface functions depend as seen in the equatorial projection. The domain D is the entire hemisphere shown in the figure. The minimal subdomain d is the region bounded by the heavy lines. An arbitrary point P with angular coordinates $(\omega_\lambda, \gamma_\lambda)$ is indicated in the figure. The meshed part of the minimal subdomain d is the finite element decomposition with 20 ω_λ and 20 γ_λ points. The boundaries B_1, B_2, and B_3 represent half-planes.

Figure 7. $J = 0$, A_1 surface functions eigenvalues $\epsilon_n(\rho)$ as a function of ρ. The energies are in eV and the distances are in bohr. The eigenvalues are calculated every 0.1 bohr.

Figure 8. $J = 0$, A_2 surface function eigenvalues as a function of ρ. See figure 5 for details.

Figure 9. $J = 0$, E surface function eigenvalues as a function of ρ. See figure 5 for details.

Figure 10. Contour plots of $J = 0$ surface function amplitudes at $\rho = 6$ bohr. Next to each panel the irreducible representation, the surface function energy and

contour interval δ are given for that panel. The contours are given in general by $0, \pm 0.1, \pm(0.1+\delta), \pm(0.1+2\delta), \ldots$. The darker contours represent the nodal lines or zeros of the function. The solid lines represent positive function values and the dashed lines represent negative function values. Separating the solid and dashed lines are the bold nodal lines. (a) The lowest energy A_1 surface function. (b) The lowest energy surface function which transfroms as row 1 of E which we indicate by E(1). (c) The lowest energy surface function which transforms as row 2 of E which we indicate by E(2). (d) The lowest energy A_2 surface function. (e) The first excited surface function which transforms as row 1 of E. (f) The first excited surface function which transforms as row 2 of E.

Figure 11. Contour plots of $J = 0$ surface function amplitudes at $\rho = 2$ bohr. The innermost two contours have a common value of 1.3. See caption to figure 10 for other details.

Figure 12. Contours plots of $J = 0$ surface function amplitudes at $\rho = 3.270145$ bohr. See caption to figure 10 for details.

Figure 13. $J = 0$, A_1 surface function probability density contours for the lowest energy surface function at $\rho = 2.$ bohr (solid lines). The potential energy contour corresponding to the surface function energy which is 3.199 eV is shown as dashed lines.

Figure 14. $J = 0$, A_1 surface function probability density contours for the lowest energy surface function at $\rho = 3.270145$ bohr (solid lines). The potential energy contour corresponding to the surface function energy which is 0.5686 eV is shown as dashed lines.

Figure 15. $J = 0$, A_1 surface function probability density contours for the lowest energy surface function at $\rho = 6.$ bohr (solid lines). The potential energy contour corresponding to the surface function energy which is 0.2666 eV is shown as dashed lines.

Figure 16. $J = 0$, E surface function amplitudes at three values of ρ for the $n = 3$ level. Dashed lines indicate negative amplitudes, solid lines indicate positive

amplitudes, and the bold solid lines represent the nodal lines. The contour values are given by $0, \pm 0.1, \pm(0.1+\delta), \pm(0.1+2\delta), \ldots$, where the δ used in each panel is given next to that panel. The left column is the first row of the E representation, indicated by E(1). The right column is the second row of E, indicated by E(2). E(1) and E(2) are degenerate and one energy is associated with each pair of contour plots. This energy being given in the space between the degenerate pairs. Panels (a) and (d) show the $n = 3$ degenerate pair at $\rho = 2.$ bohr. Panels (b) and (e) show the $n = 3$ degenerate pair at $\rho = 3.270145$ bohr. Panels (c) and (f) show the $n = 3$ degenerate pair at $\rho = 6.$ bohr.

Figure 17. $J = 0$, E surface function amplitudes at three values of ρ for the $n = 4$ level. For details, see the caption to figure 16.

Figure 18. $J = 0$, E surface function amplitudes at three values of ρ for the $n = 9$ level. For details, see the caption to figure 16.

Figure 19. $J = 0$, E surface function amplitudes at three values of ρ for the $n = 10$ level. For details, see the caption to figure 16.

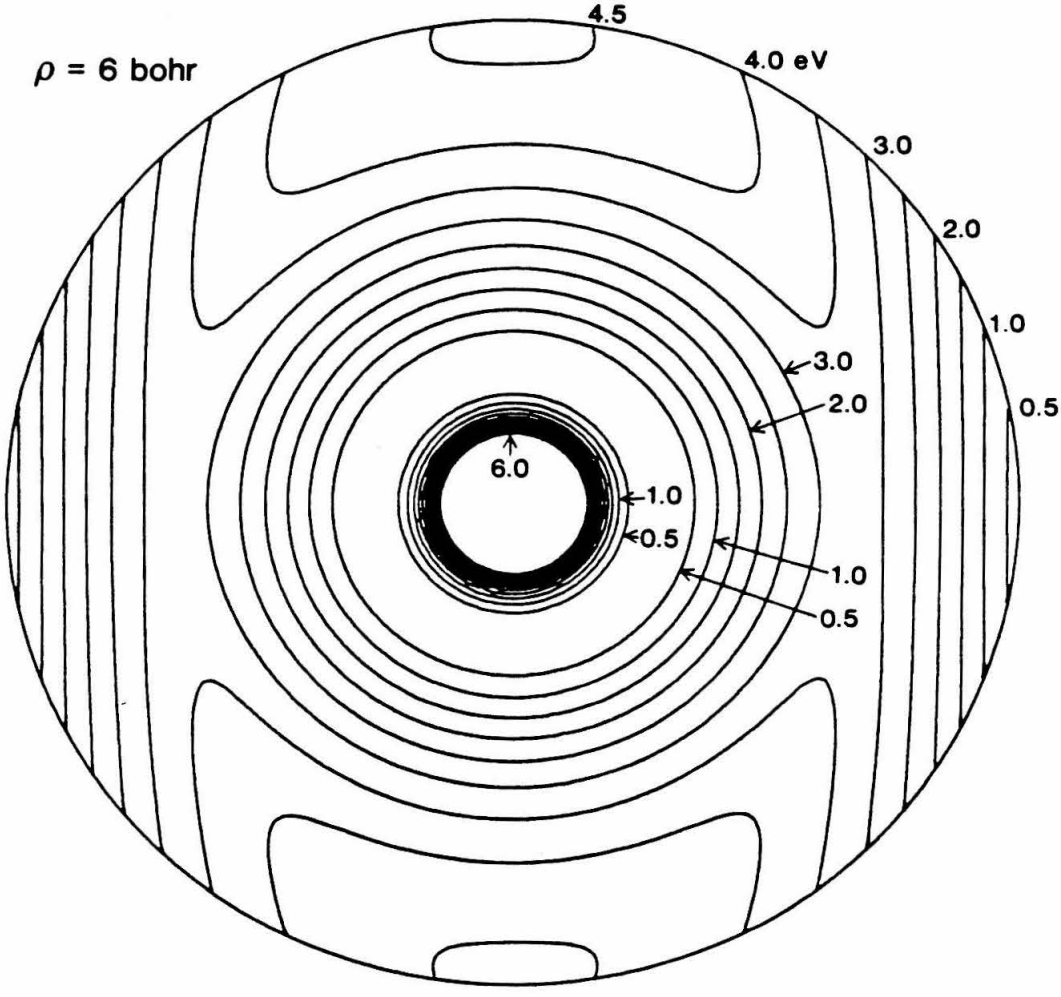

Figure 1

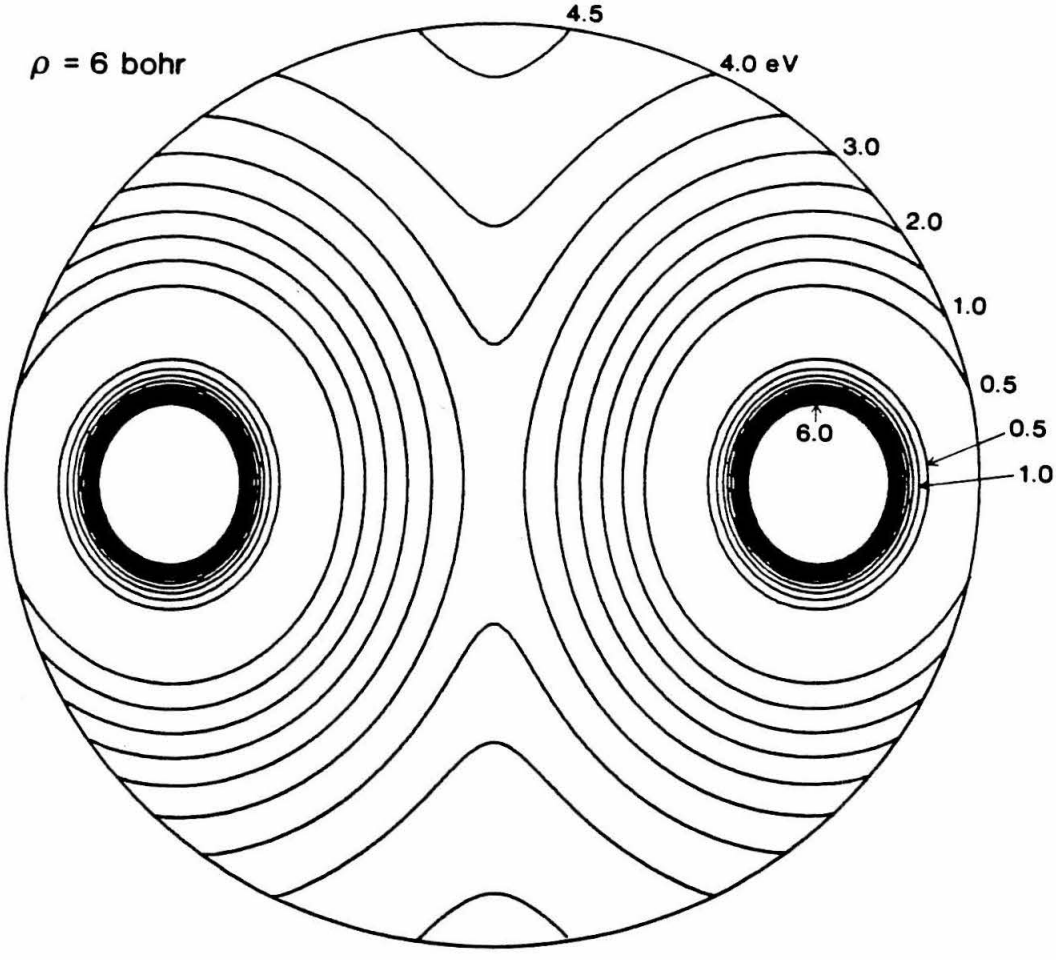

Figure 2

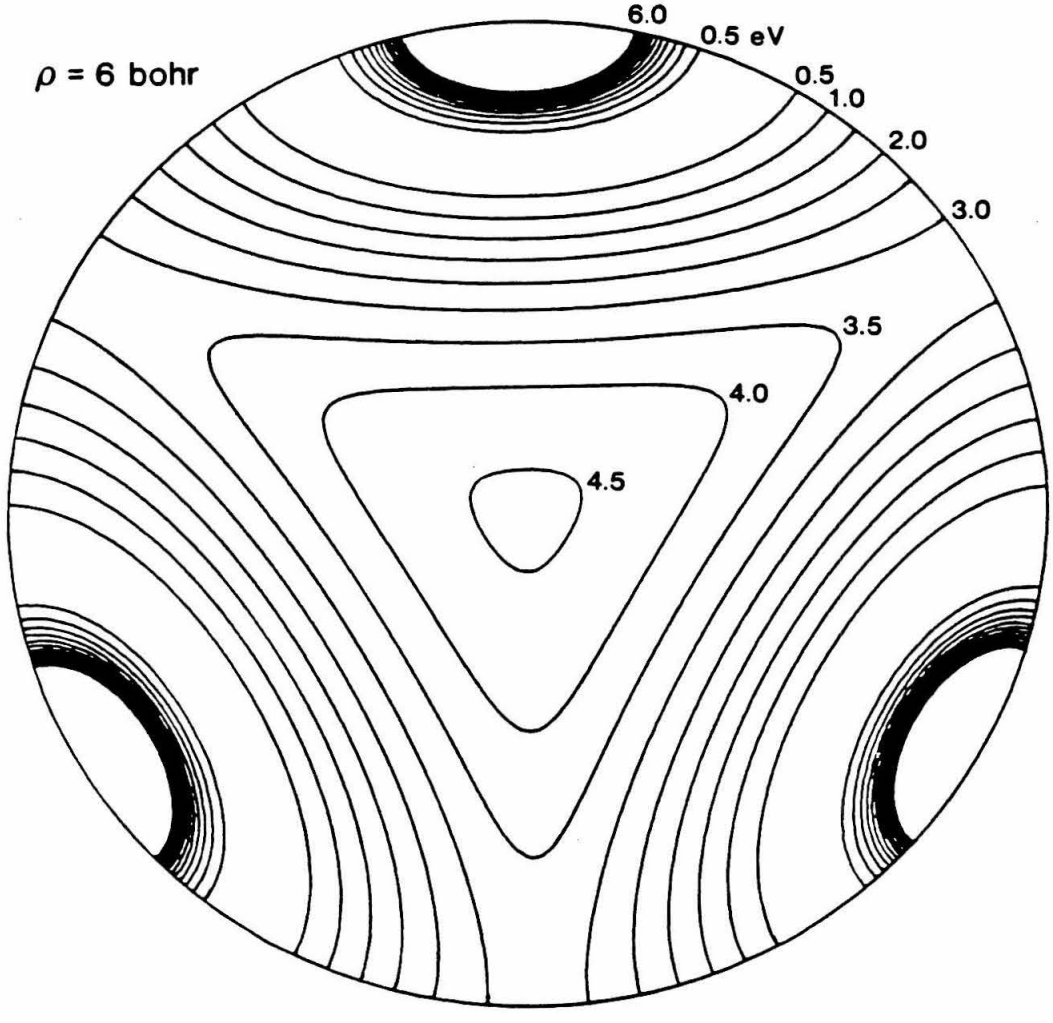

Figure 3

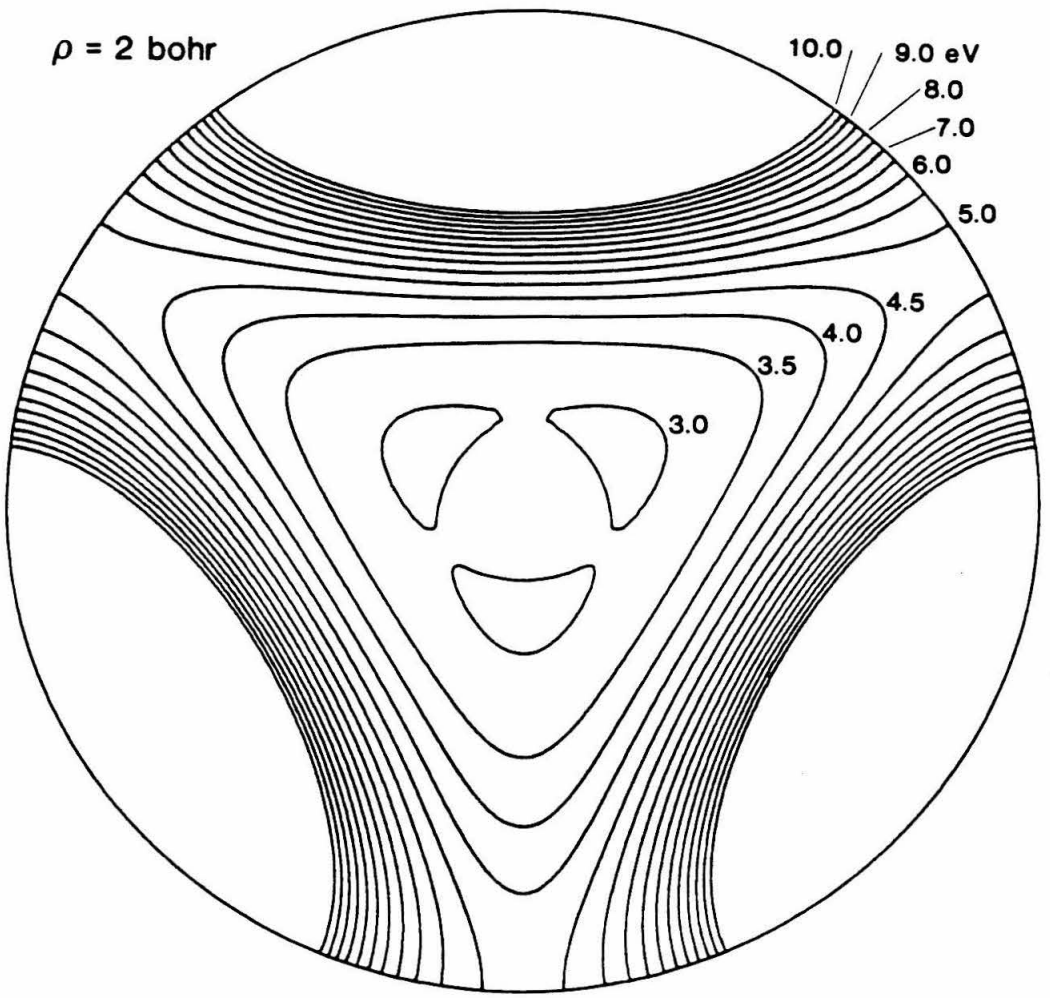

Figure 4

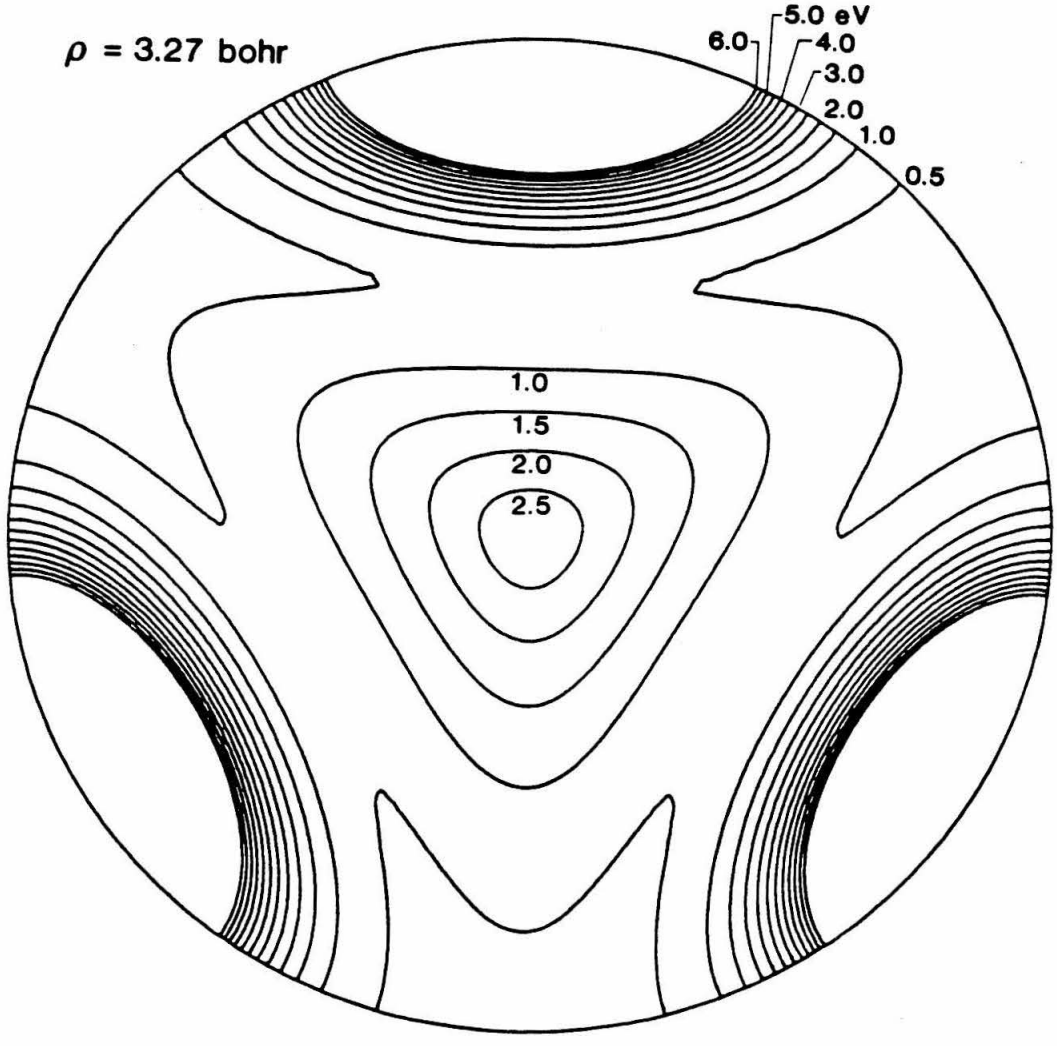

Figure 5

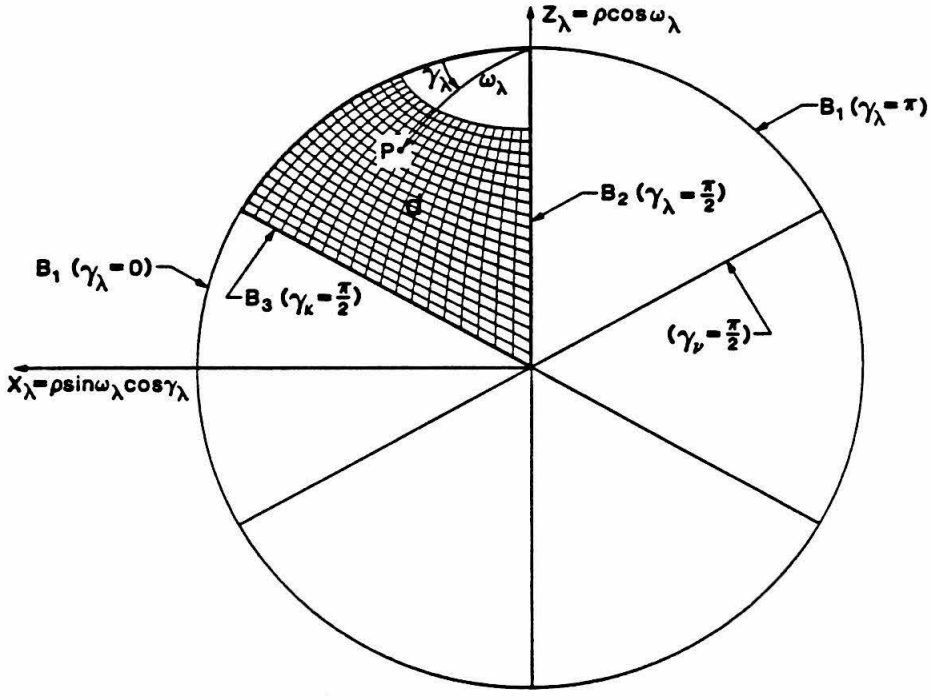
$Z_\lambda = \rho\cos\omega_\lambda$
γ_λ
ω_λ
P
$B_1\ (\gamma_\lambda = \pi)$
$B_2\ (\gamma_\lambda = \frac{\pi}{2})$
$B_1\ (\gamma_\lambda = 0)$
$B_3\ (\gamma_\kappa = \frac{\pi}{2})$
$(\gamma_\nu = \frac{\pi}{2})$
$X_\lambda = \rho\sin\omega_\lambda\cos\gamma_\lambda$

Figure 6

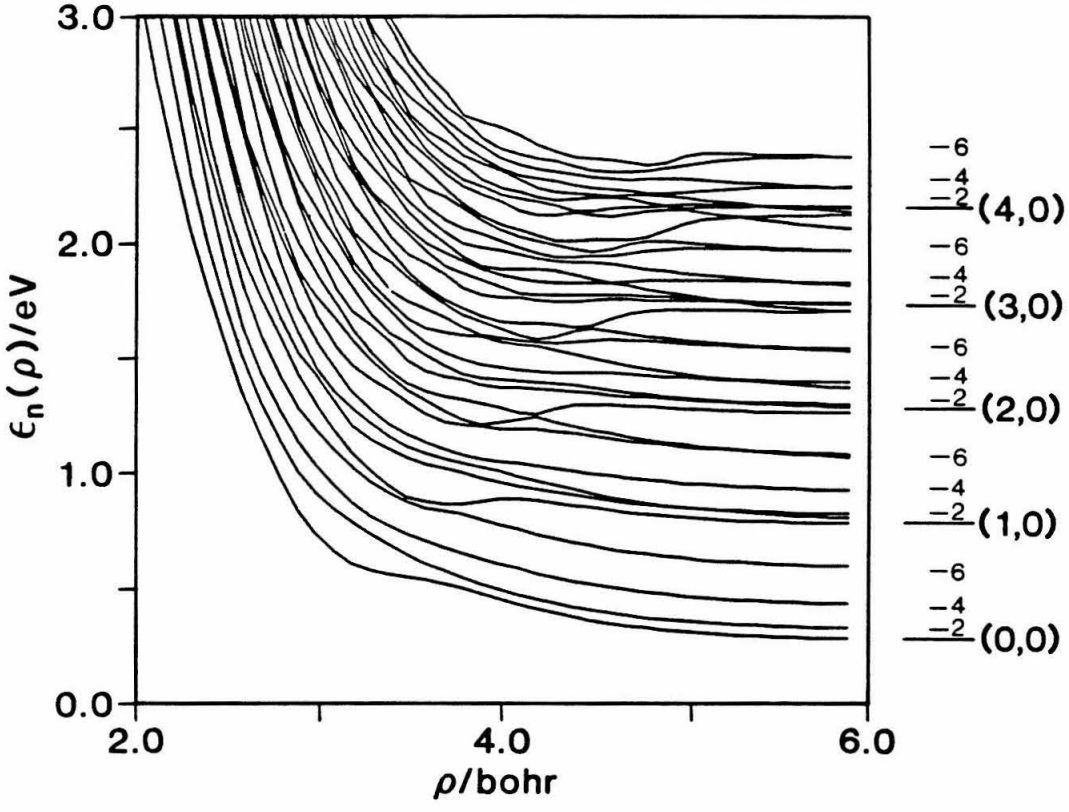
3.0
2.0
1.0
0.0
$\epsilon_n(\rho)$/eV
2.0
4.0
6.0
ρ/bohr
−6
−4
−2
(4,0)
−6
−4
−2
(3,0)
−6
−4
−2
(2,0)
−6
−4
−2
(1,0)
−6
−4
−2
(0,0)

Figure 7

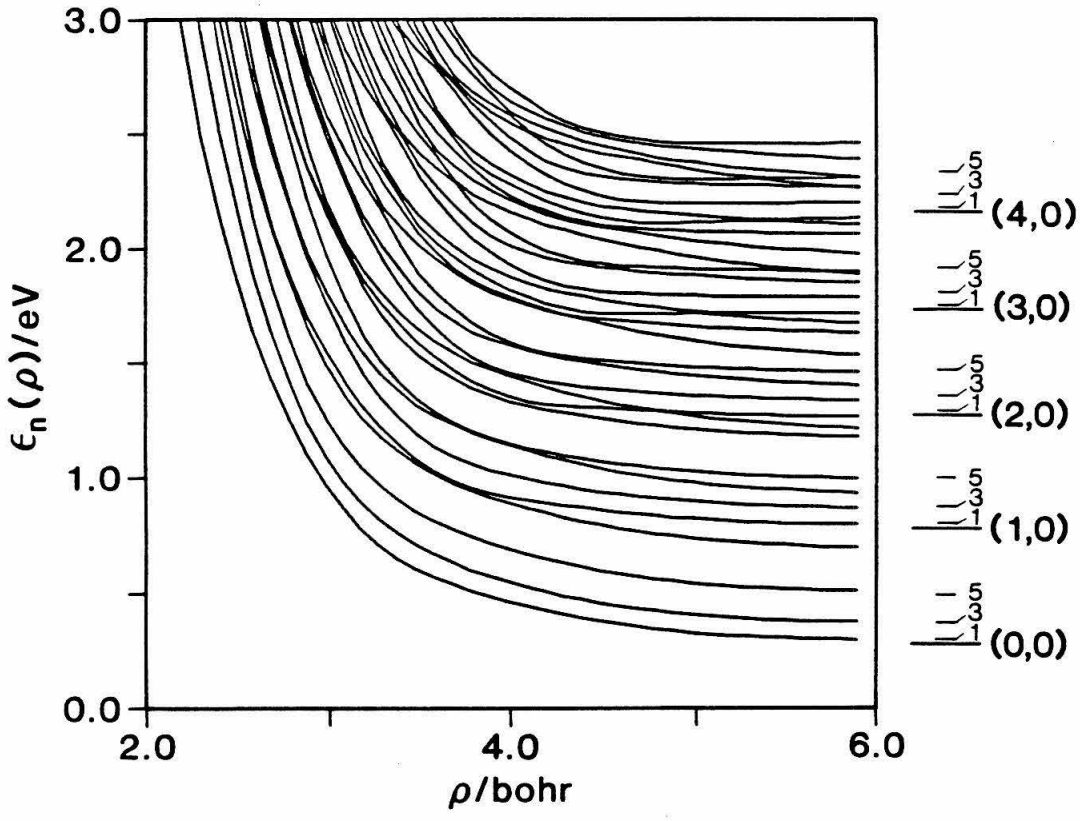

Figure 8

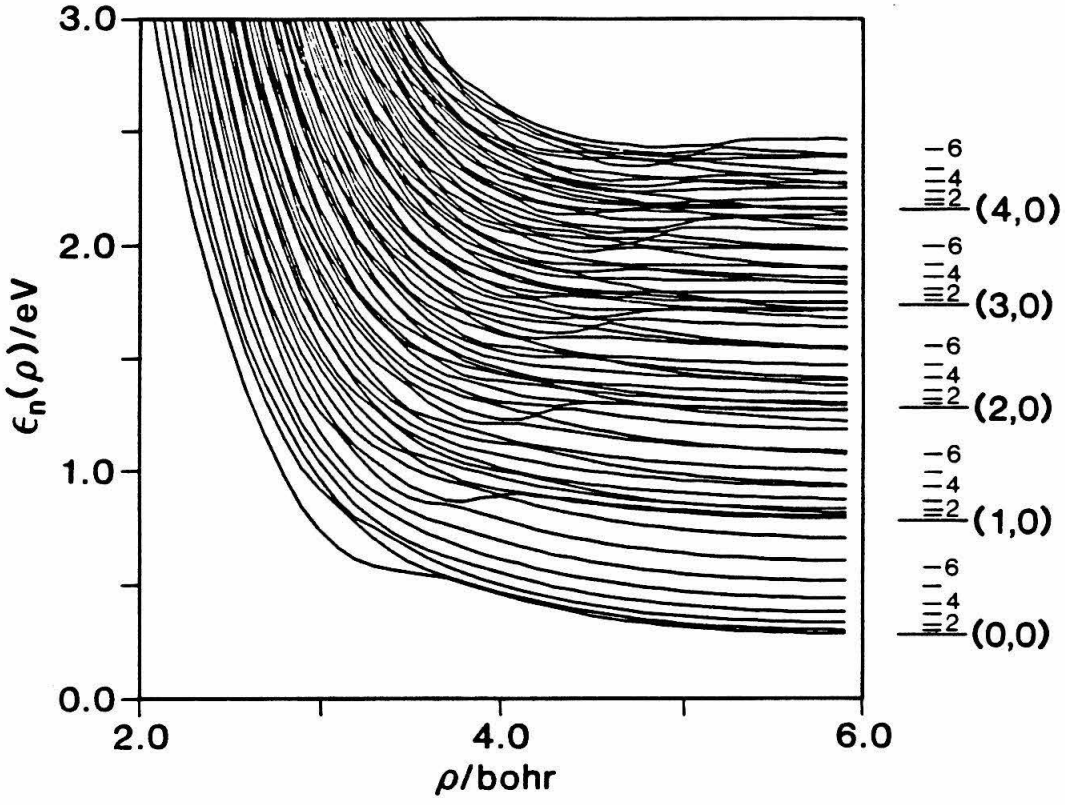

Figure 9

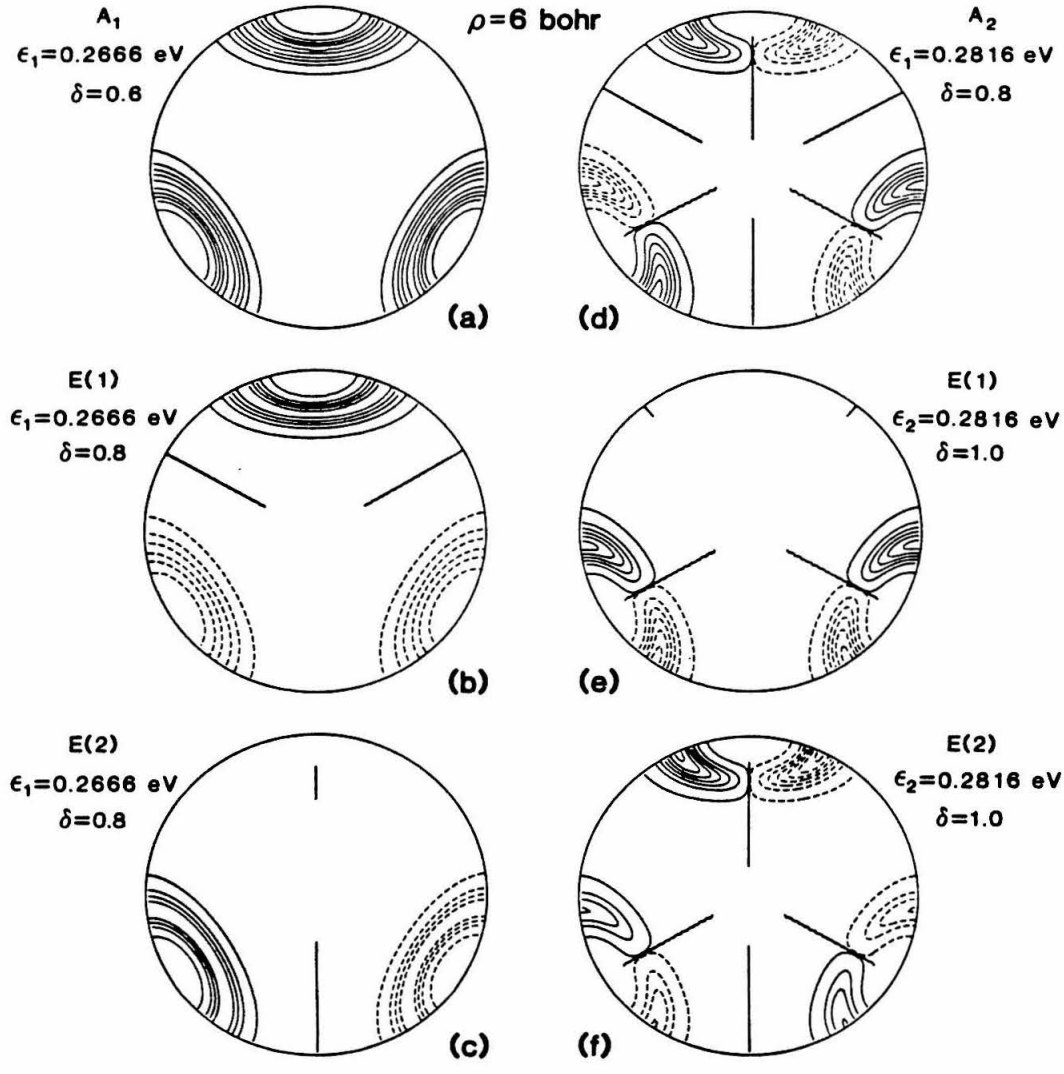
A1
ϵ1=0.2666 eV
δ=0.6
ρ=6 bohr
A2
ϵ1=0.2816 eV
δ=0.8
(a)
(d)
E(1)
ϵ1=0.2666 eV
δ=0.8
E(1)
ϵ2=0.2816 eV
δ=1.0
(b)
(e)
E(2)
ϵ1=0.2666 eV
δ=0.8
E(2)
ϵ2=0.2816 eV
δ=1.0
(c)
(f)

Figure 10

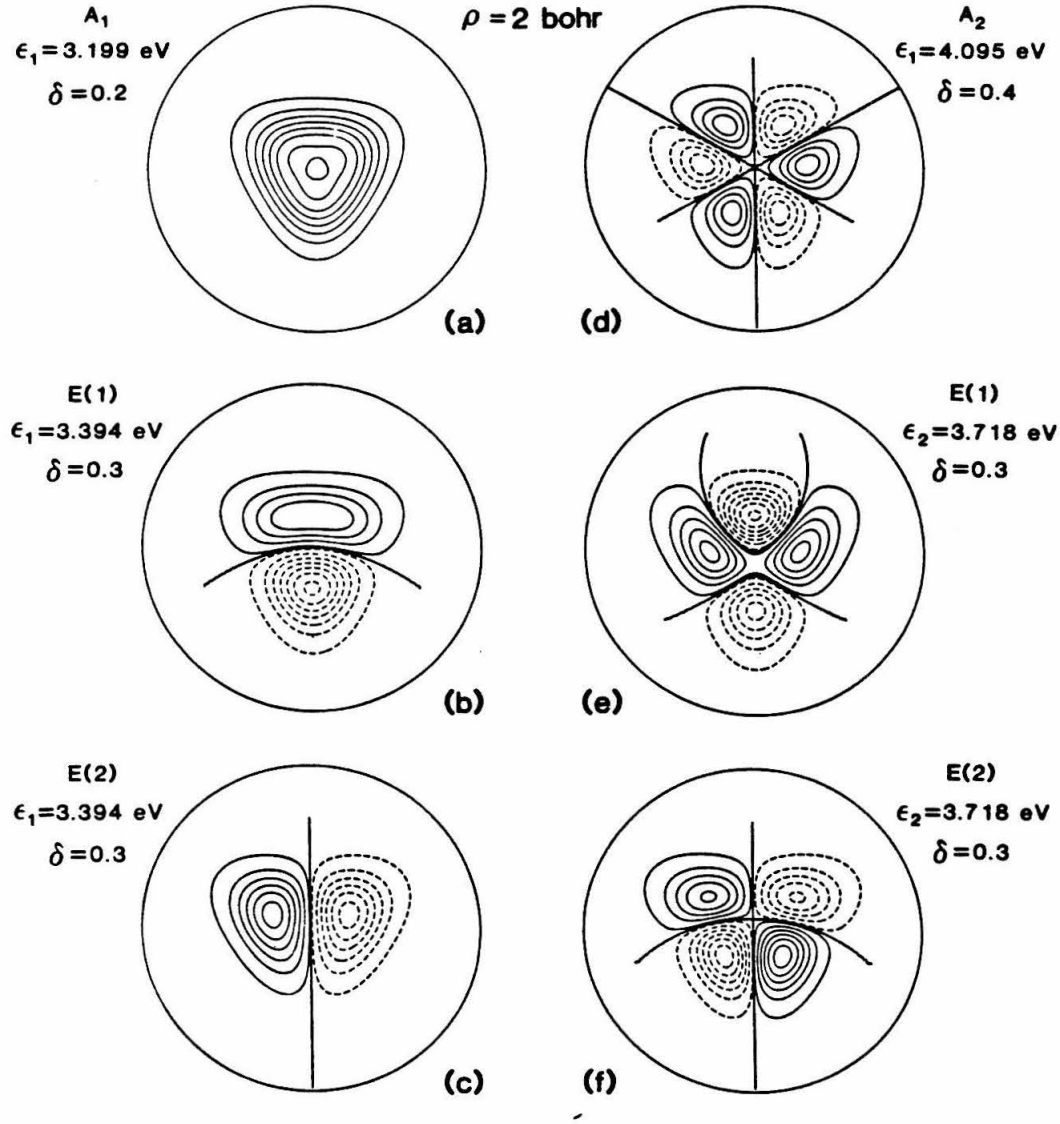
A1
ϵ1=3.199 eV
δ=0.2
ρ=2 bohr
A2
ϵ1=4.095 eV
δ=0.4
(a)
(d)
E(1)
ϵ1=3.394 eV
δ=0.3
E(1)
ϵ2=3.718 eV
δ=0.3
(b)
(e)
E(2)
ϵ1=3.394 eV
δ=0.3
E(2)
ϵ2=3.718 eV
δ=0.3
(c)
(f)

Figure 11

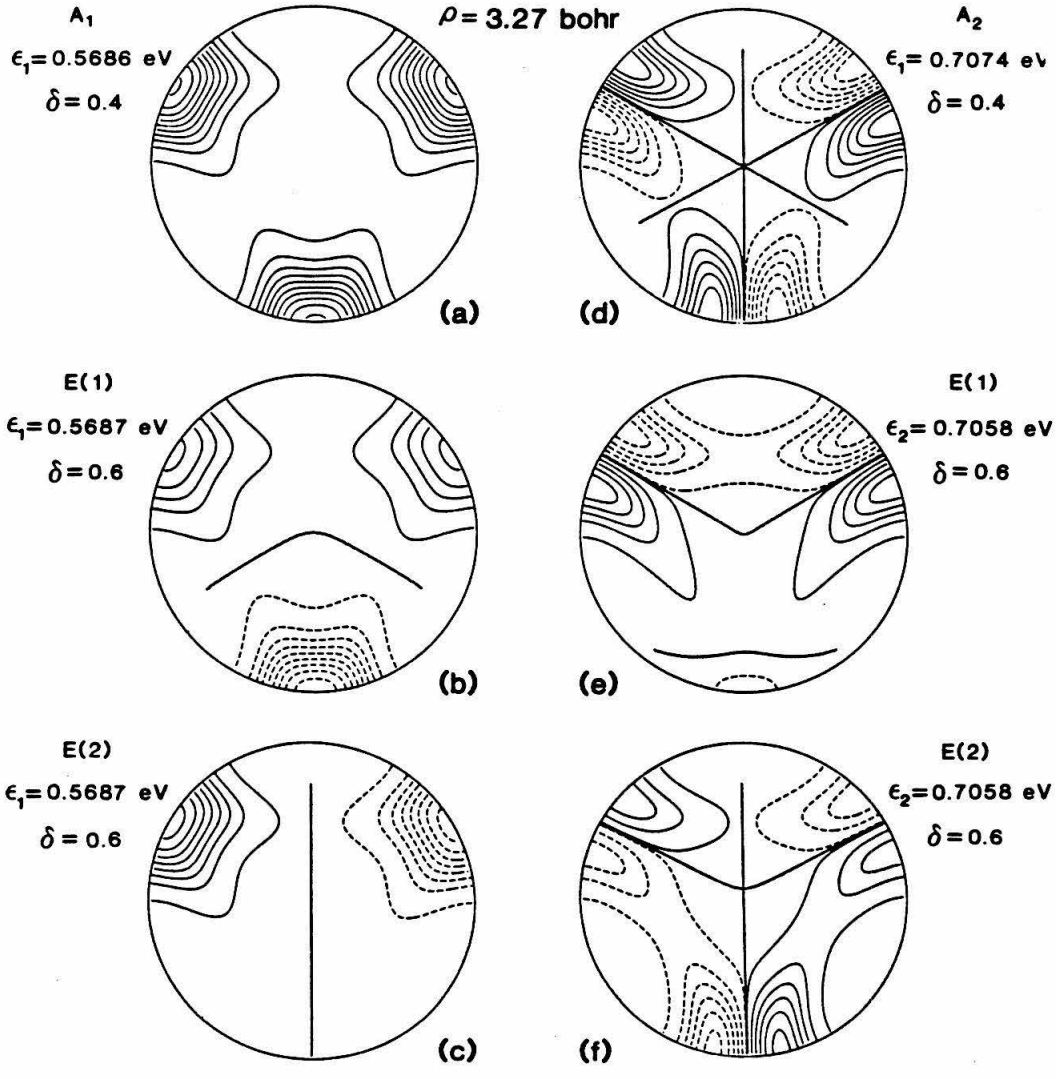
A1
ϵ1= 0.5686 eV
δ = 0.4
ρ = 3.27 bohr
(a)
A2
ϵ1= 0.7074 eV
δ = 0.4
(d)
E(1)
ϵ1= 0.5687 eV
δ = 0.6
(b)
E(1)
ϵ2= 0.7058 eV
δ = 0.6
(e)
E(2)
ϵ1= 0.5687 eV
δ = 0.6
(c)
E(2)
ϵ2= 0.7058 eV
δ = 0.6
(f)

Figure 12

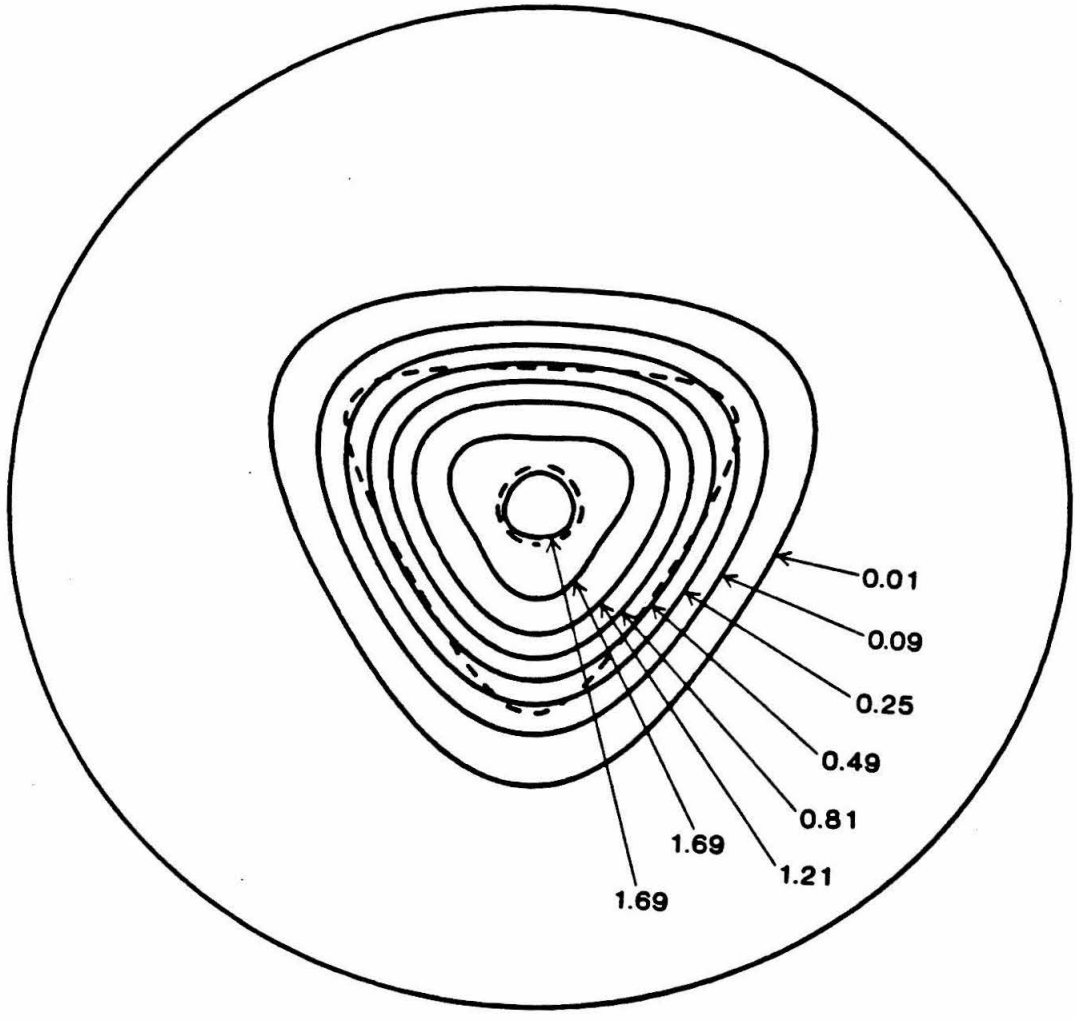

Figure 13

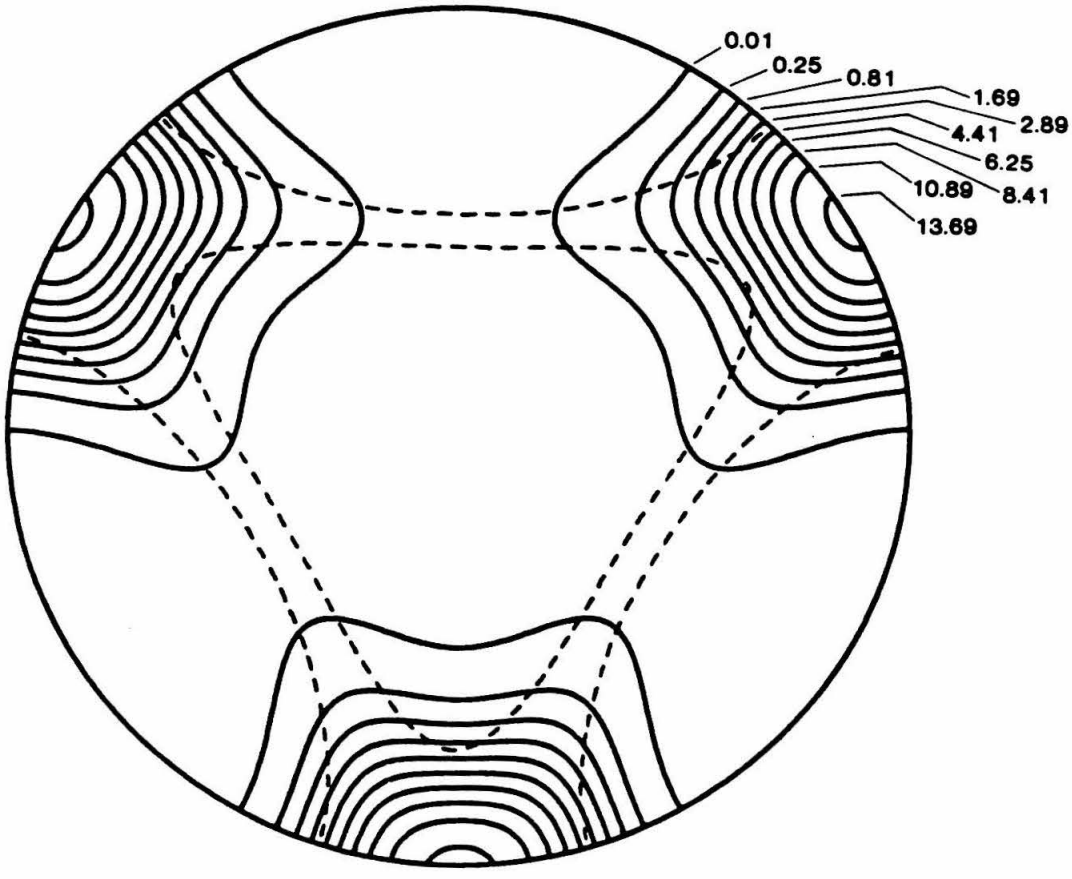

Figure 14

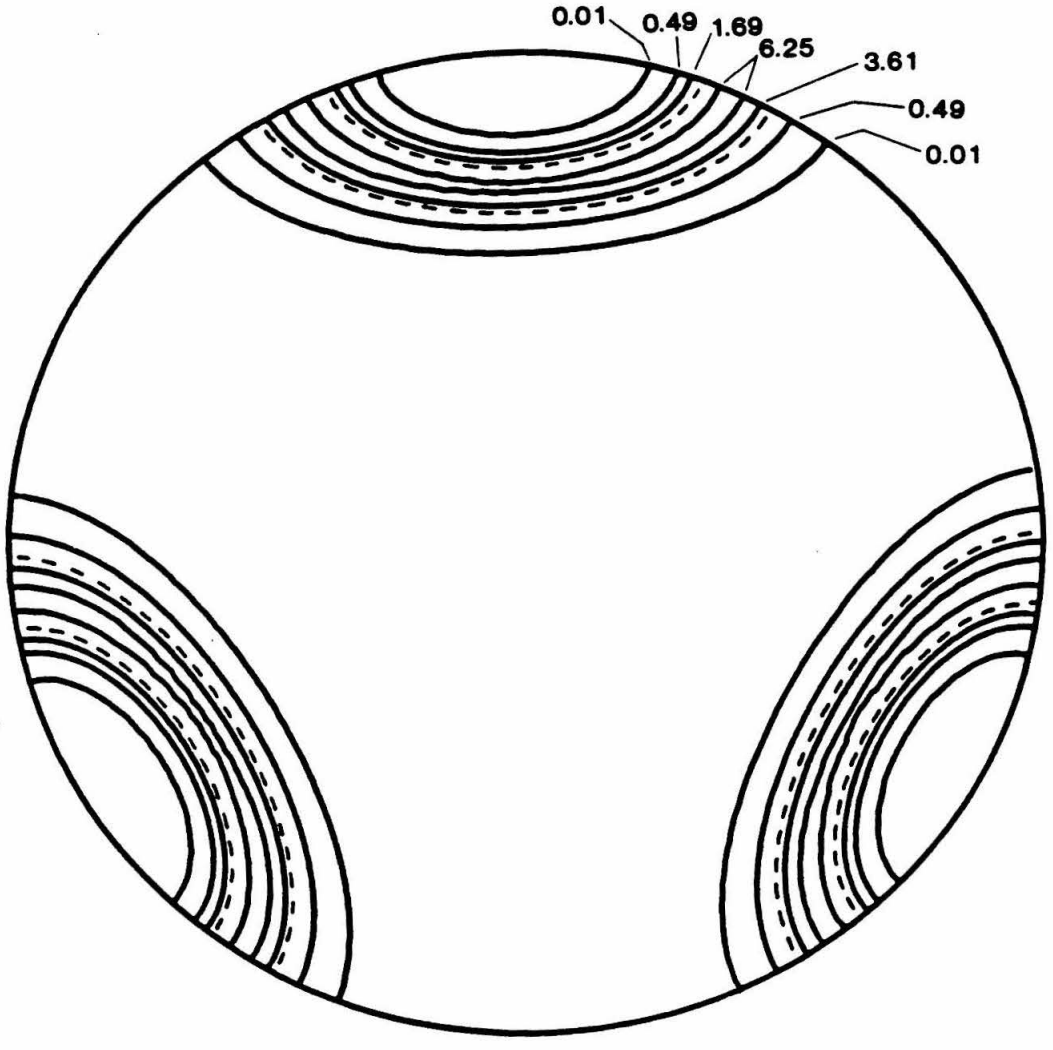

Figure 15

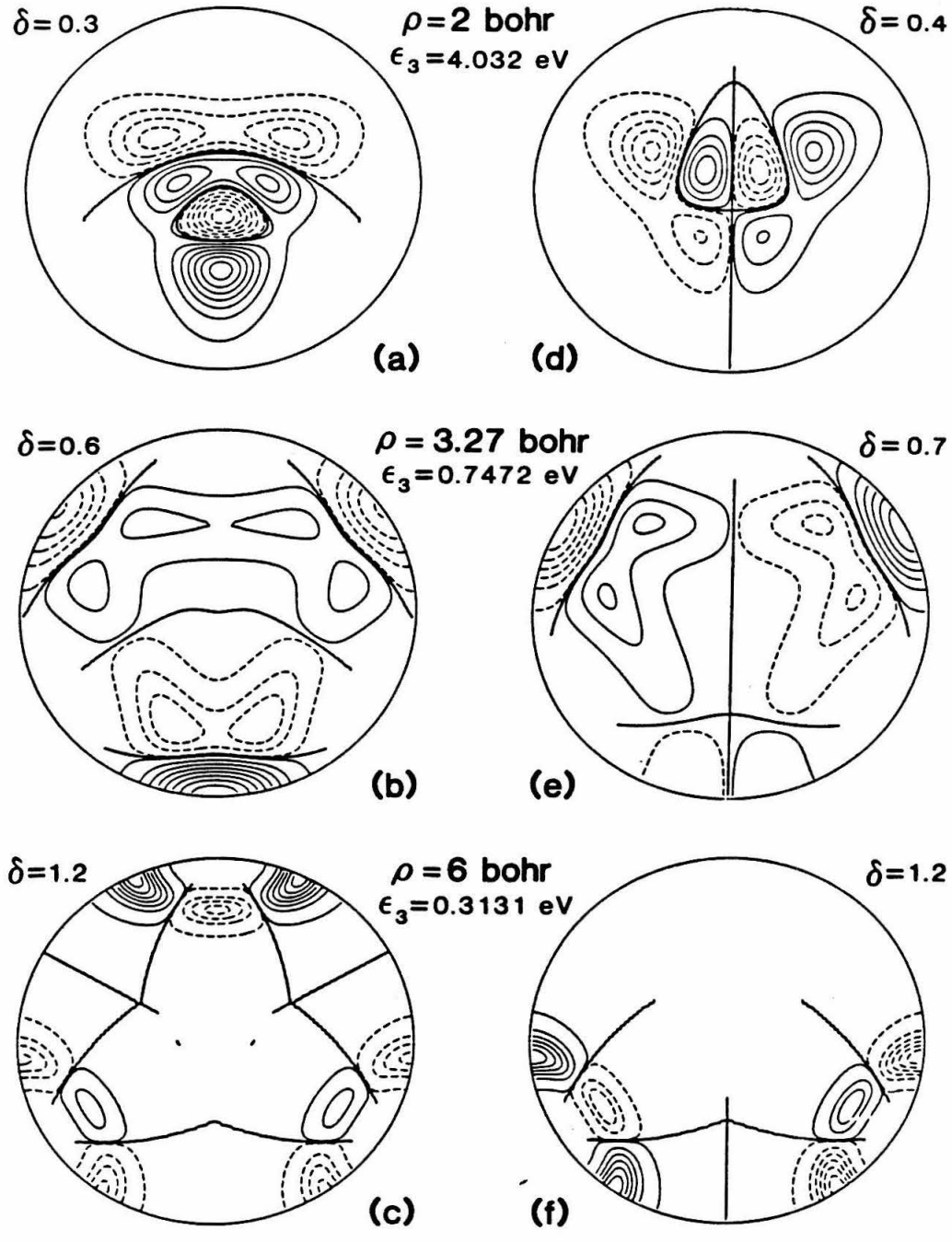
δ=0.3
ρ=2 bohr
ε3=4.032 eV
δ=0.4
(a)
(d)
δ=0.6
ρ=3.27 bohr
ε3=0.7472 eV
δ=0.7
(b)
(e)
δ=1.2
ρ=6 bohr
ε3=0.3131 eV
δ=1.2
(c)
(f)

Figure 16

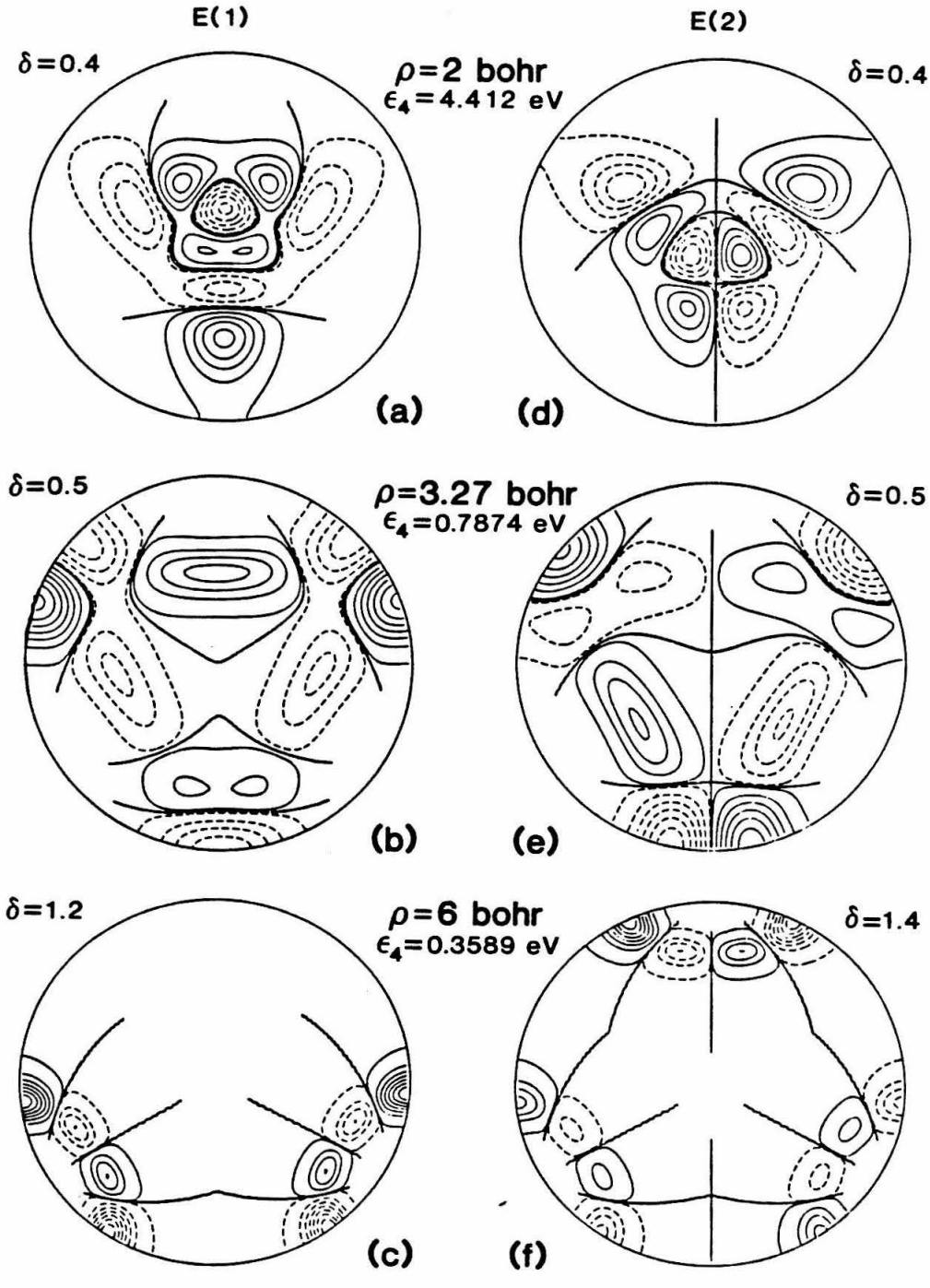
E(1)
E(2)
δ=0.4
ρ=2 bohr
ϵ4=4.412 eV
δ=0.4
(a)
(d)
δ=0.5
ρ=3.27 bohr
ϵ4=0.7874 eV
δ=0.5
(b)
(e)
δ=1.2
ρ=6 bohr
ϵ4=0.3589 eV
δ=1.4
(c)
(f)

Figure 17

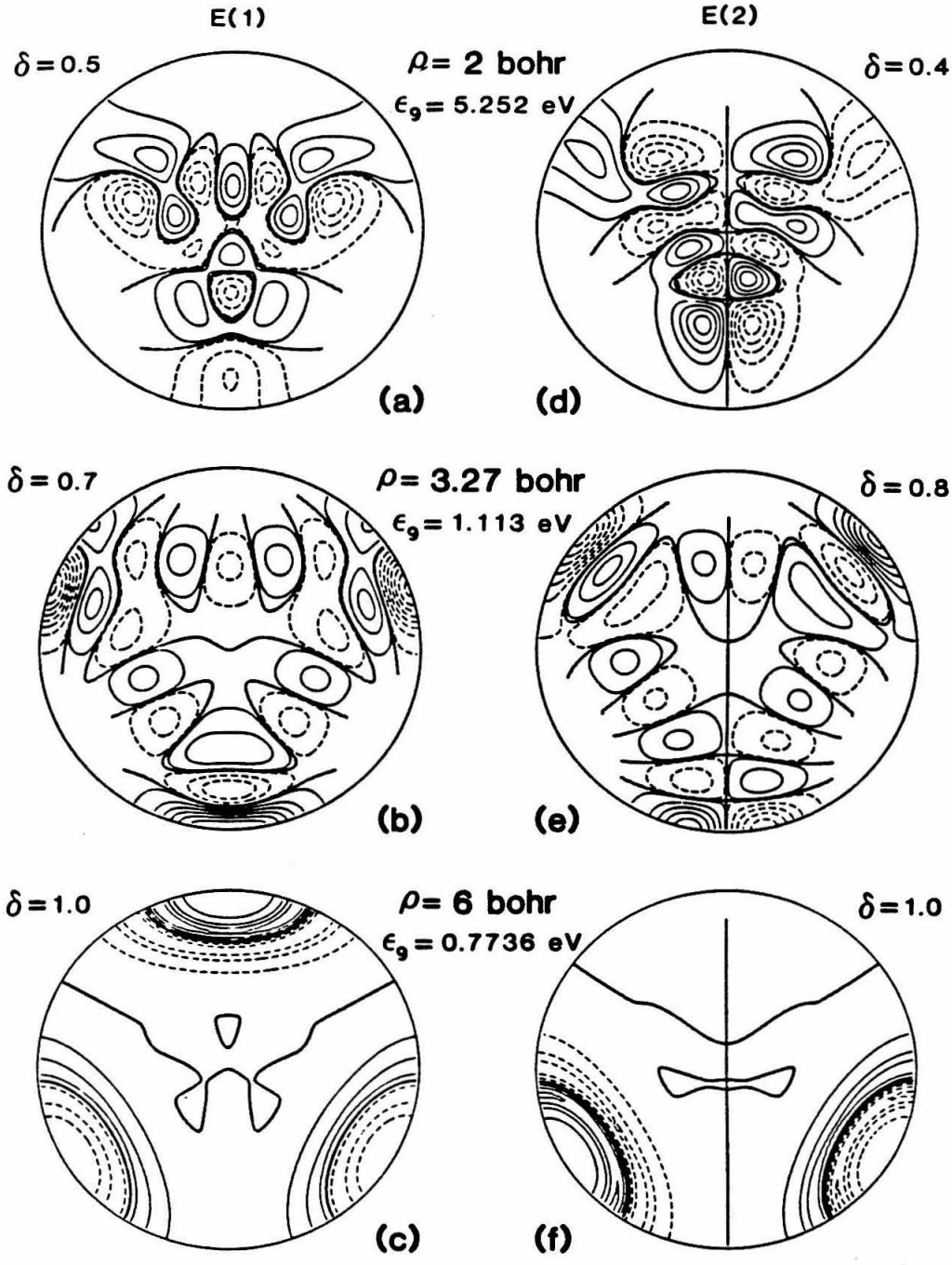
E(1)
E(2)
δ = 0.5
ρ = 2 bohr
ε9 = 5.252 eV
δ = 0.4
(a)
(d)
δ = 0.7
ρ = 3.27 bohr
ε9 = 1.113 eV
δ = 0.8
(b)
(e)
δ = 1.0
ρ = 6 bohr
ε9 = 0.7736 eV
δ = 1.0
(c)
(f)

Figure 18

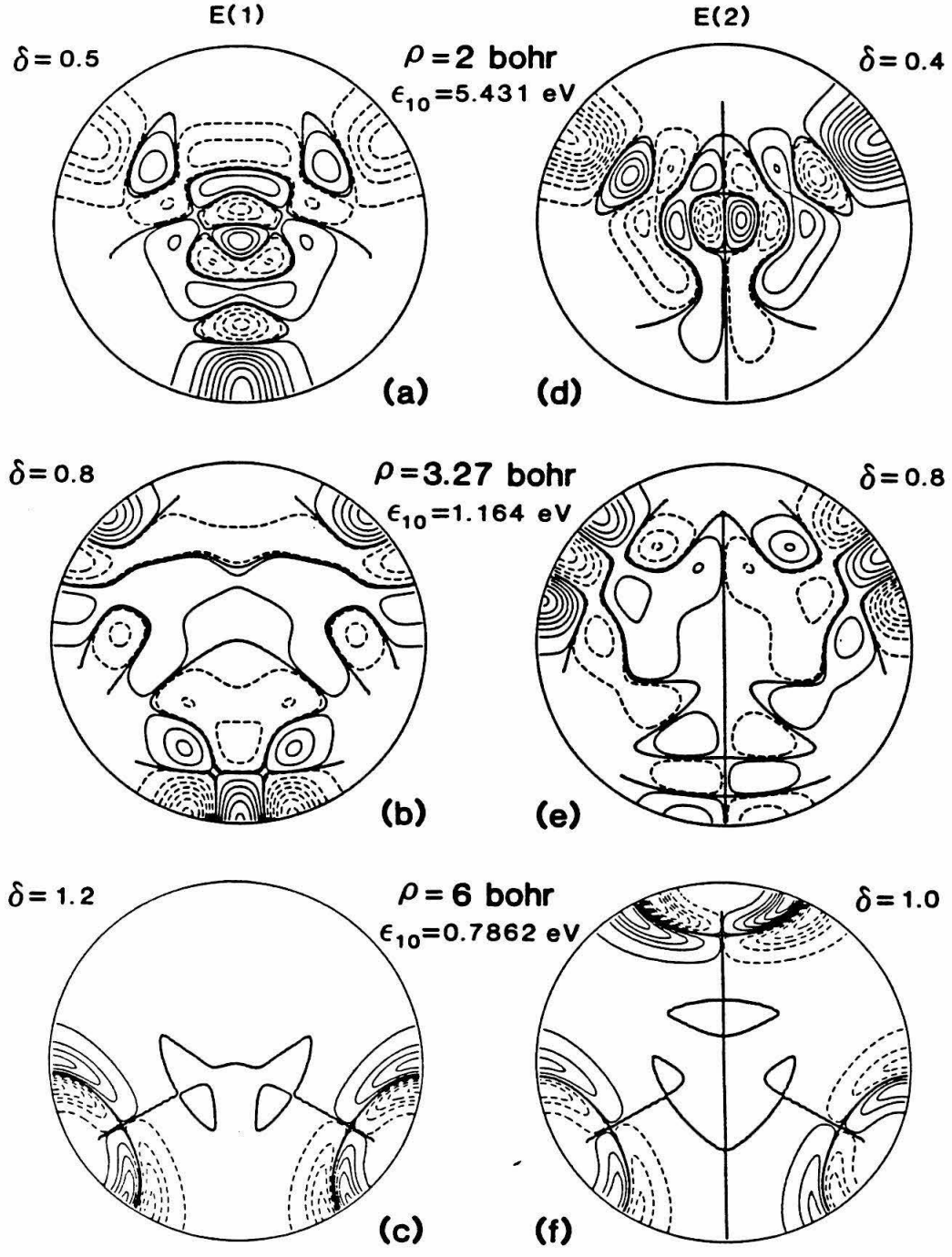
E(1)
E(2)
δ = 0.5
ρ = 2 bohr
ε10 = 5.431 eV
δ = 0.4
(a)
(d)
δ = 0.8
ρ = 3.27 bohr
ε10 = 1.164 eV
δ = 0.8
(b)
(e)
δ = 1.2
ρ = 6 bohr
ε10 = 0.7862 eV
δ = 1.0
(c)
(f)

Figure 19

Three-dimensional quantum mechanical reactive scattering using symmetrized hyperspherical coordinates[a)]

Aron Kuppermann and Paul G. Hipes[b)]
Arthur Amos Noyes Laboratory of Chemical Physics, Division of Chemistry and Chemical Engineering,[c)] California Institute of Technology, Pasadena, California 91125

(Received 20 February 1986; accepted 7 March 1986)

We report here the first three-dimensional (3D) reactive scattering calculations using symmetrized hyperspherical coordinates (SHC). They show that the 3D local hyperspherical surface function basis set leads to a very efficient computational scheme which should permit accurate reactive scattering calculations to be performed for a significantly larger number of systems than has heretofore been possible.

Approximately ten years ago the first accurate differential[1] and integral[1-3] cross section calculations for the 3D $H + H_2$ exchange reaction were reported. One of the methods[1] involved matching the solutions of the Schrödinger equation obtained for each of the three arrangement channel regions across half-planes in an internal configuration space separating those regions. The application of this method to less symmetric systems requires an excessive number of channels for satisfactory convergence. There have been no accurate 3D reactive scattering cross section calculations, involving competition among three arrangement channels,[4] reported since.

At about the same time, a system of SHC was developed.[5] Their usefulness in performing accurate and approximate 3D reactive scattering calculations was suggested,[5] and an appropriate computation methodology was outlined.[6] These coordinates are related to others introduced previously,[7] and are defined as follows. Let A, B, and C be three atoms, and $\mathbf{R}_\alpha$ and $\mathbf{r}_\alpha$ the mass scaled[8] vectors from the center of mass of BC to A and from B to C. We now define the hyperradius $\rho = (R_\alpha^2 + r_\alpha^2)^{1/2}$ and the hyperangle $\omega_\alpha = 2\tan^{-1}(r_\alpha/R_\alpha)$ in the 0 to π range. The factor of 2 in this definition is very important for symmetrizing the coordinates.[5] The body-fixed SHC are ρ, ω_α, θ_α, ϕ_α, γ_α, and ψ_α, where θ_α, ϕ_α are the space-fixed polar angles of $\mathbf{R}_\alpha$ and γ_α, ψ_α the corresponding angles of $\mathbf{r}_\alpha$ in a body-fixed frame whose polar axis is $\mathbf{R}_\alpha$.

In these SHC, the 6D Hamiltonian $\mathbf{H}$ can be written as the sum of a hyperradial kinetic energy operator $\mathbf{T}(\rho)$ and a hyperangular Hamiltonian $H(\mathbf{w}_\alpha;\rho)$ which operates on the five angles $\mathbf{w}_\alpha \equiv (\omega_\alpha,\theta_\alpha,\phi_\alpha,\gamma_\alpha,\psi_\alpha)$. The eigenfunctions of H, called local hyperspherical surface functions (LHSF), form a complete discrete orthonormal basis set which spans the 5D hyperangular space defined by $\mathbf{w}_\alpha$, for each value of ρ. They sample all regions of configuration space and, as $\rho \to \infty$, are related in a simple way to the isolated AB, BC, and CA diatom eigenfunctions. As a result, they constitute a very appropriate basis set for expanding the scattering wave function. Such an expansion leads to a set of coupled ordinary differential equations in the hyperradius, whose numerical solutions, together with a simple asymptotic analysis, furnishes the standard scattering matrix.

The usefulness of these ideas has been extensively tested for a variety of collinear systems, including $H + H_2$[9-11] and $I + HI$.[12,13] They have also been used as a tool for calculating dissociation probabilities,[14,15] and energy partitioning among the dissociation products[16] in collinear collision-induced dissociation. For collinear exchange reactions, an important feature of the surface function basis set is that it requires fewer asymptotically closed channels than do other approaches.[17-19] The reason for this high convergence efficiency with respect to the number of vibrational states is that, in the strong interaction region, the hyperangle acts as a rapidly changing variable whereas the hyperradius acts as a slow one.[20]

For 3D reactions, the corresponding LHSF can be expanded in the Wigner rotation functions of ϕ_α, θ_α, ψ_α[21] resulting in a set of coupled partial differential eigenfunction equations in the variables ω_α, γ_α. We have employed a finite element method[22] to solve these equations numerically for the $H + H_2$ system and total angular momentum $J = 0$. This approach is similar to a previous one[23] which employed a different variety of hyperspherical coordinates.[24] We then solved the associated scattering equations, using a logarithmic derivative method,[25] over the total energy range 0.5–1.0 eV, for the A_1, A_2, and E irreducible representations of the P_3

 0021-9606/86/105962-03$02.10

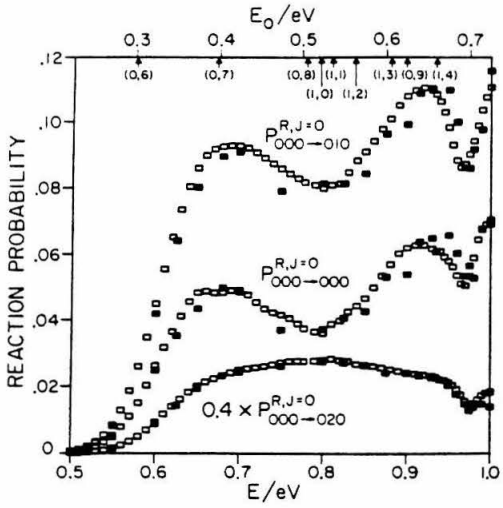

FIG. 1. Distinguishable atom $J = 0$ partial wave reaction probabilities as a function of energy for the $H + H_2(v, j, 0) \rightarrow H_2(v', j', 0)$ reaction on the Porter–Karplus potential energy surface (Ref. 29). The probabilities are denoted by the symbol $P^{R;J=0}_{v'j'0 \leftarrow vj0}$. The lower abcissa is the total energy and the upper abcissa the reagent translational energy. The vertical arrows on the upper abcissa denote the energy at which the corresponding $H_2(v, j)$ channel opens up. The open symbols represent the present results and the full ones those of a previous calculation (Ref. 1). The $P^{R,J=0}_{000\rightarrow020}$ results were multiplied by 0.4 prior to plotting.

symmetric group.[26] All LHSF were calculated for a grid of $40\,\omega_\alpha$ and $50\,\gamma_\alpha$ points. Up to 0.9 eV, $10\,A_1$, $10\,A_2$, and $20\,E$ functions were used. Between 0.9 and 1.0 eV, where a Feshbach resonance occurs,[27] those numbers were increased to 14 and 28, respectively. In all these calculations, flux was conserved to 1%. With respect to basis set size, transition probabilities greater than 0.01 were converged to 5% and the corresponding phases to 2° over the entire energy range. The corresponding probabilities, within the $v = 0$ manifold, were symmetric to 2% and convergence with respect to the grid coarseness was 3% and 3° for those probabilities and phases. Including the $v = 1$ manifold, the probabilities greater than 0.01 were symmetric to 11% and convergence of those transitions with respect to grid coarseness was 10% and 15°.

From the irreducible representation scattering matrices, distinguishable atom reaction probabilities were calculated, some of which are displayed in Fig. 1, together with the results of previous calculations.[1] For energies below 0.9 eV the two methods agree to within 12% for the probabilities in this figure and 5° for the corresponding phases, which is very encouraging.

Once the LHSF and interaction matrix elements have been obtained, the solution of the scattering equations and the calculation of the scattering matrix is very efficient, taking on an FPS 164-VAX 11/780 system, about 23 s for 10 channels and about 3 min for 20 channels. This efficiency is due in part to the absence of a matching procedure in the calculation. Instead, a simple asymptotic projection of the surface functions on the isolated diatom states is required. The surface functions themselves already span all three arrangement channels, and are energy independent.

Our finite element code for calculating the LHSF is accurate and efficient. The A_1 and A_2 functions (including the evaluation of all the interaction potential matrix elements needed for the scattering part of the calculation) required an average of only 17 s each, and the E functions utilized 34 s each. However, they were calculated at 140 γvalues of ρ, which made their evaluation dominate the calculation, for the relatively small number of channels discussed here. A variational approach promises to be significantly faster. Recently, such a method has been developed for the $e + H$ system, which takes only about 0.3 s per surface function even for $J > 0$.[28] It is currently being adapted to triatomic systems and preliminary results indicate that it will speed up the calculation of the LHSF by one to two orders of magnitude.

In conclusion, the LHSF approach to 3D reactive scattering has been successfully tested and gives strong indications that it will become a powerful tool for studying the quantum dynamics of chemical reactions, which other accurate methods have so far not permitted.

[a] Work supported in part by the U. S. Office of Scientific Research, Contract No. AFOSR-82-0341. Support from the U. S. Department of Energy, Grant No. DE-AS03-83ER13118 is also acknowledged.
[b] Work performed in partial fulfillment of the requirements for the Ph.D. degree in Chemistry at the California Institute of Technology.
[c] Contribution No. 7371.

[1] A. Kuppermann and G. C. Schatz, J. Chem. Phys. **62**, 2502 (1975); **65**, 4642, 4668 (1976).
[2] A. B. Elkowitz and R. E. Wyatt, J. Chem. Phys. **62**, 2504 (1975); **63**, 702 (1975).
[3] R. B. Walker, E. B. Stechel, and J. C. Light, J. Chem. Phys. **69**, 2922 (1978).
[4] One accurate calculation, for the H + BrH→HBr + H exchange reaction, excluding competition with the H_2 + Br abstraction channel, has been reported: D. J. Clary, J. Chem. Phys. **83**, 1685 (1985).
[5] A. Kuppermann, Chem. Phys. Lett. **32**, 374 (1975).
[6] R. T. Ling and A. Kuppermann, in *Electronic and Atomic Collisions*, edited by J. S. Risley and R. Geballe (University of Washington, Seattle, 1975), Vol. I, p. 353.
[7] R. C. Whitten and F. T. Smith, J. Math. Phys. **9**, 1103 (1968); B. R. Johnson, J. Chem. Phys. **73**, 5051 (1981).
[8] L. M. Delves, Nucl. Phys. **9**, 391 (1959); **20**, 275 (1960).
[9] A. Kuppermann, J. A. Kaye, and J. P. Dwyer, Chem. Phys. Lett. **74**, 257 (1980); J. P. Dwyer, Ph.D. thesis, California Institute of Technology, 1977.
[10] G. Hauke, J. Manz, and J. Römelt, Chem. Phys. **73**, 5040 (1980); J. Römelt, Chem. Phys. Lett. **74**, 263 (1980).
[11] K. D. Bondi and J. N. L. Connor, Chem. Phys. Lett. **92**, 570 (1982).
[12] J. A. Kaye and A. Kuppermann, Chem. Phys. Lett. **77**, 573 (1981).
[13] J. Manz and J. Römelt, Chem. Phys. Lett. **81**, 179 (1981).
[14] J. A. Kaye and A. Kuppermann, Chem. Phys. Lett. **78**, 546 (1981).
[15] J. Manz and J. Römelt, Chem. Phys. Lett. **77**, 172 (1981).
[16] J. A. Kaye and A. Kuppermann, Chem. Phys. Lett. **115**, 158 (1985).
[17] C. C. Rankin and J. C. Light, J. Chem. Phys. **51**, 1701 (1969); G. Miller and J. C. Light, *ibid.* **54**, 1635, 1643 (1971); J. C. Light and R. B. Walker, *ibid.* **65**, 4272 (1976).
[18] A. Kuppermann, in *Proceedings of the Conference on Potential Energy Surfaces in Chemistry*, edited by W. A. Lester (University of California, Santa Cruz, 1970), p. 121; Proceedings of the 7th International Conference on Physical and Electronic Atomic Collisions, 1972, p. 3; A. Kuppermann, in *Theoretical Chemistry, Theory of Scattering: Papers in Honor of Henry Eyring*, edited by D. Henderson (Academic, New York, 1981), Vol. 6A, p. 79.

[19]B. R. Johnson, Chem. Phys. Lett. **13**, 172 (1972).
[20]A. Kuppermann and J. P. Dwyer, in *Electronic and Atomic Collisions. Abstracts of Contributed Papers, 11th International Conference on Electronic and Atomic Collisions* (Society for Atomic Collision Research, Tokyo, 1979), p. 888.
[21]A. S. Davydov, *Quantum Mechanics*, translated by D. ter haar (Addison–Wesley, Reading, MA, 1965), p. 151.
[22]G. Dhatt and G. Touzot, *The Finite Element Method Displayed*, translated by G. Cantin (Wiley, New York, 1984); K. J. Bathe, *Finite Element Analysis in Engineering Procedures* (Prentice–Hall, Englewood Cliffs, 1982), pp. 672–695.
[23]M. Mishra, J. Linderberg, and Y. Öhrn, Chem. Phys. Lett. **111**, 439 (1984); J. Linderberg, Int. J. Quantum Chem. (in press).
[24]C. A. Mead, Chem. Phys. **49**, 23 (1980); J. Chem. Phys. **72**, 3839 (1980).
[25]B. R. Johnson, J. Compl. Phys. **13**, 445 (1973); J. Chem. Phys. **67**, 4086 (1977); NRCC Workshop, Lawrence Berkeley Laboratory, Report No. LBL-9501, 1979.
[26]E. P. Wigner, *Group Theory* (Academic, New York, 1959), Chaps. 7 and 13.
[27]G. C. Schatz and A. Kuppermann, Phys. Rev. Lett. **35**, 1266 (1975).
[28]D. M. Hood and A. Kuppermann, in *Theory of Chemical Reaction Dynamics*, edited by D. C. Clary (Reidel, Boston, 1986); D. M. Hood, Ph.D. thesis, California Institute of Technology, 1986.
[29]R. N. Porter and M. Karplus, J. Chem. Phys. **40**, 1105 (1964).

Volume 133, number 1 CHEMICAL PHYSICS LETTERS 2 January 1987

LIFETIME ANALYSIS OF HIGH-ENERGY RESONANCES IN THREE-DIMENSIONAL REACTIVE SCATTERING

Paul G. HIPES [1] and Aron KUPPERMANN

Arthur Amos Noyes Laboratory of Chemical Physics, Division of Chemistry and Chemical Engineering [2], California Institute of Technology, Pasadena, CA 91125, USA

Received 12 November 1986

Accurate quantum mechanical three-dimensional reactive scattering calculations for the $J=0$ partial wave of the $H+H_2$ system for total energies up to 1.6 eV have been performed using symmetrized hyperspherical coordinates. Six resonances were found having collision lifetimes which, interestingly, increase with the amount of stretching excitation and decrease with that of bending excitation.

1. Introduction

We have recently shown that the methodology based on symmetrized hyperspherical coordinates is an accurate and efficient technique for performing three-dimensional (3D) quantum mechanical reactive scattering calculations [1]. Using this methodology, we have now performed 3D reactive scattering calculations at total energies up to 1.6 eV, for the zero total angular momentum ($J=0$) partial wave of the $H+H_2$ system. This energy range exceeds slightly that for which 3D results have been reported so far [1–6]. More importantly, the degree of convergence of the present calculations and the fineness of the energy grid used permits the Eisenbud–Wigner delay time [7] and Smith's collision lifetime matrix [8] analyses to be made, even at the highest energies reported. These two techniques provide sensitive measures of the resonance structure underlying the dynamics. Below we present an outline of the methodology used, followed by the results of our calculations and their interpretation.

[1] Work performed in partial fulfillment of the requirements for the Ph.D. degree in Chemistry at the California Institute of Technology.

[2] Contribution number 7496.

2. Method

The PK2 potential energy surface [9] and the methodology based on symmetrized hyperspherical coordinates (SHC) [1,10,11] are used in these calculations. The PK2 surface has been used extensively for collinear and 3D scattering in the past and the present calculations augment the results available for this surface. The scattering wavefunction is obtained as a coupled channel expansion involving symmetrized hyperspherical coordinates. These coordinates are defined by [1,10]

$$\rho=(R_\lambda^2+r_\lambda^2)^{1/2},\quad \omega_\lambda=2\arctan(r_\lambda/R_\lambda),$$

$$\gamma_\lambda=\arccos(\boldsymbol{R}_\lambda\cdot\boldsymbol{r}_\lambda/r_\lambda R_\lambda),$$

where $\boldsymbol{r}_\lambda$ is Delves' mass-scaled diatom internuclear vector and $\boldsymbol{R}_\lambda$ Delves' mass-scaled position vector of the atom with respect to the center of mass of the diatom [10,12,13]. The corresponding Hamiltonian operator has the form

$$H=-\frac{\hbar^2}{2\mu}\left(\frac{\partial^2}{\partial\rho^2}+\frac{5}{\rho}\frac{\partial}{\partial\rho}\right)+\frac{\hat{\Lambda}^2}{2\mu\rho^2}+V(\rho,\omega_\lambda,\gamma_\lambda),$$

where

$$\hat{\Lambda}^2=\hat{L}_\omega^2+\frac{\hat{j}_\lambda^2}{\sin^2(\frac{1}{2}\omega_\lambda)}+\frac{\hat{l}_\lambda^2}{\cos^2(\frac{1}{2}\omega_\lambda)},$$

$$\hat{L}_\omega^2=-4\hbar^2\left[\frac{\partial^2}{\partial\omega_\lambda^2}+2\cot\left(\omega_\lambda\frac{\partial}{\partial\omega_\lambda}\right)\right],$$

and $\hat{j}_\lambda^2$ and $\hat{l}_\lambda^2$ are the angular momentum operators associated with r_λ and R_λ, respectively. The global reduced mass μ is defined by $[m_A m_B m_C/(m_A + m_B + m_C)]^{1/2}$ where the m_x are the masses of the three atoms A, B, and C [13]. Local hyperspherical surface functions (LHSF) $\Phi_n^{JM\Gamma\Pi}$ with eigenvalues $\epsilon_n^{J\Gamma\Pi}$ are defined by

$$[\hat{\Lambda}^2/2\mu\rho^2 + V(\rho, \omega_\lambda, \gamma_\lambda)]\ \Phi_n^{JM\Gamma\Pi}(\zeta_\lambda; \rho) = \epsilon_n^{J\Gamma\Pi}(\rho)\ \Phi_n^{JM\Gamma\Pi}(\zeta_\lambda; \rho),$$

where ζ_λ stands for the set of coordinates $(\omega_\lambda, \gamma_\lambda, \varphi_\lambda, \vartheta_\lambda, \psi_\lambda)$, $(\varphi_\lambda, \vartheta_\lambda, \psi_\lambda)$ are the Euler angles of the instantaneous triangle formed by the three atoms [2], and n is a discrete quantum number. The labels $JM\Gamma\Pi$ describe respectively the system's total angular momentum, its projection along a laboratory-fixed axis, the irreducible representation of the P_3 permutation group associated with the three identical atoms being considered, and the parity for inversion through the system's center of mass. Any solution of the Schrödinger equation, labelled by $JM\Gamma\Pi$, can be expanded in the LHSF as

$$\Psi^{JM\Gamma\Pi}(\rho, \zeta_\lambda) = \sum_{n=0}^{\infty} g_n^{J\Gamma\Pi}(\rho; \bar{\rho})\ \Phi_n^{JM\Gamma\Pi}(\zeta_\lambda; \bar{\rho}).$$

This expansion leads to a matrix initial value problem in the variable ρ. It converges rapidly for values of ρ near $\bar{\rho}$, which is responsible for the success of the LHSF as a local basis set. For a given value of J, the LHSF are expanded in the Wigner rotation matrices [14]:

$$\Phi_n^{JM\Gamma\Pi}(\zeta_\lambda; \bar{\rho}) = \sum_{\Omega_\lambda=-J}^{\Omega_\lambda=J} D^J_{M\Omega_\lambda}(\varphi_\lambda, \vartheta_\lambda, \psi_\lambda)\ \phi^{J\Gamma\Pi}_{\Omega_\lambda, n}(\omega_\lambda, \gamma_\lambda; \bar{\rho}).$$

The variational equation for the $\phi^{J=0,\Gamma\Pi}_{\Omega_\lambda,n}(\omega_\lambda, \gamma_\lambda; \bar{\rho})$, abbreviated by ϕ_n^Γ is

$$\delta \int \left[\left(\frac{\partial \phi_n^\Gamma}{\partial \omega_\lambda}\right)^2 + \left(\frac{1}{\sin \omega_\lambda} \frac{\partial \phi_n^\Gamma}{\partial \gamma_\lambda}\right)^2 + \left(\frac{\mu\bar{\rho}^2}{2\hbar^2}\right)(\phi_n^\Gamma)^2\ [V(\bar{\rho}, \omega_\lambda, \gamma_\lambda) - \epsilon_n^\Gamma(\bar{\rho})] \right] d\tau = 0,$$

where $d\tau = \sin\gamma_\lambda \sin^2\omega_\lambda\ d\gamma_\lambda\ d\omega_\lambda$ and which is then discretized via the finite element approximation [15][:] using quadrilateral elements with four nodal points. This leads to a banded generalized algebraic eigenvalue problem which is solved by one of the standard methods [16]. This finite element approach to calculating surface functions is similar to a previous one used by Mishra, Linderberg and Öhrn [17], which employs a different variety of hyperspherical coordinates due to Mead [18].

For the results reported in this paper, the expansion in LHSF includes 26 A_1 and 44 E irreducible representation functions calculated on a hyperangular mesh of 60 ω_λ and 60 γ_λ points. The remaining numerical parameters are unchanged [1]. In the present calculations, flux is conserved to better than 1% for all energies below 1.55 eV. Convergence of probabilities and phases for transitions within the set $(v=0, j<10; v=1, j<5)$ is approximately 2% and 2° with respect to both the $(\omega_\lambda, \gamma_\lambda)$ grid fineness and number of surface functions used. As before [1], for hyperradii $\rho \geq 6$ bohr, simple products of a Legendre polynomial in $\cos\gamma_\lambda$ and a quasi-vibrational function of ω_λ form the expansion basis set, in lieu of the LHSF. This set is suggested by the negligible amplitude of the scattering wavefunction in the regions of configuration space between different arrangement channels in this range of ρ and at the energies considered, and is much less expensive in computer time than the LHSF. The error resulting in the use of such a separable basis set for $\rho \geq 6$ bohr is 2% and 2°. In a recent publication [19], Wolniewicz and Hinze suggest that, for these hyperradii, the $(\omega_\lambda, \gamma_\lambda)$ coordinates lose their high efficiency for finite element LHSF calculations, and that a closely related set of symmetrized hyperspherical coordinates proposed by Johnson [20] becomes more economical. However, there is no need for calculating such LHSF since separable functions like the ones described above are equally satisfactory beyond 6 bohr. The numerical errors associated with the values of the three parameters mentioned above (number of ω_λ and γ_λ points, number of LHSF, and the hyperradius beyond which a separable basis set is used) have been found to dominate the errors associated with the remaining numerical parameters adopted [1]. Finally, before

[:] Ref. [15] is a good general text on the finite element method.

Volume 133, number 1 CHEMICAL PHYSICS LETTERS 2 January 1987

leaving the numerical aspects of the current calculations, it is important to note that no difficulty with the methodology has been encountered so far; calculations at higher collision energies simply require more LHSF on a finer mesh.

3. Results and discussion

From the irreducible representation scattering matrices, distinguishable atom transition probabilities were calculated, some of which are displayed in the top panels of figs. 1–3 and in fig. 4. The high accuracy of the calculations permits us to obtain the collision lifetime matrix [8] from the scattering matrices, which is very useful for the interpretation of the structure in these transition probability curves. In the top curves of fig. 1b, we display selected eigenvalues of the collision lifetime matrix for the A_1 irreducible representation. For each resonance, the eigenvalue shown is the only one that varies significantly with energy [21]. The usefulness of the collision lifetime matrix analysis is that a single, unambiguous energy is associated with each resonance: the position of the maximum in the eigenvalue versus energy curve. Another interesting quantity is the delay time that a wave packet, initially in state i, spends in the collision region before emerging in state f [7]. The two lowest curves in fig. 1b depict the delay times associated with the distinguishable atom, $J=0$, reactive transitions 000→000 and 000→120. Figs. 2b and 3b display the delay times for the reactive 000→020 and the non-reactive 000→120 transitions, respectively. Initially, one would expect positive delay times in the region of a resonance, reflecting the formation of a quasi-bound state. The complicated behavior of these delay time curves near a resonance reflects the interference between the resonant and direct mechanisms at play. A decomposition of the delay time into the corresponding components has been carried out for collinnear $H+H_2$ and leads to positive delay times for the resonant contribution [22], as expected. A similar result is also expected for the 3D case. This same interference mechanism is responsible for the variety of behaviors of transition probabilities with energy in the neighborhood of resonances, leading to the different kinds of line shapes displayed in figs. 1–4. As a result, transition probabilities are not nec-

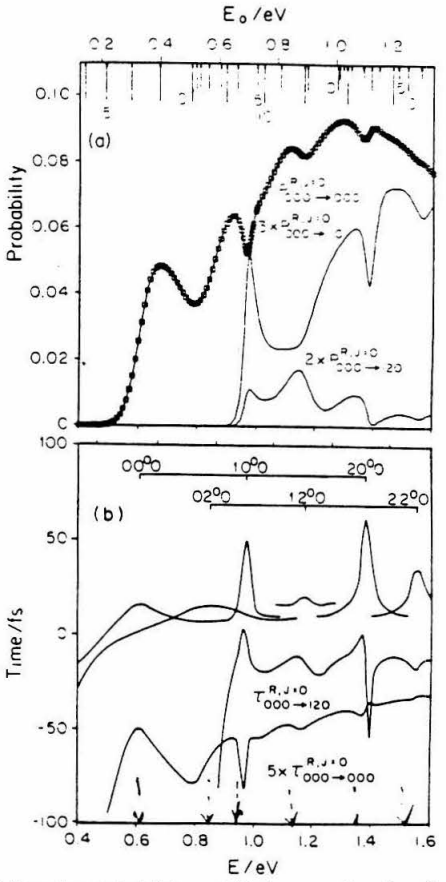

Fig. 1. Reaction probabilities and lifetimes as a function of energy for the $J=0$ partial wave of the $H+H_2(v,j,0)\rightarrow H_2(v',j',0)+H$ reaction on the PK2 potential energy surface. The lower abscissa is the total energy and the upper abscissa is the reagent translational energy. The vertical arrows on the upper abscissa denote the energies at which the corresponding $H_2(v,j)$ states open up. The length of those arrows decreases as v spans the values 0, 1, and 2. The numbers 0, 5, and 10 define a labelling for the value of j. (a) The probabilities refer to distinguishable atoms and are denoted by the symbol $P^{R,J=0}_{v'j'\leftarrow vj}$. The open square symbols on the $P^{R,J=0}_{000\rightarrow 000}$ curve indicate the energies at which the scattering calculation was performed. They are omitted from the other two curves, but the energy grid was the same for all. (b) The upper curves represent the resonant eigenvalue of the collision lifetime matrix for the A_1 irreducible representation. For visibility, a constant value of 20 fs has been added to these eigenvalues. The two lowest curves, labelled by the symbol $\tau^{R,J=0}_{vj\leftarrow v'j'}$, are the distinguishable atom delay times for the $H+H_2(v,j,0)\rightarrow H_2(v',j',0)+H$ reactive processes. The energy grid used for these lifetime calculations was 0.001 eV in the neighborhood of all but the first and last resonances and was 0.01 eV elsewhere. The labelling of the resonances at the top of this panel is described in the text.

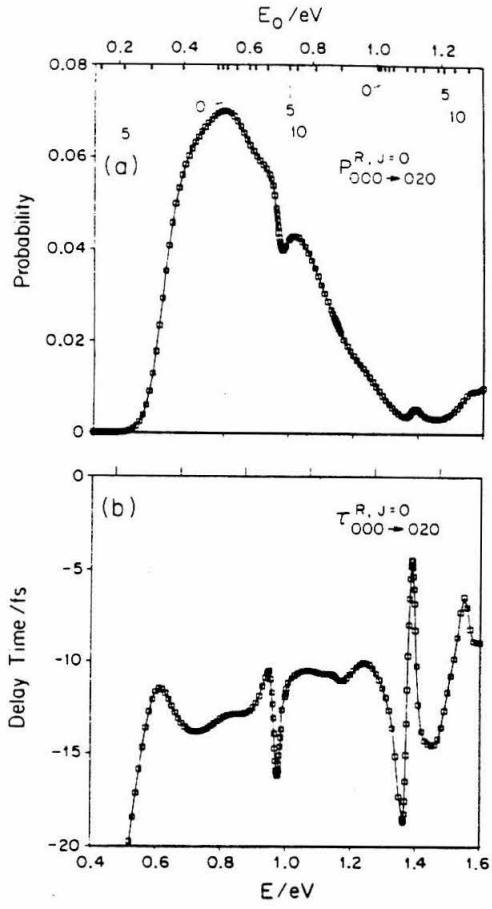

Fig. 2. Distinguishable atom reactive 000→020 transition probabilities (a) and the corresponding delay times (b). The energy grid and the labelling are the same as in fig. 1.

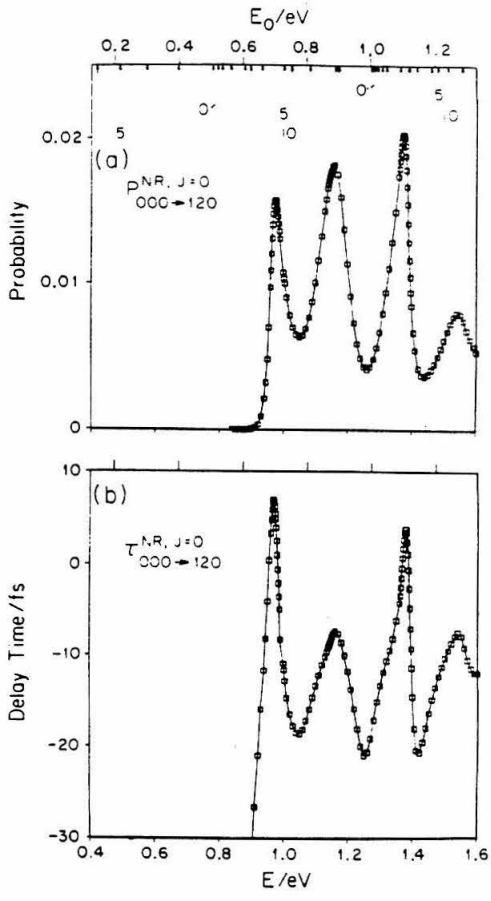

Fig. 3. Distinguishable atom non-reactive 000→120 transition probabilities (a) and the corresponding delay times (b). The energy grid and the labelling are the same as in fig. 1.

essarily extrema in these curves at resonance energies. The delay time and collision lifetime curves give, however, uncontroversial evidence that the structure observed in the transition probability curves is associated with resonance states.

From the position of the extrema of the A_1 collision lifetime curves of fig. 1b, we place the six observed resonances at 0.61, 0.847, 0.971, 1.170, 1.382, and 1.56 eV. The third and fifth of these resonances are the strongest, having lifetimes of about 42 and 50 fs, respectively, measured from the non-resonant baseline of the corresponding curves. For comparison, the symmetric stretch vibrational period for H_3 at the saddle point of the PK2 surface is about 15 fs [9]. The energies of these two 3D resonances differ from those of the first two collinear resonances on PK2 (0.88 and 1.31 eV) [23,24] by about 0.1 eV, corresponding to twice the estimated zero-point energy of a single bending mode (doubly degenerate) of H_3 at the saddle point of PK2 [4]. This suggests that they both be classified as ground states of the bending mode, as previously proposed for the

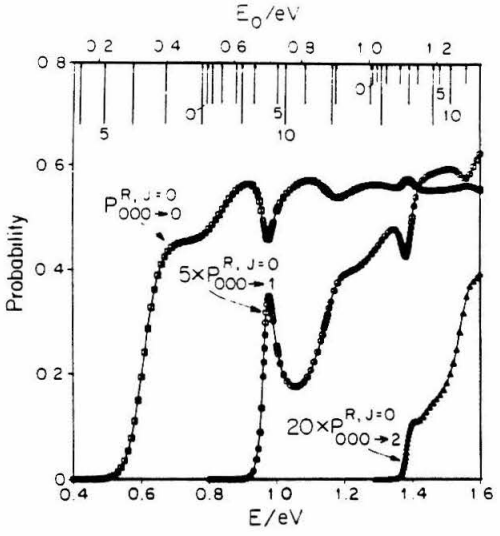

Fig. 4. Distinguishable atom reactive transition probabilities from the ground vibrational and rotational state ($v=0$, $j=0$, $m_j=0$) to all rotational states in $v=0$, $v=1$, and $v=2$ summed over both reactive arrangement channels. The energy grid and the labelling are the same as in fig. 1.

0.971 eV resonance [3][‡]. This analogy further suggests that these 0.971 and 1.382 eV resonances be classified as the first and second excited symmetric stretch states of H_3 [25–28]. It should be remembered, however, that this classification is approximate, since the collinear states are known to also have antisymmetric character [26,29] and have been successfully modeled using both hyperspherical [29,30] and natural collision coordinate [25–27] adiabatic approximations. Following Colton and Schatz [31], and Bowman [32], we will use the common spectroscopic notation for linear triatomic molecules [33], $(v_1, v_2^{\Omega_\lambda}, v_3)$ to label the resonance states, where v_1, v_2, and v_3 are the number of quanta of symmetric stretch bend, and antisymmetric stretch, respectively. The superscript $|\Omega_\lambda|$ denotes the component of vibrational angular momentum along the molecular axis and takes on the values $v_2, v_2-2, v_2-4,\ldots$ 0 if v_2 is even and $v_2, v_2-2, v_2-4,\ldots$, 1 if v_2 is odd. Since our present calculations are restricted to the zero total angular momentum partial wave, the component of the total angular momentum and hence the vibrational angular momentum along the molecular axis must vanish ($|\Omega_\lambda|=0$). We label the 0.971 and 1.382 eV 3D resonances as (1, 0[0], 0) and (2, 0[0], 0) states, respectively. Similarly, we label the remaining resonances at 0.61, 0.847, 1.170, and 1.56 eV by (0, 0[0], 0), (0, 2[0], 0), (1, 2[0], 0), (2, 2[0], 0), respectively. The weak (0, 0[0], 0) and (0, 2[0], 0) resonances were not previously detected because a collision lifetime analysis had not been performed [1–6]. It is interesting to note that in each of the two series, (0, 0[0], 0), (1, 0[0], 0), (2, 0[0], 0) and (0, 2[0], 0), (1, 2[0], 0), (2, 2[0], 0), the collision lifetime increases with the number of symmetric stretch quanta. This may be a reflection of the increasing depth of the corresponding vibrationally adiabatic wells [34] with increasing vibrational quantum number [25][=] and may enhance the chances that such resonances can be observed experimentally. In contrast, the collision lifetime of the resonance state is reduced by excitation of the bending mode.

The labelling of the (1, 0[0], 0) and (1, 2[0], 0) resonances is consistent with the recent identification made for similar $J=0$ resonances on the LSTH surface [36,37] by Colton and Schatz [31]. Furthermore, approximate theories have been used to calculate 3D resonance positions and widths [31,32,38,39]. In particular, the reduced dimensionality collinear exact quantum with adiabatic bend method (CEQB) of Bowman [32] predicts the existence of (1, 0[0], 0), (1, 2[0], 0), (2, 0[0], 0), and (2, 2[0], 0) resonances on the LSTH surface with energies of 0.974, 1.20, 1.35, and 1.50 eV, respectively, which are in remarkably good agreement with our accurate PK2 surface results. This agreement may be due to an accidental compensation for inaccuracies in the CEQB results by the difference in the potential energy surfaces used, or, more likely, it may reflect the similarity in the resonance spectrum for the two surfaces and the validity of the CEQB approximation. Finally, Pollak and Wyatt [39] have used adiabatic approximations to extend the resonant periodic orbit (RPO) method of Pollak and Child [40] to 3D $H+H_2$ on PK2. The adiabatic RPO model predicts the energy of the (1, 0[0], 0) and

[‡] The 3D resonance energy is found to be 0.975 eV in ref. [3], but we believe the current value of 0.971 eV is more accurate.

[=] See table 2 of ref. [35].

(2, 0^0, 0) resonances on PK2 to be 0.954 and 1.340 eV, respectively. They find no (1, 2^0, 0) resonance, but do find five bending excited resonances with $v_1 = 2$. In particular, their resonance labelled as $n = 2$, $m_1 = 1$, $m_2 = 1$ at 1.473 eV corresponds to the (2, 2^0, 0) resonance whose accurate energy we find to be 1.56 eV. Of the remaining RPO resonances, one has an energy beyond the range we consider and the rest do not appear in the $J = 0$ partial wave to which the current results are restricted. The agreement between the RPO and the accurate resonance energies is reasonable but not as good as that of the CEQB results.

The absence of $J = 0$ resonances having an odd number of quanta in the bending mode is easy to understand. The wavefunction representing such a mode would have a nodal line at $\gamma_\lambda = 0$. This is precluded by the boundary conditions (stemming from the single-valuedness of the wavefunction) imposed on a $J = 0$ partial wave scattering wavefunction. Likewise, an odd number of bend quanta does not occur for stable linear triatomic molecules in $J = 0$ states; otherwise, the component of the vibrational and therefore the total angular momentum along the molecular axis would not vanish [41]. The single-valuedness and vibrational angular momentum languages are mathematically equivalent.

In fig. 2, the probability and corresponding delay time for the reactive 000→020 transition are shown. The probability curve is only slightly affected by the resonances while the delay time is seen to be substantially influenced. In fig. 3, the non-reactive 000→120 transition probability and delay time are displayed. Both quantities reflect the underlying resonances dramatically. The absence of numerical noise in figs. 2 and 3 reflects the numerical stability of the SHC scattering methodology using a finite element construction of the LHSF. Finally, cumulative reaction probabilities from the ground state ($v = 0$, $j = 0$) to ($v = 0$, $j =$ all), ($v = 1$, $j =$ all), and ($v = 2$, $j =$ all) summed over the two product arrangement channels are shown in fig. 4. The relatively constant value of the ($v = 0$, $j = 0$)→($v = 0$, $j =$ all) curve above 1.0 eV is remarkable in view of the rapidly increasing number of open states with increasing energy and is suggestive of an appropriate sum rule.

4. Summary

The results obtained illustrate the effectiveness of the SHC method for performing accurate 3D scattering calculations at high energies. The quality of the results has allowed the identification of a very rich and interesting high internal excitation resonance structure in $H + H_2$ collisions via lifetime analysis. This analysis shows the existence of six resonances below 1.6 eV, and based on the energetics, the resonances are interpreted as due to the formation of a linear metastable compound state with different degrees of excitation of the symmetric stretch and bend modes. Furthermore, we find that the lifetimes of the resonant states increase with increasing excitation of the stretching vibrational mode, while excitation of the bending mode reduces these lifetimes.

Acknowledgement

Work supported in part by US Air Force Office of Scientific Research, Contract No. AFOSR-82-0341. Support from the US Department of Energy, Grant No. DE-AS03-83ER 13118 is also acknowledged. We thank the San Diego Supercomputer Center on whose Cray X-MP/48 these calculations were performed.

References

[1] A. Kuppermann and P.G. Hipes, J. Chem. Phys. 84 (1986) 5962.
[2] A. Kuppermann and G.C. Schatz, J. Chem. Phys. 62 (1975) 2502;
G.C. Schatz and A. Kuppermann, J. Chem. Phys. 65 (1976) 4642, 4668.
[3] G.C. Schatz and A. Kuppermann, Phys. Rev. Letters 35 (1975) 1266.
[4] A.B. Elkowitz and R.E. Wyatt, J. Chem. Phys. 62 (1975) 2504; 63 (1975) 702.
[5] R.B. Walker, E.B. Stechel and J.C. Light, J. Chem. Phys. 69 (1978) 2922.
[6] F. Webster and J.C. Light, J. Chem. Phys. 85 (1986) 4744.
[7] L. Eisenbud, Ph.D. Thesis, Princeton (1948);
E.P. Wigner, Phys. Rev. 98 (1955) 145.
[8] F.T. Smith, Phys. Rev. 118 (1960) 349.
[9] R.N. Porter and M. Karplus, J. Chem. Phys. 40 (1964) 1105.
[10] A. Kuppermann, Chem. Phys. Letters 32 (1975) 374.

[11] R.T. Ling and A. Kuppermann, in: Electronic and Atomic Collisions, Abstracts of Papers of the 9th International Conference on the Physics of Electronic and Atomic Collisions, Seattle, Washington, 24–30 July 1975, Vol. 1, eds. J.S. Risley and R. Geballe (Univ. Washington Press, Seattle, 1975) pp. 353, 354.
Conference on the Physics of Electronic and Atomic Collisions, Seattle, Washington, 24–30 July 1975, Vol. 1, eds. J.S. Risley and R. Geballe (Univ. Washington Press, Seattle, 1975) pp. 353, 354.
[12] L.M. Delves, Nucl. Phys. 9 (1959) 391; 20 (1960) 275.
[13] A. Kuppermann, in: Theoretical chemistry – theory of scattering: papers in honor of Henry Eyring, ed. D. Henderson (Academic Press, New York, 1981) pp. 122–124.
[14] A.S. Davydov, Quantum mechanics (Pergamon Press, New York, 1976) pp. 167–178.
[15] G. Dhatt and G. Touzot, The finite element method displayed (Wiley, New York, 1984).
[16] K. Bathe, Finite element procedures in engineering analysis (Prentice-Hall, Englewood Cliffs, 1982) pp. 672–695.
[17] M. Mishra, J. Linderberg and Y. Öhrn, Chem. Phys. Letters 111 (1984) 439;
J. Linderberg, Intern. J. Quantum Chem. 19 (1986) 467.
[18] C.A. Mead, Chem. Phys. 49 (1980) 23; J. Chem. Phys. 72 (1980) 3839.
[19] L. Wolniewicz and J. Hinze, J. Chem. Phys. 85 (1986) 2012.
[20] B.R. Johnson, J. Chem. Phys. 73 (1980) 5051.
[21] A. Kuppermann and J.A. Kaye, J. Phys. Chem. 85 (1981) 1969.
[22] G.C. Schatz and A. Kuppermann, J. Chem. Phys. 59 (1973) 964.
[23] D. Diestler, J. Chem. Phys. 54 (1971) 4547.
[24] A. Kuppermann, J.A. Kaye and J.P. Dwyer, Chem. Phys. Letters 74 (1980) 257;
J. Römelt, Chem. Phys. Letters 74 (1980) 263;
K.D. Bondi and J.N.L. Connor, Chem. Phys. Letters 92 (1982) 570.
[25] R.D. Levine and S. Wu, Chem. Phys. Letters 11 (1971) 557.
[26] A. Kuppermann, in: Potential energy surface and dynamics calculations, ed. D.G. Truhlar (Plenum Press, New York, 1981) pp. 405, 414.
[27] B.C. Garrett and D.G. Truhlar, J. Phys. Chem. 86 (1982) 1136; 87 (1983) 4554.
[28] J.M. Bowman, A. Kuppermann, J.T. Adams and D.G. Truhlar, Chem. Phys. Letters 20 (1973) 229.
[29] A. Kuppermann and J.P. Dwyer, in: Electronic and Atomic Collisions, Abstracts of Contributed Papers, 11th International Conference on the Physics of Electronic and Atomic Collisions, Kyoto, Japan (The Society for Atomic Collision Research, Tokyo, 1979) pp. 888, 889.
[30] J. Römelt, Chem. Phys. 79 (1983) 197.
[31] M.C. Colton and G.C. Schatz, Chem. Phys. Letters 124 (1986) 256.
[32] J.M. Bowman, Chem. Phys. Letters 124 (1986) 260.
[33] G. Herzberg, Infrared and Raman spectra of polyatomic molecules (Van Nostrand, Princeton, 1945) p. 272.
[34] A. Kuppermann, J. Phys. Chem. 83 (1979) 171.
[35] D.G. Truhlar and A. Kuppermann, J. Chem. Phys. 56 (1972) 2232.
[36] B. Liu, J. Chem. Phys. 58 (1973) 1925;
P. Siegbahn and B. Liu, J. Chem. Phys. 68 (1978) 2457.
[37] D.G. Truhlar and C.J. Horowitz, J. Chem. Phys. 68 (1978) 2468; 71 (1979) 1514.
[38] B.C. Garrett, D.W. Schwenke, R.T. Skodje, P. Thirumalai, T.C. Thompson and D.G. Truhlar, in: Resonances, Am. Chem. Soc. Symp. Ser., Vol. 263 (Am. Chem. Soc., Washington, 1984) p. 375.
[39] E. Pollak and R.E. Wyatt, J. Chem. Phys. 81 (1984) 1801.
[40] E. Pollak and M.S. Child, Chem. Phys. 60 (1981) 23.
[41] G. Herzberg, Chem. Phys. 60 (1981) 80.

Three-dimensional Atom-Diatom Reactive Scattering Calculations Using Symmetrized Hyperspherical Coordinates III. Scattering Results for $J = 0$ $H + H_2$ †

Paul G. Hipes ¶ and Aron Kuppermann

Arthur Amos Noyes Laboratory of Chemical Physics,
Division of Chemistry and Chemical Engineering, ‡
California Institute of Technology,
Pasadena, California 91125

(Received)

Abstract

This paper describes an accurate numerical application of the symmetrized hyperspherical coordinate formalism to quantum mechanical $H + H_2$ reactive scattering. Results from calculations using the LSTH potential energy surface are emphasized. A few results from the Porter-Karplus II surface are compared with the LSTH results. The calculations are restricted to the zero total angular momentum partial wave and span the range of total energies 0.3 eV to 1.6 eV. We present probabilities, partial wave cross sections, and a surprisal analysis. These calculations, performed at over 500 energies, represent the most extensive set of accurate results available for the $J = 0$ partial wave of any reactive system to date, and have permitted a lifetime matrix analysis to be performed. Accurate H_3 resonance energies are derived from this analysis and compared with the resonance energies assigned by other methods and models.

1. Introduction

In this paper, we present the results of three-dimensional $H + H_2$ reactive scattering calculations which use the hyperspherical coordinate formalism[1-3] described in paper I[4] of this series and the surface function basis set described in paper II.[5] The usefulness of the hyperspherical coordinate methodology for three-dimensional reactive scattering has been shown in two previous communications.[3] In the first,[3a] we showed that the new calculations agree well with the earlier ones of Schatz and Kuppermann.[6a,c] In the second,[3b] we applied the lifetime matrix analysis[7] of F. T. Smith to the scattering results for the Porter-Karplus[8] potential energy surface II (PKII) and discussed the very interesting resonance[6a,3b,9-17] structure of this system. The present paper differs from the two communications in two respects: we will emphasize the results from the LSTH[18,19] potential energy surface and a much broader spectrum of results will be included.

The scattering results in this paper are limited to the lowest total spatial angular momentum partial wave ($J = 0$). This statement does not imply that there are any dynamical approximations used in the calculations. The limitation to a single partial wave is the exploitation of a rigorous constant of the motion which is not present in a scattering experiment. Unfortunately, we cannot directly compare our results to experiments. We have not gone beyond the lowest partial wave because the finite element method we used for constructing surface functions is too expensive to be practical for $J > 2$ and there appear to be alternative methods to calculate the surface functions in a more efficient manner.[20]

As is common in atom-diatom reactive scattering calculations, we have chosen to test our new methodology on the system $H + H_2$.[21-24] There are at least three reasons for this choice. The LSTH surface is accurate enough to warrant the expenditure of the amount of computer time that such dynamics calculations currently require. Its accuracy also encourages the hope that results from experiments can be reliably compared to the results of dynamics calculations.

The second reason for choosing this system is that previous accurate calculations exist for it[6,25,26] so that the new methodology can be validated. The third reason is that $H + H_2$ consists of three identical particles and computational effort can be reduced through the use of this symmetry. It is unfortunate that this reaction is not a simple one to study in the laboratory; however, there have been some recent experiments on the dependence of final state relative populations on the relative reagent translational energy for $H + H_2$.[27]

The present calculations are a first step in establishing a computational methodolgy that is intended to provide differential cross sections for $H + H_2$ at energies above the $v = 1$ threshold and for other chemical systems. The prospect for accurate calculations of differential and integral cross sections over a large energy range for $H + H_2$ and its isotopic analogues is especially exciting in view of the number of experiments on this system. In particular, Gerrity and Vallentini[28] and Rettner, Marinero, and Zare[29] have measured relative populations of final states in pump-probe experiments on $H + D_2$ using translational energy resolved reagents. Absolute integral reaction cross sections have been measured at several energies for this reaction by Gerlach-Meyer, Kleinermanns, Linnebach, and Wolfrum[30] and by Tsukiyama, Katz, and Bersohn.[31] Differential cross sections for $D + H_2$ have been measured by Götting and Toennies[32] and by Buntin, Giese, and Gentry.[33] Because only $J = 0, 1$ results have been calculated[3,6,25,26,34–37] at the energies of these experiments, no direct comparisons have yet been made between theory and experiment. It is our hope that this situation will be quickly remedied by the theorists.

The paper is arranged as follows. In section 2, the degree of convergence of the results that follow is discussed. Section 3 presents the relationship between three kinds of scattering results: a) those labeled by the irreducible representations of P_3 (the permutation group of three identical particles); b) the Pauli antisymmetrized results; and c) those labeled as reactive and nonreactive. In

sections 4 and 5, the respective transition probabilities for the A_1 and A_2 irreducible representations are presented and discussed. In section 6, E irreducible representation $J = 0$ partial wave cross sections and probabilities are presented and analyzed. In section 7, the resonance structure of H_3 is presented. In section 8, a rotational surprisal analysis is given, and in section 9, final vibrational population ratios summed over all final rotational states are given. In section 10, our findings are summarized. All results in this paper belong to the zero total spatial angular momentum partial wave. This fact will not always be repeated with every figure and remark.

2. Convergence Considerations

Before the results of a numerical study can be interpreted, it is necessary to understand the degree to which the results are reliable. In this section, we consider the accuracy of the results with respect to the values chosen for the numerical parameters of the method. The methods used in the current calculations have been discussed in detail in two previous papers.[4,5]

The numerical parameters fall into two classes: geometric parameters and completeness parameters. The geometric ones are associated with the construction of the surface functions with the finite element scheme and the propagation of the the hyperspherical logarithmic derivative matrix as an initial value problem in ρ. The completeness parameters are the number of surface functions used in expanding the scattering wave function and the number of values of ρ at which surface functions are constructed.

There are several geometric parameters associated with the surface function construction at a single value of ρ. One of the most important is the number of finite elements used to calculate surface functions.[5] All elements used are quadrilaterals with four bilinear shape functions per element. The LSTH results are based on 4761 elements for the surface functions. The PKII results are based on 3481 elements. Convergence of the lowest 20 A_1 surface function eigenvalues

with respect to the number of elements is 0.5% for the highest eigenvalues and better for the lower ones. A similar degree of convergence is expected for the A_2 and E surface functions. Given a finite element approximation to the surface functions, the eigenvalues are improved iteratively until the relative change in them in successive iterations is one part per million. That is *not* to say that the absolute accuracy of the surface function eigenvalues is that high, but that, given the subspace defined by the finite element approximation, the best eigenvalues are determined with 1 ppm precision.

Another numerical parameter associated with the surface functions is the number of quadrature points used in the variational and interaction integrals over $(\omega_\lambda, \gamma_\lambda)$.[4,5] For all calculations, integrations are done with four Gauss-Legendre quadrature points per element. This quadrature scheme is exact for the shape functions used.

The next geometric parameter concerns one of the boundaries of the finite element domain. In order to reduce the numerical effort, we terminated the finite element mesh at a small, but nonzero value $\omega_\lambda^{\min}$ of ω_λ and at this value of ω_λ the solutions are set to zero. The value of $\omega_\lambda^{\min}$ is chosen to be small enough that the potential energy is very high so that the surface functions are negligible at smaller values of ω_λ. Convergence of the surface function eigenvalues with respect to this parameter depends on the level of excitation of these functions. The lowest surface function eigenvalues converge more quickly than the higher ones which penetrate more deeply into the classically forbidden region. In addition, there are competing effects; for a fixed number of finite elements, decreasing $\omega_\lambda^{\min}$ spreads the elements over a larger area which in turn, reduces the accuracy of the finite element approximation. The 30^{th} A_1 surface function eigenvalues vary by 0.5% when $\omega_\lambda^{\min}$ is reduced from the value used in the full scattering calculations.

There are other geometric parameters which are associated with the propagation of the logarithmic derivative matrix in ρ as an initial value problem. We have used Johnson's logarithmic derivative propagator[38] in our calculations.

One parameter used in the propagation is the initial value ρ_0 of the hyperradius at which the scattering wave function is set to zero. We have used $\rho_0 = 2.0$ bohr for the PKII calculations and $\rho_0 = 1.8$ bohr for the LSTH calculations. On the LSTH surface the use of $\rho_0 = 1.8$ bohr and $\rho_0 = 1.9$ bohr gave identical probabilities and phases to at least four figures for all energies below 1.6 eV for all scattering matrix elements.

The final value ρ_{max} of ρ at which the propagation ends and projection of the hyperspherical solutions onto the Jacobi coordinate solutions takes place is another parameter in the calculations. We used the value $\rho_{max} = 12$ bohr because the potential energy surface is that of an isolated diatomic molecule at this and larger values of the hyperradius. Convergence of scattering matrix elements with respect the value of ρ_{max} was not investigated. The range of hyperradii at which the atom is isolated from the diatomic molecule is known independently of a scattering calculation. Futhermore, extending the scattering calculations to larger hyperradii simply increases the errors due to nonorthogonal overlap matrices and roundoff. It is important to bear in mind that scattering matrix element phases are sensitive to the value of ρ_{max}, while the probabilities are not. At low translational energies, the phases are sensitive because the effective de Broglie wave length is quite long. A final parameter associated with the propagation is the length of the propagation step. We have used both 0.01 bohr and 0.005 bohr step sizes and found that the differences in probabilities are parts per million. The propagation machinery is probably the most accurate part of the calculations.

We now consider the numerical parameters which determine the completeness of the expansion of the numerical scattering wave function. There are two parameters connected with this topic. One is the number of surface functions used to expand the wave function in a single sector. A sector is defined as the range of ρ values over which a single set of surface functions is employed. The

other is the size of the sectors. These two parameters are closely related and either one can be changed to improve the completeness of the basis set. A smaller surface function set is adequate over a smaller sector and vice versa. The length of a sector we used was 0.05 bohr in the PKII calculations and 0.1 bohr in the LSTH calculations. For PKII, the A_1 and E calculations employed 26 and 43 surface functions, respectively. For LSTH, the number of A_1, A_2, and E surface functions used is 34, 33, and 65, respectively.

The ideal technique for determining the error from the finiteness of the surface function set is to use slightly fewer surface functions and find the change in the results. (Or if the computer resources are available, do a calculation with a larger number of surface functions.) Reducing the number of A_1 surface functions from 34 to 32 at 1.55 eV and leaving all other numerical parameters unchanged, we found that all probabilities are converged to 5% or better (typically convergence of probabilities is less than 1%) and phases are converged to 2° or better. For transitions to and from the highest rotational states ($j \geq 10$) with small probabilities ($\leq 10^{-4}$), the convergence is less satisfactory. The A_2 scattering matrices are converged to the same level as the A_1.

This approach has proved impossible for the E calculations due to the large number of avoided crossings in the surface function eigenvalues as functions of ρ. Specifically, we have found it impossible to omit one or two surface functions and repeat a calculation because of the resulting unacceptably large loss of particle flux. It was possible to use 65 E surface functions. The next smaller set of surface functions was 43. Comparing these two calculations is not very useful. We have no indication that the E scattering matrices are converged to a lesser degree than the A_1 scattering matrices. For example, the unitarities of the scattering matrices for all three irreducible representations become greater than a few percent at the same total energies ($\geq$ 1.6eV).

The final numerical parameter that we will discuss is the value of ρ beyond which all surface functions are assumed to have negligible amplitude between

arrangement channel regions. For sufficiently large values of the hyperradius, the surface functions may be replaced by a separable basis set. The motivation for a change in the type of basis set used is the expense of the finite element technique. We are limited in the number of elements we can afford to include due to both memory and cpu time limitations. For hyperradii at which the arrangement channels are separated by a wide classically forbidden region of configuration space and the classically allowed regions of configuration space are compact, the surface functions are localized in the arrangement channel regions. The finite element mesh is too expensive to waste on regions of configuration space where the functions are negligible and should be localized in regions where the surface functions are localized. However, for these large hyperradii at which the arrangement channels are effectively separate, the finite element approach is not necessary because a separable basis set is a very good one and much cheaper. The strength of the finite element approach is that it can represent functions with a complicated structure as in the strong interaction region. However, when the arrangement channels have separated, the solutions to the Schrödinger equation are simply perturbed diatomic molecule wave functions and the flexibility of the finite element approach is not needed. We used the separable basis set beginning at 6 bohr. Comparing calculations on the PKII surface using 6 bohr and 6.5 bohr as the hyperradius beyond which the separable basis set is used, the convergence is 2% and 2° for probabilities and phases, respectively.

Two important overall measures of the accuracy of a scattering calculation are the unitarity and symmetry of the scattering matrix. For all energies below 1.55 eV, the deviations from unitarity are 2% or less. Over the same energy range, the scattering matrix is symmetric to within 10% for elements with squared modulus greater than 0.01. These are the worst cases and at lower collision energies, the scattering matrix unitarity and symmetry are much better. We have in no way enforced either characteristic on the results. Parker, Pack, and coworkers[34] report unitarities and symmetries of 0.1% or better. This suggests

that perhaps some form of symmetrization may be taking place implicitly or explicity in their method. Otherwise, it is very interesting to understand how they have attained such unitarities since their method is much like ours.

The amount of computer time used to do a scattering calculation determines to a great extent the usefulness of the method. On a Cray X-MP/48, the finite element calculation of surface functions requires 6 seconds per surface function for the A_1 and A_2 irreducible representations and 8 seconds per surface function for the E representation based on a $70\omega_\lambda$ and $70\gamma_\lambda$ finite element mesh. The interaction and overlap matrix calculations require 8 seconds per matrix for 67 E surface functions and 6 seconds per matrix for 34 A_1 surface functions. For the interaction matrix integrals, the calculation of the potential energy is the dominant task so the number of surface functions is not a big factor in determining the computer time for these integrals. The total time required to calculate all surface and separable functions and the corresponding interaction and overlap matrices is 3.76 hours and 15.08 hours for the 34 A_1 and 67 E surface functions, respectively. In passing, we note that half of the total time used is expended on I/O with the disk drives which is necessary because of memory limitations.

The logarithmic derivative propagator requires 106 seconds for matrices of dimension 65 (E representation) and 16 seconds per energy for matrices of dimension 34 (A_1 representation). The particular irreducible representation does not influence this time. It depends only on the number of steps (1060 steps) and the dimension of the matrices. We have not optimized the propagator or several key sections of the finite element program as much as is possible, so these times are conservative. Since many hundreds of total energies are used, the total propagation time is several hours.

3. Permutation Symmetry and the Pauli Principle

The identicity of the three hydrogen atoms in the present calculations permits the classification of the spatial wave functions, scattering matrices, and

scattering amplitudes by the irreducible representation labels from the group P_3 which is the group of all possible permutations of three identical objects. In the previous papers,[4,5] we exploited this permutation symmetry to reduce the numerical effort needed to construct solutions to the nuclear Schrödinger equation. Here, we are concerned with the relations between results labeled by the P_3 irreducible representation A_1, A_2, and E, the Pauli antisymmetrized results, and the familiar reactive-nonreactive results. The irreducible representation labels used are those of the point group C_{3v} which is isomorphic with P_3 and whose representation labels have familiar meanings. The irreducible-representation-labeled solutions refer to the spatial part of the wave functions alone. All interactions which depend on nuclear spin are completely negligible at the energies of these calculations and nuclear spin did not enter into the numerical procedures.

Electronic spin was taken into account implicitly by the use of the LSTH surface (corresponding to the doublet electronic ground state of the H_3 system) and by the assumption of electronic adiabaticity of the reaction at the collision energies considered. All wave functions considered in the present paper refer to either nuclear spatial or nuclear spin wave functions.

We are free to choose the nuclear spin functions for the three particles to be simultaneous eigenfunctions of $\hat{S}^2$ and $\hat{S}_Z$ with eigenvalues $S(S+1)\hbar^2$ and $M_S\hbar$, respectively. $\hat{S}^2$ is the operator for the total nuclear spin angular momentum squared and $\hat{S}_Z$ is the operator for the space-fixed component of the total nuclear spin angular momentum. For three spin one-half nuclei, the total spin states are quartet ($S = \frac{3}{2}$) and doublet ($S = \frac{1}{2}$). The quartet spin functions are totally symmetric under any permutation operation, *i.e.*, they transform as the A_1 irreducible representation. The doublet spin functions transform as the E irreducible representation. No other nuclear spin states exist for the three hydrogen atoms.

The absence of nuclear spin-dependent interactions in the Hamiltonian permits the complete solutions of the nuclear Schrödinger equation to be written

as the direct product of a spatial wave function and any one of the spin states. Since both the spatial and spin wave functions have well defined transformation properties under the operations of P_3, the direct product solutions (total solutions) for nuclear motion do also. The direct product decompositions for C_{3v} are

$$A_1(\text{spatial}) \otimes A_1(\text{spin}) = A_1(\text{total}) \tag{1}$$

$$A_1(\text{spatial}) \otimes E(\text{spin}) = E(\text{total}) \tag{2}$$

$$A_2(\text{spatial}) \otimes A_1(\text{spin}) = A_2(\text{total}) \tag{3}$$

$$A_2(\text{spatial}) \otimes E(\text{spin}) = E(\text{total}) \tag{4}$$

$$E(\text{spatial}) \otimes A_1(\text{spin}) = E(\text{total}) \tag{5}$$

$$E(\text{spatial}) \otimes E(\text{spin}) = A_1 \oplus A_2 \oplus E(\text{total}) \tag{6}$$

In the particular case of three fermions, the Pauli principle requires the total solution to transform as A_2 under the operations of P_3. Equations (1) through (6) show that the only spatial solutions which occur in nature are those that transform as A_2 and E for three identical spin one-half nuclei. In other words, we can uniquely associate a total nuclear spin state with a spatial wave function when the Pauli principle is satisfied by the total wave function. The E spatial solutions are associated with the doublet nuclear spin state and the A_2 spatial solutions are associated with the quartet nuclear spin state. The A_1 spatial wave functions do not occur in physically acceptable solutions when the three nuclei have spin one-half. We will nevertheless present a small number of A_1 results for their theoretical interest.

It was shown in paper II[5] that the Pauli antisymmetrized differential cross sections, when summed over initial nuclear spin states and averaged over final nuclear spin states, are simple linear combinations of the corresponding spatial A_2 and E differential cross sections. When the initial rotation state of the diatomic molecule is even, the Pauli cross sections are equal to the (spatial) E cross sections, regardless of the final rotational states. If an experimentalist selects the

initial diatom rotational state to be even (para-hydrogen), then the three-particle system has been chosen to behave spatially as the E irreducible representation and to be in a doublet nuclear spin state. When the initial rotational state of the diatomic molecule is odd (ortho-hydrogen), then two possiblities exist depending on the final rotational state of the diatomic molecule. If the final rotational state is even, then the Pauli cross section is one-third of the E spatial cross section. If the final diatom rotational state is odd, the Pauli cross section equals one-third of the spatial E plus two-thirds of the spatial A_2 cross sections. In other words, the A_2 spatial wave functions are only necessary to describe the ortho to ortho transitions. If an experimentalist has no control over the initial nuclear spins of the three atoms or sensitivity to their final nuclear spins and selects the initial rotational state to be odd, then we can say that the system has a one third probability of looking like spatial E and two-thirds probability of looking like spatial A_2. If he observes even final rotational states then he is examining only the part of the system that transforms spatially as E. If he observes odd final rotational states then he is observing an admixture of the E and A_2 spatial solutions.

The most familiar representation for the results of reactive scattering calculations is the reactive-nonreactive picture which can be constructed from the P_3 irreducible representation results.[4] Reactive transitions are those in which the final arrangement channel differs from the initial one. Nonreactive transitions are those which begin and end in the same arrangement channel. In the reactive-nonreactive picture it is assumed that the particles are distinguishable whether they are identical or not. Such a procedure is allowed in classical mechanics where trajectories can be used to distinguish identical particles. In quantum mechanics, identical particles can be distinguished only if their wave packets have no overlap at any time which is not the case for a scattering experiment, so the reactive-nonreactive picture is fictious. When the particles are identical an experimentalist cannot determine if the product diatomic molecule

belongs to the same arrangement channel as the initial diatomic molecule or another arrangement channel. Mathematically, there is no difficulty in using the reactive-nonreactive picture for quantum mechanical scattering.[4] The incident plane wave is simply restricted to one arrangement channel. By contrast, the P_3 irreducible representation spatial scattering wave functions have an incident plane wave in all three arrangement channels thereby incorporating the indistinguishability of the particles.

There are cases for which it is possible to say that the transition is reactive. When the initial and final rotational states of the diatomic molecules differ by an odd number of rotational quanta, then the transition is reactive. This conclusion follows formally from the fact that the scattering amplitude and scattering matrix elements representing nonreactive transitions with an odd number of rotational quanta change vanish identically. The physics behind this conclusion is simple. There are no spin-dependent interactions by assumption. A change in the parity of the diatom's spatial wave function requires also a change in its nuclear spin state and this can only occur with an exchange of nuclei, implying a reactive transition. For transitions which involve a change in the diatom's rotational quantum number by an odd integer, the reactive cross section differs from the corresponding E irreducible representation one by the constant $\frac{1}{3}$. On the other hand, it is not possible to determine that a transition is nonreactive in an experiment.

In this paper, we will focus attention on the irreducible representation results because they are closest to nature; however, some reactive results will be presented because they have such a well established history. We are conscious that the results in this paper are restricted to the lowest total spatial angular momentum state $J = 0$ while we have emphasized comparison with experiments and nature which are not so restricted. Furthermore, it is not even true that the lowest partial wave dominates the cross section.[6c] The finite element method used for these calculations is accurate and robust, but is also expensive, so that

higher partial waves will be calculated with other techniques in development in our laboratory. In spite of the angular momentum restriction of these calculations, they represent the highest energies yet solved accurately for any reactive system and we wish to draw our conclusions from results which are are as close to nature as possible.

4. A_1 Scattering Results

The A_1 irreducible representation scattering wave function contains scattering amplitudes for transitions from even initial rotational states of the diatomic molecule to even final rotational states. As shown in section 3, it does not contribute to any Pauli antisymmetrized scattering wave function for any partial wave. This representation is of interest because it supports resonance structure and it also contributes to the reactive and nonreactive components of para to para transitions.[4] Furthermore, it is less expensive to calculate since there are fewer states open at a given total energy than for the E representation. The J partial wave, A_1 irreducible representation body-fixed scattering matrix elements $(S^{J,A_1})^{v',j',k'}_{v,j,k}$ are expressed in terms of the corresponding reactive and nonreactive scattering matrix elements $(S^J)^{\lambda',v',j',k'}_{\lambda,v,j,k}$ as

$$(S^{J,A_1})^{v',j',k'}_{v,j,k} = (S^J)^{\beta,v',j',k'}_{\beta,v,j,k} + 2(S^J)^{\beta,v',j',k'}_{\alpha,v,j,k} \tag{7}$$

where both j and j' are even. The superscripts λ', v', j', k' denote the initial arrangement channel and diatom state. The subscripts λ, v, j, k denote the final arrangement channel and diatom state. v' and v are the diatom vibrational quantum numbers, j' and j are diatom rotation quantum numbers, and k' and k are the diatom rotational angular momentum projection quantum numbers for the helicity representation.

In figure 1, we show the $J = 0$ A_1 probabilities for transitions of the type $(0,0,0) \rightarrow (0,j,0)$ for $j = 0,2,4,6$ which originate from the lowest diatomic molecule state as a function of the total energy E (lower abscissa) and initial

translational energy $E_{0,0}$ (upper abscissa). We use the notation $(v', j', k') \rightarrow (v, j, k)$ to describe the process. We will use the word *product* to refer to the final diatomic molecule whether it appears in the same arrangement channel as the initial state or not. From this figure, we can see how much rotational excitation occurs from the collision of the ground state molecule. For all of the A_1 results in this paper, ever 10^{th} data point or energy is depicted, so that the curve is not obscured by the markers. Calculations at over 500 energies were performed.

In panel (a) of figure 1, it is seen that below 0.2 eV translational energy, the probability of initial state loss is small. Above that energy, the probability of initial state loss increases very rapidly. From panel (b), we see that most of the final state population is $(0,2,0)$ for 0.3 to 0.5 eV translational energy. For translational energies around 0.6 eV, the products are roughly 30% in $(0,2,0)$ and 50% in $(0,4,0)$. At 0.8 eV translational energy, the product distribution is about 40% $(0,2,0)$, 20% $(0,4,0)$, and 20% $(0,6,0)$. One common feature of panels (b), (c), and (d) is that as the energy increases there is a threshold follow by a distinct local maximum in the probability curve. The maximum occurs at increasing translational energies as the final j increases and represents the largest absolute maximum attained in each curve. For the transition $(0,0,0) \rightarrow (0,2,0)$, the probability generally decreases following that maximum. For the transitions $(0,0,0) \rightarrow (0,4,0)$ and $(0,0,0) \rightarrow (0,6,0)$, the probability of the rotational excitation becomes comparable at higher translational energies to the maxima. In addition, the maximum probability decreases and the effective threshold for significant probability increases with increasing final j.

The alert reader will have noticed that all transitions mentioned have initial diatom rotational projection quantum numbers of zero and the corresponding final projection quantum numbers are also zero. This is a consequence of the restriction to the $J = 0$ partial wave and the helicity representation of the scattering wave function. Within the $J = 0$ partial wave, the diatom rotational projection quantum numbers must be zero.

In figure 2, we present the corresponding $J = 0$ A_1 transition probabilities for vibrationally excited H_2 initial states: $(1,0,0) \rightarrow (1,j,0)$ for $j = 0,2,4,6$. As for the ground vibrational state curves of figure 1, there is a dramatic loss of the initial state beyond an initial translational energy, which in the present case is 0.05 eV. This value for $v = 1$ is smaller than the 0.2 eV threshold of figure 1a. The probability of observing product molecules in the same state as the initial diatomic molecule falls to zero near 0.2 eV translational energy. Seventy percent of the product diatomic molecules at that energy are in the state $(1,2,0)$ as is seen in panel (b) of figure 2. Panels (c) and (d) imply that the remainder of the product must appear in the ground vibrational state because the high rotational levels do not have much probability ($\leq 1\%$) of being populated by the collision. The sharp drop in probability in panel (a) coincides energetically with the occurance of a resonance at 0.981 eV total energy.[3b] (The energies and characterization of resonances in this system are given in Table I and are discussed in more detail in section 7.) This resonance apparently causes the inital state to be completely lost and most of the product to appear in the $v = 1$,$j = 2$ state. In panel (b), the probability of exciting $(1,2,0)$ is less than 15% except in narrow regions around the two sharp peaks. For translational energies above 0.4 eV, the likelihood of exciting $(1,4,0)$ and $(1,6,0)$ from $(1,0,0)$ is about 25% and 10%, respectively. Overall, away from resonances, the there is less rotational excitation within the $v = 1$ manifold than there is within the $v = 0$ manifold when the initial rotational state is $j = 0$. We see that resonances have a dramatic effect on the final state populations of $v = 1$ when the initial state is also $v' = 1$.

In figure 3, probabilities for the transitions $(0,j',0) \rightarrow (1,0,0)$ for $j' = 0,2,4,6$ for $J = 0$ and the A_1 irreducible representation are shown. From this figure, we can assess the effectiveness of rotational energy for producing a particular vibrationally excited final state $(1,0,0)$ which has no rotational excitation. These transitions correspond to the conversion of *all* of the initial rotational energy into vibrational energy. As in figures 1 and 2, resonances have a considerable

effect on these transitions. Interestingly, in panels (a) and (b) we see that the E=0.981 eV resonance promotes the excitation of $(1,0,0)$ from $j' = 0,2$, while the E=1.36 eV resonance reduces the likelihood of the formation of $(1,0,0)$. At 1.0 eV total energy, the $j' = 0,2$ initial states are almost equally likely to result in vibrational excitation, while at the same total energy the $j = 4,6$ initial states have little probability of producing vibrational excitation. At 0.8 eV translational energy, $j' = 2,4$ initial states are almost three times as likely to cause vibrational excitation as $j' = 0$. The $j' = 4$ initial state is effective in producing $(1,0,0)$ only over the small translational energy range from about 0.8 eV to about 0.9 eV.

In summary, the $J = 0$ A_1 scattering probabilities have displayed some interesting features. The effect of resonances on the curves is quite strong. This will become even more apparent when the A_2 results are discussed in the next section because A_2 does not have resonance states at the energies we have examined. In addition to the sharp oscillations in the A_1 probabilities, this representation is *active* in the sense that the initial state of the diatomic molecule is not likely to reappear as a state of the products. Finally, high rotational excitation is not likely in the products and is not effectively converted into vibrational excitation.

5. A_2 Scattering Results

The A_2 irreducible representation scattering wave function contains only those transtition amplitudes to and from odd rotational states of the diatomic molecules. The A_2 scattering matrix elements are linear combinations of both reactive and nonreactive transitions and do have a part in nature. The Pauli principle associates these A_2 spatial results with the quartet total spin state of the nuclei. The relationship between the J partial wave A_2 body-fixed scattering matrix elements and the corresponding distinguishable particle scattering matrix elements is

$$(S^{J,A_2})^{v',j',k'}_{v,j,k} = (S^J)^{\beta,v',j',k'}_{\beta,v,j,k} + 2(S^J)^{\beta,v',j',k'}_{\alpha,v,j,k} \qquad (8)$$

where both j and j' are odd. In addition, the expressions for the distinguishable particle (reactive-nonreactive) scattering matrix elements in terms of the irreducible representation matrix elements are given in section 6.D.

In figure 4, we display transition probabilities from the initial state $(0,1,0)$, which is the lowest diatom state in this representation to final rotational states in the $v = 0$ vibrational manifold. From this figure, we can analyze about the degree of rotational excitation produced by the collision. Figure 4 is the A_2 counterpart of figure 1 and some insight is gained by comparing them. One overall characteristic of the A_2 probability curves is that they display less rotational excitation over the entire energy range shown than do the corresponding A_1 curves. Panel (d) shows that excitation to the state $(0,7,0)$ is very unlikely from the initial state $(0,1,0)$. Both the A_1 (figure 1) and A_2 (figure 4) results are similar in the occurence of maxima at successively higher energies for successively higher final rotational states. The maximum in panel (b) is at 0.4 eV translational energy; that in panel (c) occurs at 0.8 eV translational energy; and that in panel (d) is at 1.2 eV translational energy.

A very important feature of these A_2 curves is the complete lack of fine structure which suggests the absence of any resonances over this energy range. These curves are strikingly smooth in their energy dependence as compared to their A_1 counterparts in figure 1. In section 7, we will show that the lifetime matrix analysis indicates an absence of A_2 resonances over the energy range shown in figure 4.

In figure 5, the probability of rotational excitation within $v = 1$ manifold from the initial state $(1,1,0)$ for $J = 0$ A_2 is shown. This figure is the A_2 counterpart of the A_1 probabilities in figure 2. As for the ground vibrational manifold transitions in figure 4, the degree of rotational excitation is small and generally decreases for increasing amounts of rotational excitation in the product molecule. These curves also show a complete lack of any sharp resonance structure.

In figure 6, we display the probabilities for the transitions $(0, j', 0) \rightarrow (1, 1, 0)$ for $j' = 1, 3, 5, 7$ for $J = 0$ A_2. This figure is the counterpart of the A_1 results of figure 3. From figure 6, we can analyze the effectiveness of rotational excitation in promoting the formation of the $(1, 1, 0)$ vibrationally excited state. At a given total energy, initial rotational excitation does nothing to promote the formation of the product $(1, 1, 0)$. In panels (a) through (c), the probability curves are monotonically increasing functions of energy E. In panel (d) the probability curve shows a maximum. At a fixed translational energy (say 1.0 eV), $j = 3$ is no more likely to form $(1, 1, 0)$ than $j = 1$ and $j = 5, 7$ are much less likely to result in $(1, 1, 0)$. For these A_2 transitions, rotational excitation in the reagents does not promote vibrational excitation. In fact, high rotational excitation up to $j' = 7$ in the initial diatomic molecule lowers the probability of formation of $(1, 1, 0)$. Unlike the corresponding A_1 results in figure 3, resonance structure plays no part in the A_2 dynamics.

The $J = 0$ A_2 probability curves are interesting in their contrast to the A_1 curves. The A_2 probabilities show no resonance structure. The likelihood of forming diatomic states which are different from the initial diatomic states is much smaller in the case of A_2. These dynamics are probably a consequence of the nodal structure of the corresponding surface functions. The A_2 surface functions have nodal lines in the regions of configuration space which are important in causing excitation in the final diatomic molecule.

6. E Scattering Results

The E irreducible representation scattering wave function contains transitions between all energetically allowed states of the diatomic molecule, including both even and odd rotational states. The expression for the J partial wave E irreducible representation body-fixed scattering matrix elements in terms of the

corresponding distinguishable particle scattering matrix elements is: for j' and j both even

$$(S^{J,E})^{v',j',k'}_{v,j,k} = (S^J)^{\beta,v',j',k'}_{\beta,v,j,k} - (S^J)^{\beta,v',j',k'}_{\alpha,v,j,k} \qquad \text{for j' and j even} \tag{9}$$

$$(S^{J,E})^{v',j',k'}_{v,j,k} = \sqrt{3}(S^J)^{\beta,v',j',k'}_{\gamma,v,j,k} \qquad \text{for j' even and j odd} \tag{10}$$

$$(S^{J,E})^{v',j',k'}_{v,j,k} = -\sqrt{3}(S^J)^{\beta,v',j',k'}_{\gamma,v,j,k} \qquad \text{for j' odd and j even} \tag{11}$$

$$(S^{J,E})^{v',j',k'}_{v,j,k} = (S^J)^{\beta,v',j',k'}_{\beta,v,j,k} - (S^J)^{\beta,v',j',k'}_{\gamma,v,j,k} \qquad \text{for j' and j odd.} \tag{12}$$

A. Zero Impact Parameter Collisions

In this section, we present $J = 0$ partial wave cross sections for collisions in which the initial rotational state of the diatomic molecule is $j' = 0$. We have chosen to display partial cross sections instead of transition probabilities because the former are closest to physical reality and the E irreducible representation is the one which contributes to experimental cross sections. Since $\hat{\mathbf{J}} = \hat{\mathbf{j}} + \hat{\mathbf{l}}$, where $\hat{l}$ is the angular momentum associated with the relative motion of the atom with respect to the center of mass of the diatomic molecule, we conclude that for $J = j = 0$, we must have $l = 0$, where J, j, and l are the total, diatom rotational, and orbital angular momentum quantum numbers. This corresponds to collisions with zero impact parameter in classical mechanics. The final rotational state of the diatomic molecule is not restricted and we wish to understand how effective translational energy is for producing rotational excitation in the products of the collision for the E irreducible representation. This representation contains transitions between all energetically allowed states of the diatomic molecule.

For three identical atoms the $J = 0$ partial cross sections are related to the scattering matrix elements by[4]

$$\sigma^{J=0,\Gamma}_{(v',j',k')\to(v,j,k)}(\vartheta,\varphi) = \frac{\pi}{k'^2_{v',j'}} |\delta^{v',j',k'}_{v,j,k} - (S^{J=0,\Gamma})^{v',j',k'}_{v,j,k}|^2 \tag{13}$$

where

$$k'^2_{v',j'} = \frac{2\mu_{\lambda,\nu\kappa}(E - e_{v',j'})}{\hbar^2} \tag{14}$$

$$\mu_{\lambda,\nu\kappa} = \frac{2}{3}m \tag{15}$$

where $k'^2_{v',j'}$ is the initial relative wave number for total collision energy E and diatom initial state with internal energy $e_{v',j'}$, $\mu_{\lambda,\nu\kappa}$ is the reduced mass for the relative motion of the atom A_λ with respect to the center of mass of the diatomic molecule $A_\nu A_\kappa$ and m is the mass of each of the three atoms.

In figure 7, the $J = 0$ partial cross sections for the E irreducible representation transitions $(0,0,0) \rightarrow (0,j,0)$ for $j = 1,2,3,4$ are shown. Figure 7 is the E counterpart to figures 1 and 4. All transitions are to and from the lowest vibrational state of the diatomic molecule. The first observation is that there is not much rotational excitation in product H_2 as is the case for the A_1 and A_2 irreducible representations. This is consistent with the fact that the three saddle points are collinear and these are zero impact parameter collisions. Even at 1.6 eV total energy where rotational states with 13 quanta of excitation are energetically accessible, only the lowest few excited rotational product states are significantly populated by such collisions.

In figure 8, $J = 0$ partial cross sections for $(0,0,0) \rightarrow (1,j,0)$ for $j = 0,1,2,3$ for the E irreducible representation are presented. It can be seen that transitions to the state $(1,1,0)$ are significantly more probable than those to final states $(1,0,0)$, $(1,2,0)$, and $(1,3,0)$ at most collision energies. Indeed, the most likely product is $(1,1,0)$ at all collision energies. Also note that the resonance at 0.981 eV total energy greatly enhances the $(0,0,0) \rightarrow (1,1,0)$ transition. The $(0,0,0) \rightarrow (1,3,0)$ partial cross section has a pronounced maximum at 0.9 eV initial translational energy where it attains a magnitude comparable with that of the $(0,0,0) \rightarrow (1,1,0)$ transition. This maximum is probably due to the resonance with total energy 1.191 eV.

An interesting question concerns the likelihood that a vibrationally excited H_2 molecule is deactivated by a zero impact parameter collision. In figure 9, the $J = 0$ partial cross sections for the vibrational deexcitation transitions $(1,0,0) \rightarrow (0,j',0)$ for $j' = 0,1,2,3$ for the E irreducible representation are shown. Notice the different scales used in panels (a) and (b). The transitions to odd final rotational states with $v = 0$ shown in panel (b) have a factor of 10 greater partial cross sections than those to even final rotational states shown in panel (a) at translational energies below 0.5 eV. Above 0.5 eV translational energy, the final states $(0,2,0)$ and $(0,1,0)$ become equally probable. In addition, we note the pronounced effect of the resonances at 0.981 eV and 1.3653 eV total energy on the magnitude of the partial cross section, respectively for the transitions $(1,0,0) \rightarrow (0,1,0)$ and $(1,0,0) \rightarrow (0,2,0)$. Interestingly, the 1.3653 eV resonance reduces the probability of the transitions $(1,0,0) \rightarrow (0,1,0)$ and $(1,0,0) \rightarrow (0,3,0)$ while it enhances the $(1,0,0) \rightarrow (0,2,0)$ transition.

B. Effectiveness of Rotational Energy for Inducing Vibrational Excitation

For the $J = 0$ partial wave, we wish to address the question of the effectiveness of initial rotational energy in the diatomic molecule for producing a particular vibrationally excited state of the product molecule. In other words, at a fixed translational or total collision energy, is vibrational excitation more probable if the initial H_2 is rotationally hot?

In figure 10, we show $J = 0$ partial cross sections for the transitions $(0,j',0) \rightarrow (1,0,0)$ for $j' = 0,1,2,3$ for the E irreducible representation. Figure 10 is the E counterpart to figures 3 and 6. From figure 10, it is seen that the effectiveness of a given rotational state in producing the vibrationally excited state is highly dependent on the total energy of the collision. For example, the initial state $(0,3,0)$ is several times more likely to produce $(1,0,0)$ than the initial states $(0,0,0)$ or $(0,2,0)$ at total energies around 1.1 eV. In contrast, at total energies

above 1.5 eV, the initial states $(0,3,0)$ and $(0,0,0)$ have approximately equal probabilities of exciting the $v = 1$ state and the initial state $(0,2,0)$ is twice a likely to excite it. For all total energies, it is seen that adding one quantum of rotational excitation to the initial H_2 enhances the probability of forming $(1,0,0)$ by factor of 5 to 10 times relative to an initial H_2 in the ground rotational state. The initial state $(0,3,0)$ is also effective in producing the final state $(1,0,0)$ at total energies below 1.3 eV. This enhancement is not a consequence of increasing the total energy content of the system, but of the specific rotational mode of the initial diatomic molecule; otherwise, $j' = 2$ would be more effective than $j' = 1$ at the same translational energy which it is not at any energy shown.

Are these mode specific dynamics altered when a different final state in the vibrationally excited manifold is examined? To answer this question, we plot in figure 11 the partial cross sections from the same initial states to a final state with one quantum of rotational excitation: $(0,j',0) \rightarrow (1,1,0)$ for $j' = 0,1,2,3$. The $j' = 1$ initial rotational state is again more effective than $j' = 0$ for producing vibrationally excited H_2 at all collision energies. The resonance at 0.981 eV total energy dramatically enhances the probability of the transition $(0,1,0) \rightarrow (1,1,0)$ At higher collision energies, the three rotationally excited initial states are equally likely to result in the final state $(1,1,0)$. A comparison of figures 10 and 11 shows that there is less difference in partial cross sections at the high energies for the final state $(1,1,0)$ than for the final state $(1,0,0)$.

One other common feature of figures 10 and 11 deserves comment. The resonance at E=0.981 eV is strongly coupled to the initial state $(0,1,0)$ and significantly enhances its coupling to the vibrationally excited manifold.

C. Total Initial State Loss

In this section, we examine the squared modulus of the diagonal scattering matrix elements (probabilities) for the E irreducible representation. Partial cross sections are not shown because, due to the Kronecker delta in equation (13),

these are rapidly oscillating functions of the collision energy which obscures the underlying physics. The oscillations are caused by the strong dependence of the phase of the diagonal scattering matrix elements on energy.

In figure 12, we show the $J = 0$, E representation probabilities for the transitions $(0,j',0) \rightarrow (0,j',0)$ for $j' = 0,1,2,3,4,5$. In these, the final state of the H_2 molecule is the same as the initial state. The corresponding transitions in the $v = 1$ manifold are shown in figure 13. The most dramatic feature of curves in these two figures is the alternation in the degree of loss of the initial H_2 molecule state with initial rotational state. For all of these elastic E representation transitions, the probabilities are unity at low translational energies and decrease rapidly as a function of translational energy beyond some characteristic value. For even rotational states, the loss of the initial state is incomplete and becomes approximately constant as a function of energy. In contrast, for odd rotational states the loss of the initial state is almost complete. In other words, the degree of loss of the initial state is strongly dependent on the evenness or oddness of the initial rotational state. This conclusion holds for both the ground and excited vibrational manifolds.

Aside from the partial wave nature of these results, is there any sense in the comparison that we just made between these transitions, in view of the fact that ortho to ortho transitions include contributions from the A_2 irreducible representation in spin insensitive experiments? The answer is yes. The E cross sections correspond to the doublet total nuclear spin states and the A_2 cross sections correspond to the quartet spin states. It violates no physical principles to consider an experiment in which the spins of the nuclei are state selected so that a desired total nuclear spin state is achieved. That is not to say that such an experiment is technically possible; it currently is not, due to experimental difficulties, but it is conceptually feasible. It is therefore appropriate to examine transtitions with a single total nuclear spin state.

There is a simple intuitive explanation for the behavior seen in figures 12 and 13. First, recall that ortho-hydrogen has a triplet nuclear spin state and para-hydrogen has a singlet spin state (ignoring the third atom). For the E irreducible representation, the total three particle nuclear spin state is doublet. This information is enough to determine the nuclear spin state of the initial atom from the initial rotational state of the diatomic molecule. We can conclude that the initial atom nuclear spin is antiparallel to the nuclear spins of ortho-hydrogen. Therefore, the so called Pauli repulsion is not present in the E representation collisions with ortho-hydrogen initial states and the incident atom is more likely to get close to the diatomic molecule leading to transitions. In the case of para-hydrogen, the incident atom's nuclear spin is parallel to one of the nuclear spins in the diatomic molecule. The two nuclei with parallel spins experience Pauli repulsion and the incident atom has a lower probability of getting close to the diatomic molecule. The result is less loss of the initial state in the case of para-hydrogen as compared with the loss of ortho-hydrogen.

D. Reactive Probabilities Summed Over Final Rotational States

Does high rotational excitation in the initial H_2 diatomic molecule promote or inhibit *reactive* transitions? In figure 14, the energy dependence of the probability of a reactive transition from the state $(0,8,0)$ to all final rotational states in $v = 0$ and in $v = 1$ is plotted (*i.e.*, $(0,8,0) \rightarrow (0, j = all, 0)$ and $(0,8,0) \rightarrow (1, j = all, 0)$). The initial state $(0,8,0)$ of H_2 was chosen because it is almost isoenergetic with $(1,0,0)$. Transitions to $v = 2$ are negligible compared to those to $v = 0,1$ and are not displayed. From figure 14, we can see that high rotational excitation is effective is producing reactive transitions to vibrationally cold products when the collsion energy is large, but has 10% or smaller probabilities at any collision energy for exciting vibrationally hot reactive products. As a point of reference, figure 15 shows the corresponding final-j-summed reaction probabilities from the ground state of the diatomic molecule. Notice that

the maximum probability for producing vibrationally cold products from both initial states occurs at around 0.6 to 0.7 eV translational energies.

When the initial H_2 molecule is vibrationally hot and undergoes a reactive collision, is it more likely to end up in the ground or excited vibrational manifold? To address this question, the reaction probabilities for the transitions $(1,0,0) \rightarrow (v, j = all, 0)$ for $v = 0, 1$ are plotted in figure 16. At the phenomenological threshold for reaction $E_{1,0} \sim 0.2$ eV, the products are far more likely to be vibrationally hot. At translational energies above 0.4 eV, the final state populations are roughly equal in $v = 0$ and $v = 1$. Notice the effect of the resonance at 1.3653 eV total energy on these final-rotational-state-summed probabilities: The vibrationally hot product is enhanced and the vibrationally cold product is inhibited.

For completeness, we give below the expressions for the distinguishable particle scattering matrix elements in terms of the irreducible representation matrix elements.

For j and j' even:

$$(S^J)^{\beta,v',j',k'}_{\beta,v,j,k} = \frac{1}{3}\left[(S^{A_1,J})^{v',j',k'}_{v,j,k} + 2(S^{E,J})^{v',j',k'}_{v,j,k}\right] \tag{16}$$

$$(S^J)^{\beta,v',j',k'}_{\alpha,v,j,k} = \frac{1}{3}\left[(S^{A_1,J})^{v',j',k'}_{v,j,k} - (S^{E,J})^{v',j',k'}_{v,j,k}\right] \tag{17}$$

For j even and j' odd:

$$(S^J)^{\beta,v',j',k'}_{\beta,v,j,k} = 0 \tag{18}$$

$$(S^J)^{\beta,v',j',k'}_{\alpha,v,j,k} = \frac{-1}{\sqrt{3}}(S^{E,J})^{v',j',k'}_{v,j,k} \tag{19}$$

For j odd and j' even:

$$(S^J)^{\beta,v',j',k'}_{\beta,v,j,k} = 0 \tag{20}$$

$$(S^J)^{\beta,v',j',k'}_{\alpha,v,j,k} = \frac{+1}{\sqrt{3}}(S^{E,J})^{v',j',k'}_{v,j,k} \tag{21}$$

For j and j' odd:

$$(S^J)^{\beta,v',j',k'}_{\beta,v,j,k} = \frac{1}{3}\left[(S^{A_2,J})^{v',j',k'}_{v,j,k} + 2(S^{E,J})^{v',j',k'}_{v,j,k}\right] \tag{22}$$

$$(S^J)^{\beta,v',j',k'}_{\alpha,v,j,k} = \frac{1}{3}\left[(S^{A_2,J})^{v',j',k'}_{v,j,k} - (S^{E,J})^{v',j',k'}_{v,j,k}\right] \tag{23}$$

7. Resonance Structure

In the earliest days of accurate collinear reaction scattering, structure was observed in the reaction probability versus total energy curves and was attributed to an underlying metastable or resonance state.[9,10] Many examples of the resonances have been observed, quantified, and discussed for the collinear reactive scattering of three particles.[11,17] Of particular importance have been the adiabatic models of such resonances based on either periodic orbit dividing surfaces (PODS)[15,16,39] and on hyperspherical coordinates.[11,17] In this section, we discuss the lifetime analysis[7] of F. T. Smith as applied to the present scattering matrices from the LSTH potential energy surface. It has previously been shown that this analysis is capable of isolating these resonances very accurately.[40] Also discussed is the convenient classification of the resonances in terms of the quantum numbers associated with a linear stable triatomic molecule introduced by Bowman[13] and Colton and Schatz.[14]

In figures 1 through 16, we have interpreted the overall shape of the plots of transition probability or partial cross section against collision energy and commented on the corresponding dynamics. Many of the curves for the A_1 and E irreducible representations display rapid variations as a function of energy. These rapid variations are due to the formation of short-lived three-particle states in the strong interaction region of the potential energy surface.[11,3b] They can be understood as the result of interference between a direct (nonresonant) process and the resonance state.[10,11,41–43] In a sense, the curves are a vibrational spectrum of the metastable states of H_3. When the total collision energy is close

to the energy of a resonance state, the transition probability varies rapidly with energy for transitions which are strongly coupled to the resonance state.

In figures 17-19 are shown some of the eigenvalues of the collision lifetime matrix as a function of the total energy for the A_1, A_2, and E irreducible representations using the LSTH surface, respectively. For the A_1 lifetime analysis and energies near some of the resonances, scattering matrices were calculated every 0.0001 eV. For the A_2 lifetime analysis the energy spacing was as small as 0.001 eV. For all of the irreducible representations, the coarsest energy grid was 0.01 eV. The lifetime matrix eigenvalues shown in figures 17 through 19 are those that display maxima. We define these maxima as resonances, since they correspond to longer collision lifetimes than those at neighboring energies. Also indicated in these figures is the assignment of the resonance state.

In figures 17 through 19 we have intentionally omitted curves which have large eigenvalues at the opening of a new state of the diatomic molecule. It was common to obtain large lifetime matrix eigenvalues at such openings. These curves decrease rapidly with increasing energy and are quite distinct from the eigenvalue curves which are interpreted as representing resonances. The latter rise from a approximately constant baseline in a smooth manner to a maximum and fall back smoothly to the baseline. The curves that were eliminated begin at a large value and decrease rapidly with increasing energy (*i.e.*, they do not display an interior maximum). Whether these curves are due to numerical instabilities or are correct and have some straightforward interpretation is not known.

In figure 17 where the A_1 lifetime eigenvalues are displayed, there is a second curve which shows an interior maximum but is without a true baseline. There are approximately 50 energy points in this curve and it is very smooth when magnified, so it is not spurious and cannot be easily ignored. Notice also that this second curve has a maximum at energies just above the opening of a new state of the diatomic molecule and that the high energy baseline is at -40 fs while the low energy baseline is at roughly zero delay times. We are not confident

that we understand this feature of the lifetime analysis and have not assigned any quantum numbers to it, but we do not wish to omit it from our results. The corresponding lifetime analysis of PKII results does not produce such an anomalous curve.[3b]

Some parts of the curves in figures 18 and 19 are represented with a dotted line. The dotted line indicates parts of the lifetime eigenvalue curves which are subject to enough numerical noise that the exact position of the curve is uncertain. The dotted lines represent a good approximation to the lifetime curves but are not quantitatively correct.

It has been pointed out by Pollak[15] that maxima in the eigenvalues of the lifetime matrix can be due to trapping at adiabatic barriers (instead of in adiabatic wells), and he prefers not to call them resonances if this is the case. Such interpretations of the nature of metastable states are very important and interesting, but require the use of modeling for insights. For example, adiabatic models dependent vitally on the choice of coordinate systems.[15] However, when an appropriate choice of coordinates is made, the resonant periodic orbit method (RPO) accurately predicts the 3D resonance structure we observe. Nevertheless, our accurate collision lifetime results are model-independent, and we refer to any formation of a metastable state of the three particles in the strong interaction region (as manifest by a local maximum in a lifetime eigenvalue versus energy curve) as a resonance whether it can be accurately modeled as trapping at an adiabatic barrier or well. In another paper, we will describe the results of an adiabatic model of one of the strong resonances.

In a previous letter,[3b] we assigned quantum numbers to the PKII resonance states following the lead of Bowman[13] and Colton and Schatz.[14] The quantum numbers are those appropriate for a stable linear triatomic molecule and are $(v_1, v_2^{|\Omega|}, v_3)$, where v_1 is the symmetric stretch quantum number, v_2 is the bend quantum number, v_3 is the antisymmetric stretch quantum number, and Ω is the vibrational angular momentum quantum number. $\Omega\hbar$ is the component of the

total angular momentum along the molecular axis. It is called the vibrational angular momentum quantum number because it can be understood as arising from the doubly degenerate bending modes of the linear triatom system in the same way that circularly polarized light is understood as a linear superposition of linearly polarized light. We wish to be clear that the use of these quantum numbers is a convenient means of classifying the resonances, but is of limited validity. For example, the normal mode analysis of the H_3 resonances may not be valid because the resonance is weakly bound and we have made no effort to determine whether the quanta of excitation are in the symmetric stretch mode or in the antisymmetric stretch or both. The main reason the classification is sensible is that the resonances can be assigned into series with approximately constant energetic spacing.

The resonances we observe are all labelled with $\Omega = 0$, because the results are limited to the $J = 0$ partial wave. As a consequence of the vanishing of Ω, the only values of v_2 which are allowed are the even ones since v_2 has the ranges $v_2 = \Omega, \Omega - 2, \Omega - 4, \ldots, 0$ or $v_2 = \Omega, \Omega - 2, \Omega - 4, \ldots, 1$.[44]

In figures 17-19 and in Table I, we have indicated the assignments for the various maxima. These assignments are in accord with those given by Bowman and Colton and Schatz. It is of interest to compare the energies of the maxima in our lifetime analysis with the resonance energies predicted by Bowman's CEQB,[13] the CS method of Colton and Schatz,[14] the RPO model of Pollak[15,16] and the SCSA technique of Garrett and coworkers.[12] In table I, the resonance energies and assignments from our accurate calculations and the results from other methods for both the PKII and LSTH potential energy surfaces are listed.

From table I, we see that the agreement between the resonance energies found with all of these approaches is quite good. The weak resonances $(0, 0^0, 0)$ or $(0, 2^0, 0)$ which appear as maxima in the lifetime matrix eigenvalue curves had not previously been observed by approximate methods (see however reference 14). As discussed above, Pollak[15] has determined that these weak trappings of

the system in the strong interaction region are due to adiabatic barriers and we have no reason to dispute this conclusion. Bowman has observed several of the higher resonances on the LSTH surface in his approximate calculations using the collinear exact quantum bending corrected (CEQB) model and agrees very well with our accurate positions. In particular, he has noted the bending excited resonances. Colton and Schatz, using the coupled state (CS) approximation (which is exact for $J = 0$), have observed two of the resonances in table I as extrema in probability versus energy curves with positions in reasonable agreement with the accurate lifetime eigenvalue results. Pollak's extension of the periodic orbit dividing surface adiabatic model (PODS) to three-dimensions has permited the detailed assignment of the bending excited resonances and agrees very well with the exact results when the appropriate coordinate system is used. The stabilization method of Garrett, Truhlar, and coworkers[12] assigns the energies of the resonances $(1, 0^0, 0)$ and $(1, 2^0, 0)$ in good agreement with our results, but is the least accurate of the several approximate methods considered in Table I for the $(2, 0^0, 0)$ and $(2, 2^0, 0)$ resonances.

As a final comment, Pollak's[15] remarks about the effect on probability curves of the weak maximum in the lifetime matrix eigenvalue curve corresponding to the assignment $(0, 0^0, 0)$ can be evaluated. He suggests that trapping in an adiabatic barrier does not cause oscillations in the probability curves. We would like to point out that figure 1(a) does show a pronounced dip at the energy corresponding to this resonance. A more detailed modeling of the process associated with this $(0, 0^0, 0)$ lifetime matrix eigenvalue maximum is desirable.

8. Surprisal Analysis

We have performed a rotational surprisal analysis[45-47] on the $J = 0$ results for the PKII potential energy surface. The PKII surface partial cross sections for reactive transitions are used in order to compare the partial cross section surprisal with that obtained by Schatz and Kuppermann[6c] for the integral cross

sections. Our desire to compare with Schatz and Kuppermann also explains the unconventional form of the analysis given below which is identical with that performed in reference 6c.

The purpose of a surprisal analysis is to examine that part of the dynamics which is not determined by the available density of states. In pratice, the total cross section is divided by the prior distribution function which is based entirely on the available density of states. The result is a renormalized cross section which is plotted versus the parameter of interest. Such plots display the information content of the cross sections. Cross sections which follow the prior distribution have no information content in the sense that they are statistical in nature. Cross sections which deviate from the prior distribution, do so because of some underlying feature of the dynamics which is special to that system. The prior distribution function that we use is

$$P_{v,j}(E) = \frac{\rho(E - e_{v,j})}{\rho(E - e_{0,0})} \tag{24}$$

where $\rho(E^{tr}_{v,j})$ is the density of translational states (not to be confused with the hyperradius). $E^{tr}_{v,j}$ is the translational energy associated with total energy E and isolated diatomic molecule energy $e_{v,j}$. There is no factor of $2j+1$ in the density of states because for $J = 0$, the diatom rotational state projection quantum number must be 0. In other words, in the $J = 0$ partial wave, the diatomic molecule does not have access to $2j + 1$ states for each possible j, but only to one.

The surprisal analysis we perform in this paper is analagous to that in Schatz and Kuppermann[6c]. This unconventional form for the surprisal analysis is adopted in order to permit a comparison of our $J = 0$ partial cross section results to those for integral cross sections which they calculate up to 0.7 eV total energy. It was our hope that the present partial wave cross sections might have a surprisal plot similar to that of Schatz and Kuppermann, perhaps paving a way to transform the $J = 0$ partial wave cross sections into integral cross sections.

The rotational surprisal plot based on the PKII $J = 0$ partial wave cross sections is plotted in figure 20. The abscissa is the internal energy content of the product H_2 and the ordinate is the appropriate partial cross section divided by the prior distribution function. Each curve represents a differerent total collision energy. Only the points have meaning and the curve is made of straight line segments connecting the points corresponding to the same total energy. The use of dashed and solid lines is for clarity. We see that the results do not fall on straight lines, but are quite oscillatory, especially at increasing total collision energies. A comparison of our low energy surprisal curves with those of Schatz and Kuppermann (figure 23 of reference 6c) shows that the rotational surprisal analysis based on partial wave cross sections produces curves which do not have the same shape or slope as those based on integral cross sections even for E $\leq$ 0.7 eV. This is disappointing; however, the large deviations from straight lines shown in figure 20 of this paper are interesting and unexpected, indicating that partial cross sections are less subject to a surprisal parameterization than are integral cross sections.

9. Final State Vibrational Population Ratios

As a final topic, we examine the ratio of nascent populations of the the vibrationally hot and vibrationally cold products under single translational energy conditions. The initial distribution of H_2 states is assumed to be Boltzmann with a temperature of 298.15 K and the reagent H_2 is assumed to be entirely para-H_2. The initial para-H_2 distribution of states does include the $2j' + 1$ degeneracy factor associated with the diatomic molecule's initial rotational state j' and the appropriate nuclear spin statistics. The nascent final state populations are calculated from the $J = 0$ partial wave cross sections at a fixed initial relative translational energy summed over all final rotational states within the vibational manifold of interest. If the real experiment were somehow restricted to be in the $J = 0$ total spatial angular momenum state, then these population ratios would

be exact. Unfortunately, the partial cross sections make only a small contribution to the total cross section for $H + H_2$ [6c] and we do not wish to imply that these ratios can be compared meaningfully with experimental results. We simply wish to examine the dynamical characteristics of our $J = 0$ results.

In figures 21 through 23, the ratio of the nascent $v = 1$ population to the nascent $v = 0$ population as a function of the initial translational energy of the reagents is plotted as a solid line for reactive, nonreactive, and Pauli antisymmetrized cross sections, respectively. The dashed line in each figure represents the same ratio for the case when the initial para-hydrogen is not thermal but rather all in the $j' = 0$ state. Also shown as arrows at the top of each figure are the positions of the resonances as determined by the lifetime matrix analysis. Each resonance is marked by two arrows because that abscissa in figures 21 through 23 is initial relative translational energy. The value of this energy for which a resonance state is excited is dependent on the initial state of H_2. The two resonance energies marked correspond to initial rotational states $j' = 0$ (long arrows) and $j' = 2$ (short arrows). These two initial rotational states are the only para-H_2 states thermally populated at room temperature to any significant extent.

From the $J = 0$ nascent vibrational population ratios shown in figures 21 through 23, one can clearly see that the resonance structure manifests itself even with the thermal averaging of initial states and summing over final j states. One hopes that similar plots using the total cross sections will also show the underlying resonance features which these partial wave results do. Notice that all three representations (reactive, nonreactive, and Pauli antisymmetrized) show structure due to the resonances labeled $(1, 0^0, 0)$ and $(2, 0^0, 0)$ and none of them are much affected by the weak $(1, 2^0, 0)$ resonance; however, the strong $(2, 2^0, 0)$ resonance at about 1.55 eV total energy is seen only in the reactive representation. Such nacent vibrational state population ratios may allow experimentalists to uncover resonance structure.[27]

The resonance labeled as $(0, 2^0, 0)$ is not apparent in figures 21 through 23 because the probability of forming $v = 1$ is vanishing at the translational energies corresponding to this resonance.

The nascent final vibrational state population ratio appears to be a good method for searching for resonances experimentally. The strong resonances do significantly affect the ratio of $v = 1$ to $v = 0$ populations at the $J = 0$ level. Whether this is also true for the integral cross sections is a matter for future calculations and experiments.

10. Summary

The results of an accurate calculation of $J = 0$ partial wave scattering using symmetrized hyperspherical coordinates for the reactive system $H + H_2$ have been presented and discussed. Although partial wave results seldom dominate in chemical reactions, we have tried to interpret our results in a physical setting. We have examined the efficacy of various internal states of H_2 for inhibiting or enhancing state to state processes. We have also considered the question of final state populations in several ways. One of the most important themes in this exposition is the significance of the underlying resonance structure on the dynamics of $H + H_2$. It is our hope that these accurate $J = 0$ results shall soon be extended to $J > 0$ to yield differential and integral cross sections across resonance energies.

References

† Work supported in part by the U.S. Air Force Office of Scientific Research, Contract No. AFOSR-82-0341. Support from the U.S. Department of Energy, Grant No. DE-AS03-83ER 13118 is also acknowledged. We thank the San Diego Supercomputer Center on whose Cray X-MP/48 the calculations were performed.

¶ Work performed in partial fulfillment of the requirements for the Ph.D. degree in Chemistry at the California Institute of Technology.

‡ Contribution number

1. A. Kuppermann, *Chem. Phys. Lett.* **32**, 374 (1975).
2. R. T. Ling and A. Kuppermann, in: **Electronic and Atomic Collisions, Abstracts of Papers of the 9th International Conference on the Physics of Electronic and Atomic Collisions**, Seattle, Washington, 24-30 July, 1975, Vol 1., eds. J. S. Risley and R. Geballe (Univ. Washington Press, Seatle, 1975) pp. 353,354.
3. (a) A. Kuppermann and P. G. Hipes, *J. Chem. Phys.* **84**, 5962 (1986); (b) P. G. Hipes and A. Kuppermann, *Chem. Phys. Lett.* **133**, 1 (1987).
4. The first paper in this series.
5. The second paper in this series.
6. (a) G. C. Schatz and A. Kuppermann, *J. Chem. Phys.* **62**, 2502 (1975); (b) **65**, 4642 (1976); (c) 4668 (1976).
7. F. T. Smith, *Phys. Rev.* **118**, 349 (1960).
8. R. N. Porter and M. Karplus, *J. Chem. Phys.* **40**, 1105 (1964).
9. R. D. Levine and S. Wu, *Chem. Phys. Lett.* **11**, 557 (1971).
10. G. C. Schatz and A. Kuppermann, *J. Chem. Phys.* **59**, 964 (1973).
11. A. Kuppermann, in: **Potential Energy Surface and Dynamics Calculations**, ed. by D. G. Truhlar (Plenum Press, New York, 1981)pp. 405, 414.

12. B. C. Garrett, D. W. Schwenke, R. T. Skodje, D. Thirumalai, T. C. Thompson, and D. G. Truhlar, in: **Resonances** *Am. Chem. Soc. Symp. Ser.* **263**, (Am. Chem. Soc., Washington, 1984) p.375.
13. J. M. Bowman, *Chem. Phys. Lett.* **124**, 260 (1986).
14. M. C. Colton and G. C. Schatz, *Intern. J. Chem. Kinet.* **18**, 961 (1986).
15. E. Pollak, *Chem. Phys. Lett.* **137**, 171 (1987).
16. E. Pollak, *J. Phys. Chem.* **90**, 3619 (1986).
17. J. Römelt, *Chem. Phys.* **79**, 197 (1983); J. Römelt and E. Pollak, in: **Resonances**, *Am. Chem. Soc. Symp. Ser.* **263** (Am. Chem. Soc., Washington, 1984) pp.353,374; and references therein.
18. B. Liu, *J. Chem. Phys.* **58**, 1925 (1973); P. Siegbahn and B. Liu, *J. Chem. Phys.* **68**, 2457 (1978).
19. D. G. Truhlar and C. J. Horowitz, *J. Chem. Phys.* **68**, 2468 (1978); **E71**, 1514 (1979).
20. S. A. Cuccaro and A. Kuppermann, manuscript in preparation.
21. G. C. Schatz, in: **Theory of Chemical Reaction Dynamics**, ed. by D. C. Clary , Proceedings of NATO Workshop, Orsay, France, 1986, pp.1,26.
22. J. M. Bowman, *Adv. Chem. Phys.* **61**, 115 (1985).
23. B. C. Garrett and D. G. Truhlar, *Ann. Rev. Phys. Chem.* **35**, 159 (1984).
24. D. G. Truhlar and R. E. Wyatt, *Ann. Rev. Phys. Chem.* **27**, 1 (1976).
25. A. B. Elkowitz and R. E. Wyatt, *J. Chem. Phys.* **62**, 2504 (1975); **63**, 702 (1975).
26. R. B. Walker, E. B. Stechel, and J. C. Light, *J. Chem. Phys.* **69**, 2922 (1978).
27. J. J. Vallentini, private communication.
28. D. P. Gerrity and J. J. Vallentini, *J. Chem. Phys.* **81**, 1298 (1984); **82**, 1323 (1985); **83**, 2207 (1985).
29. E. E. Marinero, C. T. Rettner, and R. N. Zare, *J. Chem. Phys.* **80**, 4142 (1984).

30. U. Gerlach-Meyer, K. Kleinermanns, E. Linnebach, and J. Wolfrum, *J. Chem. Phys.* **86**, 3047 (1987).

31. K. Tsukiyama, B. Katz, and R. Bersohn, *J. Chem. Phys.* **84**, 1446 (1986).

32. R. Götting, H. R. Mayne, and J. P. Toennies, *J. Chem. Phys.* **85**, 6396 (1986); R. Götting, J. P. Toennies, and M. Vodegel, *Intern. J. Chem. Kinet.* **18**, 949 (1987); R. Götting, V. Herrero, J. P. Toennies, and M. Vodegel, *Chem. Phys. Lett.* **137**, 524 (1987).

33. S. A. Buntin, C. F. Giese, and W. R. Gentry, *J. Chem. Phys.* **87**, 1443 (1987).

34. G. A. Parker, R. T. Pack, B. J. Archer, and R. B. Walker, *Chem. Phys. Lett.* **137**, 564 (1987); R. T. Pack and G. A. Parker, *J. Chem. Phys.* **87**, 3888 (1987).

35. F. Webster and J. C. Light, *J. Chem. Phys.* **85**, 4744 (1986).

36. K. Haug, D. W. Schwenke, Y. Shima, D. G. Truhlar, J. Zhang, and D. J. Kouri, *J. Phys. Chem.* **90**, 6757 (1986).

37. J. Z. H. Zhang and W. H. Miller, *Chem. Phys. Lett.* **140**, 329 (1987).

38. B. R. Johnson, *J. Comp. Phys.* **13**, 445 (1973); **67**, 4086 (1977); NRCC Workshop, Lawrence Berkeley Laboratory, Report No. LBL-9501, 1979.

39. **Theory of Chemical Reaction Dynamics**, ed. M. Baer (CRC Press, Boca Raton, Florida, 1985).

40. A. Kuppermann and J. A. Kaye, *J. Phys. Chem.* **85**, 1969 (1981).

41. E. F. Hayes and R. B. Walker, in: **Resonances**, *Am. Chem. Soc. Symp. Ser.* **263** (Am. Chem. Soc., Washington, 1984) p.493.

42. D. W. Schwenke and D. G. Truhlar, *J. Chem. Phys.* **87**, 1095 (1987).

43. B. Gazdy and J. M. Bowman, submitted to *Phys. Rev. A*.

44. G. Herzberg, **Infrared and Raman Spectra of Polyatomic Molecules**, (Van Nostrand, Princeton, 1945) p.272.

45. A. Ben-Shaul, R. D. Levine, and R. B. Bernstein, *Chem. Phys. Lett.* **15**, 160 (1972); *J. Chem. Phys.* **57**, 5427 (1972).

46. R. B. Bernstein, **Chemical Dynamics Via Molecular Beam and Laser Techniques**, (Clarendon Press, Oxford, 1982) pp.196,225.

47. R. D. Levine and R. B. Bernstein, **Molecular Reaction Dynamics and Chemical Reactivity** (Oxford Univ. Press, New York, 1987) pp. 260,275.

TABLE I. Resonance energies.[a]

	LSTH					PKII	
Assign-ment	present results	CEQB[b]	CS[c]	RPO[d]	SCSA[e]	present results	RPO[f]
(0,0°,0)	0.65					0.61	0.61[g]
(0,2°,0)	0.880					0.847	0.85[g]
(1,0°,0)	0.981	0.974	0.98	0.981	0.984	0.971	0.975
(1,2°,0)	1.191	1.20	1.20	1.186	1.196	1.170	1.17[g]
(2,0°,0)	1.3635	1.35		1.374	1.242	1.382	1.366
(2,2°,0)	1.55 ± 0.02	1.50		1.545	1.464	1.56	1.542

[a]All energies are in units of eV measured from the bottom of the isolated H_2 potential well.

[b]Reference 13

[c]Reference 14

[d]Reference 16

[e]Reference 12

[f]Reference 15

[g]Adiabatic Barriers

Figure Captions and Figures

Figure 1. A_1 transition probabilities as a function of total energy for transitions of the type $(0,0,0) \rightarrow (0,j,0), j = 0,2,4,6$ for $H + H_2$ on the LSTH potential energy surface. For the A_1 representation, the results of only one out of every ten energies at which scattering calculations were made are depicted, for clarity of the curves. The lower abscissas in each panel indicates the total system energy E, whereas the upper abscissas represent the initial translational energy. The arrows pointing to the upper abscissa indicate the threshold energies for the opening of the (v,j) states of H_2. The longer arrows correspond to $v = 0$, the medium length ones to $v = 1$ and the shorter ones to $v = 2$.

Figure 2. A_1 transition probabilities as a function of total energy for transitions of the type $(1,0,0) \rightarrow (1,j,0), j = 0,2,4,6$ for $H + H_2$ on the LSTH potential energy surface. See caption of figure 1 for additional information.

Figure 3. A_1 transition probabilities as a function of total energy for transitions of the type $(0,j',0) \rightarrow (1,0,0), j' = 0,2,4,6$ for $H + H_2$ on the LSTH potential energy surface. See caption of figure 1 for additional information.

Figure 4. A_2 transition probabilities as a function of total energy for transitions of the type $(0,1,0) \rightarrow (0,j,0), j = 1,3,5,7$ for $H + H_2$ on the LSTH potential energy surface. See caption of figure 1 for additional information.

Figure 5. A_2 transition probabilities as a function of total energy for transitions of the type $(1,1,0) \rightarrow (1,j,0), j = 1,3,5,7$ for $H + H_2$ on the LSTH potential energy surface. See caption of figure 1 for additional information.

Figure 6. A_2 transition probabilities as a function of total energy for transitions of the type $(0,j',0) \rightarrow (1,1,0), j' = 0,2,4,6$ for $H + H_2$ on the LSTH potential energy surface. See caption of figure 1 for additional information.

Figure 7. $E\ J = 0$ partial cross sections as a function of total energy for transitions of the type $(0,0,0) \rightarrow (0,j,0), j = 1,2,3,4$ for $H + H_2$ on the LSTH potential energy surface. See caption of figure 1 for additional information.

Figure 8. $E\ J\ =\ 0$ partial cross sections as a function of total energy for transitions of the type $(1,0,0) \rightarrow (1,j,0), j = 0,1,2,3$ for $H + H_2$ on the LSTH potential energy surface. See caption of figure 1 for additional information.

Figure 9. $E\ J\ =\ 0$ partial cross sections as a function of total energy for transitions of the type $(1,0,0) \rightarrow (0,j,0), j = 0,1,2,3$ for $H + H_2$ on the LSTH potential energy surface. See caption of figure 1 for additional information.

Figure 10. $E\ J\ =\ 0$ partial cross sections as a function of total energy for transitions of the type $(0,j',0) \rightarrow (1,0,0), j' = 0,1,2,3$ for $H + H_2$ on the LSTH potential energy surface. See caption of figure 1 for additional information.

Figure 11. $E\ J\ =\ 0$ partial cross sections as a function of total energy for transitions of the type $(0,j',0) \rightarrow (1,1,0), j' = 0,1,2,3$ for $H + H_2$ on the LSTH potential energy surface. See caption of figure 1 for additional information.

Figure 12. E transition probabilities as a function of total energy for transitions of the type $(0,j',0) \rightarrow (0,j',0), j' = 0,1,2,3,4,5$ for $H + H_2$ on the LSTH potential energy surface. See caption of figure 1 for additional information.

Figure 13. E transition probabilities as a function of total energy for transitions of the type $(1,j',0) \rightarrow (1,j',0), j' = 0,1,2,3,4,5$ for $H + H_2$ on the LSTH potential energy surface. See caption of figure 1 for additional information.

Figure 14. Reactive transition probabilities as a function of total energy for transitions of the type $(0,8,0) \rightarrow (v, j = all, 0), v = 0,1$ for $H + H_2$ on the LSTH potential energy surface. See caption of figure 1 for additional information.

Figure 15. Reactive transition probabilities as a function of total energy for transitions of the type $(0,0,0) \rightarrow (v, j = all, 0), v = 0,1$ for $H + H_2$ on the LSTH potential energy surface. See caption of figure 1 for additional information.

Figure 16. Reactive transition probabilities as a function of total energy for transitions of the type $(1,0,0) \rightarrow (v, j = all, 0), v = 0,1$ for $H + H_2$ on the LSTH potential energy surface. See caption of figure 1 for additional information.

Figure 17. Highest eigenvalues of the F. T. Smith lifetime matrix as a function of total energy for $J = 0$ of the A_1 irreducible representation for $H + H_2$ on the

LSTH potential energy surface. The arrows at the top of the figure indicate the threshold for opening of the (v,j) states of H_2. The number of energies used in this plot is of the order of 500. The quantum numbers assigned to the maxima in the eigenvalue curve are also indicated in the figure. See text for discussion of the second curve shown.

Figure 18. Highest eigenvalues of the F. T. Smith lifetime matrix as a function of total energy for $J = 0$ of the A_2 irreducible representation for $H + H_2$ on the LSTH potential energy surface. The number of energies used in this plot is of the order of 300. See caption of figure 17 for additional information.

Figure 19. Highest eigenvalues of the F. T. Smith lifetime matrix as a function of total energy for $J = 0$ of the E irreducible representation for $H + H_2$ on the LSTH potential energy surface. The number of energies used in this plot is of the order of 100. See caption of figure 17 for additional information.

Figure 20. Rotational surprisal plot of the reactive representation transitions $(0,0,0) \rightarrow (0,j,0), j = 0,1,2,3,\ldots$ on the PKII surface. The abscissa is the final state rotational energy, $P_{v,j}(E)$ is the prior distribution function defined in equation (23), and $Q^{R,J=0}_{(0,0,0)\rightarrow(0,j,0)}$ is the partial cross section for the $(0,0,0) \rightarrow (0,j,0)$ transitions. The little upward arrows indicate the energies of the produce $(0,j,0)$ states of H_2. Each curve is labeled by the corresponding total energy E.

Figure 21. Ratio of nascent $v = 1$ to $v = 0$ vibrational state reactive populations (distinguishable atom representation) as a function of the translational energy of the reagents. $Q^{R,J=0}_{\mathbf{thermal}\rightarrow\mathbf{v}}$ refers to a thermal population of initial rotational states for para-hydrogen at T=298.15 K. The arrows pointing to the upper abscissa represent resonance positions, as explained in the text.

Figure 22. Ratio of nascent $v = 1$ to $v = 0$ vibrational state nonreactive populations as a function of the translational energy of the reagents. $Q^{NR,J=0}_{\mathbf{thermal}\rightarrow\mathbf{v}}$ refers to a thermal population of initial rotational states for para-hydrogen at T=298.15 K. The arrows pointing to the upper abscissa represent resonance positions, as explained in the text.

Figure 23. Ratio of nascent $v = 1$ to $v = 0$ vibrational state populations as a function of the translational energy of the reagents for Pauli antisymmetrized partial cross sections. $Q^{J=0}_{\mathbf{thermal}\rightarrow\mathbf{v}}$ refers to a thermal population of initial rotational states for para-hydrogen at T=298.15 K. The arrows pointing to the upper abscissa represent resonance positions, as explained in the text.

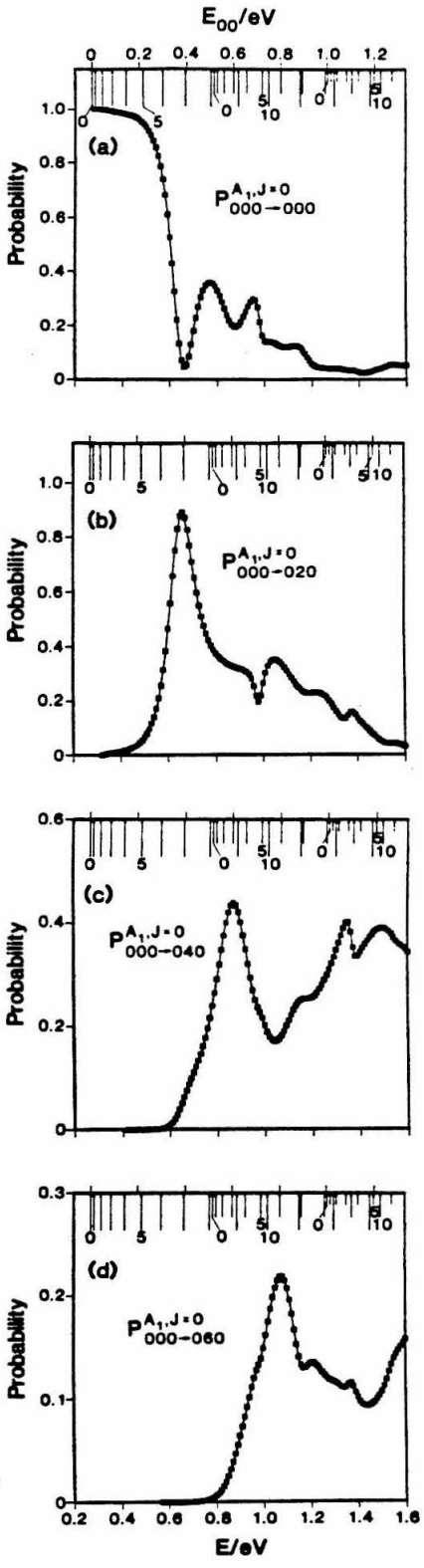
E00/eV
0 0.2 0.4 0.6 0.8 1.0 1.2
(a)
P A1,J=0 000−000
(b)
P A1,J=0 000−020
(c)
P A1,J=0 000−040
(d)
P A1,J=0 000−060
Probability
0.2 0.4 0.6 0.8 1.0 1.2 1.4 1.6
E/eV

Figure 1.

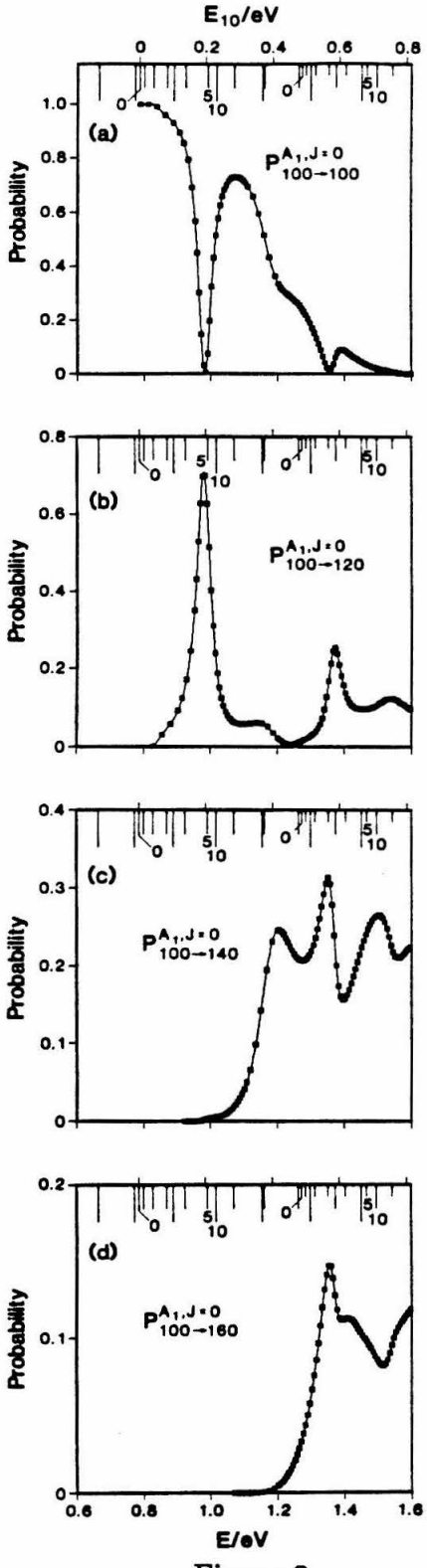
E10/eV
0
0.2
0.4
0.6
0.8
(a)
P A1,J=0 100→100
(b)
P A1,J=0 100→120
(c)
P A1,J=0 100→140
(d)
P A1,J=0 100→160
Probability
1.0
1.2
1.4
1.6
E/eV

Figure 2.

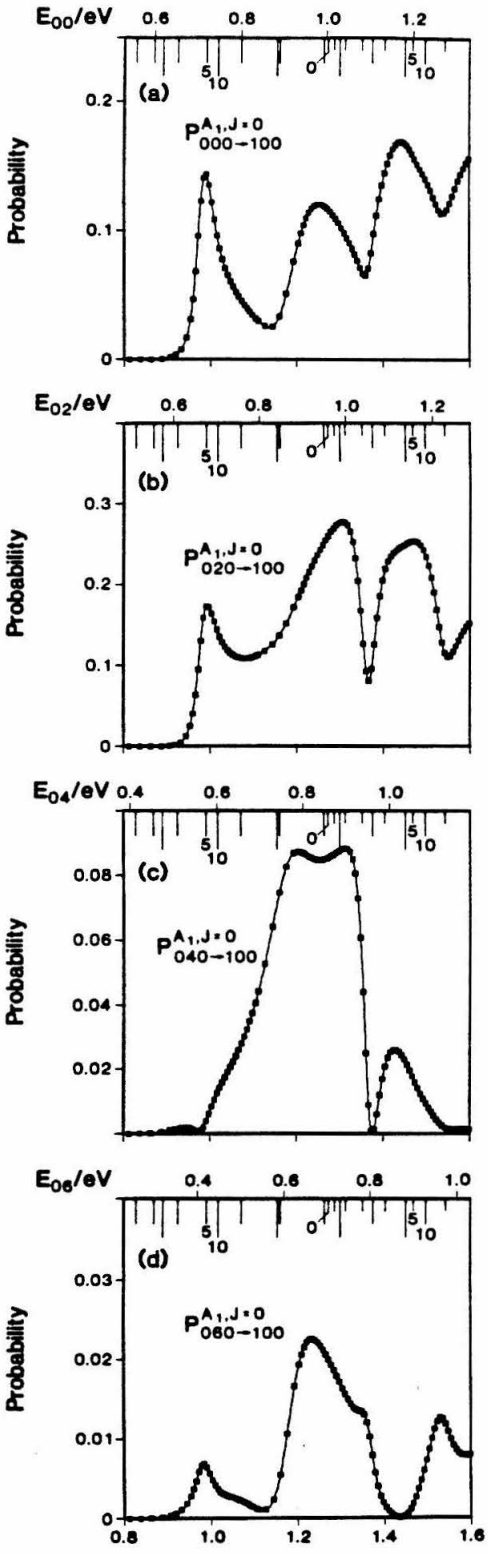
E00/eV
0.6
0.8
1.0
1.2
5
10
0
5
10
(a)
P A1,J=0 000−100
Probability
0.2
0.1
0
E02/eV
0.6
0.8
1.0
1.2
(b)
P A1,J=0 020−100
0.3
0.2
0.1
0
E04/eV
0.4
0.6
0.8
1.0
(c)
P A1,J=0 040−100
0.08
0.06
0.04
0.02
E06/eV
0.4
0.6
0.8
1.0
(d)
P A1,J=0 060−100
0.03
0.02
0.01
0
0.8
1.0
1.2
1.4
1.6
E/eV

Figure 3.

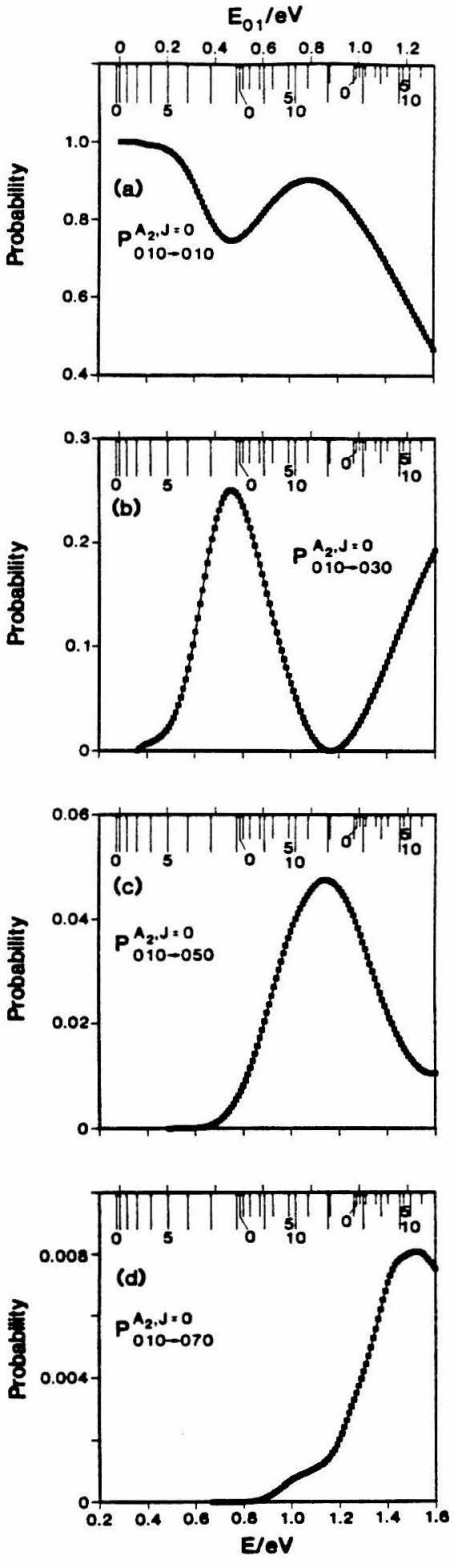
E01/eV
0 0.2 0.4 0.6 0.8 1.0 1.2
0 5 0 5 10 0 5 10
Probability
1.0
0.8
0.6
0.4
(a)
P A2,J=0 010→010
0.3
0.2
0.1
0
(b)
P A2,J=0 010→030
0.06
0.04
0.02
0
(c)
P A2,J=0 010→050
0.008
0.004
0
(d)
P A2,J=0 010→070
0.2 0.4 0.6 0.8 1.0 1.2 1.4 1.6
E/eV

Figure 4.

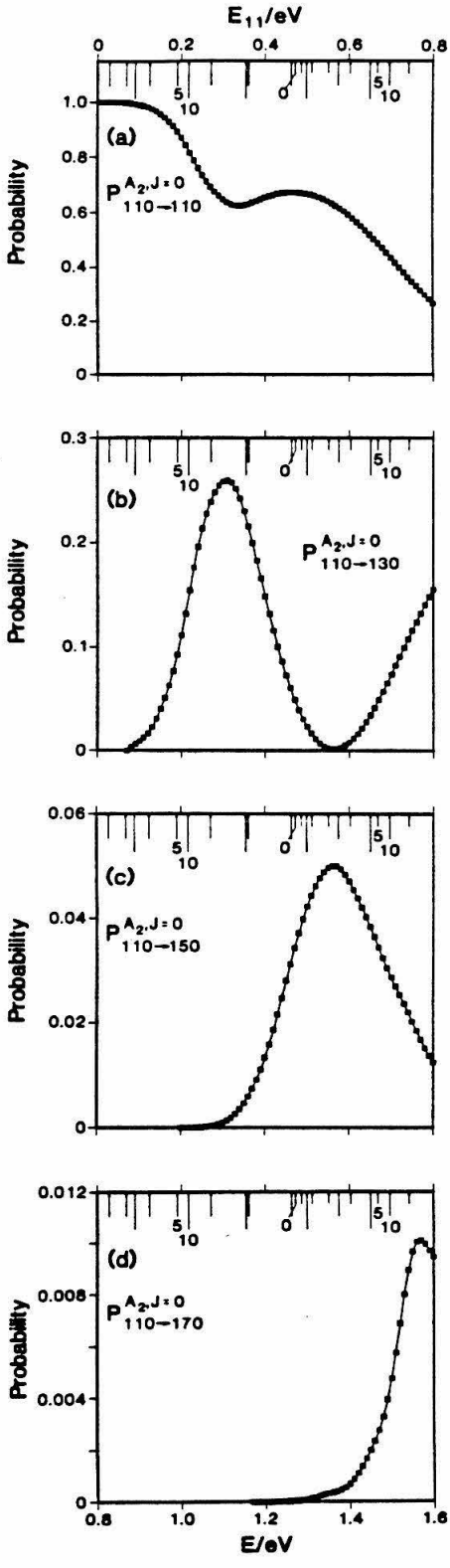
E11/eV
0
0.2
0.4
0.6
0.8
5
10
0
5
10
(a)
P A2,J=0 110→110
Probability
1.0
0.8
0.6
0.4
0.2
0
(b)
P A2,J=0 110→130
0.3
0.2
0.1
(c)
P A2,J=0 110→150
0.06
0.04
0.02
(d)
P A2,J=0 110→170
0.012
0.008
0.004
0.8
1.0
1.2
1.4
1.6
E/eV

Figure 5.

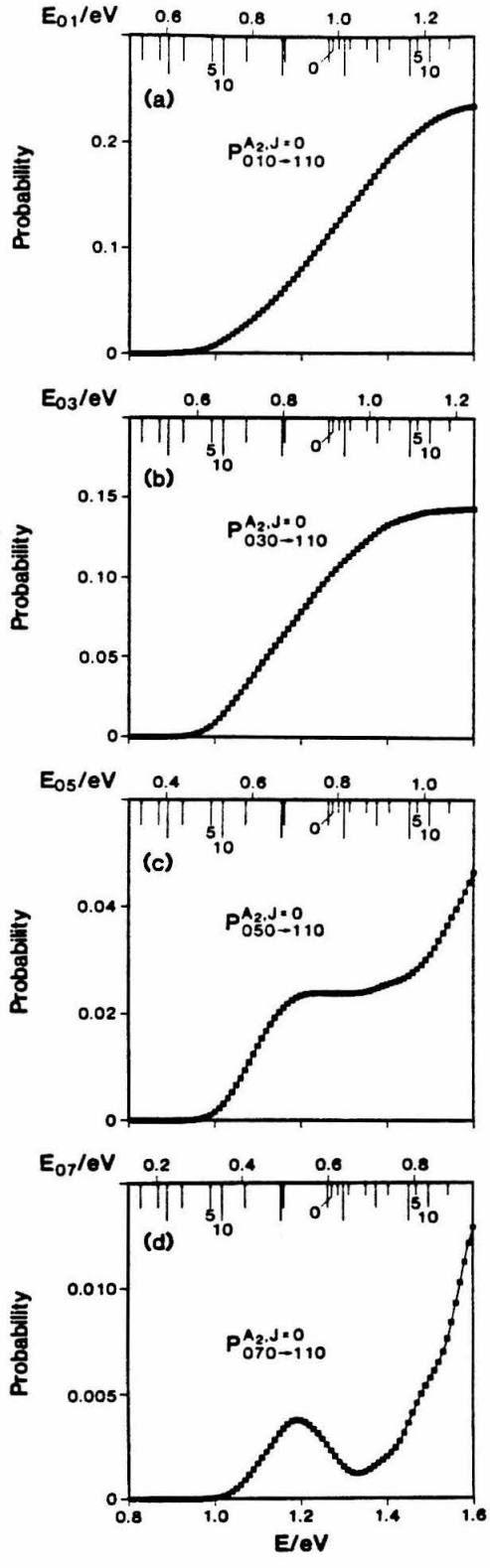
E01/eV
0.6
0.8
1.0
1.2
5
10
0
5
10
(a)
Probability
0.2
0.1
0
P A2,J=0 010→110
E03/eV
0.6
0.8
1.0
1.2
(b)
0.15
0.10
0.05
0
P A2,J=0 030→110
E05/eV
0.4
0.6
0.8
1.0
(c)
0.04
0.02
0
P A2,J=0 050→110
E07/eV
0.2
0.4
0.6
0.8
(d)
0.010
0.005
0
P A2,J=0 070→110
0.8
1.0
1.2
1.4
1.6
E/eV

Figure 6.

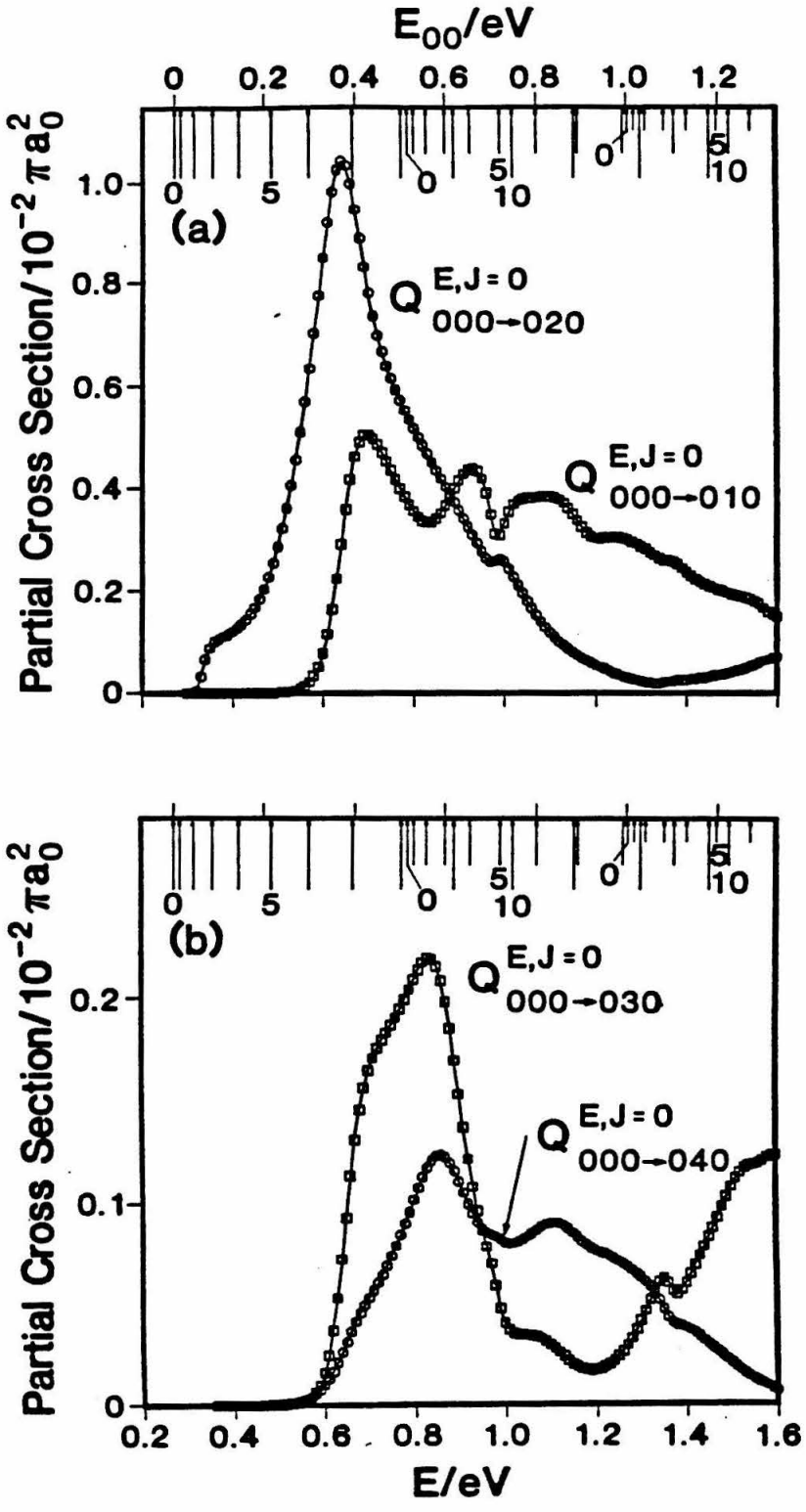
E00/eV
0
0.2
0.4
0.6
0.8
1.0
1.2
Partial Cross Section/10-2 πa02
(a)
Q E,J = 0 000→020
Q E,J = 0 000→010
(b)
Q E,J = 0 000→030
Q E,J = 0 000→040
E/eV

Figure 7.

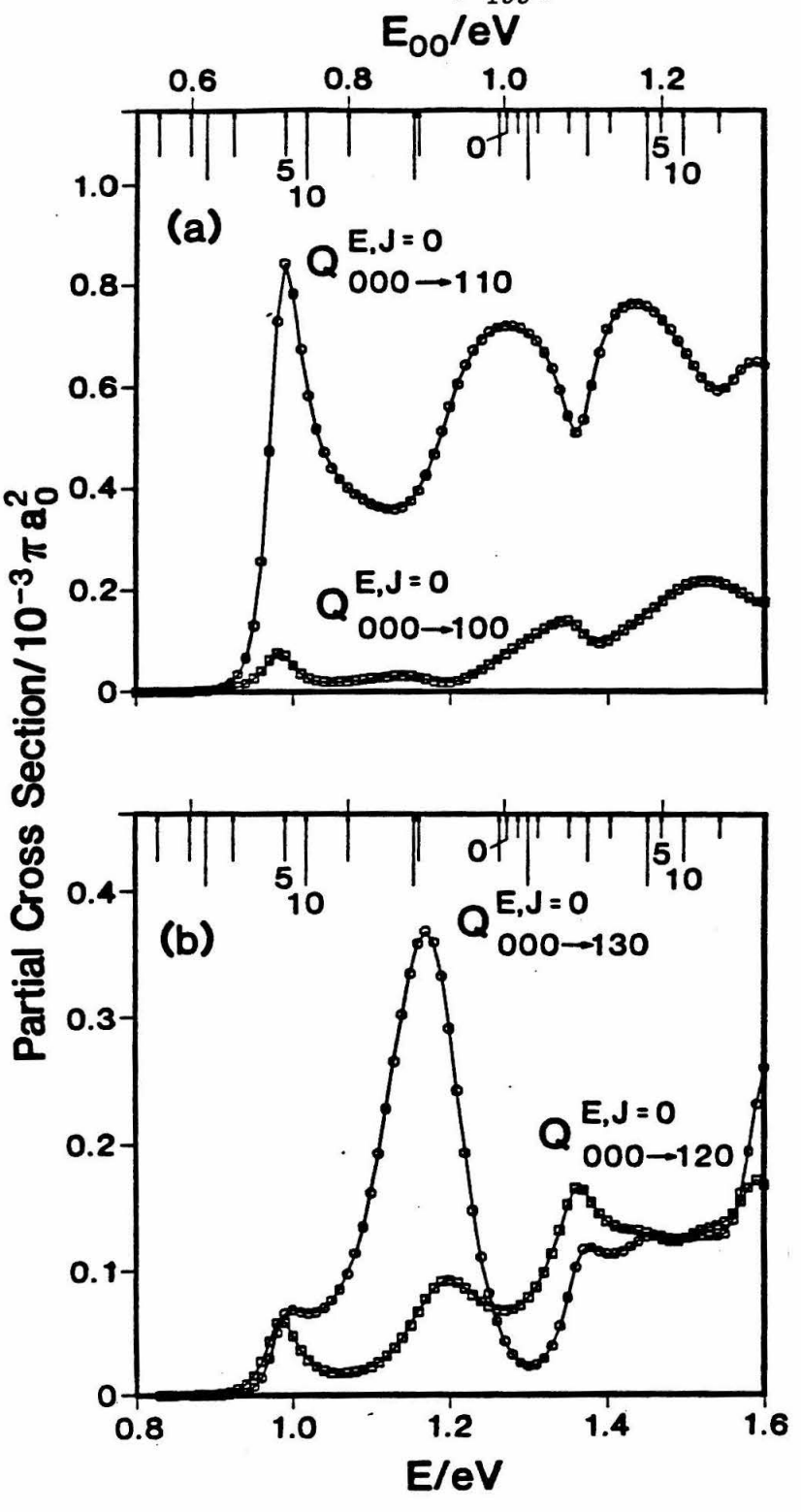
E00/eV
0.6
0.8
1.0
1.2
0
5
10
(a)
Q E,J = 0 000→110
Q E,J = 0 000→100
(b)
Q E,J = 0 000→130
Q E,J = 0 000→120
Partial Cross Section/10^-3 π a0^2
E/eV
0.8
1.0
1.2
1.4
1.6

Figure 8.

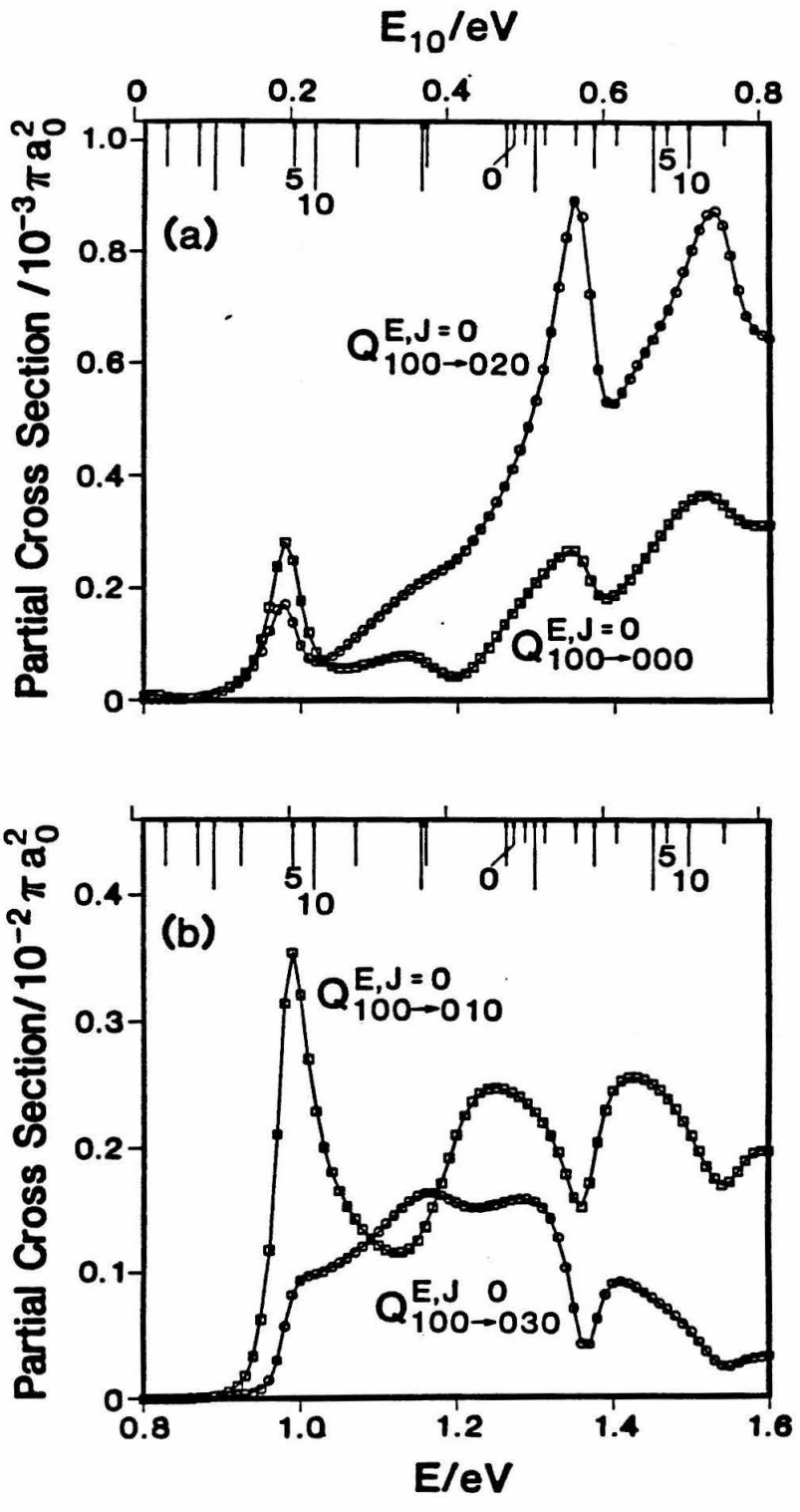
E10/eV
0
0.2
0.4
0.6
0.8
5
10
0
5
10
(a)
Partial Cross Section /10-3πa02
1.0
0.8
0.6
0.4
0.2
0
Q E,J = 0 100→020
Q E,J = 0 100→000
(b)
Partial Cross Section/10-2πa02
0.4
0.3
0.2
0.1
0
Q E,J = 0 100→010
Q E,J 0 100→030
0.8
1.0
1.2
1.4
1.6
E/eV

Figure 9.

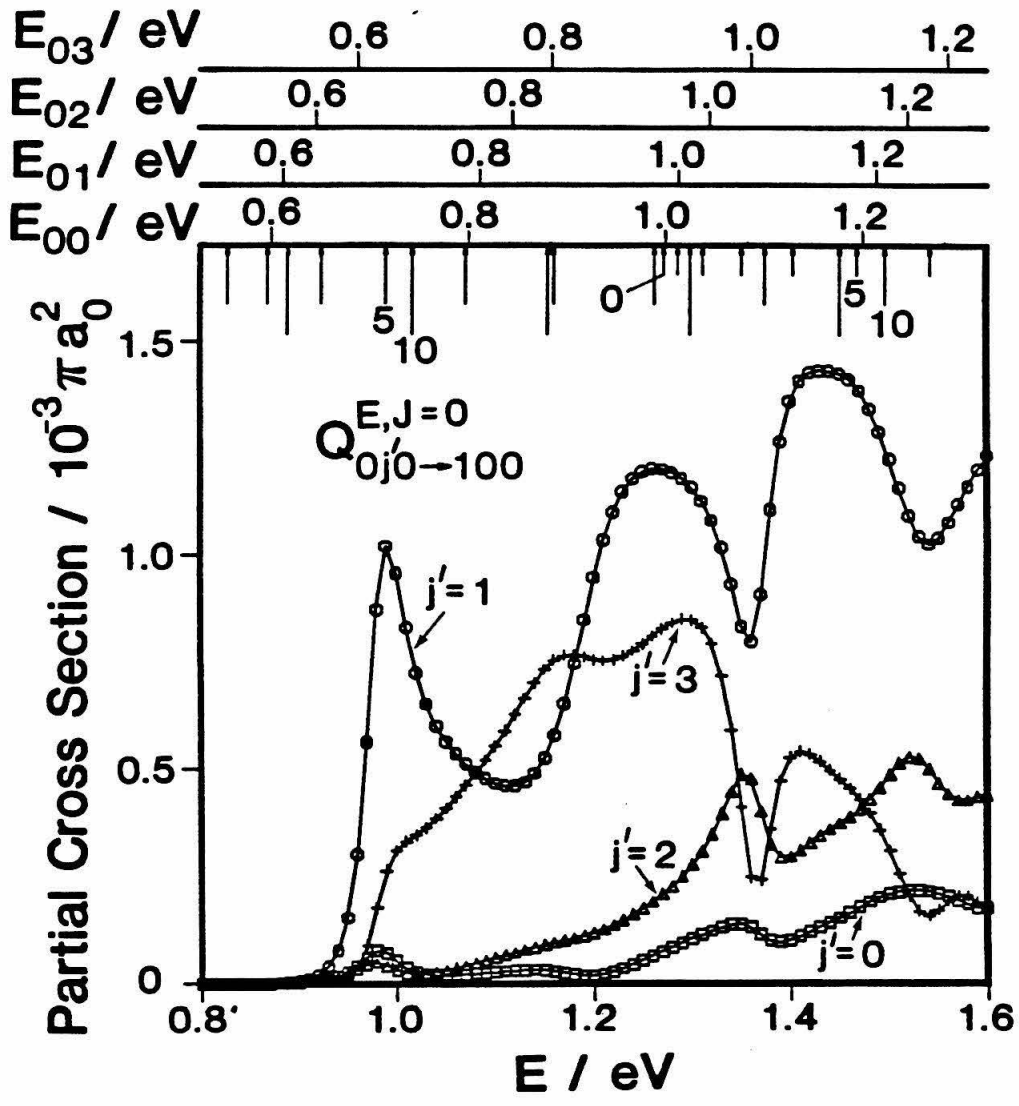
E03 / eV
E02 / eV
E01 / eV
E00 / eV
0.6
0.8
1.0
1.2
0
5
10
Partial Cross Section / 10-3 π a02
1.5
1.0
0.5
0
E,J=0
Q 0j'0→100
j'=1
j'=3
j'=2
j'=0
0.8
1.0
1.2
1.4
1.6
E / eV

Figure 10.

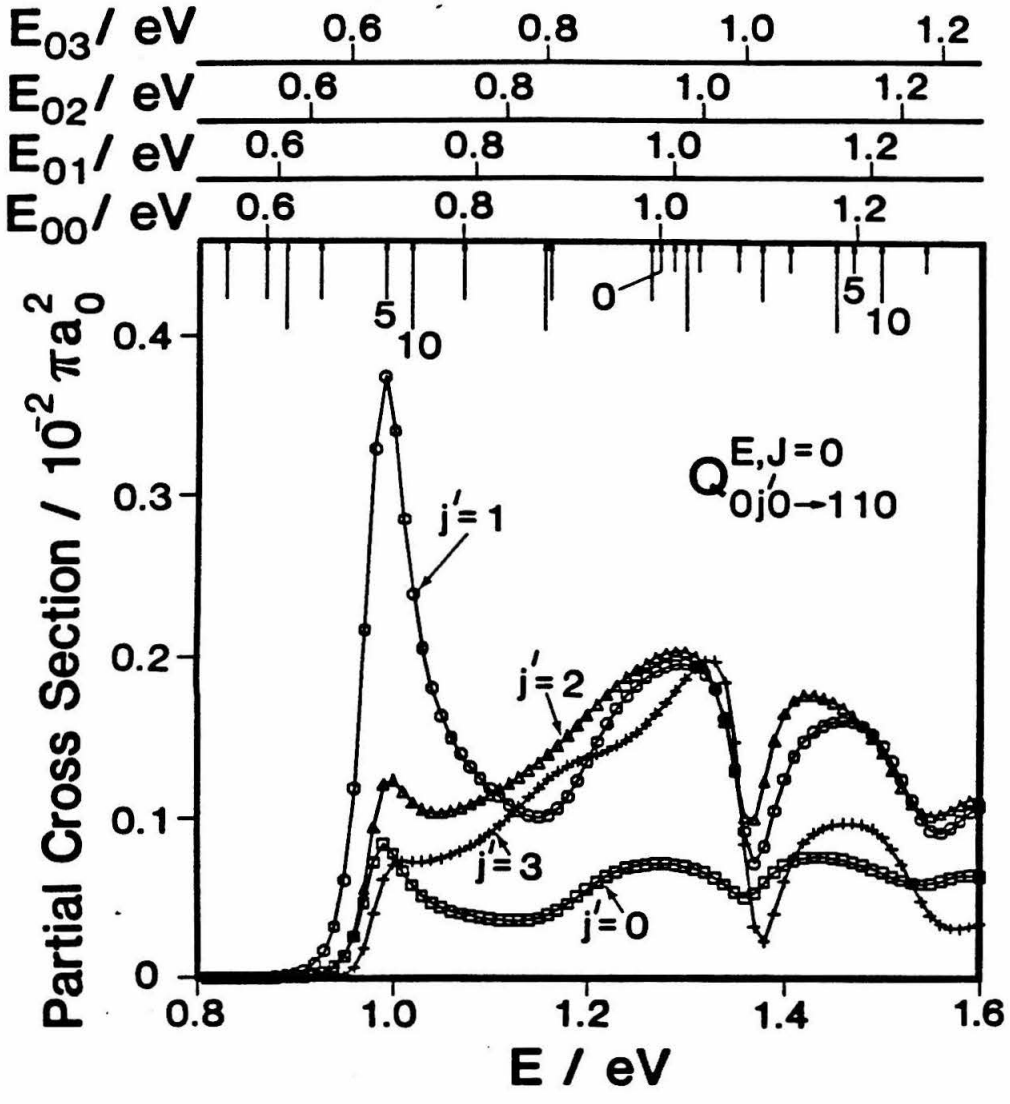
E03/ eV
E02/ eV
E01/ eV
E00/ eV
0.6
0.8
1.0
1.2
0
5
10
Partial Cross Section / 10-2 πa02
0.4
0.3
0.2
0.1
0
j'=1
j'=2
j'=3
j'=0
Q E,J=0 0j'0→110
0.8
1.0
1.2
1.4
1.6
E / eV

Figure 11.

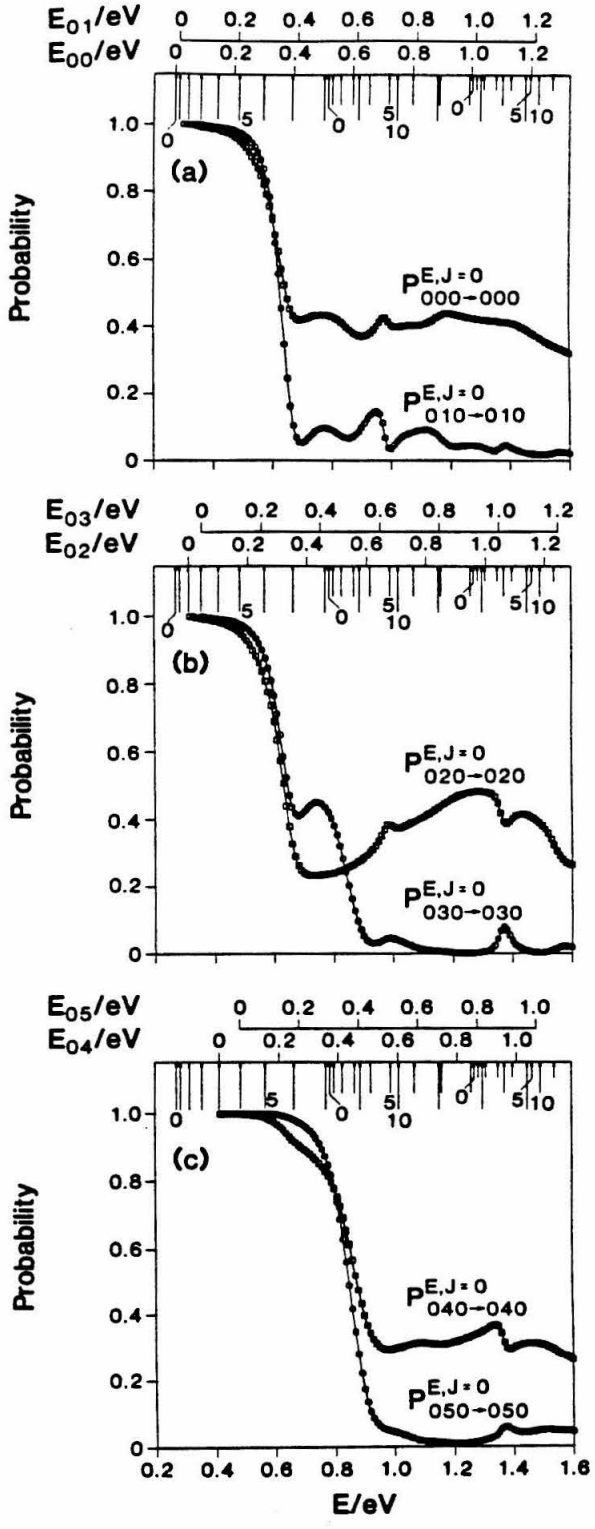
E01/eV
E00/eV
(a)
Probability
P E,J=0 000→000
P E,J=0 010→010
E03/eV
E02/eV
(b)
Probability
P E,J=0 020→020
P E,J=0 030→030
E05/eV
E04/eV
(c)
Probability
P E,J=0 040→040
P E,J=0 050→050
E/eV

Figure 12.

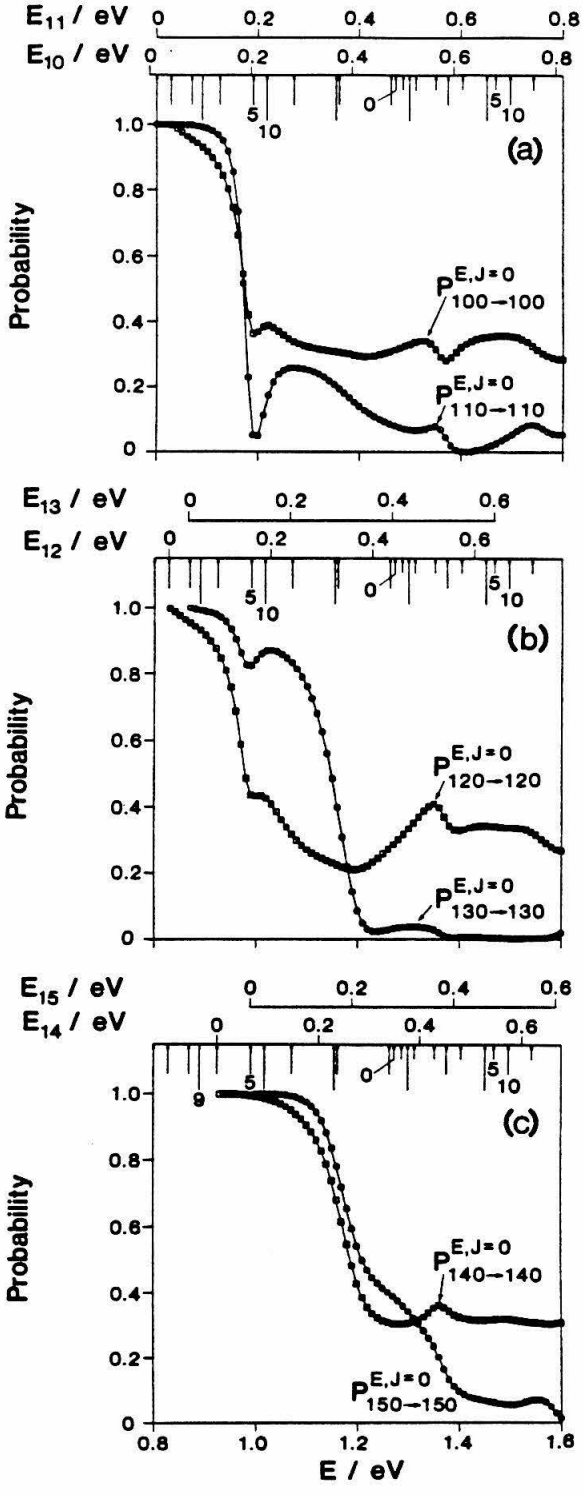
E11 / eV
E10 / eV
Probability
(a)
P E,J=0 100→100
P E,J=0 110→110
E13 / eV
E12 / eV
(b)
P E,J=0 120→120
P E,J=0 130→130
E15 / eV
E14 / eV
(c)
P E,J=0 140→140
P E,J=0 150→150
E / eV

Figure 13.

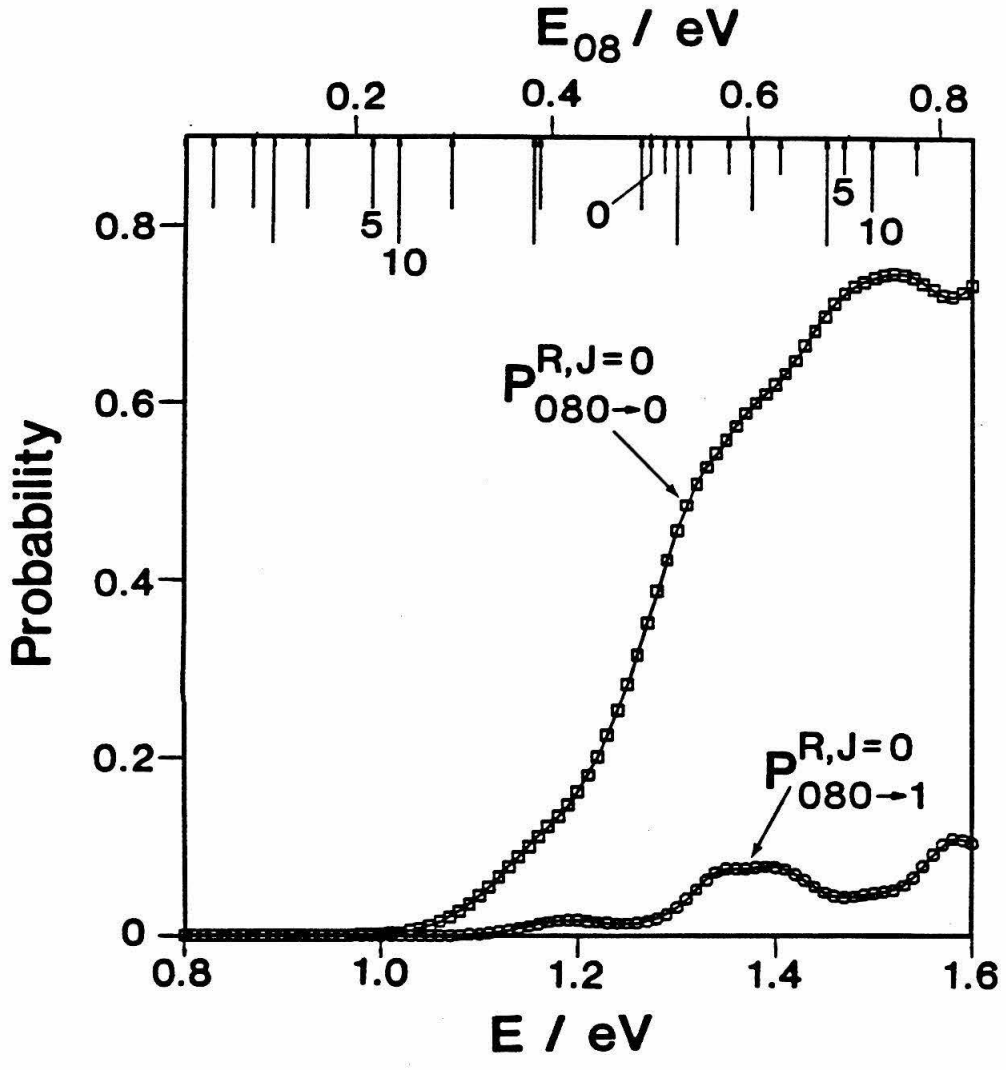
E08 / eV
0.2
0.4
0.6
0.8
0
5
10
5
10
Probability
0.8
0.6
0.4
0.2
0
P R,J=0 080→0
P R,J=0 080→1
0.8
1.0
1.2
1.4
1.6
E / eV

Figure 14.

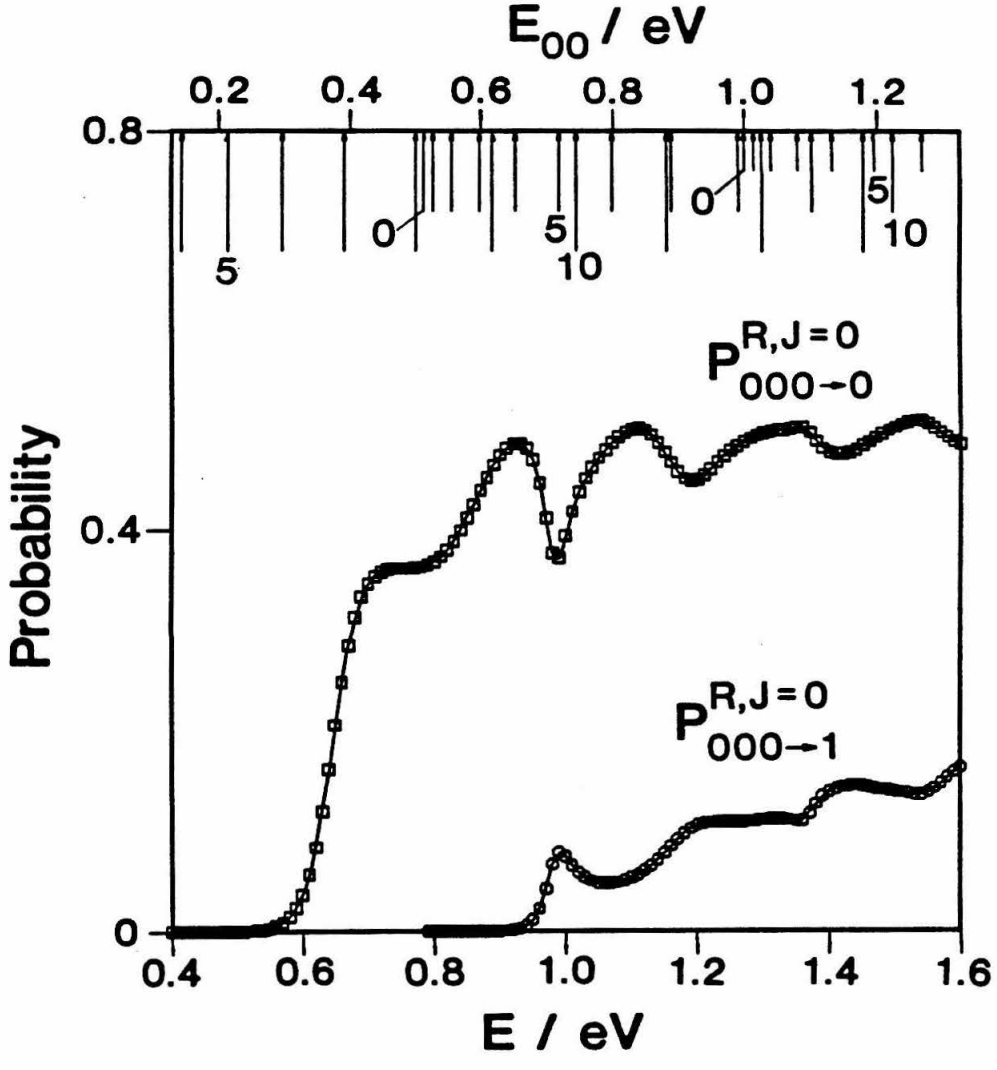
E00 / eV
0.2
0.4
0.6
0.8
1.0
1.2
0.8
0
5
0
5
10
0
5
10
P R,J=0 000→0
Probability
0.4
P R,J=0 000→1
0
0.4
0.6
0.8
1.0
1.2
1.4
1.6
E / eV

Figure 15.

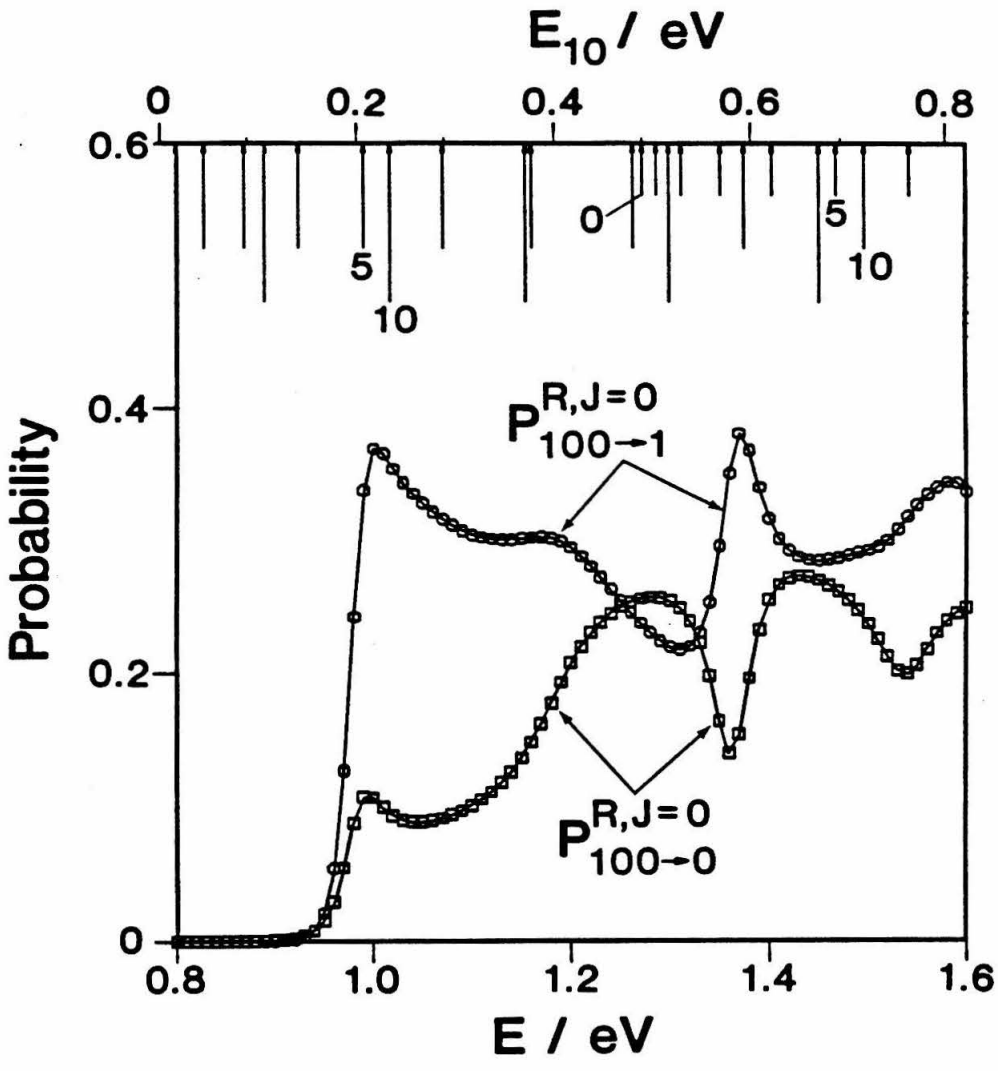
E10 / eV
0
0.2
0.4
0.6
0.8
0.6
0
5
10
5
10
0.4
Probability
P R,J=0 100→1
0.2
P R,J=0 100→0
0
0.8
1.0
1.2
1.4
1.6
E / eV

Figure 16.

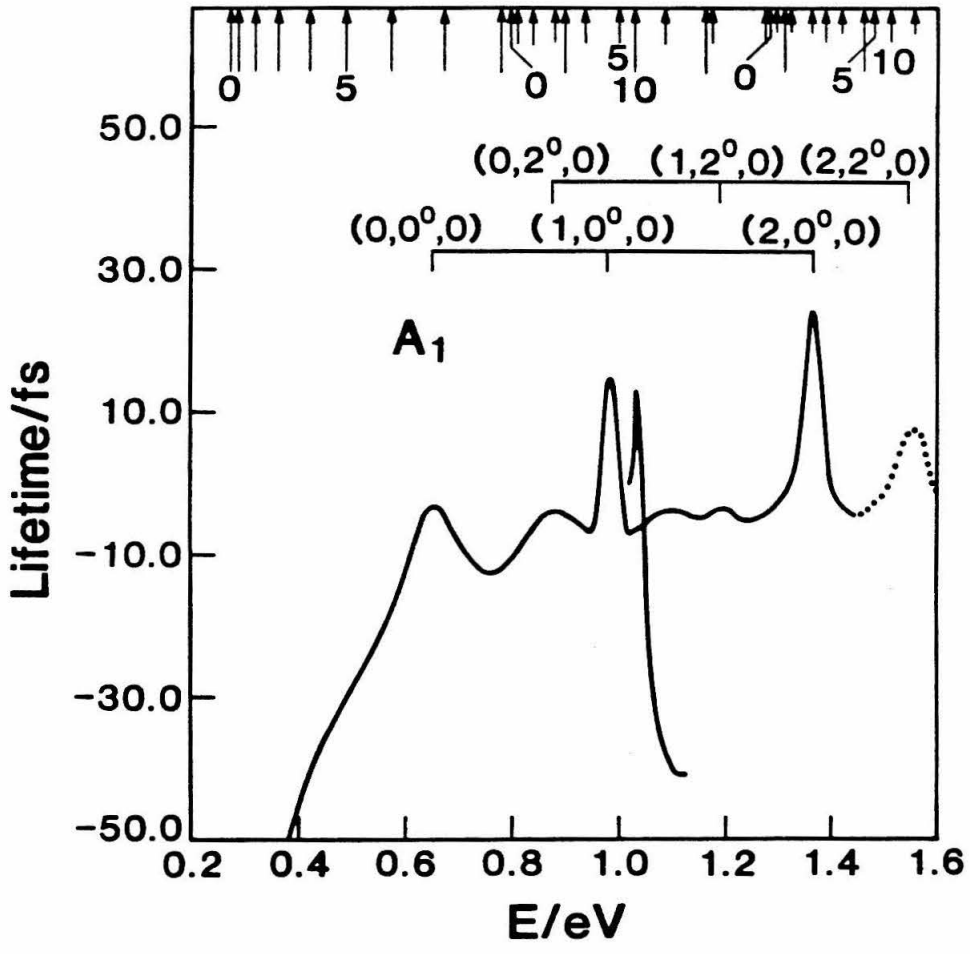
0
5
0
5
10
0
5
10
(0,2⁰,0)
(1,2⁰,0)
(2,2⁰,0)
(0,0⁰,0)
(1,0⁰,0)
(2,0⁰,0)
A1
50.0
30.0
10.0
-10.0
-30.0
-50.0
Lifetime/fs
0.2
0.4
0.6
0.8
1.0
1.2
1.4
1.6
E/eV

Figure 17.

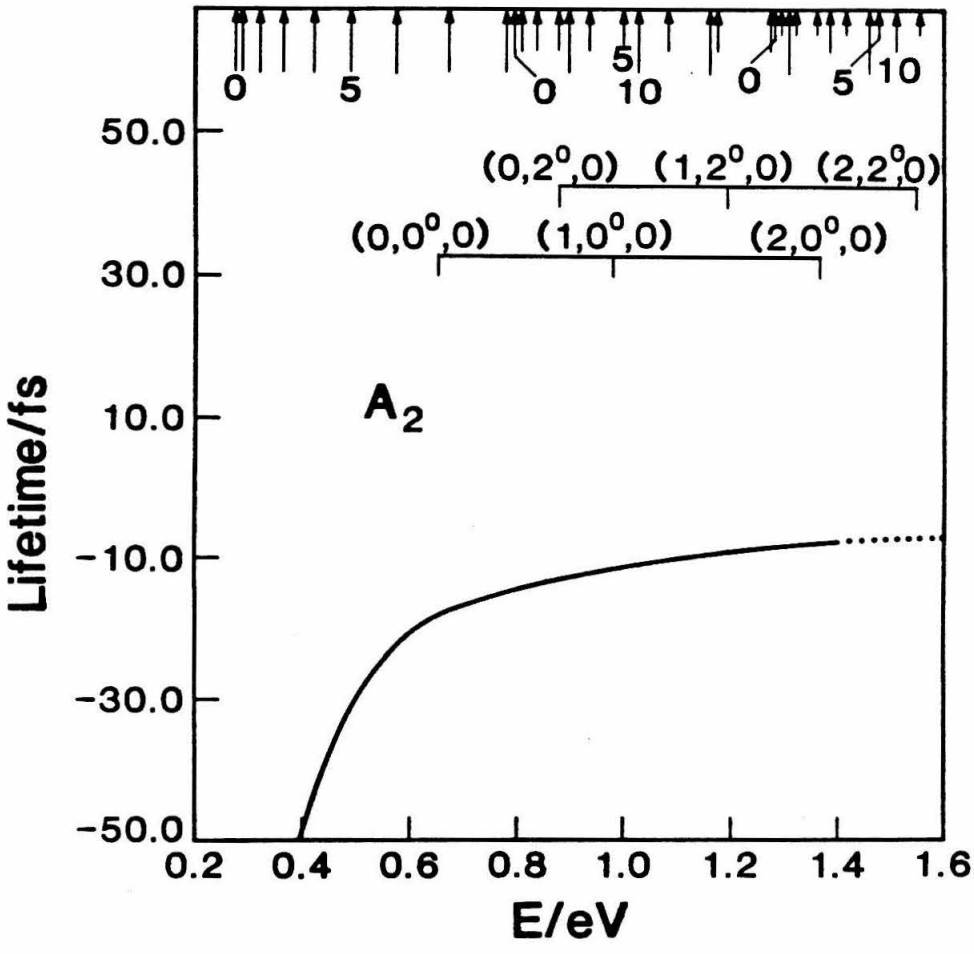
0
5
0
5
10
0
5
10
50.0
(0,2°,0) (1,2°,0) (2,2°,0)
(0,0°,0) (1,0°,0) (2,0°,0)
30.0
10.0
A2
-10.0
-30.0
-50.0
Lifetime/fs
0.2
0.4
0.6
0.8
1.0
1.2
1.4
1.6
E/eV

Figure 18.

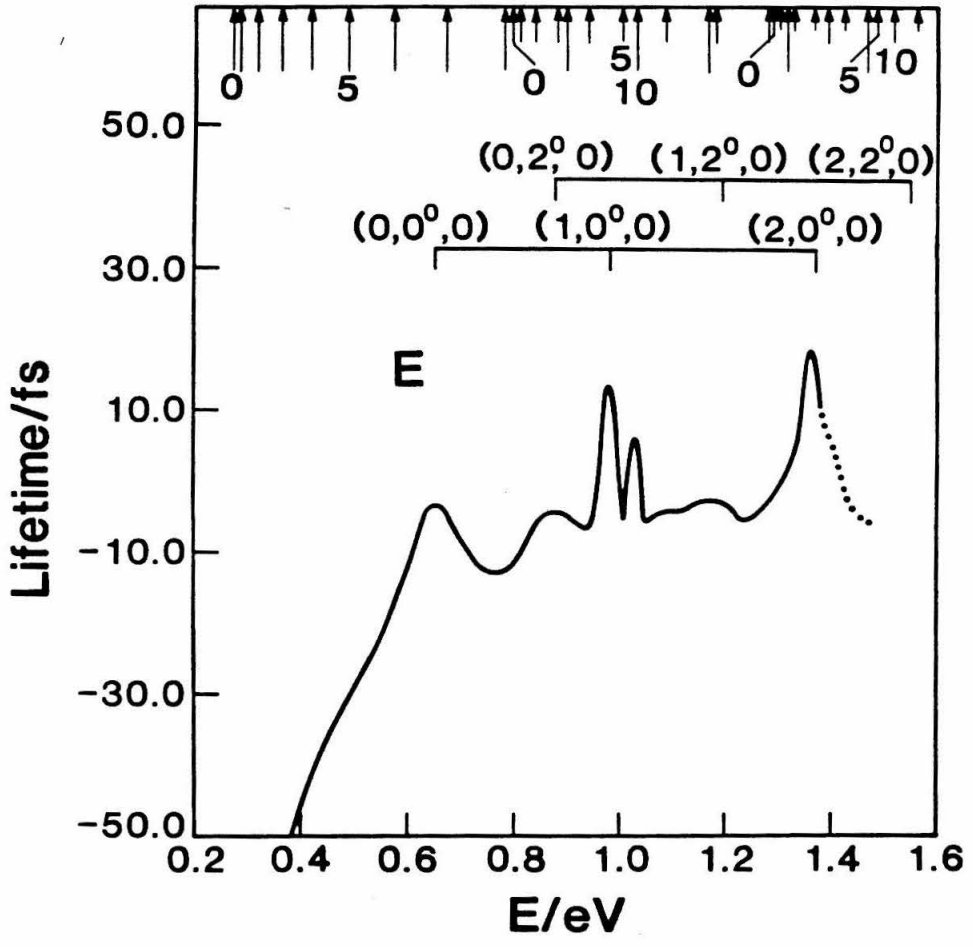
0
5
0
5
10
0
5
10
(0,2^0,0) (1,2^0,0) (2,2^0,0)
(0,0^0,0) (1,0^0,0) (2,0^0,0)
E
50.0
30.0
10.0
-10.0
-30.0
-50.0
Lifetime/fs
0.2
0.4
0.6
0.8
1.0
1.2
1.4
1.6
E/eV

Figure 19.

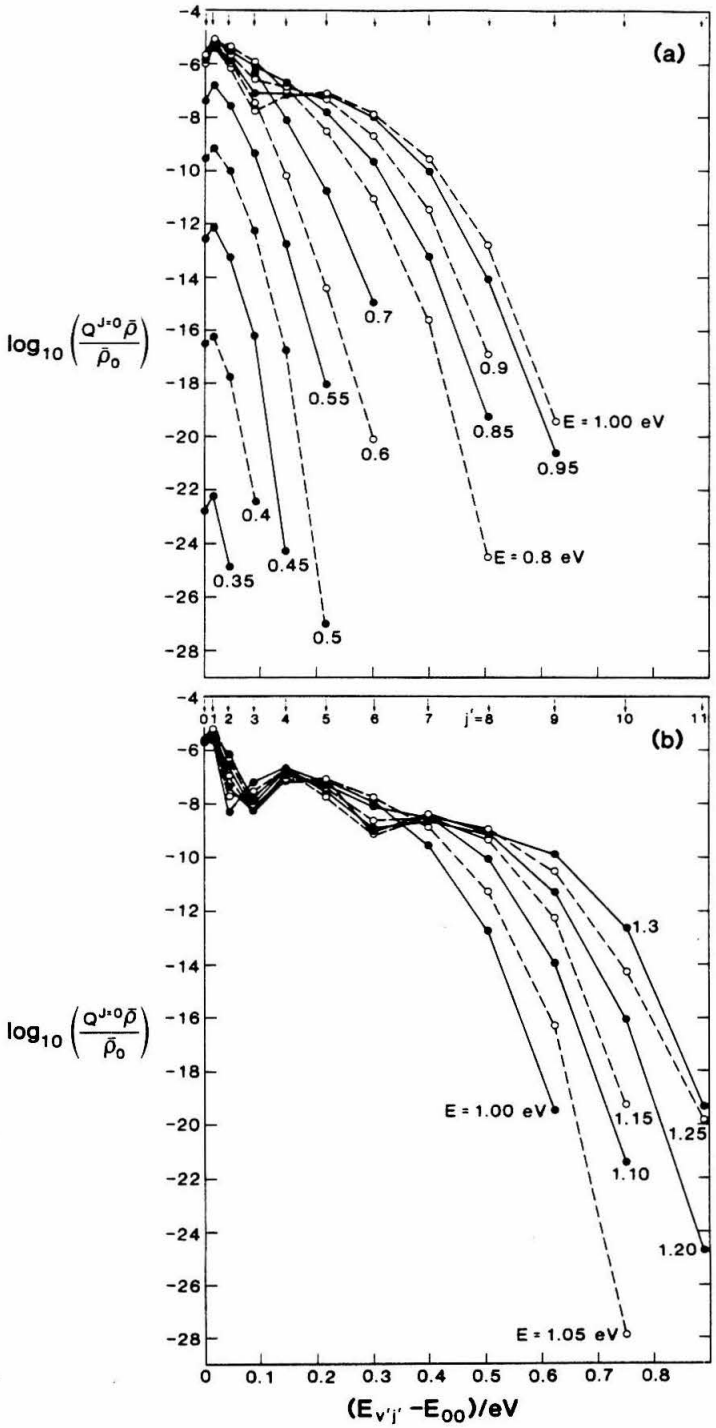
(a)
(b)
$\log_{10}\left(\frac{Q^{J=0}\bar{\rho}}{\bar{\rho}_0}\right)$
E = 1.00 eV
E = 0.8 eV
E = 1.05 eV
0.35
0.4
0.45
0.5
0.55
0.6
0.7
0.85
0.9
0.95
1.10
1.15
1.20
1.25
1.3
j' = 8
$(E_{v'j'} - E_{00})/eV$

Figure 20.

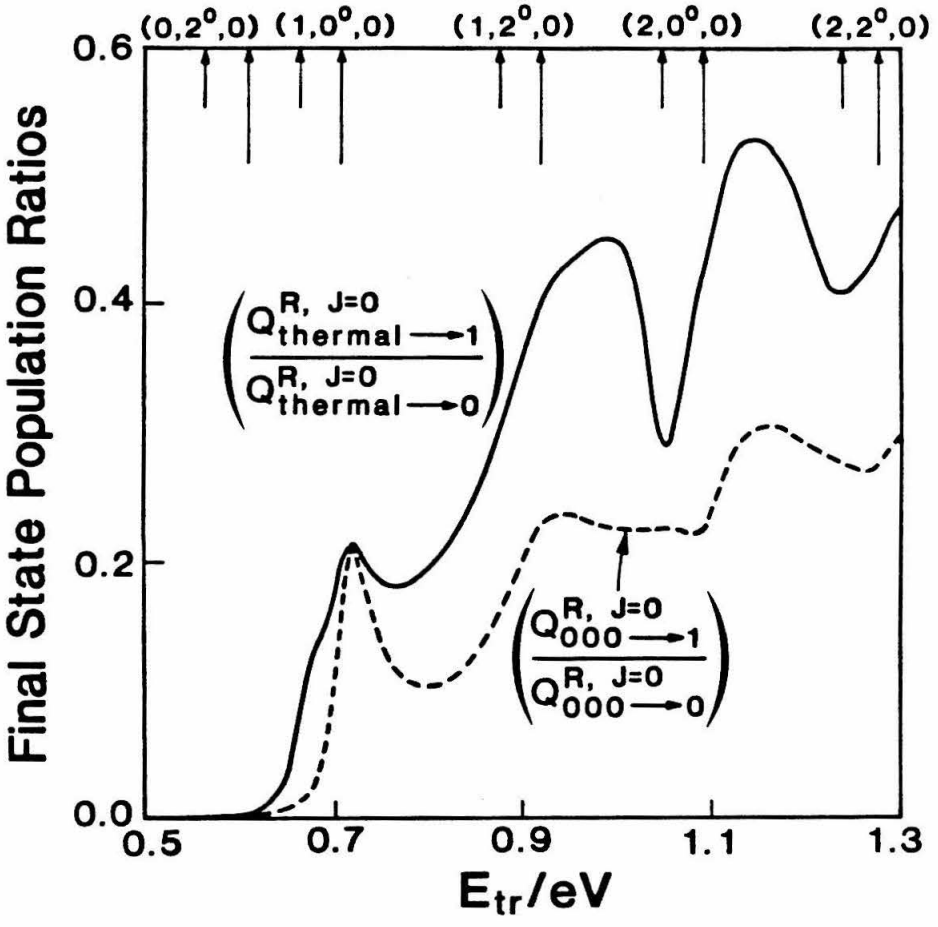
(0,2°,0)
(1,0°,0)
(1,2°,0)
(2,0°,0)
(2,2°,0)
0.6
0.4
0.2
0.0
Final State Population Ratios
$\left(\frac{Q^{R,\ J=0}_{thermal \rightarrow 1}}{Q^{R,\ J=0}_{thermal \rightarrow 0}}\right)$
$\left(\frac{Q^{R,\ J=0}_{000 \rightarrow 1}}{Q^{R,\ J=0}_{000 \rightarrow 0}}\right)$
0.5
0.7
0.9
1.1
1.3
E_{tr}/eV

Figure 21.

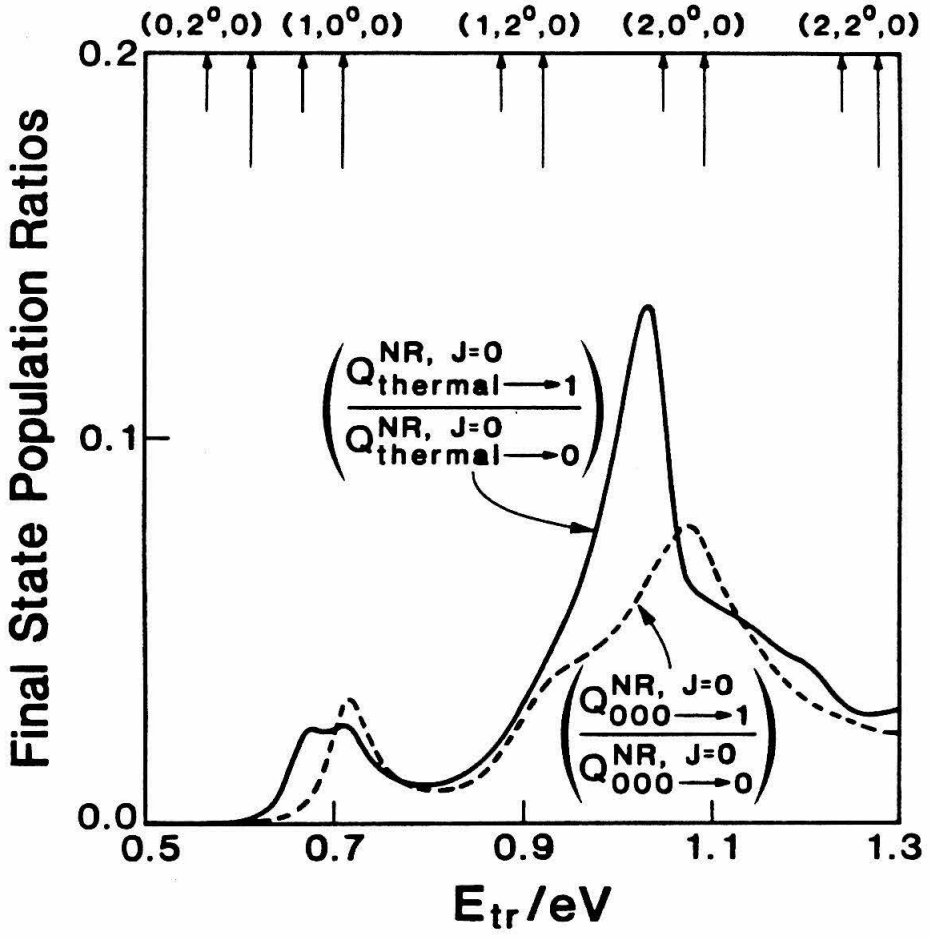
(0,2⁰,0)
(1,0⁰,0)
(1,2⁰,0)
(2,0⁰,0)
(2,2⁰,0)
0.2
0.1
0.0
Final State Population Ratios
$\left(\frac{Q^{NR,\ J=0}_{thermal\rightarrow 1}}{Q^{NR,\ J=0}_{thermal\rightarrow 0}}\right)$
$\left(\frac{Q^{NR,\ J=0}_{000\rightarrow 1}}{Q^{NR,\ J=0}_{000\rightarrow 0}}\right)$
0.5
0.7
0.9
1.1
1.3
E_{tr}/eV

Figure 22.

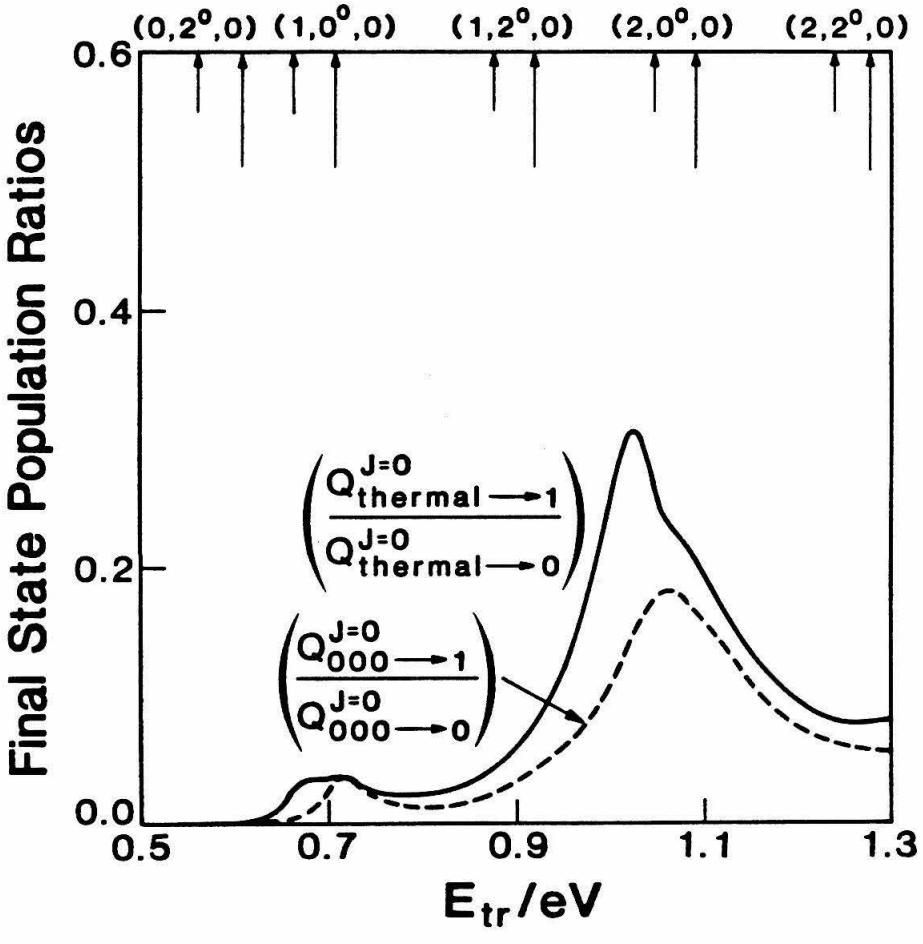
(0,2⁰,0)
(1,0⁰,0)
(1,2⁰,0)
(2,0⁰,0)
(2,2⁰,0)
0.6
0.4
0.2
0.0
Final State Population Ratios
$\left(\frac{Q^{J=0}_{thermal\rightarrow 1}}{Q^{J=0}_{thermal\rightarrow 0}}\right)$
$\left(\frac{Q^{J=0}_{000\rightarrow 1}}{Q^{J=0}_{000\rightarrow 0}}\right)$
0.5
0.7
0.9
1.1
1.3
E_{tr}/eV

Figure 23.

Gauss-Jordan Matrix Inversion with Partial Pivoting on the Caltech Mark II Hypercube

Abstract

The performance of an implementation of Gauss-Jordan matrix inversion[1,2] on the Caltech Mark II hypercube[3] is explored in this document. The inverter employs partial pivoting without scaling and double precision arithmetic. After some introductory remarks, the sequential Gaussian elimination and Gauss-Jordan algorithms are outlined, followed by remarks concerning their parallel implementations. The reasons for the superiority of parallel Gauss-Jordan inversion over parallel Gaussian elimination are discussed. Next, empirical and theoretical efficiencies for our program as a function of matrix dimension for different numbers and configurations of processors are presented. The empirical efficiencies are based on actual timings of the parallel matrix inversion program. An operations count for the parallel inversion algorithm is the basis for theoretical efficiencies which are in *quantitative* agreement with the empirical efficiencies.

1. Introduction

This paper is concerned with how well a multiprocessor computer can be utilized to execute a standard algorithm from linear algebra: matrix inversion. Matrix inversion provides a relatively simple algorithm with which to explore the issues germane to parallel computing with the Caltech hypercube. As scientists interested in large scale scientific programming, we are also interested in parallel computers because they may offer the increased performance our applications require for solution. There is no better way to assess the potential for such machines than to write parallel programs and measure their performance. In addition, matrix inversion is a standard part of any linear algebra library. Such libraries are

critical for the evolution of parallel computers into useful tools for large scale scientific simulations. The recent introduction of commercial hypercube computers by several companies is a sign that hypercubes may become viable supercomputers.

A particular application for which supercomputer performance is necessary and in which our interests lie is scattering theory as it applies to chemical dynamics. The collision of an atom and a diatomic molecule is described quantum mechanically by a partial differential equation. One technique for solving this differential equation requires the integration of large systems of ordinary differential equations. Matrix inversion is a part (along with matrix multiplication) of one algorithm commonly used to integrate systems of ordinary differential equations.[4] The writing and understanding of a parallel matrix inverter addresses both the needs of our current research efforts and our desire to explore the next generation of computers.

From the scientific programmer's point of view, the principal motivations for developing parallel codes are the prospect of large total memory and short execution times through the use of multiple processors. Many scientific programs require large data sets, so the availability of large total memory is advantageous because it eliminates the need for frequent data transfers between disk and memory. In addition to large data sets, these programs typically involve a very large amount of floating point arithmetic. The strategy in using multiple processors to reduce execution time is to distribute the floating point work among the processors. If the penalties incurred by distribution of the work load are not too great, then execution time can be significantly reduced relative to that on a single processor. Supercomputer level performance is achieved when a large number of processors can be used on a task effectively. The degree to which multiple computers reduce the execution time is referred to as the efficiency; perfect efficiency is realized when N processors execute a task with N times the speed of one processor.

There are three factors which determine the efficiency of a parallel algorithm. The first is work load inhomogeneity which occurs when a subset of the processors performs a disproportionate fraction of the work. Work load inhomogeneity affects the efficiency adversely because some of the processors become idle while others are still working. The goal of any parallel algorithm is to distribute the tasks uniformly among the processors so that no processor has more work than any other. The second issue is the interprocessor communication which is usually necessary in a parallel algorithm. The communication of data contained in one processor and needed in another is a task which is absent in a sequential program and can decrease the efficiency of a parallel algorithm. If a processor is idle while awaiting data from another processor, then that processor is being used inefficiently. A moment's reflection shows that the important quantity in determining efficiency is not the total number of communications, but the ratio of communications to processor work load. If this ratio is low, then efficiency is high because the processor work load dominates the communication costs. The third issue is software overhead. The distribution of a task over multiple processors invariably means that some integer arithmetic and logic will have to be added to a sequential algorithm to produce a parallel algorithm. The integer arithmetic and logic are required to switch on and off different sections of code and to control interprocessor communications. The software overhead, if it is significant in comparison with the remaining tasks, decreases the efficiency of the parallel code. In short, if a parallel algorithm has a higher operations count than the sequential version, due to communications, redundant computations, or software overhead, then the extra work lowers the efficiency. The successful parallel algorithms are those that minimize the work load imbalance, the ratio of communication to floating point arithmetic, and the software overhead.

There is one further issue which effects the efficiency of a parallel algorithm's performance. Once a strategy for dividing up a task and organizing the necessary communications is chosen, then each processor will have a set of tasks to execute.

The translation of these single processor tasks into machine instructions affects the overall performance of the parallel code. We have in mind particularly the effectiveness with which floating point arithmetic and the associated local memory accessing are handled in each processor. The term fine grain performance refers to the character of the machine level code that is used for a given task set on one processor. It is our intention to remain unentangled by this issue, in part because of lack of expertise at the machine language level of coding and in part because variations in the efficiency of the machine code will affect parallel efficiencies only slightly, if the machine code is reasonably good. Our primary interest is in finding algorithms with inherent parallelism and the exploitation of that parallelism.

As examples of how fine grain performance can affect efficiency measurements, consider the following situations. Use of assembly language can result in a better code than that generated by a C language compiler, but comparing a parallel code written in the language C with a sequential code written in assembly language biases the efficiency observed for the parallel code. Such a comparison does not accurately reflect the parallelism inherent in the algorithm. This is an obvious mistake to avoid; however, there are more subtle program differences that affect execution times such as the use of more memory to avoid unfavorable memory accessing in loops. This is well demonstrated by the following experience. Two sequential versions of the basic Gauss-Jordan algorithm were created in C by different people. One of the sequential inversion programs ran slower than a *parallel* program when each were run on the same single processor. In other words, the difference in execution time for the two sequential programs was greater than the additional execution time used by the software overhead in a parallel program for the hypercube. Loop organization and memory accessing order were found to be the important differences between the two sequential codes. The lesson is that the software overhead costs in the parallel inverter are comparable to the variation in performance encountered in different implementations of a sequential algorithm.

In an effort to avoid the effect of fine grain performance differences on efficiency measurements, all parallel code efficiencies are referenced to single processor runs of a slightly modified version of the parallel code. The modified code is produced by removing all references to communication routines and all logic and integer arithmetic needed in the parallel code. The result is a sequential code which is very close to the parallel code. (An alternative is to base the efficiency of the parallel program on the performance of a sequential routine from a standard library. The problem with this is that a pedestrian C program is being compared with an optimized sequential program. In this approach, fine grain performance differences are entangled with the measure of exploitation of parallelism.) It is likely that the machine level code of the parallel program can be improved, but the behavior of the present code should represent the nature of the algorithm (as distinct from its implementation).

2. Caltech Hypercube Hardware

The multiple processor machine used for this work is a collection of identical Intel 8086/8087 based computers linked together by communication paths with a hypercube connectivity.[3] To define hypercube connectivity consider 2^M processors each labeled with a M bit binary number where $M = 0, 1, 2, \ldots$. Each processor has M communication channels, one channel to each processor which carries a binary label differing by one bit from the given processor's label. For example, an eight processor hypercube can be visualized as geometric cube where a processor is placed at each of the cube's eight vertices and the communication channels are the edges of the cube. The machine used to obtain the timings presented in this paper is constructed of 32 processors.

There is no shared memory on the Mark II Hypercube. Each processor has its own local memory. For a processor to fetch data from the memory of another processor, an explicit communication protocol must be written into the user's source code. This difference between data passing on the hypercube and how

data are handled on a sequential machine is similar to the difference between programming in machine language and programming in a higher level language. When writing a program in a higher level language, data in memory are referenced by using variable names and the programmer need not be aware of the way in which the machine actually fetches data to the processor and puts it back in memory. In contrast, when coding in machine language, the programmer must explicitly fetch data from memory, and put it back. The hypercube programmer encounters both types of data handling: if the data are in the local memory of the processor that requires it, then he can reference the data with variable names; if the data are in another processor, then he must explicitly retrieve it by using the interprocessor communication routines. The system routines necessary for a variety of interprocessor communications are available to the user of the hypercube. The inversion codes under discussion in this paper were all run using the crystalline operating system developed at Caltech. Further information on the software and hardware for the Caltech Mark II hypercube can be found in reference 3.

No comparison of the Mark II hypercube with other machines is made and no absolute times for execution are reported. The reasons for this are evident. The efficiency of a program will be largly unaffected by changes in hardware given an invariant ratio of floating point speed to communication speed, and certainly the asymptotic performance of a program with matrix size will be unaffected. The same is not true of absolute execution times; they are strongly hardware dependent. In addition, efficiencies will not be greatly altered by improvements in the fine details of the program.

3. Sequential Gaussian Elimination

It will be useful to review Gaussian elimination with partial pivoting as it applies to matrix inversion on a sequential computer.[5] Gaussian elimination directly (in a finite number of steps) reduces the coefficient matrix of a system of equations

$$\mathbf{Ax} = \mathbf{b} \text{ with } \mathbf{A} \in \mathbf{R}^{n \times n} \text{ and } \mathbf{x}, \mathbf{b} \in \mathbf{R}^{n}$$

to diagonal form in two phases: forward reduction and back substitution. Recall that the solution to a system of linear algebraic equations is unchanged by additions of multiples of any equation to any other equation. Such operations provide the means for transforming the coefficient matrix to diagonal form. In the first phase, matrix elements below the diagonal are systematically reduced to zero beginning with the first column and ending with the last column. In the first step, multiples of the first row are added to the following rows. The multiples are chosen to produce zeros in the first column below the diagonal. In the second step of the forward reduction, mutliples of the second row of the matrix are added to the following rows in order to produce zeros in the second column below the diagonal. The forward reduction phase ends after $(n-1)$ steps and produces an upper triangular matrix from the coefficient matrix. In a similar fashion, the back substitution phase consists of bringing to zero the matrix elements above the diagonal beginning with the last column and ending with the first. In the first step of back substitution, multiples of the last row are added to the rows above it to produce zeros in the last column above the diagonal. Back substitution ends after $(n-1)$ steps. As a result of the transformations in the forward reduction and back substitution, the matrix **A** becomes a diagonal matrix. The same sequence of operations is carried out on the right hand side vector **b**. After the coefficient matrix is transformed into a unit matrix, the modified right hand side vector is the solution.

Inversion can be considered as a special application of Gaussian elimination: to find the inverse of the coefficient matrix, we choose a special set of $\mathbf{b}_i = \mathbf{e}_i$ where $i = 1, 2, \ldots, n$ and $\mathbf{e}_i$ is the ith unit vector with 1 as its ith entry and zeros for the remaining components. Therefore, for inversion, there are n simultaneous **b** vectors and the solution is an n × n matrix.

$$\mathbf{AX} = \mathbf{I} \text{ with } \mathbf{A}, \mathbf{X}, \text{ and } \mathbf{I} \in \mathbf{R}^{\mathbf{n}\times\mathbf{n}}$$

where **I** is the unit matrix.

Gaussian elimination prescribes a finite number of steps which will bring the coefficient matrix to diagonal form if the matrix is positive definite or diagonally dominate. At each step, the row of the matrix used to achieve zeros in one column is called the pivot row and the diagonal element of the pivot row is called the pivot element. Notice that the pivot element is in the same column that is to be made zero below the diagonal. The multiples of the pivot row necessary to produce a column of zeros are called multipliers. This algorithm will fail if a pivot element is zero. In many cases, this failure can be surmounted by using partial pivoting.

Partial pivoting is the standard technique to reduce numerical instability and avoid catastrophic failure during the direct solution of systems of linear equations. Numerical instability in direct methods of solving linear systems (of which Gaussian elimination and Gauss-Jordan inversion are examples) occurs because of very large multipliers which, in turn, are due to very small pivot elements. When a large multiple of the pivot row is added to another row of the matrix, finite precision arithmetic leads to a loss of the information contained in the non-pivot row. The result is a row which is nearly dependent on the pivot row and therfore, a nearly singular matrix. Given a particular column, i, that is to be made zero, partial pivoting involves choosing from the active rows, that row with the largest element in absolute value in column i as the pivot row. This leads to multipliers that are always less than unity, hence rounding errors are reduced. A second situation which requires pivoting has nothing to do with numerical instability; a zero pivot element can be encountered in a perfectly well conditioned matrix. As an example, consider the two by two unit matrix with the rows interchanged. Without pivoting, the first element of the first row is taken as the pivot element. Obviously no multiple of the first row of this matrix will produce a zero in the first column when added to the second row. Partial pivoting prevents the failure of the program in this situation.

Once the pivot row is selected, the matrix rows are interchanged so that the pivot element is brought to the diagonal position. We shall always assume that the

pivot element is on the diagonal for ease of discussion. The rest of the Gaussian elimination algorithm is unchanged once the pivot row is selected. If a nonzero pivot element can be found at all stages of the forward reduction with pivoting, then the algorthm will produce the inverse and the original matrix is nonsingular. After the coefficient matrix has been transformed into the unit matrix, the columns of the solution matrix must be permuted in the inverse order of the row exchanges. For the convenience of the reader, we provide an outline of our implementation of a Gaussian elimination method for matrix inversion on a sequential machine.

4. Observations on Sequential Gaussian Elimination

A few general observations on Gaussian elimination, as it applies to matrix inversion, are in order. We will see that inversion requires fewer operations than the general application of Gaussian elimination. Secondly, the inverse construction can be overlaid in the same data space as the transformed coefficient matrix thus forming a composite matrix. Thirdly, rows of the composite matrix become inactive during the algorithm, but the columns do not. This will have important consequences for the parallel version of the code. All of these observations will apply to the parallel implementation of Gaussian elimination as well as the sequential implementation.

The operations count to solve a *general* linear system with n equations and n right hand side vectors is $\frac{4}{3}n^3$, where the term operations count refers to the number of multiplications required. The operations count for matrix inversion is n^3, where n is the matrix dimension.[2,5] The operations count savings associated with matrix inversion comes about because of the special nature of the right hand side vectors (*i.e.*, only one nonzero element in each column). These savings exist in the parallel version also.

As a second point, the nonzero elements of the inverse construct can be stored where zeros are produced in the original matrix during forward reduction. The inverse construct begins as the unit matrix. As one column of the construct becomes

nonzero, the corresponding column of the transformed coefficient matrix becomes zero. This feature exists throughout the forward reduction. A organizational benefit of the storage of the transformed coefficient matrix and the inverse construct in a composite matrix is that the single matrix is transformed as a whole because the two parts transform in the same way. At the end of forward reduction, the coefficient matrix is an upper triangular matrix with ones on the diagonal and the identity matrix has become a lower triangular matrix. The inverse construct must be moved into separate data space before back substitution begins because it becomes full immediately.

A third feature of Gaussian elimination is the growth of inactive matrix rows in both phases of the algorithm. Both inversion and the solution of general systems of equations have this characteristic. An inactive matrix row is one which is not modified further. The inactive matrix rows occur because the rows above the pivot row are not altered during the forward reduction and those below the pivot row are not altered during back substitution. For the solution of a general system of equations, the columns of the coefficient matrix become inactive also. In the special case of inversion, this growth of inactive columns is avoided by realizing that the inverse construct gains a new *active* matrix column precisely when the coefficient matrix loses one. Storage of the inverse construct where zeros are produced in the coefficient matrix during forward reduction yields a composite matrix whose columns are always active. During the back substitution, the inversion construct is a full matrix with no inactive columns and the coefficient matrix is not modified further. We conclude that any application of Gaussian elimination implies the growth of inactive matrix rows and that, in contrast to the general system of linear equations, matrix inversion can be accomplished without incurring inactive matrix columns.

The remarks above hold for inversion in general; however, we wish to point out a feature of the particular algorithm just given. The multipliers for a given pivot row are calculated all at once and stored in a second array and the pivot row

is stored in a third array. It turns out that, even on a single processor, calculating the multipliers for all rows at once and storage of the pivot row in separate memory enhances program performance by simplifying the transformation loop. The cost is some extra memory. For the purely sequential version of the algorithm, this extra memory usage can be avoided. In the parallel version, this choice appears naturally, as will be discussed later in the paper.

5. Sequential Gauss-Jordan Inversion

The sequential Gauss-Jordan algorithm is an algorithm for in-place matrix inversion. It can be thought of as a simple modification of Gaussian elimination and has the same operations count: the elements of a column of the matrix, both below and above the diagonal, are set to zero in each step. (In Gaussian elimination, elements in a column below the diagonal are set to zero during the forward reduction phase and elements in a column above the diagonal are set to zero during the back substitution phase.) As a result, no back substitution loop is needed nor is any extra memory for the inverse.

On sequential computers, LU decomposition, which is closely related to Gaussian elimination, has largely replaced Gauss-Jordan inversion since the inverse of a matrix can be obtained from its LU decomposition in the same total number of operations. In addition, the LU decomposition is a useful first step in many other applications. However, for a parallel computer, Gauss-Jordan inversion has the advantage that no matrix rows become inactive at any stage of the algorithm. We shall see that this has several benefits.

In order to understand how parallel Gauss Jordan inversion is superior to inversion by Gaussian elimination, when the sequential versions of these two algorithms are different only in organization, we must discuss parallel Gaussian elimination and its problems.

6. Parallel Gaussian Elimination

The parallel matrix inversion program based on Gaussian elimination will be briefly reviewed. It is discussed more fully in an earlier memo.[6] (The first discussion of linear algebra on the hypercube is presented by Fox.[7]) Once this parallel algorithm is outlined, its modifications to yield the parallel Gauss Jordan inverter will be simple, but with significant advantages.

The basic strategy is to translate the sequential Gaussian elimination algorithm into a parallel algorithm with a minimum number of alterations. The two tasks that must be introduced into the sequential code are data distribution among the processors and interprocessor communications. Data distribution is set up at the beginning of the run when the complete data set is passed to every processor from the disk drive of the host sequential computer (e.g. VAX). The source code in each processor must contain logic which determines that part of the data set to be stored in its local memory. (Local refers to an individual processor.) After the initial down loading of data, a processor must communicate with other processors to fetch data that it does not have in local memory. Based on the data distribution chosen and the algorithm, the parallel processor program must be organized to initiate interprocessor communications when additional data in needed to proceed with the task. The communication routines available in the Crystalline operating system must be called by both transmitting and receiving processors. The topics of data distribution and interprocessor communication may be clarified by considering a concrete application.

How the global data (matrix) is distributed among the processors is the first decision that must be made and is closely linked with the algorithm chosen. It is important to distribute the data in such a manner that the interprocessor communication is minimized. For matrix inversion, the data distribution is straightforward. Imagine that the processors are laid out in a two dimensional array. A hypercube architecture machine can always be configured as a two dimensional

array of processors. A function, appropriately named *whoami*, provides the necessary information for the application program in each node to understand how to communicate to its four nearest neighbors and what its coordinates are in the two dimensional array of processors. The communication channels for the two dimensional array of processors are along the column and the row containing the processor. Next, imagine superimposing the matrix onto the array of processors and placing each element of the matrix in the processor which it coincides with. This will be called the *naive* data distribution scheme. Our only modification of this idea for Gaussian elimination (see references 6 and 7) is that consecutive matrix rows are placed in consecutive rows of processors modulo the number of rows of processors. This is called the *shuffled-row* data distribution scheme and is used to reduce work load imbalance as we shall see. In either case, a matrix column is contained in a single column of processors and a matrix row in a single row of processors.

In order to be precise, the formulas for distributing the matrix are given. Let N_r and N_c be the number of processor rows and columns, respectively. Then matrix element $a(i,j)$ is placed in processor row I and column J according to

$$I = \frac{i}{N_r}; \qquad J = \frac{j}{N_c} \qquad \text{naive}$$

when the naive distribution is employed and

$$I = i \text{ modulo } N_r; \qquad J = \frac{j}{N_c} \qquad \text{shuffled-row}$$

when the shuffled-row distribution is employed. The arithmetic is strictly integer in these formulas.

Cartoons of the naive and shuffled-row distribution of a four by four matrix over a two by two arrangement of processors are shown below.

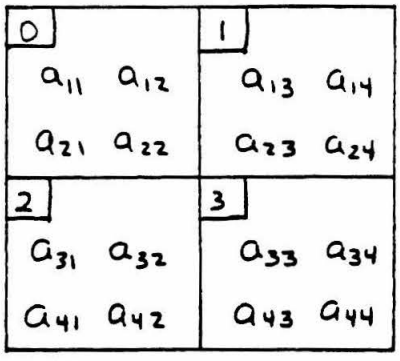

naive

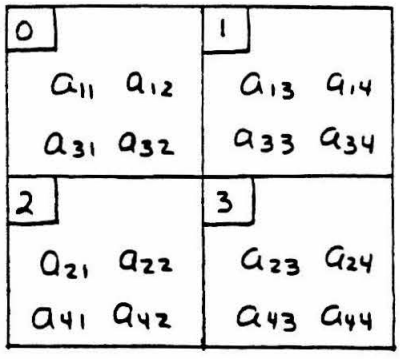

shuffled-row

Once the matrix is distributed among the hypercube processors, parallel Gaussian elimination is essentially the same as the sequential version described above. The distinctions are that a processor works on its subset of the matrix instead of the entire matrix and that communications occur when a processor needs data held in another processor. Communications are necessary to provide a copy of the pivot row and the multipliers to every processor. Once a processor has these, the transformation of its part of the matrix is identical to that in the sequential algorithm.

Multiples of the pivot row of the matrix are added to other matrix rows in order to produce a column of zeros, so the pivot row must be passed to other processor rows containing active matrix rows. One row of processors contains the pivot row at the beginning of each sweep through the matrix, and other rows of processors need the pivot row. Each processor requires only those elements of the pivot row contained in the same column of processors. To see this, remember that each processor holds a fraction of the total number of columns. It needs only the same columns of the pivot row. Since the data are distributed in such a manner that any matrix column is contained in a single column of processors,

the pivot row section contained in a given column of processors is passed to other processors in the same processor column. In other words, the pivot row needs only be passed to a subset of processors and the communications are row-wise (*i.e.*, no data are passed to processors in other columns of the processor array). Once each processor has a copy of that part of the pivot row which it needs, the multpliers are calculated and communicated.

The multipliers are calculated using the pivot element and the matrix column that is to be set to zero in that step. These data are available in one column of processors and the multipliers must be passed to the remaining processor columns. A given row of the matrix is contained in a single row of processors. The multiplier for each matrix row will be calculated in one processor in the same row of processors; therefore, the communication path for passing multipliers is across processor columns. The cartoon below illustrates the data flow for the communication of the pivot row and the multipliers. The data flow patterns are the same for both Gaussian elimination and Gauss-Jordan inversion.

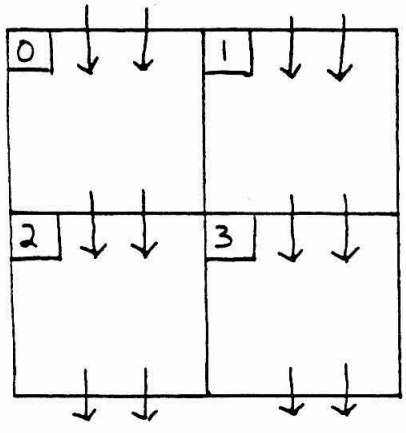

pivot row passing

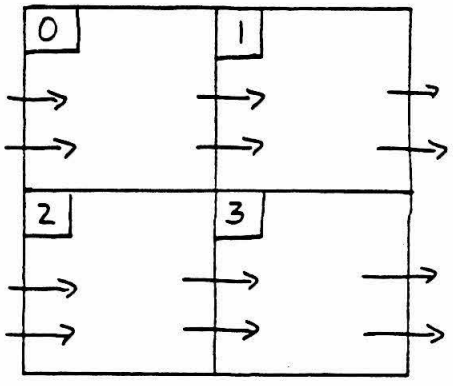

multiplier passing

Now that the data distribution scheme and the algorithm's outline have been described, a few remarks about these are possible. The shuffled row data distribution is necessary for an efficient ***Gaussian elimination*** algorithm because it leads to a homogeneous work load among the processors as the forward reduction

or back substitution progresses. The growth of inactive (unmodified) rows of the matrix in both phases of Gaussian elimination decreases the work load in all of the processors. One matrix row becomes inactive at each step. The shuffled-row distribution causes each successive inactive matrix row to appear in a successive row of processors. In other words, any processor contains no more than one inactive matrix row more than any other processor. By keeping the active matrix rows distributed uniformly among the processors, the work load decreases homogeneously. It is important to optimum throughput that the work load remain uniformly distributed at all times; otherwise, a small number of processors are overburdened while others are idle. The effective number of processors will then be less than the actual number, and the parallel computer will not perform as desired.

In contrast to the shuffled-row scheme, the naive data distribution scheme with Gaussian elimination permits entire rows of processors to become idle when they contain only inactive matrix rows, while other processor rows contain no inactive matrix rows. (*e.g.*, consider the first and last rows of processors at an intermediate part of the inversion). In fact, the last row of processors contains no inactive matrix rows for most of the execution when the naive data distribution is used with Gaussian elimination. Since these are the rate determining processors, it is as if there were no inactive matrix rows in the parallel algorithm as there are in the sequential algorithm.

Work load inhomogeneity also arises during the calculation of the multipliers: only one processor column is responsible for finding them and the remaining processors must wait. This is not very detrimental to efficiency because the work involved is negligible compared to the remaining floating point arithmetic that the processor must carry out. In addition, as the work load of the entire machine decreases, the number of multipliers decreases commensurately and the work load inhomogeneity is not aggrevated.

The rows of the matrix are shuffled to maintain work load homogeneity, but why not the matrix columns? The columns of the matrix remain active and there

is no need to insure that the active columns remain homogeneously distributed. In contrast, for LU decomposition, one would want to shuffle the matrix columns as well as its rows, since both become inactive as the decomposition progresses.

Work load decrease among the processors is harmful for another reason besides the inhomogeneity problems it raises: parallel computer efficiency depends on a high ratio of floating point operations to interprocessor communications. Declining floating point arithmetic in many processors coupled with a constant communication overhead leads to inefficient parallel algorithms. In the case of inactive matrix rows this is exactly what is happening. Every processor must pass the pivot row to its neighbor regardless of the number of active matrix rows it contains. The effect is not so important in the multiplier communication. As the work load of the processor row decreases, the number of multipliers communicated also declines so that the ratio of communication to multiplication is constant.

We have described how the parallel computing issues set forth in the first paragraphs of the paper affect Gaussion elimination inversion. The bottom line is whether or not the additional operations, most notably communications, are negligible in comparision to those require to complete the given task in each processor. The reason communications are emphasized is that each word communicated requires a time on the order of that needed for floating point multiplication of the word. The integer arithmetic and logic in the software overhead for a parallel code is much faster and unless there is a very large amount of it, it is not influential on parallel performance. We will see below how the Gauss-Jordan algorithm for matrix inversion naturally lessens these problems.

7. Parallel Gauss-Jordan Inversion

In parallel Gauss-Jordan inversion, the matrix elements above and below the diagonal are zeroed in each sweep. This removes the need for a back substitution loop and separate storage for the inverse matrix. As a result, the work load is more homogeneous, there are fewer interprocessor communication calls, and the

software is simplified. Furthermore, just as in the sequential versions, the floating point operations count is the same for inversion by Gaussian elimination and Gauss-Jordan inversion.

The absence of a back substitution loop and the fact that all nondiagonal elements of a matrix column are zeroed in each sweep imply that no matrix rows become inactive and the shuffled-row data distribution is unnecessary. Instead, the naive data distribution scheme is used. In addition, no matrix columns become inactive during matrix inversion in Gauss-Jordan inversion for the same reasons as the case of Gaussian elimination; therefore, the only source of work load inhomogeneity is the calculation of multipliers. The Gauss-Jordan algorithm offers nearly homogeneous and constant work load distribution with no need for sophisticated data distribution schemes. This is one of the criteria for an effective parallel code.

Another advantage of Gauss-Jordan inversion over Gaussian elimination is that half as many calls are required to the communication routines, and more data are passed in each call. Both parallel algorithms must communicate exactly the same amount of data and over the same pathways. The differences are the absence of a back substitution loop with its many communication calls and the concommitant increase in the data passed in each commmunication call in the Gauss-Jordan algorithm. Since pipelined data passing routines are available, the program benefits from fewer, more efficient communications calls. (The time for interprocessor communication is a linear function of the number of words communicated with a constant term that is comparable to the coefficient of the linear term. Therefore, the communication time per word is twice as long for one word as it is for a multiword communication call.) Minimizing the interprocessor communication load is the second requirement for efficient use of the hypercube computer.

The last criterium we listed for an effective parallel code is low software overhead. With Gauss-Jordan inversion, the length of the program is $\frac{1}{3}$ that of the parallel inversion code using Gaussian elimination, which implies a substantial reduction of logic and switching overhead. This reduced overhead follows from the

absence of a back substitution loop and the need to separate the inverse construct from the original matrix. We conclude that Gauss-Jordan inversion in better than Gaussian elimination in all categories.

8. Parallel Partial Pivtoing

We have not yet considered the issues involved in partial pivoting on the hypercube. Pivoting degrades the efficiency of the parallel code because of the increased communication costs which are not compensated for by increased floating point work. Furthermore, the extra work involved in locating the pivot row is done in one processor column; hence, it is not uniformly distributed. We shall see in section 9, that pivoting does not reduce the parallel inversion efficiency to any great extent.

Partial pivoting insures that rounding errors are minimized by using mulipliers that are less than unity. Each sweep in Gauss-Jordan inversion zeros the nondiagonal elements of a column of the matrix. For the parallel algorithm, we have stored the matrix such that a matrix column is contained in a single column of processors. Each processor in the processor column must search through its part of the matrix column and choose the largest element in absolute value. Then each processor in the column of processors compares the pivot candidate from each other processor and takes the largest. The only subtlety occurs when two candidates for the pivot element are exactly equal in magnitude. In this case, a consistent convention must be in place so that every processor makes the same choice concerning which row of processors will hold the pivot row. The communication calls needed for the pivot row selection are relatively slow since only one word is passed in each communication routine reference. At the end of the search, every processor must know which row of processors contains the pivot row. This requires that the column of processors which has determined the pivot row communicate column-wise to the remaining processor columns.

At the conclusion of the algorithm, the matrix columns must be interchanged to undo the effects of pivoting. The columns are permuted in the reverse order of the row interchanges. This task entails communicating every matrix column to every column of processors. The communications are efficient since they are multiword data transfers. The column permutation requires no floating point work.

The extra work necessary for partial pivoting is poorly distributed and involves much communication, but will be seen to not significantly reduce efficiencies because the extra work is negligible compared to the other tasks. The complete C program for the hypercube is reproduced in the appendix and may be consulted for the details of the pivoting process.

9. Efficiency Measurements

Efficiency, ϵ, is defined as

$$\epsilon = \left(\frac{1}{\mathrm{N}}\right) \cdot \frac{\text{time on a single processor}}{\text{time on N processors}}$$

where N is the number of processors. The single processor times are obtained from runs on a single node of the hypercube. For the results discussed in this section, the single processor times are derived from runs of *the same program* after removing the overhead of the parallel code (*i.e.* after removing the communication calls and the switching logic). We will refer to this modified parallel code as the sequential code for remainder of the paper. The sequential code is *not* an optimized library routine. The efficiency is unity when the time to complete a given task on one processor is reduced by $\frac{1}{\mathrm{N}}$ when N processors are used. Perfect efficiency implies that an N processor machine is N times faster than a single processor. Communication overhead, idle processors, and extra operations prevent the realization of unit efficiency.

The efficiency of a parallel algorithm is salient because of the notion of using more processors to solve larger problems. Increasing the size of a task on a fixed

number of processors typically increases the efficiency towards some asymptote. If this asymptote decreases with an increasing number of processors, then the hope of solving problems that are currently too big by using parallel machines with a large number of processors is diminished. We will demonstrate that asymptotic efficiency approaches unity for the parallel Gauss-Jordan inversion program on all machines tested.

The time required to transfer the matrix between the VAX disk drivers and the hypercube is not included in the efficiencies. Note that communication with the VAX disk drives is not performed during the matrix inversion. It occurs when the original matrix is down loaded onto the hypercube.

Before giving the measured efficiencies, it is interesting to measure the cost of the software overhead in the parallel program. This is accomplished by running the complete parallel code and the sequential code on a single processor. The parallel program, even when run on a single processor, still contains substantial logic and integer arithmetic along with calls to communication routines which are not a part of a sequential program. The ratio of execution times of the sequential program and the parallel code run on a single processor as a function of matrix dimension is shown in figure 1. Both the pivoting and nonpivoting versions of Gauss-Jordan inversion are shown. The ratio of sequential code execution time to that of a single processor run of the parallel code gives a measure of the software overhead in the parallel code. From figure 1, we conclude that the software overhead necessary in a parallel code is of diminishing significance for increasing matrix size, and except for the smallest matrices, the ratio of times is near unity. We see that in the case of parallel matrix inversion, the distinction between single processor runs of the parallel code and the sequential code is not important.

In figure 2 efficiencies for Gauss-Jordan inversion with pivoting as a function of the full matrix dimension are plotted for 2, 4, 8, 16, and 32 processors. The solid curves are straight line segments connecting the data points for a fixed number of processors and are provided as an aid in examining the data. The dimensions

of the matrices inverted are integral multiples of the number of processor rows and columns. This insures that the same number of matrix rows and columns are stored in every processor.

The hypercube cannot allows be arranged in a *square* array of processors. The number of processors in a hypercube is expressible as $N = 2^M$ where $M = 0, 1, 2, \ldots$. If M is even, then the two dimensional array of processors can be chosen to have equal numbers of processor rows and columns. If M is odd, then there must be at least a factor of 2 difference in the number of rows and columns of processors. For the curves in figure 2, the processors are configured with equal numbers of rows and columns of processors if M is even, and, if M is odd, the number of processor columns is twice the number of rows. These are the most efficient configurations of a fixed number of processors for Gauss-Jordan inversion with pivoting. This statement will be verified below. The efficiency is a monotonically increasing function of matrix dimension for a fixed number of processors. We can conclude that the work load imbalance and communication and software overhead are of diminishing importance as the matrix size increases. For any fixed matrix dimension, increasing the number of processors reduces the efficiency since it decreases the work load of all the processors.

For the larger matrices, the efficiencies are 90% or higher for all numbers of processors examined in this study. The *rate* at which the efficiency approaches unity with increasing matrix dimension is smaller for larger numbers of processors, but the efficiencies do not appear to have an asymptote less than unity for any of the machines used. We conclude that for a fixed number of processors, the efficiency can be made as close to unity as desired by increasing the size of the matrix to be inverted. We will validate this finding again when we perform an operations count on the parallel algorithm in the next section.

For global matrix dimensions greater than 88, the efficiencies are based on extrapolated sequential code times. The available memory of a single processor impresses a limit on the size of a matrix that can be stored and inverted. A single

page of memory on the Mark II boards (64K bytes) is sufficient for a 88 by 88 double precision matrix. The extrapolation is based on fitting the single node times to a cubic polynomial for matrices with dimension 64, 72, 80, and 88. For documentation purposes, the cubic polynomial used is

$$(\frac{37}{3072})n^3 + \frac{n^2}{128} + 3.1\bar{6}n - 76 = \text{single node time in } 10^{-2}\text{seconds}$$

where n is the matrix dimension. The coefficient of the n^3 term implies an effective time of 60 μs per operation where an operation is 64 bit floating point addition or multiplication . This is in fair agreement with the corresponding true hardware time measured by Otto and Kolawa of 40 μs.[8] Of course the inversion code contains substantially more than a set of simple multiplications and additions which is reflected in the larger effective single operation time. The comparison between the effective operation time and the pure hardware time is made so that the extrapolation is substantiated.

The assertion, that a square or nearly square array of processors is the optimum configuration for Gauss-Jordan matrix inversion, is substantiated in figures 3 through 7. In these figures, efficiencies as a function of global matrix dimension are plotted for 2, 4, 8, 16, and 32 processors, respectively. In each figure, different curves correspond to different configurations of the processors. The best performance is achieved from a configuration as close to square as possible. If there must be an unequal number of rows and columns of processors, then the numbers should differ by only a factor of 2 and, it is slightly better to have more columns than rows of processors. The worst configurations are rings of processors and of the two possible ring arrangements, a single column of processors is the least efficient. The analysis showing that a square or almost square (if necessary due to the number of processors) array of processors is optimum for matrix algebra was first done by Fox.[7,9] The current empirical results support his conclusion.

As extreme examples, the two possible rings of processors provide insight into the relative importance of the communication costs and work load imbalances in

Gauss-Jordan inversion. A ring arrangement of processors takes the form of a single column or a single row of processors. A single column of processors has no work load inhomogeneity and reduced communication load: (1) there are no processors idle while multipliers are being calculated; (2) no multipliers need to be communicated since that requires column-wise data transfer and there is only one column; (3) partial pivoting leaves no processors idle; and (4) the final column exchange requires no data transfer. In contrast, a single row of processors boasts the advantage that the search for a pivot row and the subsequent row exchange need no communications. Since the best arrangement of processors is the one that is most nearly square, no single factor dominates. When the processors are not arranged in a square, it appears that the pivot row search and exchange are the most detrimental to the performance since it is better to have more processor columns than rows.

It is interesting to investigate the effect of turning off pivoting in the inverter. Figure 8 displays the efficiency of the Gauss-Jordan algorithm *without* partial pivoting as a function of global matrix dimension. Each curve represents the best arrangement of the given number of processors. No extrapolated data are presented. From studying different configurations of processors, we have again found that the best arrangement of processors is that with the same number of processor rows and columns. This is the same conclusion reached in the pivoting version. If the processor array must be rectangular, then it is slightly better to have twice as many processor rows as columns, in contrast to the pivoting version. This difference can be rationalized as follows. In the nonpivoting version, the only work load inhomogeneity is the calculation of the multipliers. This favors a small number of columns of processors.

Partial pivoting lowers the parallel efficiency slightly, but we can see by comparing figures 2 and 8 that the differences are not large. Pivoting requires some inhomogeneously distributed work and more communication among the processors. In spite of these differences between the pivoting and nonpivoting versions,

the square array of processors is the most efficient for both. This implies that the optimum configuration of processors minimizes the average communication path lengths in both the row and column directions. The fact that using partial pivoting lowers the efficiency is of academic interest only since it is a necessity in any general purpose inversion package. Matrix inversion without partial pivoting can be used only in special circumstances (*e.g.* for a well-conditioned, positive definite matrix).

Finally, we present the efficiencies for matrix inversion with parallel Gaussian elimination in figure 9. This version does not perform pivoting. Figures 8 and 9 have the same scales to facilitate comparison. The general shape of the efficiency curves is the same for both Gaussian elimination and Gauss-Jordan inversion, although the absolute positions of the curves are quite different. The Gauss-Jordan inverter is clearly more efficient than the Gaussian elimination inverter. This conclusion should come as no surprise in light of the earlier discussions: the Gauss-Jordan algorithm provides several enhancements over Gaussian elimination with no detracting features. Although the empirical efficiencies are hard evidence for our thesis that Gauss-Jordan matrix inversion is very efficient on the hypercube computers that we tested, an operations count is necessary to extend our understanding to the general hypercube and larger matrices.

10. Operations Count

An operations count gives confidence that the implementation of an algorithm is behaving correctly. By counting the total number of multiplications, additions, and communications in the slowest processor, the theoretical efficiency of the parallel algorithm with respect to a sequential algorithm is determined. How well the empirical efficiencies agree with the theoretical ones reflects the quality of the implementation of the algorithm. In addition, the theoretical efficiency, if it agrees well with the observed, can be used to extrapolate to parallel machines or matrix dimensions not accessible currently. It is particularly important to establish

whether on not the asymptotic efficiency at large matrix dimensions depends on the number of processors used.

The operations count for parallel Gauss-Jordan inversion will include communication, multiplication, and addition costs. First, we will count the total number of communications to complete the inversion algorithm in the slowest processors. Next, the multiplication and addition count will be done for the slowest processor. Both floating point multiplication and addition are included because they require about the same amount of time (38.8 μs and 38.1 μs, respectively)[8] on the Intel 8086/87 processors. By definition, the slowest processor at any stage is that one which has the heaviest communication or multiplication load. Notice that the operations count is concerned with one processor's tasks *not* with the total operations of all the processors. Pivoting is ignored in our first operations count, but will be incorporated later in this section. The symbols used in this operations count are:

n = number of matrix rows in each processor

r = number of processor rows/number of processor columns

nr = number of matrix columns in each processor

N = number of rows of processors

$\frac{N}{r}$ = number of columns of processors

C = total number of communications

C_{piv} = total number of communications to pass pivot rows

C_{mult} = total number of communications to pass multipliers

M = total number of multiplications

A = total number of additions

$dim = nN$ = dimension of global matrix

Interprocessor communications are required to pass the pivot rows and the multipliers. To transfer a single pivot row, each processor communicates $n \cdot r$ words

of data. This must be done for each global matrix row, so n^2rN words must be passed. To communicate the multipliers requires n words be passed for each global matrix row. The result is n^2N communications to pass the multipliers. We find that the total communications count is

$$C = C_{piv} + C_{mult} \tag{1}$$

$$C_{piv} = n^2Nr \tag{2}$$

$$C_{mult} = n^2N \tag{3}$$

The slowest parallel processor performs the same number of multiplications on its subblock of the matrix as is required by the sequential matrix inversion algorithm for a matrix of the same dimension as the subblock. For each global matrix row, n multipliers are calculated resulting in a subtotal of n^2N multiplications. Given the n multipliers and the nr elements of the pivot row, each processor must perform n^2r multiplications and n^2r additions for each global matrix row for a subtotal of n^3rN multiplications and the same number of additions.

$$M = n^2N + n^3rN \tag{4}$$

$$A = n^3rN \tag{5}$$

Equation (4) overestimates the effective number of multiplications. It assumes that the processors in other columns are idle while the multipliers are calculated. In fact, the other processor columns are idle only when the multipliers are calculated for the first time in a processor column. This is easily seen by example. The first set of multipliers are calculated in the first column of processors while the other processor columns are idle. After that, the other processor columns are n steps behind the first processor column and do not become idle waiting for the multipliers. Each time a processor column first calculates the multipliers, the other processor columns wait. The new expression for M is

$$M = nN/r + n^3rN \tag{6}$$

In order to find a single operations count that includes communications, multiplications, and additions, C must be converted into effective multiplications. Multiplications and additions take the same amount of time.[8] Let λ_i represent the ratio of multiplication to communication time. Multiplication time is that necessary to fetch two floating point numbers from memory, multiply them, and put them back in memory. Communication time is the time per word to transfer i words between neighboring processors in a single call to a communication routine. The total communication time varies linearly with the number of words transmitted.[8]

$$t_{comm}(i)/\mu s = 82i + 90 \tag{7}$$

where i is the number of 64-bit words passed in a single transfer and includes both reading and writing. The communication time per word is longer for one word than for many words due to the startup time which is independent of the number of words transmitted. $\lambda_i = \lambda_\infty$ within 1% when $i > 100$. λ_i allows the conversion of communication time into effective multiplication time so that communication count can be added to the operations count resulting in a total parallel operations count. The total operations count for the parallel Gauss-Jordan inversion algorithm *without pivoting* is

$$\text{Total effective multiplications} = M + A + \lambda_n C_{mult} + \lambda_{nr} C_{piv} \tag{8}$$

$$\text{Total effective multiplications} = 2n^3 rN + nN/r + n^2 N(r\lambda_{nr} + \lambda_n) \tag{9}$$

which can be simplified for n large enough to set $\lambda_{nr} = \lambda_n = \lambda_\infty$.

$$\text{Total effective multiplications} = 2n^3 rN + nN/r + \lambda_\infty n^2 N(r+1) \tag{10}$$

The leading term in the multiplication count goes like n^3 and that in the communication count goes like n^2 for a fixed number of processors. For $n \to \infty$, the multiplication count dominates the total parallel execution time. In particular, the communication time can be made negligible compared to the floating point

arithmetic time. Fox pointed out that this observation holds in most parallel linear algebra algorithms for the hypercube if the data in distributed sensibly. It is important that the coefficient of the n^3 term is linear in N, because this leads to unit asymptotic efficiency regardless of the number of processors. If the cubic term varies with a higher power of N, then unit asymptotic efficiency would not be achievable.

The sequential algorithm requires $2(dim^3 - dim^2)$ floating point operations to second order in the matrix dimension and no communications. Using the definition of efficiency, we find

$$\epsilon = \frac{1 - \frac{1}{dim}}{1 + \frac{\alpha}{n} + \frac{\beta}{n^2}} \text{ where } \alpha = \frac{\lambda_\infty (r+1)}{2r} \text{ and } \beta = \frac{1}{2r^2} \tag{11}$$

This theoretical efficiency simplifies for large matrices and large n to

$$\epsilon = 1 - \frac{\alpha}{n} \tag{12}$$

where α in independent of n, the number of matrix rows in each processor and N, the number of processor rows. This expression shows that for any given number of processors, the theoretical efficiency tends to unity as the matrix dimension increases.

It is implicit in the discussion above that there is one value of λ for all of the communications. This is valid if the number of matrix rows and columns in each processor is large enough to use the asymptotic value of the communication time per word. The timing information for multiplication and communication on the Mark II hypercube is determined by the hardware and is given by Otto and Kolawa.[8] From this reference, the value of $\lambda_\infty \approx 1$. Given this single, hardware dependent parameter, the expression for the efficiency depends only on the number and configuration of the processors and the size of the matrix (*i.e.*, the expression provides an absolute value for the efficiency). In the efficiency estimates given below, we used the full expression (9) for the execution time of the parallel code and the linear equation (7) for $t_{comm}(i)$.

Figure 10 shows the predicted and observed efficiencies. The theoretical efficiencies are calculated for the same matrix sizes as those for which efficiency was measured. The empirical efficiencies are represented by the markers with no connecting curve. The theoretical efficiencies are unmarked and are connected by straight line segments. The highest theoretical curve corresponds to the highest empirical data. The next highest curve corresponds to the next highest markers and so on. Only unextrapolated times are listed because the extrapolation is less reliable than the efficiency estimate. The operations count could be used to extrapolate the single node times in principle, but it is desirable to avoid extrapolation with a expression which is the object of our tests. The agreement between the theoretical efficiencies, which have no adjustable parameters, and the observed efficiencies in all cases shows that the program is well behaved and that all the important issues in this parallel program are accounted for. Most importantly, the conclusion that unit efficiency is achievable with large matrix sizes on any number of processors is supported by the level of accuracy of the theoretical efficiency for the cases that are accessible.

Including partial pivoting in the parallel operations count increases the number of communications and does not affect the number of multiplications and additions. $N-1$ communications of a single word occur for each pivot row selection, yielding a total of $(N \cdot n - 1) \cdot (N - 1)$ communications. To permute the matrix columns at the end of the algorithm requires $2 \cdot (n \cdot N - 1) \cdot n$ communications: $(N \cdot n - 1)$ column exchanges are required, each column exchange requires 2 columns be passed, and each column contains n elements locally. The column permutations allow n words to be transfered in a communication routine call and hence require less time per word than the single word communication calls needed in the pivot row selection process. The following total operations count is obtained for Gauss-Jordan matrix inversion with pivoting on the hypercube.

$$Total = 2n^3rN + nN/r + \lambda_\infty n^2 N(r+3) + \lambda_1 nN(N-1) \qquad (13)$$

We have again assumed that $\lambda_{nr} = \lambda_n = \lambda_\infty$. Since pivoting does not affect the number of multiplications, the multiplication count still goes like n^3 in leading order. The communication count still goes like n^2 to leading order, but the corresponding coefficient is different for the pivoting and nonpivoting versions. Pivoting has introduced a term linear in n that behaves like N^2, the square of the number of processor rows. The N^2 term reflects the communication load in the pivot row selection task and can be nonnegligible for large numbers of processors and modest matrix sizes. For a fixed number of processors, it can be made negligible to the floating point work by increasing the dimension of the matrix. The efficiency estimate for the pivoting version of Gauss-Jordan inversion is

$$\epsilon = \frac{1 - \frac{1}{dim}}{1 + \frac{\alpha}{n} + \frac{\beta}{n^2}}; \text{ where } \alpha = \frac{\lambda_\infty (r+3)}{2r} \text{ and } \beta = \frac{1 + \lambda_1 (N-1) r}{2r^2}$$

For $n >> N$, this simplifies to the same form as the nonpivoting efficiency

$$\epsilon = 1 - \frac{\alpha}{n}$$

We have assumed that the operations count for the pivoting version of the sequential algorithm is unchanged since it involves inequality evaluations and intraprocessor data relocation are neglected but no floating point work.

Theoretical efficiencies for the parallel Gauss-Jordan inverter with pivoting do not agree well with the observed. In all cases the theoretical estimates are too low. It is our belief that the discrepancy arises from neglect of the inequality evaluations, intraprocessor data movement, and loop overhead which are substantially increased in the pivoting version of both the sequential and parallel codes. The pivot selection part of the parallel code is roughly one half of the total source code. It is our experience that this many lines of code take nonnegligible execution time, even if the tasks do not involve floating point arithmetic. This non-floating point work is not included in our operations count for either the parallel or sequential codes. In principle, these tasks can be timed and included in the operations count, but this is typically not done and will not be done here. For the largest matrices,

the pivoting efficiency estimate is within a few percent of the observed. Our conclusion is that for very large matrices, the parallel software overhead is negligible, but not for intermediate and small matrices. The nonpivoting efficiency estimates are in good accord with the observed for all matrix sizes because there is very little software overhead. Given the pedestrian nature of the parallel operations count, it is remarkable that the efficiency estimates for the nonpivoting version agree with the observed as well as they do. (Recall that the theoretical efficiency is an absolute prediction based on hardware performance and the algorithm.) An improvement in the efficiency estimates for the pivoting version will require that the other operations performed by the code be included in the count in addition to the arithmetic operations and communications.

11. Summary

In summary, the Gauss-Jordan matrix inversion algorithm with pivoting is an efficient algorithm for parallel computation. Some of the reasons for this efficiency have been discussed. Two important observations are that the work load of each processor is nearly constant throughout the algorithm and is homogeneously distributed among the processors. In addition, references to communication routines are kept a low as possible. Most importantly, we have seen that the communication costs increase more slowly n^2 than the floating point costs n^3 with increasing local matrix subblock size n. For this reason, floating point work dominates the communication costs for large matrices and the parallel program is efficient.

In contrast, Gaussian elimination applied to matrix inversion involves decreasing work loads in each processor and it was necessary to distribute the data in such a manner that the work load remained homogeneously distributed throughout the processors. Gaussian elimination uses twice as many references to the communications routines in order to transfer the same amount of data. Since pipelined communications are available, this increase in the number of references is detrimental to efficiencies: the effective communication costs are higher because each

communication takes more time. In spite of these shortcomings, Gaussian elimination does have an asymptotic efficiency of unity.[6] It is simply not as efficient as Gauss-Jordan inversion on a given matrix and hypercube computer.

It is remarkable that the parallel implementations of two essentially equivalent sequential algorithms have very different characteristics and that one is clearly superior. One would not choose between Gaussian elimination and Gauss-Jordan inversion for a sequential machine based on performance considerations; however, for a parallel machine one would do just that.

We have shown that the Gauss-Jordan algorithm is well understood by the agreement between the theoretical efficiencies and the empirical ones. The theoretical efficiency supports our conclusion that unit efficiency is possible for this program on any size hypercube in the limit of large matrix sizes. Although we have measured the performance of our program on a wide range of matrix sizes and on the possible configurations of 2,4,8,16, and 32 processor hypercubes, current machine memory is insufficient for empirical verification of our conclusions of unit asymptotic efficiencies to the degree that we would like. In spite of the small matrix sizes that could be studied, we observed better than 90% efficiency on all of the hypercube computers.

If parallel algorithms which perform as well as Gauss-Jordan inversion can be found for most linear algebra tasks, then parallel computing has the potential of providing the performance necessary to address some very large problems in scientific computation.

Acknowledgements: One of us (Paul Hipes) would like to thank Peter Noerdlinger for pointing out some potential problems in the pivot row selection part of the parallel program.

References

[1] The superiority of the Gauss-Jordan algorithm over Gaussian elimination was first suggested to us by Charles Lawson of Jet Propulsion Laboratory in a perceptive memo following a seminar given by one of the authors.

[2] J. Stoer and R. Bulirsch, **Introduction to Numerical Analysis** , (Springer-Verlag, New York, 1980), pp.169-172.

[3a] G. Fox and S. Otto, "Concurrent Computation and the Theory of Complex Systems", Caltech internal document,C^3P 255 (CALT-68-1353), March 3, 1986.

[3b] G. Fox, "The Performance of the Caltech Hypercube in Scientific Calculations: A Preliminary Analysis", April 1985; invited talk at the symposium on "Algorithms, Architecture, and the Future of Scientific Computation", Austin, Texas, March 1985, (*University of Texas Press*, Austin, Texas, 1986).

[3c] G. Fox, G. Lyzenga, D. Rogstad, S. Otto, "The Caltech Concurrent Computation Program-Project Description", March 1985, in proceedings of "The 1985 ASME International Computers in Engineering", August 4-8, 1985, (Boston); published by ASME, 1985.

[3d] G. Fox and S. Otto, "The Caltech Concurrent Computation Program-A Status Report", December 2, 1985, To be published in *Computers in Mechanical Engineering*, published by ASME (Springer-Verlag, 1986).

[3e] G. Fox, M. Johnson, G. Lyzenga, S. Otto, and J. Salmon, "Solving Problems on Concurrent Processors Volume 1: Overview and General Techniques", (book in preparation).

[3f] J. Tuazon, J. Peterson, M. Pniel, and D. Lieberman(JPL), "Caltech\JPL Hypercube Concurrent Processor", in Proceedings of 1985 International Conference on Parallel Processing in St. Charles, Ill., August 20-23, 1985.

[4] B. R. Johnson, *J. Comput. Phys.***13**,445(1973); F. Mruhala and D. Secrest, *J. Chem. Phys.***78**,5954(1983).

[5] A. Jennings, **Matrix Computation for Scientists and Engineers** (Wiley, New York) 1977.

[6] P. Hipes and A. Kuppermann, "Atom-Diatom Cross Section Calculations on Concurrent Computers: Matrix Inversion", unpublished Caltech Report.

[7] G. Fox, "Matrix Operations on the Homogeneous Machine", Caltech preprint CALT-68-939, DOE Research and Development Report(1982).

[8] S. Otto and A. Kolawa, "Performance of the Mark II and Intel Hypercubes", unpublished Caltech Report C^3P-254 (February 1986).

[9] G. Fox, A.J.G. Hey, and S. Otto, "Matrix Algorithms on the Hypercube I: Matrix Multiplication", October 1985 (to be published in *Parallel Computing*).

Figure Captions

Figure 1. Ratio of the execution time of a true sequential version of Gauss-Jordan inversion to the execution time of the hypercube version of Gauss-Jordan inversion on a single processor as a function of the global matrix dimension on the Caltech Mark II hypercube. The ratios of execution times without partial pivoting are represented by square markers. The ratios with partial pivoting enabled are represented by triangular markers. The curves are straight line segments connecting the corresponding markers and are used to guide the eye. The term global matrix dimension is used to denote the dimension of the full matrix regardless of the number of processors.

Figure 2. Efficiency of Gauss-Jordan matrix inversion with partial pivoting on the Caltech Mark II hypercube as a function of the global matrix dimension. Different markers and curves correspond to different total numbers of processors working in parallel as indicated by the label on each curve. The number of rows and columns of processors used is the most efficient arrangement for that number of processors (see text). Squares refer to configurations of the hypercube with two processors. Pluses refer to a four processor configuration. Circles refer to an eight processor configuration. Crosses refer to a sixteen processor configuration. Triangles refer to a thirty two processor configuration. Straight line segements between markers are simply a guide to the eye.

Figure 3. Efficiency of Gauss-Jordan matrix inversion with partial pivoting on two processor configurations of the Caltech Mark II hypercube as a function of the global matrix dimension. The ordered pair of numbers labeling each curve gives the number of rows of processors and the number of columns as (number of rows of processors, number of columns of processors). Straight line segments between the markers are simply a guide to the eye.

Figure 4. Efficiency of Gauss-Jordan matrix inversion with partial pivoting on four processor configurations of the Caltech Mark II hypercube as a function of the global matrix dimension. See figure 3 for details.

Figure 5. Efficiency of Gauss-Jordan matrix inversion with partial pivoting on eight processor configurations of the Caltech Mark II hypercube as a function of the global matrix dimension. See figure 3 for details.

Figure 6. Efficiency of Gauss-Jordan matrix inversion with partial pivoting on sixteen processor configurations of the Caltech Mark II hypercube as a function of the global matrix dimension. See figure 3 for details.

Figure 7. Efficiency of Gauss-Jordan matrix inversion with partial pivoting on thirty-two processor configurations of the Caltech Mark II hypercube as a function of the global matrix dimension. See figure 3 for details.

Figure 8. Efficiency of Gauss-Jordan matrix inversion *without* partial pivoting for the most efficient configurations of the Caltech Mark II hypercube as a function of the global matrix dimension. Different markers and curves refer to different total numbers of processors as indicated by the curve labels in the figure. The straight line segments between the markers are simply a guide for the eye.

Figure 9. Efficiency of Gaussian elimination inversion *without* partial pivoting on the Caltech Mark II hypercube for the most efficient configuration of the processors as a function of global matrix dimension. Different markers and curves refer to different total numbers of processors. The ordered-pair label associate with each curve in the figure indicates the number of rows of processors and the number of columns of processors as (number of processor rows, number of processor columns). The product of the two elements of the ordered pair is equal to the total number of processors for that curve. The straight line segment between the markers are simply a guide to the eye.

Figure 10. Empirical and theoretical efficiencies for Gauss-Jordan matrix inversion *without* partial pivoting on the Caltech Mark II hypercube as a function of global matrix dimension. Different markers and curves refer to different total numbers of processors arranged in the most efficient configuration. The total number of processors is indicated by the label associated with each curve. The curves are theoretical efficiencies derived from formal operations counts for a variety of

total numbers of processors. The markers are empirical efficiencies for the same configurations and total numbers of processors as the theoretical curves. The uppermost curve corresponds to a total number of two processors and is associated with the uppermost markers (squares). The second curve from the top corresponds to a total of four processors and is associated with the pluses. The third curve from the top corresponds to a total of eight processors and is associated with the circles. The fourth curve from the top corresponds to a total of sixteen processors and is associated with the crosses. The bottommost curve corresponds to thirty-two processors and is associated with the lowest set of markers (second set of squares). The sections of the curves between the abscissa values corresponding to the markers are straight line segments and are not based on the theoretical analysis.

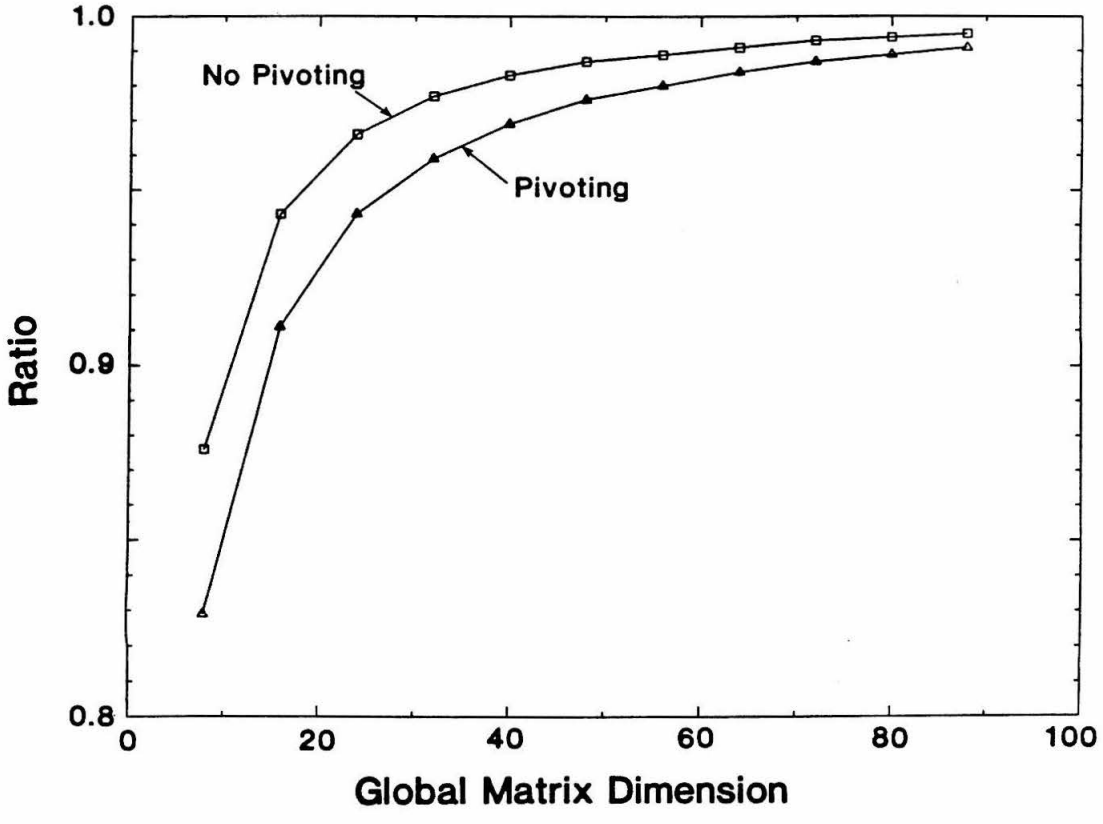
1.0
0.9
0.8
Ratio
No Pivoting
Pivoting
0
20
40
60
80
100
Global Matrix Dimension

Figure 1.

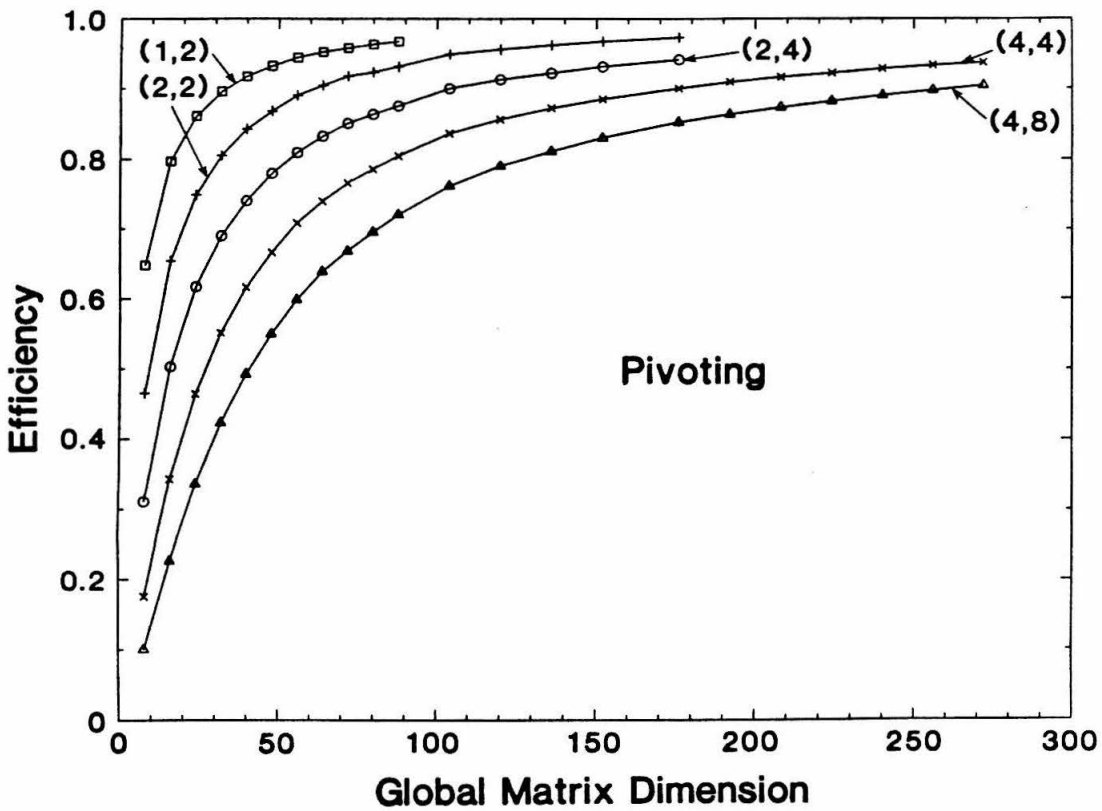
1.0
0.8
0.6
0.4
0.2
0
Efficiency
(1,2)
(2,2)
(2,4)
(4,4)
(4,8)
Pivoting
0
50
100
150
200
250
300
Global Matrix Dimension

Figure 2.

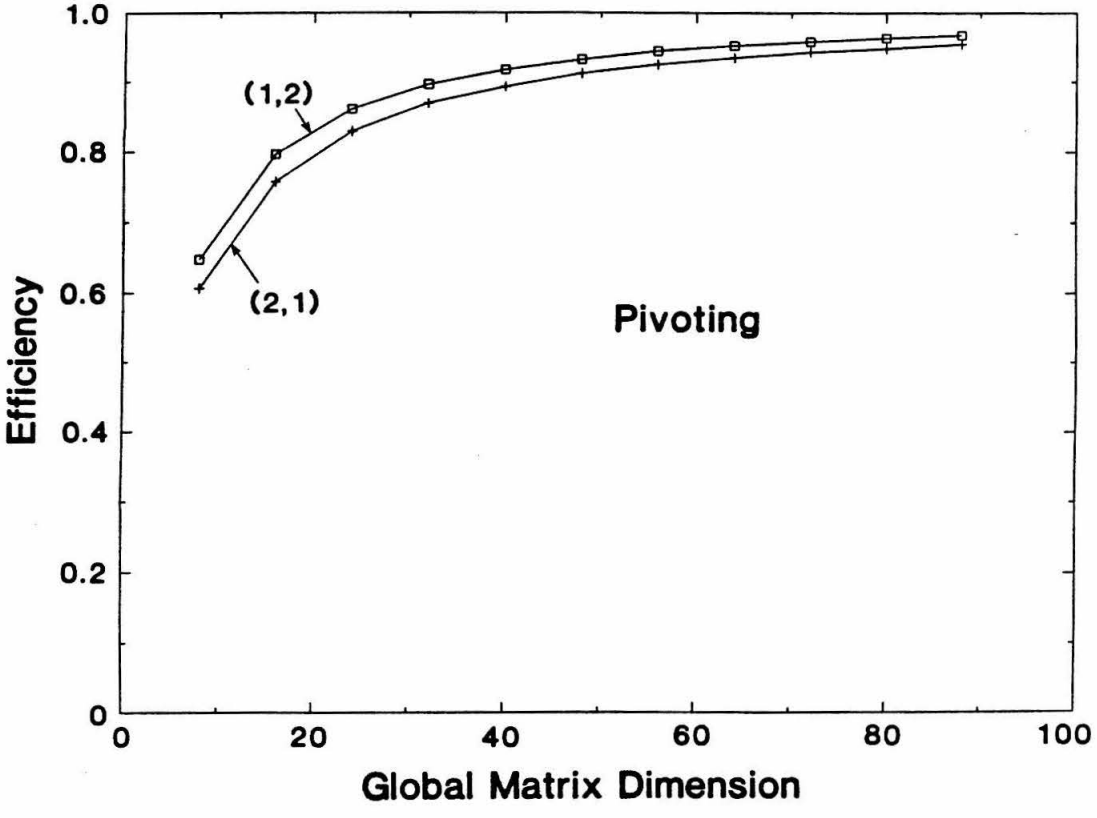
1.0
0.8
0.6
0.4
0.2
0
Efficiency
(1,2)
(2,1)
Pivoting
0
20
40
60
80
100
Global Matrix Dimension

Figure 3.

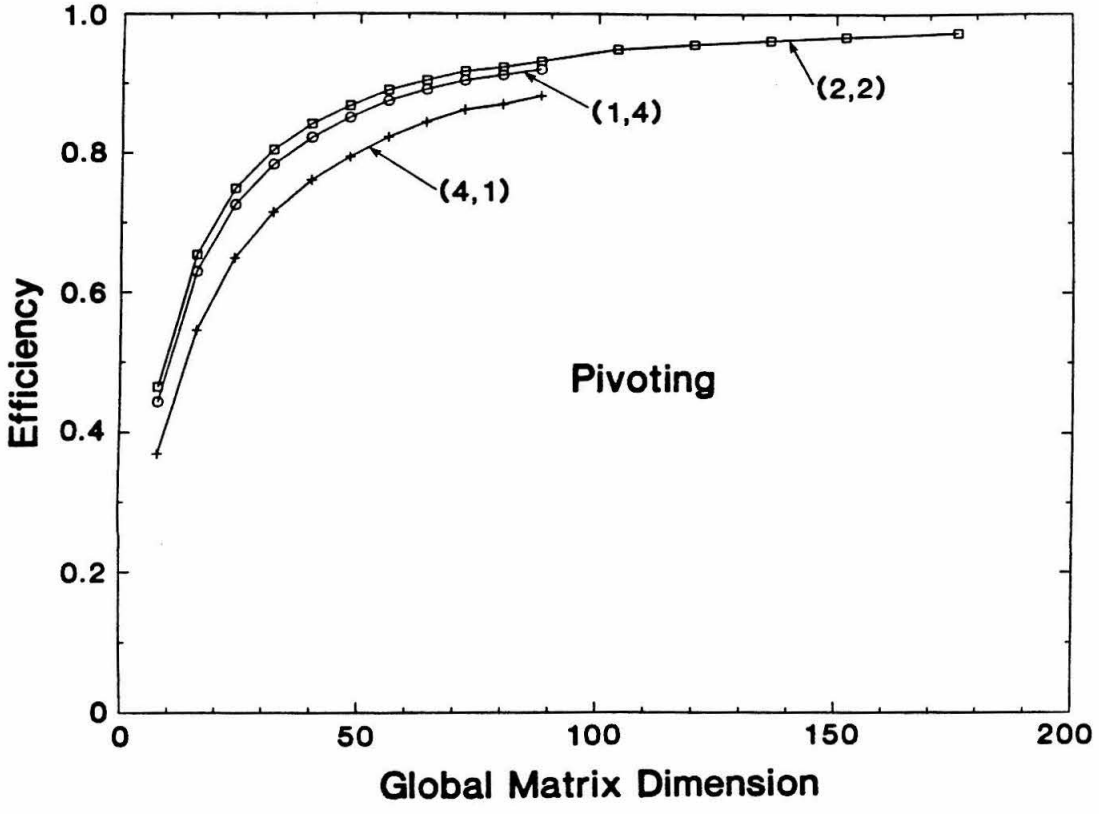
1.0
0.8
0.6
0.4
0.2
0
Efficiency
0
50
100
150
200
Global Matrix Dimension
Pivoting
(2,2)
(1,4)
(4,1)

Figure 4.

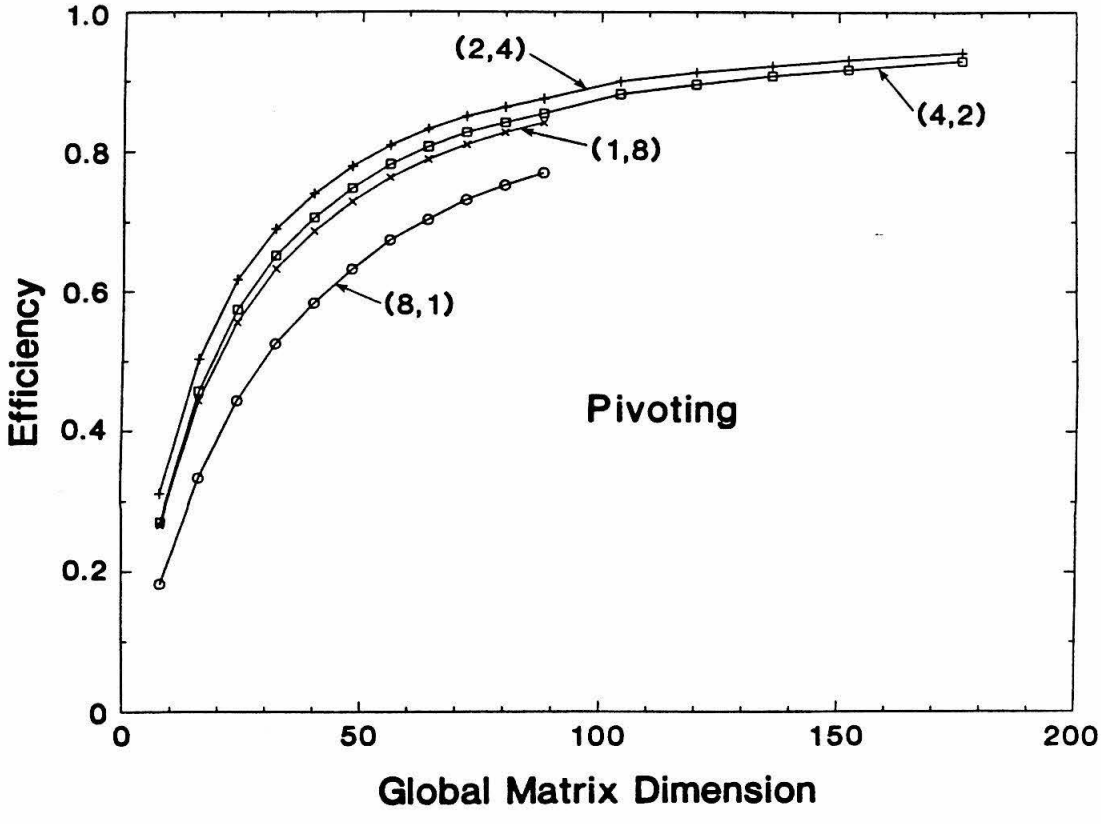
1.0
0.8
0.6
0.4
0.2
0
Efficiency
0
50
100
150
200
Global Matrix Dimension
(2,4)
(4,2)
(1,8)
(8,1)
Pivoting

Figure 5.

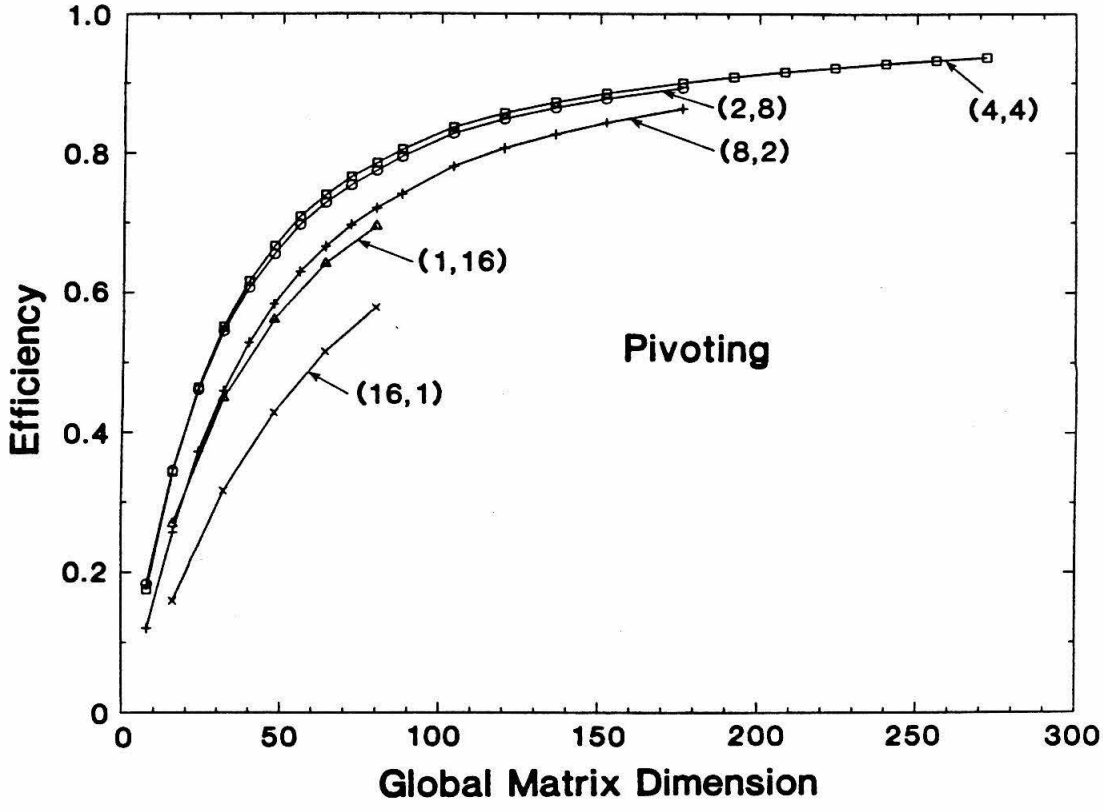
1.0
0.8
0.6
0.4
0.2
0
Efficiency
0
50
100
150
200
250
300
Global Matrix Dimension
(2,8)
(4,4)
(8,2)
(1,16)
Pivoting
(16,1)

Figure 6.

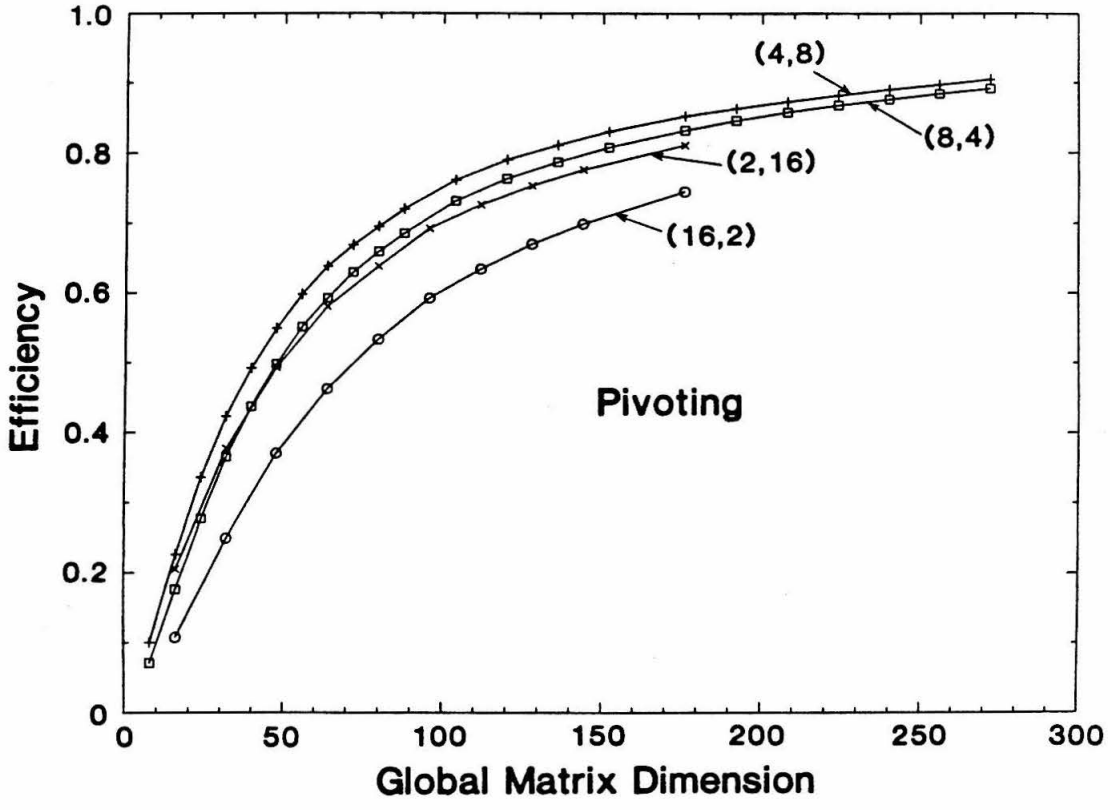
1.0
0.8
0.6
0.4
0.2
0
Efficiency
0
50
100
150
200
250
300
Global Matrix Dimension
(4,8)
(8,4)
(2,16)
(16,2)
Pivoting

Figure 7.

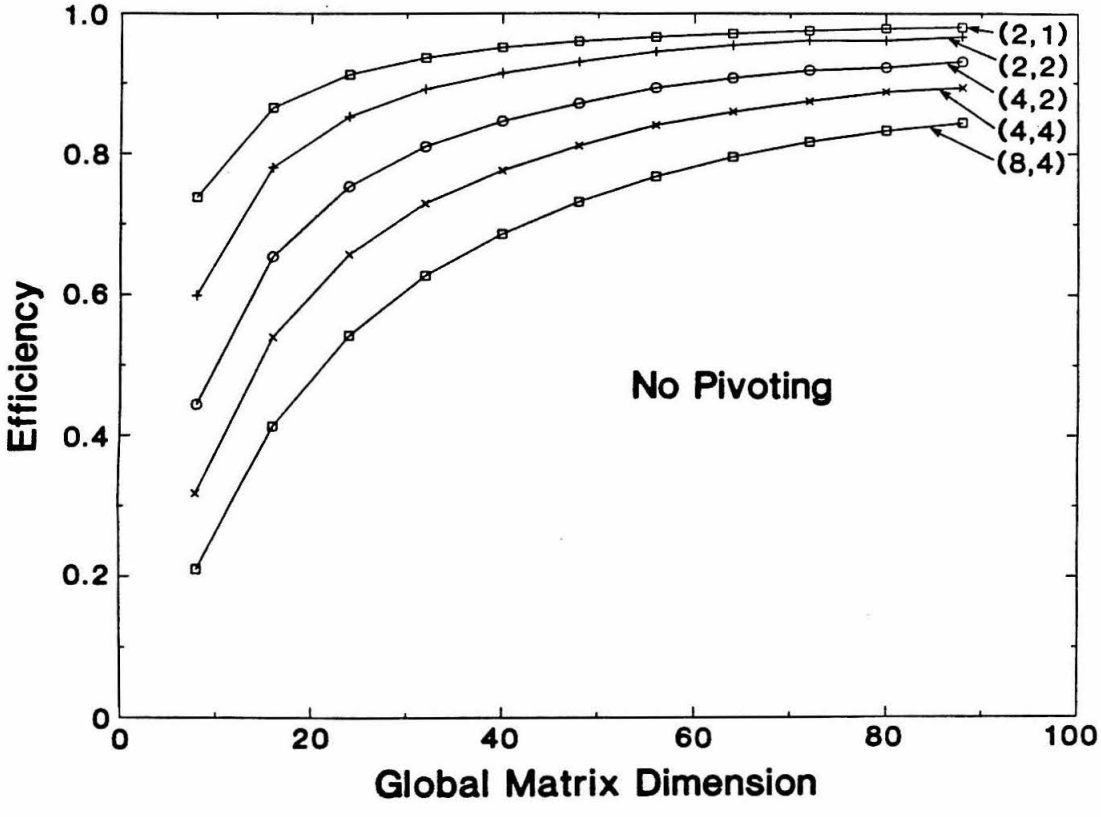
1.0
0.8
0.6
0.4
0.2
0
Efficiency
0
20
40
60
80
100
Global Matrix Dimension
No Pivoting
(2,1)
(2,2)
(4,2)
(4,4)
(8,4)

Figure 8.

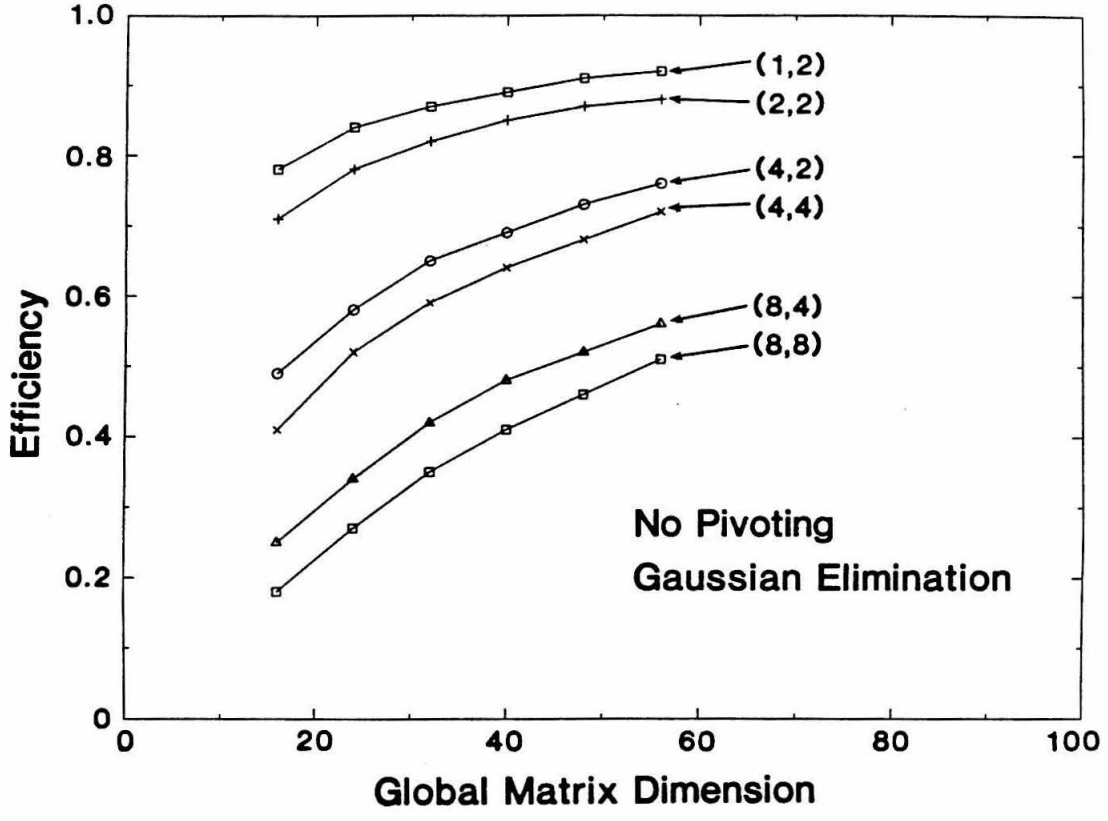
1.0
0.8
0.6
0.4
0.2
0
Efficiency
0
20
40
60
80
100
Global Matrix Dimension
(1,2)
(2,2)
(4,2)
(4,4)
(8,4)
(8,8)
No Pivoting
Gaussian Elimination

Figure 9.

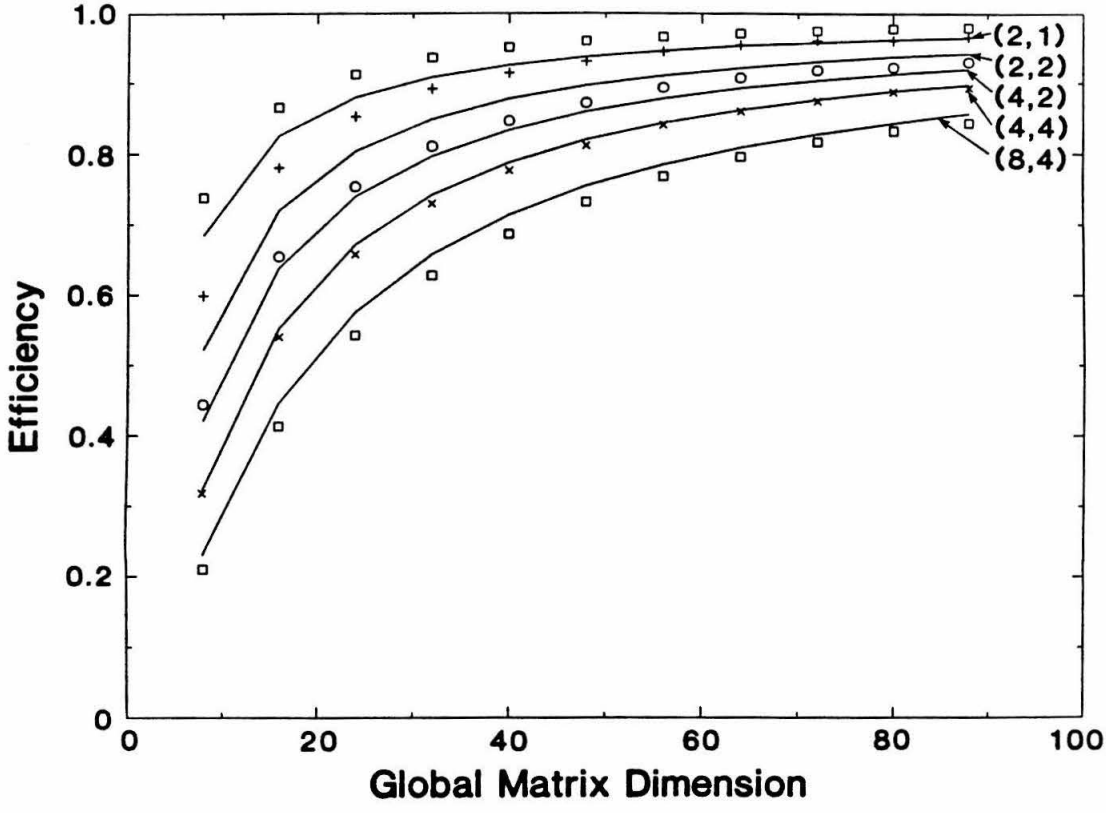
1.0
0.8
0.6
0.4
0.2
0
Efficiency
0
20
40
60
80
100
Global Matrix Dimension
(2,1)
(2,2)
(4,2)
(4,4)
(8,4)

Figure 10.

Reprinted from The Journal of Physical Chemistry, 1986, 90, 3630

A Test of the Babamov–Marcus Vibrationally Adiabatic Theory of Hydrogen Atom Transfer Reactions

Paul G. Hipes[†] and Aron Kuppermann*

Arthur Amos Noyes Laboratory of Chemical Physics, California Institute of Technology,[‡] Pasadena, California 91125 *(Received: January 29, 1986; In Final Form: April 16, 1986)*

Accurate quantum-mechanical reaction probability calculations for a collinear triatomic model of the abstraction of a hydrogen atom from a methane molecule by a methyl radical were performed. The calculations used the method of hyperspherical coordinates and a LEPS potential energy surface having a realistic (13.86 kcal/mol) barrier to reaction. With the same surface, the same reaction probabilities were calculated by using the Babamov–Marcus vibrationally adiabatic model. It was found that for reagents in their ground and first two vibrationally excited states, this model displayed a dynamically correct qualitative behavior. In addition, the reaction probability from the ground vibrational state was accurate to within 6% for translational energies from 0.35 to 0.51 eV.

Introduction

The abstraction of a hydrogen atom from a molecule by a methyl radical is a commonly studied reaction. Arrhenius parameters derived from gas-phase kinetics studies have been tabulated.[1] There has also been much interest in the hydrogen atom abstraction from small organic molecules by methyl radicals in frozen matrices.[2-6] This interest is stimulated by the observation of finite, temperature-independent rate constants at very low temperatures. This phenomenon is interpreted as a manifestation of quantum-mechanical tunneling through a potential energy barrier. The low-temperature experiments are often analyzed with the aid of corrections to transition-state theory to account for tunneling.[7,8] The corrections are based on the solution of one-dimensional barrier penetration problems. A different approach is to model the tunneling in the hydrogen atom transfer by a collinear, three-particle reaction. Although the collinear (two-mathematical-dimensional) constraint is rather severe, some important aspects of the dynamics of light-particle transfer can be gleaned from such a study, not only at the low translational energies at which tunneling is important but also at significantly higher energies.

Collinear heavy–light–heavy (H–L–H) mass systems have generated substantial theoretical activity recently. Until the introduction of hyperspherical coordinates to collinear reactive scattering,[9,10] these systems were difficult to treat quantum mechanically.[11] Now a variety of symmetric[12-15] (A + BA) and asymmetric[16-19] (A + BC) systems have been solved accurately. Some general characteristics of reaction probabilities for the heavy–light–heavy systems have emerged: pronounced oscillatory dependence on collision energy and near conservation of translational energy.[12-15,20] The latter characteristic is equivalent to vibrational adiabaticity in symmetric systems and has been exploited to develop efficient and accurate approximations for collinear reactive scattering in both symmetric[15,20-22] and asymmetric[18,19,23-25] systems. Resonance positions and widths have been approximated in heavy–light–heavy and in more general systems by using the ideas of adiabatic separation of degrees of freedom.[13,15,17,22,26-32] Efforts to extend the collinear heavy–light–heavy results to 3D[33-35] have suggested that the oscillatory collinear reactive probabilities may be manifested as oscillatory cross sections in the real world. It should be recognized that the current intense interest in adiabatic separation of variables has its origins in the early work of Marcus.[36]

In this paper, we present the results of accurate quantum-mechanical calculations for a collinear model of the hydrogen atom exchange between a methane molecule and a methyl radical. The methyl moiety is represented by a structureless point having the mass of the methyl radical. Hyperspherical coordinates are used to formulate the scattering problem exactly.[9,10] Accurate solutions

TABLE I: LEPS Potential Energy Surface Parameters and Characteristics

	C–H interaction	C–C interaction
β/bohr^{-1}	0.9420	0.815
R_e/bohr	2.0662	2.910
D_e/eV	4.7270	3.660
Δ	0.1850	0

barrier height: 13.86 kcal/mol
skew angle: 20.4°
$E(n=0)$ = 0.1803 eV
$E(n=1)$ = 0.5304 eV
$E(n=2)$ = 0.8665 eV
M_H = 1.0078 amu
M_{CH_3} = 15.0235 amu

[†] Work performed in partial fulfillment of the requirements for the Ph.D. degree in Chemistry at the California Institute of Technology.
[‡] Contribution No. 7359.

(1) Kondratiev, V. N. *Rate Constants of Gas Phase Reactions*; Nauka: Moscow, 1970.
(2) Sprague, E. D.; Williams, F. *J. Am. Chem. Soc.* **1971**, *93*, 787.
(3) LeRoy, R. J.; Sprague, E. D.; Williams, F. *J. Phys. Chem.* **1972**, *76*, 546.
(4) Hudson, R. L.; Shiotani, M.; Williams, F. *Chem. Phys. Lett.* **1976**, *48*, 193.
(5) Benderskii, V. A.; Philippov, P. G.; Dakhnovskii, Yu. I.; Ovchinnikov, A. A. *Chem. Phys.* **1982**, *67*, 301.
(6) Trakhtenberg, L. I.; Klochikhin, V. L.; Pshezhetsky, S. Ya. *Chem. Phys.* **1982**, *69*, 121.
(7) Bell, R. P. *The Tunnel Effect in Chemistry*; Chapman and Hall: New York, 1980.
(8) Truhlar, D. G.; Isaacson, A. D.; Garrett, B. C. In *The Theory of Chemical Reaction Dynamics*; Baer, M., Ed.; Chemical Rubber Company: Boca Raton, FL, 1985; Vol. IV, pp 92–110.
(9) (a) Kuppermann, A.; Kaye, J. A.; Dwyer, J. P. *Chem. Phys. Lett.* **1980**, *74*, 257. (b) Dwyer, J. P. Ph.D. Thesis, California Institute of Technology, 1977.
(10) Hauke, G.; Manz, J.; Römelt, J. *J. Chem. Phys.* **1980**, *73*, 5040.
(11) Baer, M. *J. Chem. Phys.* **1975**, *62*, 305.
(12) Manz, J.; Römelt, J. *Chem. Phys. Lett.* **1980**, *76*, 337.
(13) Kaye, J. A.; Kuppermann, A. *Chem. Phys. Lett.* **1981**, *77*, 573.
(14) Manz, J.; Römelt, J. *Chem. Phys. Lett.* **1981**, *81*, 179.
(15) Bondi, D. K.; Connor, J. N. L.; Manz, J.; Römelt, J. *Mol. Phys.* **1983**, *50*, 467.
(16) Kaye, J. A.; Kuppermann, A. *Chem. Phys. Lett.* **1982**, *92*, 574.
(17) Gertitschke, P. L.; Manz, J.; Römelt, J.; Schor, H. H. R. *J. Chem. Phys.* **1985**, *83*, 208.
(18) Coveney, P. V.; Child, M. S.; Römelt, J. *Chem. Phys. Lett.* **1985**, *120*, 349.
(19) Abusalbi, N.; Kouri, D. J.; Lopez, V.; Babamov, V. K.; Marcus, R. A. *Chem. Phys. Lett.* **1984**, *103*, 458.
(20) Hiller, C.; Manz, J.; Miller, W. H.; Römelt, J. *J. Chem. Phys.* **1983**, *78*, 3850.
(21) Babamov, V. K.; Marcus, R. A. *J. Chem. Phys.* **1981**, *74*, 1790.
(22) Aquilanti, V.; Cavalli, S.; Lagana, A. *Chem. Phys. Lett.* **1982**, *93*, 179.
(23) Babamov, V. K.; Lopez, V.; Marcus, R. A. *J. Chem. Phys.* **1983**, *78*, 5621; *Chem. Phys. Lett.* **1983**, *101*, 507; *J. Chem. Phys.* **1984**, *80*, 1812; *J. Chem. Phys.* **1984**, *81*, 3962.
(24) Nakamura, H. *J. Phys. Chem.* **1984**, *88*, 4812.

0022-3654/86/2090-3630$01.50/0

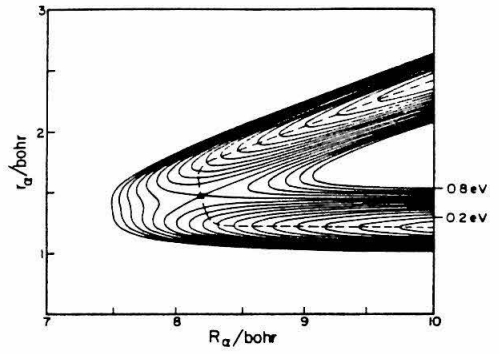

Figure 1. Potential energy contours for the model H_3C–H–CH_3 LEPS surface in Delves mass scaled coordinates (solid lines). The lowest contour is for 0.16 eV, the highest is for 0.8 eV, and the energy increment between consecutive contours is 0.04 eV. The dashed line is the minimum energy path.

to the Schrödinger equation are generated numerically by using a diabatic representation. Reaction probabilities from the lowest three vibrational levels are presented. In addition, transition probabilities calculated by using the Babamov–Marcus vibrationally adiabatic model[21] for symmetric, collinear, heavy–light–heavy systems are compared with the accurate results. This model and its extension to asymmetric systems have been shown to be good at rather low translational energies for reaction from the lowest vibrational level[15,20,22] and from the first vibrationally excited level of the reagent.[19] We will examine the applicability of the adiabatic model for transitions from the first two excited vibrational levels of the reagent in addition to those from the lowest level.

Potential Energy Surface and Convergence

The potential energy surface is of the LEPS form,[37,38] and potential contours are shown in Figure 1. This surface was previously used by Ovchinnikova[39] and by Babamov and Marcus.[21] The barrier height is 13.86 kcal/mol, in accord with the gas-phase activation energy. The LEPS parameters are listed in Table I along with some surface characteristics. It should be noted that the asymptotic Morse parameters do not reproduce any spectroscopic transitions of methane.

The hyperspherical coordinate method used to accurately solve the Schrödinger equation for a collinear, three-particle system has been described elsewhere[9] and will not be repeated here. The adiabatic model will be discussed after the accurate results are presented. The convergence of the accurate numerical results with respect to basis size, projection distance, and other numerical parameters was investigated. The number of circular rings into which configuration space was divided, with a single set of constant hyperradius basis functions per ring, was 40. A basis set of four even and four odd functions was found to be adequate for convergence of the P^R_{00} (see Figure 2) within 1% over the energy range studied (0.2–1.15-eV total energy, with respect to the bottom of the isolated H–CH_3 diatom potential energy curve). P^R_{11} required five even and five odd basis functions, and P^R_{22} required seven even and seven odd basis functions for the same degree of convergence. The numerical method involves a projection of the solutions onto an asymptotic atom–diatom basis set prior to the calculation of the scattering matrix and transition probabilities. For the latter to become independent of the atom–diatom distance at which this projection is performed, to within the convergence mentioned, it sufficed to integrate the coupled radial equations from an initial value of the hyperradius of 5.4 bohrs out to 20 bohrs.

The adiabatic model used requires the solution of two uncoupled ordinary differential equations to obtain phase shifts, and convergence was obtained with respect to the corresponding discretization parameters.

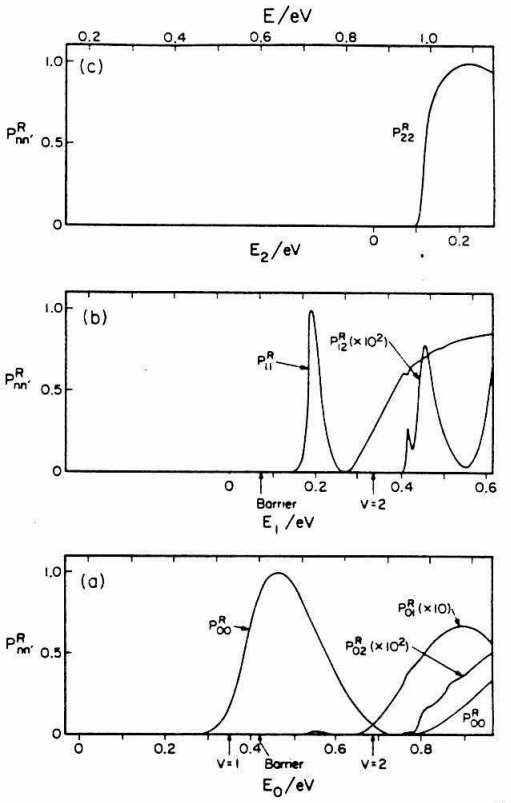

Figure 2. Accurate transition probabilities as a function of energy. $P^R_{nn'}$ indicates the reaction probability from vibrational level n of the reagents to the vibrational level n' of the reaction products. The scale on the bottom abscissa on each panel denotes the translational energy of the reagent. The scale on the upper abscissa of the top panel denotes the total system energy measured from the bottom of the isolated reagent potential energy curve. This scale is common to all panels. The number in parentheses beside some of the curves indicates the factor used to multiply the results before plotting. The arrows labeled "barrier" in the bottom abscissa of panels a and b indicate the energy of the classical barrier height.

Results of Accurate Calculations

Figure 2 shows the accurate reaction probabilities from the first three levels of the reagent. The first feature of the results which

(25) Nakamura, H.; Ohsaki, A. *J. Chem. Phys.* **1985**, *83*, 1599.
(26) Kuppermann, A.; Dwyer, J. P. *Abstracts of Papers*, 11th International Conference on the Physics of Electronic and Atomic Collisions, Kyoto, Japan; Society for Atomic Collision Research: Tokyo, Japan, 1979; pp 888, 889.
(27) Launay, J. M.; LeDourneuf, M. *J. Phys. B* **1982**, *15*, L455.
(28) Römelt, J. *Chem. Phys.* **1983**, *79*, 197.
(29) Manz, J.; Schor, H. H. R. *Chem. Phys. Lett.* **1984**, *107*, 542.
(30) Kulander, K. C.; Manz, J.; Schor, H. H. R. *J. Chem. Phys.* **1985**, *82*, 3088.
(31) Manz, J.; Pollak, E.; Römelt, J. *Chem. Phys. Lett.* **1982**, *86*, 26.
(32) Pollak, E.; Römelt, J. *J. Chem. Phys.* **1984**, *80*, 3613.
(33) Pollak, E.; Baer, M.; Abusalbi, N.; Kouri, D. *Chem. Phys.* **1985**, *99*, 15.
(34) Abusalbi, N.; Kim, S. H.; Kouri, D. J.; Baer, M. *Chem. Phys. Lett.* **1984**, *112*, 502.
(35) Baer, M.; Last, I. *Chem. Phys. Lett.* **1985**, *119*, 393.
(36) Marcus, R. A. *J. Chem. Phys.* **1964**, *41*, 603, 610; *J. Chem. Phys.* **1965**, *43*, 1598.
(37) Sato, S. *J. Chem. Phys.* **1955**, *23*, 592, 2465.
(38) Kuntz, P. J. In *Dynamics of Molecular Collisions* – Part B, Miller, W. H., Ed.; Plenum: New York, 1976; pp 65–69.
(39) Ovchinnikova, M. Ya. *Chem. Phys.* **1979**, *36*, 85.

is noticed is the dominance of reactive transitions which preserve the vibrational quantum number (i.e., vibrationally adiabatic transitions). Reactive transitions between the states whose quantum numbers differ by unity are an order of magnitude smaller than the adiabatic ones. A change of two vibrational quanta is 2 orders of magnitude less probable than conservation of the quantum number. (The small oscillations in the P^0_{02} curve of Figure 2 probably represent numerical inaccuracies.) This near conservation of vibrational quantum number has been observed in a number of other collinear calculations consisting of the transfer of a light particle between two heavier ones (H–L–H) of equal mass.[12-15]

The effect is kinematic in origin and is explained by an argument analogous to that used in the Born–Oppenheimer separation of nuclear and electronic motion.[21,40] At low translational energies, the light particle (the hydrogen atom in the present case) vibrates quickly on the time scale of the heavy-particle motion. In an approximate sense, the two heavy particles approach and recede in a potential averaged over the vibrational motion of the light particle. As the translational energy of relative motion increases, the decoupling of the vibrational and translational motion is less accurate. It is inherent in this picture that the vibrational quantum number is unaffected by the collision of the atom and the diatomic molecule and hence is adiabatic. The concept that the transfer of a light particle between heavy ones can be approached via an adiabatic separation between the corresponding degrees of freedom has been used previously, as discussed in the Introduction. It has also been argued that a natural adiabatic separation between the hyperradial and hyperangular motions exists for general mass combinations when hyperspherical coordinates are utilized.[26,41] This near-adiabatic separation is responsible for the rapid convergence of coupled channel expansions in these coordinates. The general argument for the separation of time scales in reactive transitions focuses attention on the strong interaction region of the potential energy surface (Figure 1). In this region, as the particle moves from reagent channel to product channel, the hyperangle (plane polar angle for collinear triatomic systems) changes by a large fraction of its allowed range while the hyperradius (plane polar radius for collinear triatomic systems) changes relatively little, which results in an adiabatic separation of angular and radial motion.[9b,26] However, as pointed out by Babamov and Marcus,[21] the class of heavy–light–heavy mass combinations is the one for which the adiabatic separation is expected to be most valid. Under these conditions, only vibrationally adiabatic transfer processes would be expected. This agrees qualitatively with the results in Figure 2.

Another prominent characteristic of the accurate results is the significant degree of tunneling from the lowest vibrational level of the reagent to that of the product. For energies above the classical barrier height, to determine the fraction of reactive probability flux which passes into the product channel via tunneling through classically forbidden regions of configuration space requires an analysis of the probability current density streamlines.[42a] However, below the classical barrier height, any reactive flux is necessarily due to tunneling. From Figure 2a, we see that the probability for reaction from the $n = 0$ level of the reagent to the $n = 0$ level of the product is significant at energies below the classical barrier. For energies close to that barrier but still below it, the reactive pathway dominates over the nonreactive one. The physical reason for the prominence of tunneling is the heavy–light–heavy mass combination. Such mass combinations lead to small Delves skew angles.[42b] A particle approaching the strong interaction region does not have to penetrate the barrier at the saddle point to move into the product channel. It can cut the corner over a significant portion of configuration space for which the classically forbidden region is narrow (i.e., has a width of the order of the system's local de Broglie wavelength or less[42c]). The heavy–light–heavy mass combination increases this region of configuration space. The result is increased tunneling for such combinations. In the low-temperature abstraction of hydrogen atoms by radicals, the presence of apparent tunneling phenomena is not at all surprising from a theoretical standpoint. It has long been understood that tunneling probabilities in one dimension increase as the particle mass decreases. The collinear model, which involves two mathematical dimensions, has led us to a clearer perspective, namely that tunneling can occur by corner-cutting away from the saddle point.[42a,43]

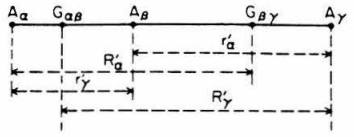

Figure 3. Coordinates for a collinear triatomic system.

In summary, the reaction dynamics of this collinear model of hydrogen atom abstraction from methane by a methyl radical is characterized by dominance of vibrational adiabaticity and significant tunneling from the $n = 0$ level.

Vibrationally Adiabatic Model

The treatment given here roughly parallels that of ref 21 and is provided for completeness. Let A_α, A_β, and A_γ represent the three atoms of mass m_α, m_β, and m_γ, respectively. We define two sets of coordinates R_α', r_α' and R_γ', r_γ' shown in Figure 3, where $G_{\beta\gamma}$ and $G_{\alpha\beta}$ are the centers of mass of $A_\beta A_\gamma$ and $A_\alpha A_\beta$, respectively. Let the subscript λ take on the values α or γ. Both sets of coordinates can then be represented by R_λ', r_λ'. We now define the Delves scaled coordinates[44,45] R_λ, r_λ as

$$R_\lambda = a_\lambda R_\lambda' \tag{1}$$

$$r_\lambda = a_\lambda^{-1} r_\lambda' \tag{2}$$

where

$$a_\lambda = (\mu_{\lambda,\nu\kappa}/\mu_{\nu\kappa})^{1/4} \tag{3}$$

$$\mu_{\lambda,\nu\kappa} = \frac{m_\lambda(m_\nu + m_\kappa)}{m_\lambda + m_\nu + m_\kappa} \tag{4}$$

and

$$\mu_{\nu\kappa} = \frac{m_\nu m_\kappa}{m_\nu + m_\kappa} \tag{5}$$

The set of indices $\lambda,\nu\kappa$ stands for either $\alpha,\beta\gamma$ or $\gamma,\beta\alpha$.

The hyperspherical coordinates ρ and ϑ_λ are defined by[9,10,44,45]

$$\rho = (R_\lambda^2 + r_\lambda^2)^{1/2} \tag{6}$$

$$\vartheta_\lambda = \arctan(r_\lambda/R_\lambda) \qquad 0 \le \vartheta_\lambda \le \pi/2 \tag{7}$$

The Schrödinger equation in these coordinates is

$$\left[\frac{-\hbar^2}{2\mu}\left(\frac{\partial^2}{\partial\rho^2} + \frac{1}{\rho}\frac{\partial}{\partial\rho} + \frac{1}{\rho^2}\frac{\partial^2}{\partial\vartheta_\lambda^2}\right) + V(\rho,\vartheta_\lambda) - E\right]\psi(\rho,\vartheta_\lambda) = 0 \tag{8}$$

where

$$\mu = \left(\frac{m_\alpha m_\beta m_\gamma}{m_\alpha + m_\beta + m_\gamma}\right)^{1/2} \tag{9}$$

(40) Born, M.; Oppenheimer, J. R. *Ann. Phys.* **1927**, *84*, 457.
(41) Fano, U. *Phys. Rev. A* **1981**, *24*, 2402.
(42) Kuppermann, A. In *Theoretical Chemistry: Advances and Perspectives*; Henderson, D., Ed.; Academic: New York, 1981; Vol 6A, (a) pp 100–107, (b) p 85, (c) pp 86–87.
(43) Garrett, B. C.; Truhlar, D. G.; Wagner, A. F.; Dunning, Jr., T. H. *J. Chem. Phys.* **1983**, *78*, 4400.
(44) Delves, L. M. *Nucl. Phys.* **1959**, *9*, 391.
(45) Delves, L. M. *Nucl. Phys.* **1960**, *20*, 275.

A discrete basis set in the hyperangle ϑ_λ is defined by

$$\left[-\frac{\hbar^2}{2\mu\rho^2}\frac{d^2}{d\vartheta_\lambda^2} + V(\rho,\vartheta_\lambda) - \epsilon_n(\rho)\right]\chi_n(\vartheta_\lambda;\rho) = 0 \quad (10)$$

with

$$\chi_n(\vartheta_\lambda=0;\rho) = \chi_n(\vartheta_\lambda=\vartheta_{\lambda max};\rho) = 0 \quad (11)$$

and

$$\int_0^{\vartheta_{\lambda max}} \chi_n(\vartheta_\lambda;\rho)\,\chi_{n'}(\vartheta_\lambda;\rho)\,d\vartheta_\lambda = \delta_n^{n'} \quad (12)$$

where ρ is considered a parameter and $\vartheta_{\lambda max}$ is the Delves skew angle. When the wave function $\psi(\rho,\vartheta_\lambda)$ is expanded in this basis set, according to

$$\psi(\rho,\vartheta_\lambda) = \rho^{-1/2}\sum_{n=0}^{\infty} g_n(\rho)\,\chi_n(\vartheta_\lambda;\rho) \quad (13)$$

an infinite set of coupled, ordinary differential equations, equivalent to the original Schrödinger equation, results:

$$\left[\frac{-\hbar^2}{2\mu}\frac{d^2}{d\rho^2} + \epsilon_n(\rho) - E - \frac{\hbar^2}{8\mu\rho^2}\right]g_n(\rho) + \sum_{n'=0}^{\infty}\left(\frac{-\hbar^2}{2\mu}\left\langle\chi_n\left|\frac{\partial^2}{\partial\rho^2}\right|\chi_{n'}\right\rangle - \frac{\hbar^2}{\mu}\left\langle\chi_n\left|\frac{\partial}{\partial\rho}\right|\chi_{n'}\right\rangle\frac{d}{d\rho}\right)g_{n'}(\rho) = 0 \quad (14)$$

For a symmetric mass combination, the solutions can be chosen to have a definite parity, even or odd. Solutions of different parity are rigorously decoupled. If the entire sum over n' in eq 14 is neglected, a single ordinary differential equation for each n and each parity results. This neglect is the central feature of the adiabatic approximation. The scattering matrix can then be expressed in terms of the resulting even and odd phase shifts.[21] The square of the elements of this matrix gives the corresponding transition probabilities $P_{nn'}^R$, according to

$$P_{nn'}^R = \sin^2(\delta_n^s - \delta_n^a) \quad (15)$$

where δ_n^s is the phase shift for the symmetric solution for state n and δ_n^a is that for the corresponding antisymmetric solution.[46] The numerical procedure used for implementing the adiabatic approximation was as follows. The eigenvalue equation (10) for $\epsilon_n(\rho)$ was solved for a grid of values of ρ. These eigenvalues form part of an effective potential for the $g_n(\rho)$. They are depicted in Figure 4 for $n = 0$, 1, 2 as asymptotically degenerate pairs of curves, the lower curve of each pair corresponding to even parity and the upper one to odd parity. The (uncoupled) ordinary differential equation for the adiabatic model $g_n(\rho)$ was then solved numerically, as an initial value problem, by using an Adams–Moulton integrator, and from the asymptotic behavior of the $g_n(\rho)$ at large ρ, the phase shifts were obtained. It should be stressed that the scheme just outlined is 2 orders of magnitude faster than a solution of the set of coupled differential equations (14) which must be used in general. The diagonal term $(\hbar^2/2\mu)\langle\chi_n|\partial^2/\partial\rho^2|\chi_n\rangle$ was not included in the effective potential used to calculate $g_n(\rho)$. Römelt[28] has shown that this diagonal term is important for the adiabatic modeling of resonances in non-heavy–light–heavy systems. The diagonal term $\langle\chi_n|\partial/\partial\rho|\chi_n\rangle$ is identically zero for real χ_n, as in the present case.

Figure 5 shows the reactive probabilities calculated with the adiabatic model along with the corresponding probabilities obtained from the accurate calculations. It can be seen that the adiabatic model results for $n = 0$ agree very well with the accurate ones for low translational energies. For example, at translational energies in the range 0.35–0.51 eV, the difference between the two is only 6% or less. For higher energies, these approximate $n = 0$ results show the qualitative behavior of the accurate ones

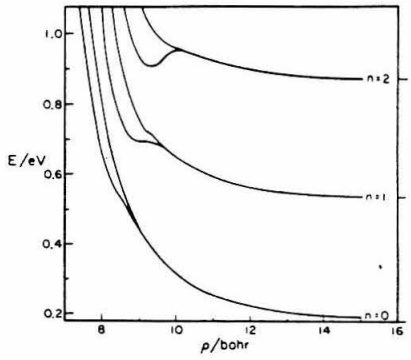

Figure 4. Eigenvalues $\epsilon_n(\rho)$ of the adiabatic basis as a function of the hyperradius. The eigenvalues are measured from the bottom of the isolated reagent molecule potential energy curve. The tic marks on the right vertical axis represent the isolated reagent eigenvalues. These curves become pairwise degenerate as ρ increases. For each such pair, the lower (upper) curve corresponds to even (odd) parity.

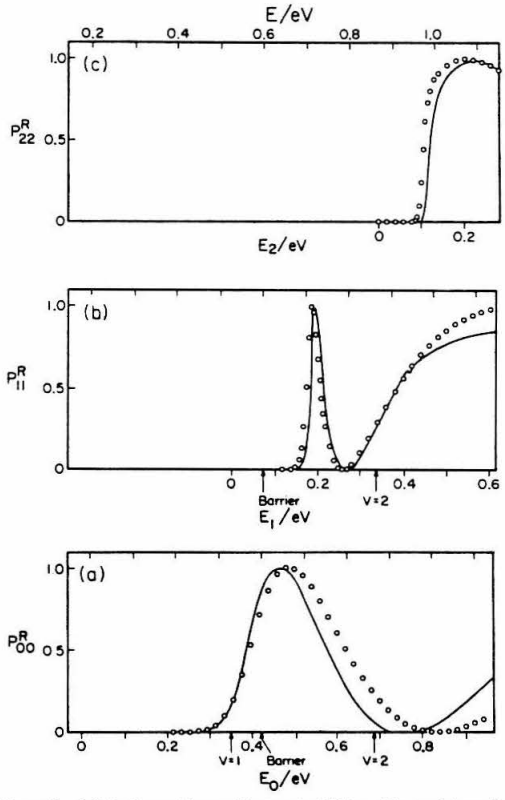

Figure 5. Adiabatic model transition probabilities. The model results are presented by open circles (O), and the corresponding accurate results are represented by the solid lines and are the same as in Figure 2. Scales are the same as in Figure 2.

but are shifted in energy. The correct qualitative behavior is also displayed by the $n = 1$ and $n = 2$ adiabatic model results, again with a slight energy shift. This suggests that improvements in this model may be possible via energy scaling, first-order per-

(46) Mott, N. F.; Massey, H. S. W. *Theory of Atomic Collisions*, 3rd ed.; Oxford University Press: Oxford, 1965; p 349.

turbation corrections, optical potentials, or other appropriate approaches. From these results, it appears that for heavy–light–heavy systems like the one studied in this paper, the hyperspherical adiabatic decoupling approximation provides a good qualitative picture of the dynamics even for vibrationally excited reagents. This is very significant since the difference in computational effort between the accurate and approximate methods is substantial and because of the insight this model provides. The qualitative correctness of the decoupling approximation for vibrationally excited reagent states for the present symmetric system is in accord with the results of Abusalbi et al.[19] for reaction from the first excited state of an asymmetric system. Low translational energy processes are chemically very important, and accurate dynamical approximations such as the one developed by Babamov and Marcus[21] are very useful.

Conclusions

We have presented the results of an accurate quantum-mechanical calculation for a collinearly constrained model of the abstraction of a hydrogen atom from methane by a methyl radical. The dynamics have the general characteristics already noted for other heavy–light–heavy systems. The rather large barrier to reaction (13.86 kcal/mol), involving a saddle point whose energy is greater than that of the ground-state reagent, allows tunneling to be observed clearly. For heavy–light–heavy systems with small barriers to reaction (less than 2 kcal/mol)[13,14,16] the detection of tunneling is less straightforward. We have tested the hyperspherical vibrationally adiabatic model of Babamov and Marcus[21] and found that it describes the general dynamics of this system rather well for the ground and the first two vibrationally excited states of the reagents. In addition, the reaction probabilities for the ground state of the reagent are accurate to within 6% for translational energies in the range 0.35–0.51 eV.

Acknowledgment. This work was supported in part by the Air Force Office of Scientific Research (Contract No. AFSOR-82-0341).

Registry No. Methane, 74-82-8; methyl, 2229-07-4.